Mathematical modeling of molecular mechanisms governing cell cycle progression in *Caulobacter crescentus* and differentiation of immune system progenitor cells.

Bronson R. Weston

Dissertation submitted to the faculty of the Virginia Polytechnic Institute and State University in partial fulfillment of the requirements for the degree of

Doctor of Philosophy
in
Genetics, Bioinformatics and Computational Biology

John J. Tyson, Chair
Yang Cao
Birgit Scharf
William Baumann

December 15, 2020
Blacksburg, VA

Keywords: Systems biology, asymmetrical cell division, protein regulatory networks, hematopoiesis

Mathematical modeling of molecular mechanisms governing cell cycle progression in *Caulobacter crescentus* and differentiation of immune system progenitor cells.

Bronson R. Weston

ABSTRACT

Mathematical modeling of biological systems can be useful to reveal new insights into biological observations. Here we apply mathematical modeling to study the underlying molecular networks driving observed behaviors of two systems. First, we apply systems biology and dynamic systems theory techniques to reveal new insights into the process of hematopoiesis. More specifically, we search the literature to deduce the underlying molecular mechanism that drives cell fate determination in granulocyte-monocyte progenitor (GMP) cells that are exposed to various cytokines. By converting this molecular mechanism into a set of ordinary differential equations (ODEs), we acquired new insights into the behavior of differentiating GMP cells.

Next, we explore the cell cycle of the model prokaryotic organism, *Caulobacter crescentus*. *Caulobacter* is a uniquely successful oligotrophic bacterium, found abundantly in freshwater systems. While it is not a pathogenic species, *Caulobacter* is extremely well studied due to its distinguishable asymmetrical morphology and the ability to synchronize populations by cell cycle stage. We built a detailed mathematical model of the molecular mechanism driving the cell cycle. This research suggests a previously unknown role for the unknown form of the master regulator, CtrA, in regulating the G1-S transition. Furthermore, we incorporate a nutrient signaling model into the cell cycle model to investigate how *Caulobacter* responds to nutrient deprivation. We find that regulation of DivK phosphorylation is an essential component of the nutrient signaling pathway and demonstrate how starvation signals work together in synergy to manifest in observed cell cycle response.

Mathematical modeling of molecular mechanisms governing cell cycle progression in *Caulobacter crescentus* and differentiation of immune system progenitor cells.

Bronson R. Weston

GENERAL AUDIENCE ABSTRACT

Every cell in the human body has the same DNA, yet there are cells of all kinds with different jobs, appearances and behaviors. This simple concept is a consequence of complex regulatory systems within cells that dictate what genes are expressed and when. This dissertation breaks down the molecular mechanisms that regulate gene expression in cells and how these mechanisms result in the interesting behaviors and morphologies that have been observed experimentally. By deriving mathematical equations to describe the molecular mechanisms, we simulate how cell behavior might change under different conditions to make novel discoveries. More specifically, we utilize these techniques to study the freshwater bacterium, *Caulobacter crescentus*, and human cells of the white blood cell lineage. We utilize our models to identify previously unknown aspects of the molecular mechanisms, develop explanations for mysterious cell behaviors and provide interesting predictions that have not been explored experimentally.

Acknowledgements

To my primary advisor, Dr. John J. Tyson: I appreciate all of the wisdom you have passed to me, the time you have spent on reading and editing my dense scientific papers, and for your continuous support for the five and a half years I have attended Virginia Tech. Even after your retirement, you continue to provide unparalleled guidance. Thank you.

To my secondary advisors, Dr. Liwu Li and Dr. Yang Cao: Without you, my studies would not have been possible. I appreciate all of your support over the years.

To my committee: Thank you for your challenging questions and for reading through this lengthy dissertation. Most importantly, thank you for (hopefully) approving my PhD.

To my lab mate, Chunrui Xu: It has been awesome working with you! I have great respect for your work ethic and your dedication to our projects. Thank you for all of your help over the last few years. It has been a pleasure to work with you.

To my immediate family: Rebekah, Sabrina, Susan, and Bret. Thank you from the bottom of my heart for your unconditional love. Without your love and encouragement, I would not be where I am today. Thank you for your persistent phone calls, reminding me to speak with you when I get lost in my studies. And thank you for always believing in me. Specifically, to my mother, Susan: Thank you for all of your financial support. From hiring a tutor for me when I was 2-3 years behind in elementary school to assisting me with my medical bills after my leg fracture last year. I appreciate everything you have done for me.

To all of the friends that I have made on this journey in Blacksburg, thank you. Being there to get some beers, to go on a hike, or just to chat has made all the difference in my ability to cope with the stresses of PhD life.

To my beloved girlfriend, Alexis. I thank you with all my heart for your immeasurable love, which has made difficult times so much easier. Your drive to improve as a person has helped me continue to strive for personal growth. Your work ethic and dedication to your studies have helped to keep me focused on my own studies. I could always count on you to support me when my motivation was lacking. Thank you.

Lastly, I give my eternal thanks to my old professor, advisor and friend, Dr. Prasad Dhurjati. You helped me discover my passion for systems biology and research. You helped me

to decide on attending Virginia Tech to study in the Tyson lab. I even discovered my passion for the gut microbiome through my research with you, and now I am pursuing a career in the microbiome sector. I cannot imagine where I would be if it were not for your mentorship, but I would certainly not be where I am today. I am forever thankful for your wisdom, enthusiasm, support, and generous spirit. May your soul forever rest in peace.

Attributions

The work described in this dissertation is supported by the NIH grant, HL115835, and the NSF grants, NSF 1613741 and NSF 1909122. Additionally, support was provided by the program of Genetics, Bioinformatics and Computational Biology at Virginia Tech. The funders had no role in study design, data collection and analysis, decision to publish, or preparation of manuscripts.

Chapters 2-5 in this dissertation consist of manuscripts that have been published or will be submitted for publication in the near future.

Chapter 2: Weston, B. R., Li, L., & Tyson, J. J. (2018). Mathematical analysis of cytokine-induced differentiation of granulocyte-monocyte progenitor cells. Frontiers in immunology, 9, 2048.
Chapter 3 and 4: Weston, B. R., Cao, Y., & Tyson, J. J. Computational Investigation of CtrA:*Cori* Binding Suggests a New Role for Unphosphorylated CtrA in the *Caulobacter crescentus* Cell Cycle. (To be submitted)
Chapter 5: Weston, B. R., Xu, C., Cao, Y., & Tyson, J. J. Coping with Stress: The *Caulobacter* approach. (To be submitted)

The contributions of co-authors are as follows:

Dr. John J. Tyson aided in the conceptualization and the derivation of the models. He is a co-author author on all manuscripts/chapters incorporated into this dissertation and the corresponding author on the manuscript corresponding to Chapter 2. He assisted in the writing of manuscripts and provided office space and materials (e.g. computers) for the projects.

Dr. Yang Cao provided funding for Chapters 3, 4 and 5 of this dissertation and is the corresponding author on relevant manuscripts. He provided insight into computational methods and helped in the conceptualization of these chapters.

Dr. Liwu Li provided partial funding for the project of Chapter 2 and played a heavy role in the conceptualization of the relevant research. He is a co-author of the relevant manuscript.

Chunrui Xu will be a co-first author on the manuscript corresponding to Chapter 5 (to be submitted). She assisted in the development of figures, literature review, development of the model and result simulations and analysis.

Table of Contents

Acknowledgements iv

Attributions vi

Chapter 1 : Introduction 1

1.1 Cellular differentiation and division 1

1.2 Hematopoiesis 1

1.3 *Caulobacter crescentus* is a model organism 3

1.4 Implementing a systems approach to study molecular biology 4

1.5 Mathematical modeling of differentiation and cell cycle dynamic 5

Chapter 2 : Mathematical Analysis of Cytokine-Induced Differentiation of Granulocyte-Monocyte Progenitor Cells 7

2.1 Abstract 7

2.2 Introduction 8

2.3 Materials and methods 10

2.3.1 The proposed regulatory network and its molecular basis 10

2.3.2 Conversion of the interaction diagram into a mathematical model 14

2.3.3 Computational methods 16

2.3.4 Assumptions 18

2.4 Results 19

2.4.1 A motif for GMP cell differentiation 19

2.4.2 M-CSF induces monopoiesis 23

2.4.3 G-CSF induces granulopoiesis 24

2.4.4 Low concentrations of GM-CSF favor monopoiesis while higher concentrations favor granulopoiesis 26

2.4.5 GM-CSF induces M-MDSC differentiation 30

2.4.6 Combined treatment with G-CSF and M-CSF results in a heterogeneous population of granulocytes and monocytes 34

2.4.7 G-CSF can push cells towards monopoiesis in low signaling conditions 35

2.4.8 G-CSF can inhibit or encourage M-MDSC development when paired with M-CSF and GM-CSF 37

2.4.9 M-CSF can induce M-MDSC differentiation when mixed with GM-CSF 37

2.5 Discussion 38

2.5.1 Concentration-dependent effects of GM-CSF signaling on GMP differentiation 38

2.5.2 Differences among CSF-induced differentiation processes 39

2.5.3 GM-CSFR expression patterns of myeloid cells 40

2.5.4 Dynamics of the monocytic myeloid-derived suppressor cell 41
2.5.5 CSF synergies and crosstalks 42
2.5.6 CSFs as clinical targets 42
2.5.7 Network Topology 44
2.5.8 Limitations of model 44
2.5.9 Summary 45
Chapter 3 : Deriving a Mathematical Model of the *Caulobacter* cell cycle 47
3.1 Model Derivation 47
3.1.1 Modeling Genetic Regulation 47
3.1.2 Protein Complexes and Phosphorylation 51
3.1.3 Localization 53
3.1.4 Swarmer vs. Stalked Simulations 55
3.1.5 CtrA/*Cori* Binding 55
3.1.6 Considering Increased Complexity of CtrA:DNA binding 59
3.1.7 Chromosome Replication 61
3.2 Biological Mechanisms 63
3.2.1 Methylation of DNA 63
3.2.2 Regulation of CtrA 64
3.2.3 CckA kinase/phosphatase regulation 66
3.2.4 Regulation of DnaA and GcrA 66
3.2.5 PleC and DivJ 68
3.2.6 cdG 70
3.2.7 Z-ring 71
3.2.8 Cell growth 73
3.3 Parameter Estimation 74
3.3.1 Random-walk algorithm 74
3.3.2 Cost Function 77
Chapter 4 : Computational Investigation of CtrA:*Cori* Binding Suggests a New Role for Unphosphorylated CtrA in the *Caulobacter crescentus* Cell Cycle 84
4.1 Abstract 84
4.2 Introduction 84
4.3 Materials and Methods 88
4.3.1 General Simulation Methodology 88
4.3.2 Quantification and Statistical Analysis 89
4.4 Results 89

4.4.1 CtrA competes with CtrA~P for *Cori* binding sites. 90
4.4.2 Caulobacter Cell Cycle Model 94
4.4.3 Unphosphorylated CtrA interacts with *Cori* to ensure timely initiation of chromosome replication 98
4.4.4 Parameter sets tuned without the $CtrA_U$:*Cori* interaction alleviate high rates of cell cycle arrest but deviate from experimental observations 100
4.4.5 Introducing $CtrA_U$:*Cori* interactions improves the behavior of $CORI^-$ simulations 103
4.5 Discussion 103
Chapter 5 : Molecular mechanisms of cell cycle arrest in carbon and nitrogen starved *Caulobacter* populations 112
5.1 Abstract 112
5.2 Introduction 113
5.2.1 Molecular Response to Carbon and Nitrogen Starvation in *Caulobacter* 114
5.3 Methods 117
5.3.1 Improvement to SciP modeling 118
5.3.2 Modeling PTS^{Ntr}/SpoT nutrient signaling cascade through cdG: 118
5.3.3 Modelling other Starvation Signaling Pathways 119
5.3.4 An unknown Kinase likely contributes to the transition into S phase through phosphorylating the two response regulators - PleD and DivK 122
Modifications to modeling the ClpXP and adaptor complex: 123
5.3.5 Changes to modeling of active DivJ 124
5.3.6 Calculating DivK~P/$DivK_T$ Bifurcation Regions: 127
5.3.7 Deriving Parameter Sets 128
5.4 Results 129
5.4.1 Investigating Performance of Model 129
5.4.2 Introducing Known Signaling Mechanisms of Carbon/Nitrogen Starvation (Signal 1) Results in secondary G1 arrest 133
5.4.3 Introducing signals (Signal 2) that influence CckA, DivL and DivK levels leads to slight improvements in performance 136
5.4.4 Investigation into DivK regulation 137
5.4.5 Simulation of Signal 3 – Impaired PleC proteolysis 141
5.4.6 Simulation of Signal 4 – reduced synthesis of CtrA 143
5.4.7 Simulation of Signal 5 – Impaired DivJ synthesis 146
5.5 Discussion 148
Chapter 6 : Advancements to the field and future work 151
6.1 Overview of this work and corresponding advancements to the field 151

6.2 Future work opportunities 153
6.2.1 GMP related projects 153
6.2.2 *Caulobacter* ODE projects 154
6.2.3 *Caulobacter* PDE projects 155
Appendix A. Supplementary Material for Chapter 2 157
A.1 Model Tuning: 157
A.2 Model Predictions: 158
A.3 Figures 160
A.4 Tables 168
Appendix B. Supplementary Material for Chapter 4 172
B.1 Equations and Simulation Events Governing Cell Cycle Model 172
B.1.1 Governing Equations 172
B.1.2 Events and switches: 176
B.1.3 Concentration shifts due to Cytokinesis: 177
B.2 Figures 180
B.3 Tables 184
Appendix C. Supplementary Material for Chapter 5 197
C.1 Equations and Simulation Events Governing Cell Cycle Model 197
C.1.1 Governing Equations 197
C.1.2 Reduced DivK Model 202
C.1.2 Figures 204
C.3 Tables 207
References 212

List of Figures

Figure 1.1) Hematopoiesis is a series of differentiation steps leading to functional white and red blood cells. 2
Figure 1.2) Life cycle of *Caulobacter crescentus* 4
Figure 2.1) Hematopoietic lineages derived from granulocyte-monocyte progenitor (GMP) cells. 9
Figure 2.2) Regulatory network driving GMP differentiation in response to M-CSF, G-CSF, and GM-CSF. 11
Figure 2.3) Protein activity over time during M-CSF and G-CSF induced differentiation. 21
Figure 2.4) Nullcline movement due to M-CSF eliminates the GMP state and induces differentiation into the monocyte lineage. 22
Figure 2.5) Bifurcation diagram with respect to M-CSF concentration. 24
Figure 2.6) Phase plane and bifurcation in response to G-CSF. 25
Figure 2.7) GM-CSF induces monopoiesis and granulopoiesis at low and high concentrations, respectively. 28
Figure 2.8) GM-CSF induces M-MDSC differentiation. 31
Figure 2.9) Nullcline shifts, in response to changes in GM-CSF concentration, illustrate the switch from monocyte state to M-MDSC. 34
Figure 2.10) Simulated composition of stochastically generated populations of cells in response to various combinations of cytokines. 36
Figure 3.1) Calibrating DNA binding parameters with data from Siam and Marczynski, 2000. 58
Figure 3.2) Investigating behavior of complex CtrA:DNA binding model. 61
Figure 3.3) Normalized mRNA expression of Z-ring relevant genes. 72
Figure 4.1) Master regulators control progression through the C. crescentus cell cycle. 86
Figure 4.2) Unphosphorylated CtrA competes with CtrA~P for Cori binding sites. 92
Figure 4.3) Wiring diagram of the molecular mechanisms underlying the cell cycle model of C. crescentus. 95
Figure 4.4) SLOW and QUICK swarmer cell simulations fit experimental data well. 96
Figure 4.5) Parameter sets agree well with experimentally observed strain viability. 97
Figure 4.6) Chromosome replication and cell division times are influenced by the interaction of unphosphorylated CtrA with Cori binding sites 100
Figure 4.7) *Cori* physiology and regulation. 106
Figure 5.1) Nitrogen/Carbon starvation leads to G1 arrest. 117
Figure 5.2) Wiring diagram of regulatory interactions captured by the model. 130
Figure 5.3) Model and parameter sets fit experimental data reasonably well. 131
Figure 5.4) Starvation Signal 1 performs poorly. 135
Figure 5.5) DivK~P exhibits bistable behavior over a range of PleC and DivJ concentrations. 138
Figure 5.6) Swarmer cells that exhibit secondary G1 arrest cross the PleC threshold faster than those that exhibit immediate G1 arrest. 140
Figure 5.7) Starvation Signal 3 simulations fit experimental observations well with the exception of CtrA expression. 142
Figure 5.8) Starvation Signal 4 agrees well with experimental observations. 145
Figure 5.9) Starvation Signal 5 agrees well with experimental observations. 147
Figure A.1) An iterative search for the Gfi-1 solution. 160
Figure A.2) Differentiation times under different cytokine conditions. 161

Figure A.3) GM-CSF can induce a monocyte to morph into an M-MDSC phenotype in a reversible process.....162
Figure A.4) Phase plane and cell trajectories describe the system under M-CSF and G-CSF stimulation. 163
Figure A.5) Heat map of the population fraction that differentiates into monocytes under M-CSF and G-CSF stimulation. 164
Figure A.6) Heat map of the population fraction that differentiates into monocytes under GM-CSF and G-CSF stimulation. 165
Figure A.7) Heat map of the population fraction that differentiates into granulocytes under GM-CSF and M-CSF stimulation.....166
Figure A.8) Heatmap of GMP cell differentiation ratios when GM-CSF is paired with equal stimulation of G-CSF and M-CSF. 167
Figure B.1) Wild Type simulations with SLOW seed parameter set. 180
Figure B.2) Wild Type simulations with QUICK seed parameter set. 181
Figure B.3) Wild Type simulations with CORI- seed parameter set. 182
Figure B.4) $[CtrA]_T$ and [cdG] peaks are greater in $CORI^-$ parameter sets than in QUICK and SLOW.....183
Figure C.1) Simulations of wild-type swarmer cell 204
Figure C.2) Signal 2 simulation results.....205
Figure C.3) Removing cdG and SpmX inhibition in Signal 4 and 5 results in secondary swarmer cell cycle arrest. 206

List of Tables

Table 2.1) Population ratios over a range of GM-CSF concentrations. 32
Table 3.1) Kinetics of DNA/CtrA binding 56
Table 3.2) Complex DNA/CtrA~P binding model 60
Table 3.3) Details on parameter estimation stages 76
Table 3.4) Sources of data used for parameterization of WT cells. 78
Table 5.1) Signaling targets and arrest statistics. 120
Table 5.2) DivK~P levels in various mutant strains. 133
Table A.1) Chapter 2 Equations 168
Table A.2) Chapter 2 Parameter Values. 170
Table A.3) Chapter 2 Initial Simulation Conditions. 171
Table B.1) Parameters 184
Table B.2) Mutant Descriptions 187
Table B.3) Arrest in SLOW simulations. 191
Table B.4) **A**rrest in QUICK simulations 193
Table B.5) Arrest in CORI⁻ simulations 195
Table C.1) Parameters 207
Table C.2) Alternative Signals 211

Chapter 1 : Introduction

1.1 Cellular differentiation and division

For organisms to be successful, cells must grow, divide and regulate their genetic expression based on environmental conditions. When a cell's genetic regulation is manipulated to cause significant changes in the cell's appearance and/or behavior, it is called differentiation. For some organisms and cell lines, differentiation and division are part of the same process. For instance, *Caulobacter crescentus*, an alphaproteobacterium, divides and differentiates simultaneously as two inseparable components of it's life cycle. When environmental conditions are unfavorable, *Caulobacter* will simultaneously stop dividing and differentiating [1]. In contrast, other species and cell lines, such as the hematopoietic cell line (eukaryotic cells) differentiate independently of proliferation [2].

There are several differences and similarities between the differentiation process of *Caulobacter* and hematopoietic cells. Both utilize environmental signals to modify activity of transcription factors to determine genetic regulation [3], [4]. However, while *Caulobacter* divides and differentiates in a cyclical process, hematopoietic cells differentiate irreversibly into terminal phenotypes. In this chapter, we explore the significance of the differentiation process of *Caulobacter* and cells of the hematopoietic lineage. We further discuss different mathematical approaches to study the cellular processes of these two fascinating biological systems.

1.2 Hematopoiesis

Hematopoietic stem cells are stored in the bone marrow of humans and differentiate into all types of blood cells in a process called hematopoiesis. The range of terminal phenotypes of the hematopoietic lineage are numerous and diverse. Hematopoietic stem cells transition into terminal phenotypes in stages, making a binary decision between two cell fates in each differentiation step (Figure 1.1). Each differentiation event is regulated by a network of proteins, which typically include a set of antagonistic transcription factors to ensure that lineage

commitment is irreversible and binary. Signaling molecules, called cytokines, induce the differentiation response by manipulating the activity of these antagonistic transcription factors [3], [5].

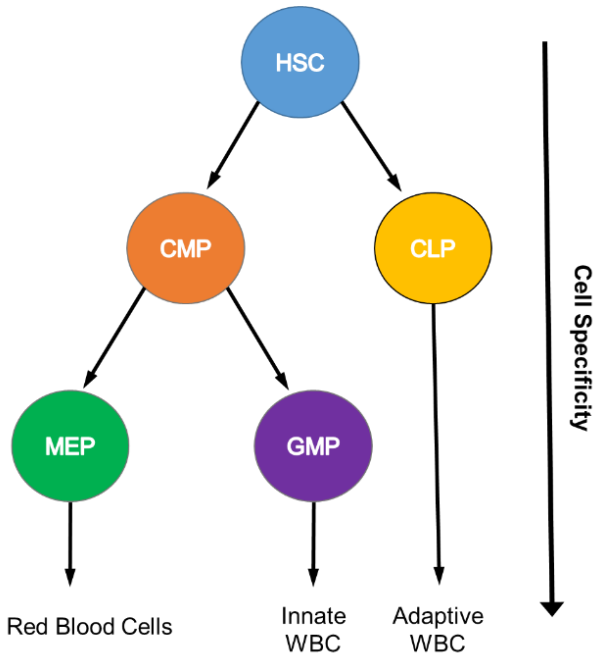

Figure 1.1) Hematopoiesis is a series of differentiation steps leading to functional white and red blood cells. Hematopoiesis is a series of differentiation steps leading to functional white and red blood cells.
HSC = Hematopoietic Stem Cell; CLP = Common-Lymphoid Progenitor; CMP = Common Myeloid Progenitor; MEP = Megakaryocyte and Erythroid Progenitor; GMP = Granulocyte-Monocyte Progenitor; WBC = White Blood Cell.

In this dissertation, we explore the underlying molecular network of granulocyte-monocyte progenitor (GMP) cells (also called granulocyte-macrophage progenitors), which are partially matured cells of the hematopoietic lineage. GMP cells are responsible for differentiating into white blood cells of the innate immune system. The monocytic lineage specializes in phagocytosis of bacteria, phages and cellular debris and consists of antigen-presenting cells [5], [6]. In contrast, the granulocytic lineage generally does not present antigens and is equipped with granules that contain a variety of substances used to fight infections. This cell line includes neutrophils, the most abundant type of white blood cell and the first responders to inflammation

[7], [8]. Differentiation is induced by a variety of cytokines [9], as discussed in Chapter 2. It is known that GMP cells favor granulopoiesis with granulocyte-colony stimulating factor (G-CSF) and high concentrations of granulocyte/macrophage-CSF (GM-CSF) while macrophage-CSF (M-CSF) and low concentrations of GM-CSF favor monopoiesis [5], [10]–[12]. However, how GMP cells commit to one lineage of another at the molecular level is poorly understood. It is particularly important to understand how cytokines guide lineage commitment in GMP cells, as these cells are essential for the immune system to function properly. Mismanagement of GMP differentiation can result in a variety of life-threatening disorders [13]–[15].

1.3 *Caulobacter crescentus* is a model organism

Caulobacter crescentus is an extremely successful oligotroph found primarily in freshwater systems. Although the bacterium is not pathogenic, it is a well-studied model organism of asymmetrical division in prokaryotes [16], [17]. *Caulobacter* is uniquely suitable to study due to its phenotypic differences through the different phases of the cell cycle (Figure 1.2). It begins the cell cycle in G1, where it expresses a flagellum. The flagellum enables *Caulobacter* to move through its environment in search of nutrients. If environmental conditions are suitable, it will transition into S phase and simultaneously release its flagellum and synthesize a stalk with an adhesive at the end known as a hold-fast. Interestingly, the *Caulobacter* hold-fast is the strongest biological adhesive ever measured [18]. The hold-fast secures *Caulobacter* to an object, such as a rock or log, in its local environment. *Caulobacter* continues to grow throughout S phase and G2 and synthesizes a flagellum at the pole opposite to the stalk. This is referred to as a pre-divisional cell. Finally, the cell divides into two daughter cells of different morphologies. The swarmer cell enters G1 phase and the stalked cell immediately enters S phase if environmental conditions are suitable [17], [19].

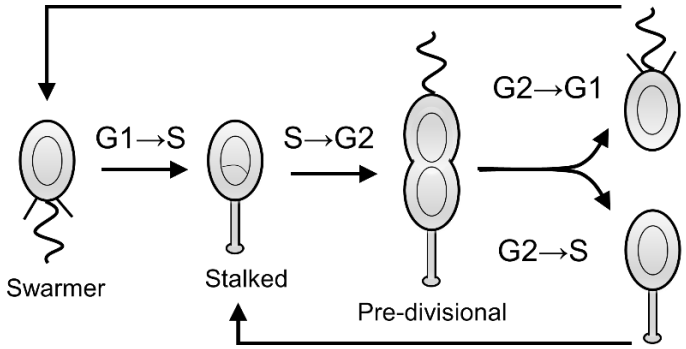

Figure 1.2) Life cycle of *Caulobacter crescentus*

A population of NA1000 *C. crescentus* cells can be centrifuged to separate swarmer cells from stalked and pre-divisional cells. As swarmer cells will all be in the G1 phase, isolating swarmer cells from the population allows one to develop a new population with synchronized cell cycles[20]. This capability makes *Caulobacter* uniquely suitable to study the temporal dynamics of the cell cycle. A common technique utilized by experimental biologists is to run western blots at different time points post synchronization to learn how protein expression varies over time [21]–[24]. Utilizing fluorescent tags is also frequently used to learn how proteins localize throughout the cell cycle [22], [24]–[26].

1.4 Implementing a systems approach to study molecular biology

Systems biology takes a holistic approach to investigate biological problems, considering how multiple pieces of a system work together to explain behavior rather than studying each aspect in isolation [27]. However, this approach not unique to biology. To an individual without intimate knowledge of molecular biology, the utility of the approach may be better understood by utilizing examples that lie outside of the molecular realm. For instance, one may consider the process by which an astrophysicist predicts whether or not an asteroid will collide with earth. First, one might consider the trajectory of the earth through space and the trajectory of the asteroid. This is analogous to studying the asteroid and earth in isolation (rather than utilizing a systems approach) and in this case, one may inaccurately predict that the asteroid will collide with the earth. In reality, the trajectory of the asteroid is also dependent on the gravity of other large bodies in the solar system. If the asteroid was passing by Mars, for example, the gravity of

mars would likely manipulate the asteroid's path and it may not come anywhere near earth. The gravity of other objects, such as the sun, may also influence its trajectory. An astrophysicist would take a systems approach, modeling the gravitational interactions of numerous bodies in the solar system to predict the trajectory of the asteroid. In molecular biology, a systems approach offers similar improvements in our ability to make predictions.

In this dissertation, we primarily utilize the systems approach to make three kinds of predictions. 1) We deduce non-intuitive predictions regarding the behavior of cells under conditions that have yet to be observed. 2) We utilize what is known about individual molecular interactions to explain behavior on the larger systems level. 3) We find that what is known about a biological system is insufficient to explain behavior that has been observed in experiments and postulate what must be present in the molecular mechanism to explain the observed behavior. The example of the asteroid is primarily analogous to the first kind of prediction. Similarly, in Chapter 2 we predict that low doses of G-CSF and M-CSF can work synergistically to induce monopoiesis. Chapter 2 also provides a good example of the second type of prediction: We demonstrate how previously identified molecular interactions cumulatively can explain complex differentiation behavior. An excellent example of the third type of prediction can be found in Chapter 5, where we show that a mechanism enhancing DivK phosphatase activity (or reducing DivK kinase activity) in response to nitrogen and carbon starvation is necessary to explain experimentally observed behavior of starved *Caulobacter* cells. Overall, each chapter contains numerous predictions corresponding to these three categories.

1.5 Mathematical modeling of differentiation and cell cycle dynamic

The systems approach is a powerful method that reaches its full potential due to the implementation of mathematics [27]. In the example with the asteroid, an astrophysicist would not be able to accurately predict the trajectory by simply thinking about the gravity of bodies of the solar system. As biological systems are often extremely complicated, mathematics is utilized in systems biology to investigate these systems and provide insights that would be difficult to achieve through human intuition alone [28], [29]. Here we derive differential equations to describe the molecular mechanisms underlying GMP differentiation and the *Caulobacter* cell

cycle. Notably, these two systems operate very differently and therefore require different methodologies for effective analysis. GMP differentiation is influenced by environmental signals to make decisive lineage commitment steps. In such a scenario, the GMP cell can be thought of as a stable state but, when properly stimulated, will destabilize and move to an alternative stable state. In contrast, *Caulobacter* differentiates and divides in a cyclical process. In mathematical terms, *Caulobacter* differentiation operates under a stable limit cycle while GMP cell differentiation operates through discrete steps in a bifurcating system. In Chapter 2, we utilize dynamic systems theory to investigate the bifurcation behavior of GMP cells, and how cytokine signals manipulate steady states to result in differentiation. In *Caulobacter*, the limit cycle can be destabilized from a mutation or due to environmental stressors, resulting in cell cycle arrest. In Chapter 4, we investigate how binding of unphosphorylated CtrA with the chromosome origin of replication influences the *Caulobacter* cell cycle (or limit cycle). In Chapter 5 we learn that *Caulobacter* navigates through a bifurcation in each stage of the cell cycle, and that carbon and nitrogen influence the bifurcation behavior to induce rapid G1 arrest in swarmer cell populations.

Chapter 2 : Mathematical Analysis of Cytokine-Induced Differentiation of Granulocyte-Monocyte Progenitor Cells

Bronson R. Weston[1], Liwu Li[2], and John J. Tyson[2]

[1] Program in Genetics, Bioinformatics, and Computational Biology, Virginia Polytechnic Institute and State University, Blacksburg VA, USA

[2] Department of Biological Sciences, Virginia Polytechnic Institute and State University, Blacksburg, VA, USA

2.1 Abstract

Granulocyte-monocyte progenitor (GMP) cells play a vital role in the immune system by maturing into a variety of white blood cells, including neutrophils and macrophages, depending on exposure to cytokines such as various types of colony stimulating factors (CSF). Granulocyte-CSF (G-CSF) induces granulopoiesis and macrophage-CSF (M-CSF) induces monopoiesis, while granulocyte/macrophage-CSF (GM-CSF) favors monocytic and granulocytic differentiation at low and high concentrations, respectively. Although these differentiation pathways are well documented, the mechanisms behind the diverse behavioral responses of GMP cells to CSFs are not well understood. In this paper, we propose a mechanism of interacting CSF-receptors and transcription factors that control GMP differentiation, convert the mechanism into a set of differential equations, and explore the properties of this mathematical model using dynamical systems theory. Our model reproduces numerous experimental observations of GMP cell differentiation in response to varying dosages of G-CSF, M-CSF and GM-CSF. In particular, we are able to reproduce the concentration-dependent behavior of GM-CSF induced differentiation, and propose a mechanism driving this behavior. In addition, we explore the differentiation of a fourth phenotype, monocytic myeloid-derived suppressor cells (M-MDSC), showing how they might fit into the classical pathways of GMP differentiation and how progenitor cells can be primed for M-MDSC differentiation. Finally, we use the model to make novel predictions that can be explored by future experimental studies.

2.2 Introduction

Hematopoietic stem cells differentiate into blood cells (neutrophils, monocytes, red blood cells, etc.) in a finely regulated process called hematopoiesis. In this branching process, each branch point represents a cell differentiating into one of two alternative lineages. Stimulatory factors, such as cytokines, induce differentiation into one lineage over another, and cross-antagonistic transcription factors maintain commitment to the chosen lineage [5], [30]. In the myeloid branch of hematopoiesis, granulocyte-monocyte progenitor (GMP) cells differentiate into essential cells of the innate immune system, including granulocytes (neutrophils, eosinophils and basophils) and monocytes (which further differentiate into macrophages and dendritic cells), depending on the local concentrations of specific colony stimulating factors (CSFs) [31], [32]. Therefore, proper orchestration of GMP differentiation is of vital significance to human health. For instance, myeloid cells are often targeted with CSFs to treat a variety of diseases including arthritis, infections, pneumonia, cancer, type 1 diabetes and neutropenia [13]–[15]. A better understanding of the biological responses of myeloid cells to these stimuli will be useful to refine and develop new therapeutic strategies.

It is well known that G-CSF and M-CSF induce differentiation of granulocytes and monocytes, respectively, while a range of concentration-dependent behaviors can be observed in response to GM-CSF. GMP populations favor monopoiesis at low concentrations of GM-CSF and granulopoiesis at higher concentrations [5], [10]–[12]. Figure 2.1 provides a schematic illustration of GMP differentiation. Critical proteins for granulocytic commitment include CCAAT enhancer-binding proteins (C/EBPα and C/EBPβ), growth-factor independent-1 protein (Gfi-1), GM-CSF receptor (GM-CSFR), and G-CSF receptor (G-CSFR). Proteins involved in monocytic commitment include PU.1 (a protein encoded by the *SPI1* gene in humans), early growth response proteins 1 and 2 (Egr-1 and Egr-2), interferon-regulatory factor 8 (IRF8), M-CSF receptor (M-CSFR), and GM-CSFR [5], [9], [33]–[38].

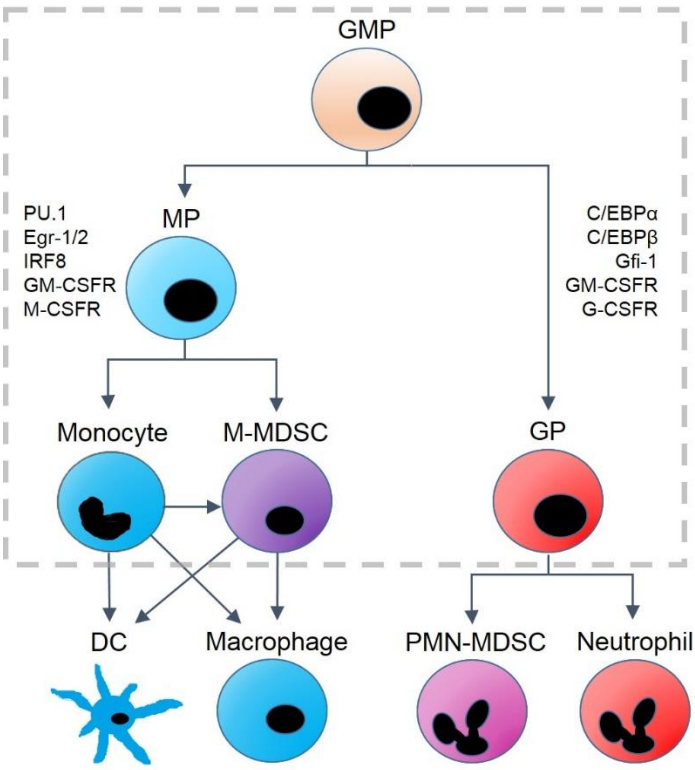

Figure 2.1) Hematopoietic lineages derived from granulocyte-monocyte progenitor (GMP) cells. GMP differentiation into monocyte progenitors (MP) or granulocyte progenitors (GP) results in changes of protein expression. GP cells are associated with the upregulation of C/EBPα, C/EBPβ, Gfi-1, G-CSFR and GM-CSFR. Monopoiesis is associated with upregulation of PU.1, Egr-1/2, IRF8, M-CSF, and GM-CSFR. MP cells differentiate into monocytes and monocytic myeloid-derived suppressor cells (M-MDSC), and monocytes can be converted into M-MDSCs under some conditions. Monocytic precursors terminally differentiate into dendritic cells (DC) and macrophages, while GP cells differentiate into polymorphonuclear (PMN-) MDSCs and neutrophils as well as eosinophils and basophils (not shown). The model we propose is designed to capture the dynamics within the gray, dashed box.

Despite the vital roles that cells of the GMP lineage play in the body, much is still unknown about the dynamics of their differentiation. Laslo et al. suggested that PU.1 and C/EBPα stimulate cross-antagonistic transcription factors, Egr-2 and Gfi-1, to maintain granulocytic and monocytic commitment, respectively [9]. This cross-antagonistic relationship, which is thought to be critical to gene regulation within the myeloid lineage, was modeled by Laslo et al. with a simple, symmetrical, interaction motif that exhibits lineage commitment of monocytes and granulocytes in response to external signals. However, the simple motif they propose cannot explain more complex behavior, such as GMP responses to low and high doses of GM-CSF. It is also not well understood how GMP cells respond to varying concentrations and combinations of cytokines, nor how GMP cells differentiate into myeloid-derived suppressor cells (MDSCs),

which are immature myeloid cells that exhibit both granulocytic and monocytic traits [39]–[41]. MDSCs have anti-inflammatory properties and serve a beneficial role in a variety of pathological conditions [42], [43]; nonetheless, they are more often associated with promotion of cancer growth. It is well documented that MDSCs promote angiogenesis and metastasis, and many studies suggest that suppression of these cells may be a promising clinical target in cancer therapy [39], [44]–[49]. While originally lumped into one heterogeneous group, MDSCs have been reclassified into two separate types: polymorphonuclear (PMN)-MDSCs and monocytic (M)-MDSCs [39], [44], [50]. Distinguishing between these subsets is crucial, as they have different mechanisms of immunosuppression, respond to different cytokines, and are more closely associated with different tissues and cancers [44], [51], [52]. While PMN-MDSCs typically exist at higher population densities than M-MDSCs, M-MDSCs are more potent suppressors of inflammation on a per-cell basis [51], [53]. Of the two subsets, we will focus on M-MDSCs, as our model does not include the downstream transcription factors necessary to distinguish between PMN-MDSCs and other cells of the granulocyte lineage.

In this paper, we propose a new model of the internal regulatory network that governs GMP cell differentiation and how various cytokine signals feed into this regulatory network. We convert our network diagram into a set of nonlinear ordinary differential equations (ODEs) and study their properties by dynamical systems theory. We first explore the polarization of GMP cells resulting from G-CSF and M-CSF signals. Next we explore the dynamics of the system in response to GM-CSF and propose a mechanism driving the complex behavior observed in GM-CSF experiments. We also explore how M-MDSCs may fit into this differentiation scheme, including the stability of the state and the nature of the phenotype itself. Finally, we evaluate the system's response to cytokine combinations and provide insight into the spectrum of behaviors induced by signaling crosstalk.

2.3 Materials and methods

2.3.1 The proposed regulatory network and its molecular basis

PU.1 and C/EBPα are thought to be master regulators of myelopoiesis, as C/EBPα favors granulopoiesis and PU.1 favors monopoiesis [54], [55]. In this subsection we summarize the experimental evidences characterizing the interactions of PU.1, C/EBPα and their closely

interacting partners, in order to motivate the regulatory network (Figure 2.2A) that we will use to understand the differentiation of GMP cells.

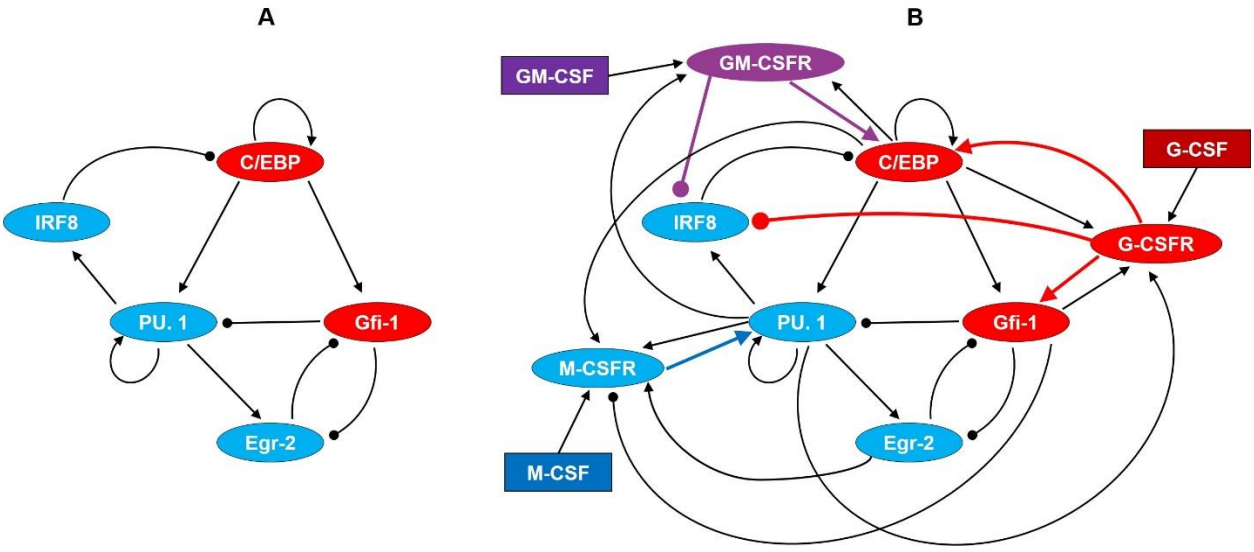

Figure 2.2) Regulatory network driving GMP differentiation in response to M-CSF, G-CSF, and GM-CSF. (A)Transcription factor network. (B) Cytokine signaling and regulatory network. Regulatory motifs are expressed in terms of direct and indirect interactions among proteins, where a line with an arrow head represents the activation of one protein by another and a line with a circular head represents inhibition. Blue and red ovals denote proteins highly expressed in monocyte and granulocyte lineages, respectively. GM-CSFR is represented by a purple oval as it can signal for both monopoiesis and granulopoiesis. Cytokines are denoted by rectangles.

First of all, we note that the roles of C/EBPα and C/EBPβ appear to be redundant in hematopoiesis. When the *C/EBPβ* gene was knocked in to the *C/EBPα* locus, no significant changes in hematopoiesis or gene expression were ascertained. Since these proteins have highly conserved C-terminal dimerization- and DNA-binding domains, it is reasonable to assume that they bind to the same promoter sites [56]. It is possible, indeed probable, that these proteins have differences in regulation at the transcriptional level; however, it has been demonstrated that GM-CSF and G-CSF upregulate both C/EBPα and C/EBPβ [57], [58]. Furthermore, both C/EBPα and C/EBPβ exhibit positive autoregulation [59], [60]. Due to this overlap of structure and function, we lump C/EBPα and C/EBPβ into one node/variable, called C/EBP. Unless otherwise specified, "C/EBP" will refer to the combination of C/EBPα and C/EBPβ rather than the entire family of C/EBP transcription factors.

The interactions between PU.1 and C/EBP are intriguing, as they have both antagonistic and synergetic relationships (Figure 2.2A). It has been demonstrated that the promoter of the *SPI1* gene (encoding the PU.1 protein) has multiple potential C/EBP binding sites, and that C/EBPα

can induce PU.1 expression by directly binding to the promoter to activate transcription [61], [62]. Alternatively, C/EBPα can inhibit PU.1 indirectly by upregulating the *Gfi1* gene [63]. Gfi-1 in turn, physically binds with PU.1 to inhibit its activity as a transcription factor [64]. These affects are amplified, since PU.1 auto-activates its own promoter site [65]. Furthermore, Gfi-1 binds directly to numerous PU.1 target genes to repress PU.1's transcriptional activities [64]. We suspect that this process could further inhibit *SPI1* transcription, given possible positive feedback loops between PU.1 and its downstream targets. In addition, PU.1 antagonizes C/EBP either directly or through activation of IRF8, which creates a mutual inhibition circuit between PU.1 and C/EBP [66], [67]. IRF8 physically interacts with C/EBPα to prevent it from binding to chromatin and promoting transcription of target genes [68]. While, to the best of our knowledge, no studies have demonstrated that C/EBPβ is inhibited by IRF8, it has been demonstrated that IRF8 also binds to and inhibits C/EBPε, suggesting that it may function similarly on C/EBPβ [68]. Furthermore, it has been shown that IRF8-knockdown induces C/EBPβ expression in dendritic cells [69]. PU.1 has also been shown to inhibit the transcriptional activity of C/EBPα and C/EBPβ in adipocyte differentiation via direct protein-protein interactions [67]. Similar interactions may occur in myelopoiesis, as it has been shown that C/EBPα directly interacts with PU.1 to block PU.1-induced dendritic cell commitment [70]. Despite this evidence, we do not model the potential direct interaction between PU.1 and C/EBP as regulatory details are not clear in regard to GMP differentiation, and a mutual inhibitory relationship is already captured within our motif.

Egr-2, another downstream transcription factor promoted by PU.1, forms a complex with Nab-2 to inhibit Gfi-1. Similarly, Gfi-1 regulates Egr-1 and -2 to reduce the concentration of the Nab/Egr complex [9], [71]. Thus, the Egr-Gfi-1 relationship creates a second layer of antagonism within this myeloid differentiation system. Since Gfi-1 can inhibit Egr expression, but not Nab, we simplify our model by excluding Nab, with the assumption that the concentrations of the Egr-Nab complex will be proportional to the concentration of Egr.

Within our model, three receptors (M-CSFR, G-CSFR, and GM-CSFR) transduce cytokine signals to regulate transcription factor activity (Figure 2.2B). These transcription factors, in turn, regulate expression of the receptors, thereby creating positive and negative feedback loops. We model PU.1 as the primary target of M-CSF signaling, since M-CSF induces monocyte

differentiation and PU.1 is a master regulator of monopoiesis. Although we do not know of any confirmed pathway, it is known that M-CSF can signal through ERK to activate a transcription factor, Sp1, which can bind to multiple sites on the *SPI1* promoter [65], [72]. Thus, it is plausible that M-CSF induces PU.1 expression through Sp1. PU.1, as well as C/EBPα, C/EBPβ and Egr-2, bind to the M-CSFR promoter region to activate transcription, creating a positive feedback loop between PU.1 and M-CSFR [5], [35], [71], [73]. Gfi-1, however, binds to the promoter to disrupt transcription [74].

G-CSFR signals primarily to STAT3 and SHP2, resulting in upregulation of C/EBPα and C/EBPβ [54], [57], [75]. SHP2 activates RUNX1, which in turn promotes Gfi-1 expression via promoter regulation [76], [77]. Thus, G-CSFR activates Gfi-1 by a mechanism independent of C/EBPα, and we simplify this interaction in our model by having G-CSFR directly upregulate Gfi-1 when bound to its ligand. C/EBP, PU.1 and Gfi-1 promote G-CSFR activity, but through different mechanisms. C/EBPα, C/EBPβ and PU.1 bind directly to the G-CSFR promoter to upregulate G-CSFR expression, while Gfi-1 represses miR-21 and miR196b, which both inhibit G-CSF-mediated granulopoiesis [35], [78]. Furthermore, Gfi-1 promotes Ras guanine nucleotide releasing protein 1 (RasGRP1), which regulates G-CSFR-induced Ras activation [79]. C/EBPα transactivation activity is also enhanced by G-CSF-induced Ras signaling [80]. Thus, while C/EBP and PU.1 directly induce G-CSFR expression, Gfi-1 enhances the capacity for G-CSFR signaling by regulating signal transduction intermediates. These interactions create a positive feedback loop consisting of C/EBP, Gfi-1, and G-CSFR. This feedback loop extends when considering the effects of G-CSFR signaling on IRF8, as G-CSF can inhibit IRF8 indirectly through the STAT3 pathway and SHP2. It was demonstrated that SHP2 activates STAT5 which inhibits transcription of the *IRF8* gene [81], [82].

GM-CSF drives granulopoiesis through similar mechanisms as G-CSF; however, GM-CSF signals primarily through STAT5 rather than STAT3 [58], [83]. Experimental evidence suggests that upregulation of C/EBPα in pre-basophil and mast cell progenitors is STAT5-dependent [84]. Thus, it is likely that GM-CSF-activated STAT5 results in the upregulation of C/EBP in GMP cells. As mentioned earlier, STAT5 also represses IRF8 transcription, and therefore GM-CSFR signaling should repress IRF8. GM-CSFR expression is upregulated by C/EBPα, C/EBPβ and PU.1 via transcriptional promotion [5], [35], [85].

2.3.2 Conversion of the interaction diagram into a mathematical model

To convert the interaction diagram in Figure 2.2B into a set of nonlinear ODEs, we use a formalism called "standard component" modeling [86]. Each of the eight proteins in Figure 2.2B (excluding cytokines) is governed by an ODE of the form:

$$\frac{dX_i}{dt} = \rho_i \left(\frac{1}{1+e^{-\sigma_i W_i}} - X_i \right) \quad (1)$$

$$W_i = \omega_i^o + \sum_{j=1}^{N} \omega_{i,j} X_j \quad (2)$$

The (relative) concentration or activity of protein *i* is denoted by the variable $X_i(t)$, $0 \leq X_i(t) \leq 1$. The function $W_i(X_j)$ accounts for all interactions within the network that directly affect the rate of change of X_i such that $\omega_{i,,j}$ quantifies the direction and strength of the affect that protein *j* exerts on protein *i*. Negative values represent inhibition while positive values represent activation. The time scale for the rate of change of $X_i(t)$ is determined by $1/\rho_i$. The value of ω_i^o determines the value of X_i when it is not receiving stimulus from any X_j. One unit of the time variable, *t*, is roughly 1 h in our simulations.

The nonlinear function, $H(W) = 1/(1+e^{-\sigma W})$, in this ODE is a sigmoidal function of *W*, with steepness determined by the parameter σ. Many biological phenomena such as phosphorylation cascades and transcriptional regulation are characterized by sigmoidal response curves. Our sigmoidal function $H(W)$ captures such behavior in a very convenient way. As an example, we show the case of C/EBP activity:

$$\frac{d[\mathrm{C/EBP}]_\mathrm{T}}{dt} = \rho_\mathrm{TF} \left(\frac{1}{1+e^{-\sigma W_\mathrm{C/EBP}}} - [\mathrm{C/EBP}]_\mathrm{T} \right) \quad (3)$$

$$W_\mathrm{C/EBP} = \omega^\mathrm{o}_\mathrm{C/EBP} + \omega_\mathrm{C/EBP,C/EBP}[\mathrm{C/EBP}]_\mathrm{F} + \omega_\mathrm{C/EBP,GMCSFR}[\mathrm{GMCSFR{:}\,GMCSF}] + \omega_\mathrm{C/EBP,GCSFR}[\mathrm{GCSFR{:}\,GCSF}] \quad (4)$$

We use ρ_TF rather than $\rho_\mathrm{C/EBP}$ as all transcription factors have the same time scale in our model.

Note that this ODE distinguishes between two concentrations of C/EBP: its "total" concentration, $[\mathrm{C/EBP}]_\mathrm{T}$, and the concentration of the "free" form of the protein, $[\mathrm{C/EBP}]_\mathrm{F}$. C/EBP is considered free when it's not bound to IRF8, therefore $[\mathrm{C/EBP}]_\mathrm{F}$ represents the active portion of $[\mathrm{C/EBP}]_\mathrm{T}$, where

$$[\mathrm{C/EBP}]_\mathrm{T} = [\mathrm{C/EBP}]_\mathrm{F} + [\mathrm{C/EBP{:}\,IRF8}] \quad (5)$$

and [C/EBP:IRF8] denotes the concentration of the C/EBP-IRF8 complex. Similarly,

$$[\mathrm{IRF8}]_\mathrm{T} = [\mathrm{IRF8}]_\mathrm{F} + [\mathrm{C/EBP{:}\,IRF8}] \quad (6)$$

Since protein-protein binding is governed by the law of mass action, and the timescale for association and dissociation of proteins is likely to be much faster than other time scales in the model, we assume that, at any given time, the reaction $[\mathrm{C/EBP}]_\mathrm{F} + [\mathrm{IRF8}]_\mathrm{F} \leftrightharpoons [\mathrm{C/EBP{:}IRF8}]$ is at equilibrium. Thus,

$$K_\mathrm{eq} = \frac{[\mathrm{C/EBP{:}IRF8}]}{[\mathrm{C/EBP}]_\mathrm{F}\cdot[\mathrm{IRF8}]_\mathrm{F}} \ . \quad (7)$$

Using Eqs. 5-7 we can obtain an equation for $[\mathrm{C/EBP}]_\mathrm{T}$ as a function of $[\mathrm{C/EBP}]_\mathrm{F}$ and $[\mathrm{IRF8}]_\mathrm{T}$:

$$[\mathrm{C/EBP}]_\mathrm{T} = [\mathrm{C/EBP}]_\mathrm{F}\cdot\left(1 + \frac{\mathrm{K_{eq}}\cdot[\mathrm{IRF8}]_\mathrm{T}}{1+K_\mathrm{eq}\cdot[\mathrm{C/EBP}]_\mathrm{F}}\right) \quad (8)$$

and an equation for $[\mathrm{C/EBP}]_\mathrm{F}$ as a function of $[\mathrm{C/EBP}]_\mathrm{T}$ and $[\mathrm{IRF8}]_\mathrm{T}$

$$[\mathrm{C/EBP}]_\mathrm{F} = \frac{1}{2}\left(-b + \sqrt{b^2 + \frac{4[\mathrm{C/EBP}]_\mathrm{T}}{K_\mathrm{eq}}}\right) \quad (9)$$

where $b = [\mathrm{IRF8}]_\mathrm{T} + \frac{1}{K_\mathrm{eq}} - [\mathrm{C/EBP}]_\mathrm{T}$. (10)

Regarding binding of external cytokines to their membrane-bound receptors, we assume that the cytokine concentration, [L], is constant and much greater than the total concentration of receptors, $[\mathrm{R}]_\mathrm{T}$. In this case, the concentration of the receptor:cytokine complex, [R:L], is given by the function:

$$[\mathrm{R{:}\,L}] = \frac{[\mathrm{L}][\mathrm{R}]_\mathrm{T}}{[\mathrm{L}]+K_\mathrm{d}} \quad (11)$$

where K_d is the dissociation constant of the receptor:cytokine complex. The cytokine concentrations are "inputs" to the model, the total receptor concentrations are dynamic variables of the model.

Parameter values were hand-tuned so that the behavior of the system in response to cytokines aligns with experimental observations. For a more detailed discussion on parameter tuning, a table of parameter values and the complete set of equations constituting our mathematical model, see Appendix A.

2.3.3 Computational methods

All quantitative simulations were computed using the deterministic ODE solver, ode45, in MATLAB. To simulate a population of GMP cells, we generate a set of cells with stochastically varying initial conditions, taking the steady state concentrations of all variables in a naïve GMP cell (with no cytokine stimulation) and varying each initial concentration by a random factor drawn from a normal distribution with mean =1 and standard deviation = 0.2.

Although our model consists of eight nonlinear ODEs, we characterize its behavior in a pseudo-phase plane spanned by only two variables: [PU.1] and $[C/EBP]_T$. To do so, we demand that the other six variables are in pseudo-steady state by setting the right-hand-sides of those six ODEs = 0. Looking at the structure of those six ODEs (in Table A.1), we see all six pseudo-steady state concentrations can be written as explicit functions of [PU.1], $[C/EBP]_F$ and [Gfi1]. For example, the pseudo-steady state value of $[IRF8]_T$ is a function of [PU.1] and the complexes [GMCSFR:GMCSF] and [GCSFR:GCSF]. From Eq. (11), these concentrations are functions of the stimulus parameters, [GMCSF] and [GCSF], and of the pseudo-steady state values of $[GMCSFR]_T$ and $[GCSFR]_T$, which in turn are functions, respectively, of [PU.1] and $[C/EBP]_F$ and of [PU.1], $[C/EBP]_F$ and [Gfi1]. From Eq. (7), we can express $[C/EBP]_T$ as a function of $[C/EBP]_F$ and $[IRF8]_T$. By this line of reasoning, we can reduce the 8-dimensional system of ODEs to three variables, [PU.1], $[C/EBP]_T$ and [Gfi1].

To reduce this system to two variables, we must express the pseudo-steady state concentration of Gfi-1 as a function of [PU.1] and $[C/EBP]_T$. We cannot provide an explicit representation of this function but we can find it by an iterative numerical approach. For any combination of values of $[C/EBP]_F$ and [PU.1], we subdivide the interval $[Gfi1] \in [0,1]$ into one hundred subintervals of length 0.01 and compute the value of $d[Gfi1]/dt$ at the ends of each segment (see, e.g., Figure A.1). Any subinterval for which the sign of $d[Gfi1]/dt$ changes is further subdivided into ten sub-

subintervals, and the iterative process is repeated until we have good approximation of the pseudo-steady state (pss) value(s) of [Gfi1] for the given pair of [PU.1] and $[C/EBP]_F$ values. We solve for $[Gfi1]_{pss}$ with a tolerance of 10^{-9}. (We acknowledge that Newton's method would have been a more efficient approach; however, this method works all the same.)

Since each point along the PU.1 pseudo-nullcline has a fixed value of $[C/EBP]_F$, we calculate solutions for the PU.1 nullcline over a range of $[C/EBP]_F$ values. Stringing these solutions together, we acquire the desired nullcline. We can find the [PU.1] nullcline solutions for any $[C/EBP]_F$ value, as we did for finding $[Gfi1]_{pss}$, by generating a subdivision of [PU.1] values between 0 and 1. For each [PU.1] value we solve for $[Gfi1]_{pss}$ as above. As mentioned previously, given a set of $[C/EBP]_F$, [PU.1], and [Gfi1] concentrations we can numerically solve for every other variable's steady state solution. Thus, we are able to calculate $d[PU.1]/dt$, and then to find the nullcline for [PU.1], where $d[PU.1]/dt = 0$. In this case, we use a tolerance of 10^{-7} rather than 10^{-9}. Similarly, we solve for the $[C/EBP]_F$ nullcline using the same method with a tolerance of 10^{-8}. (We use different tolerances for different solutions due to different sensitivities and computational times.) Once we have acquired our pseudo-nullclines for the $[C/EBP]_F$–[PU.1] phase plane, we convert $[C/EBP]_F$ to $[C/EBP]_T$ and plot the nullclines in the $[C/EBP]_T$– [PU.1] phase plane. While unconventional and computationally taxing, our methods yield smoother, more accurate curves than we were able to obtain using XPPAUT, and we could do all our computations within MATLAB rather than switching between MATLAB and some other bifurcation software.

Bifurcation diagrams were generated in a similar, non-conventional fashion. Bifurcation diagrams are based on steady state solutions of all 8 variables. Given a set of approximate steady state values, we use MATLAB's fminsearch function to find values of $[C/EBP]_F$ and [PU.1] that minimize the objective function $((d[C/EBP]_F/dt)^2 + (d[PU.1]/dt)^2)^{1/2}$ given that all other variables are at steady state. (To find $[Gfi\text{-}1]_{ss}$ we use the same iterative technique specified earlier.) Once a solution for $[C/EBP]_F$ and [PU.1] is found, we use that solution as an initial guess for the next step (after making a small change to the value of the bifurcation parameter) and search for the new solution. Close to saddle-node bifurcation points, where the derivative of $[PU.1]_{ss}$ with respect to the bifurcation parameter becomes very large, we hold the bifurcation parameter constant, and take a small step in the value of [PU.1]. We then use fminsearch to find the

solution of $[C/EBP]_F$ and the bifurcation parameter at that given [PU.1] value. To evaluate stability, we use a typical eigenvalue analysis.

To construct heat maps, we simulate 500 stochastically generated cells, using the method specified earlier, under each cytokine condition. Using the differentiated population's ratios, each pixel was assigned an RGB value determined by the following equation:

$$[R, G, B] = \left[\left(\frac{\mathrm{GP}}{\phi}\right)^{\frac{1}{3}}, \left(\frac{\mathrm{MMDSC}}{\phi}\right)^{\frac{1}{3}}, \left(\frac{\mathrm{MO}}{\phi}\right)^{\frac{1}{3}}\right] \quad (12)$$

$$\phi = Max(\mathrm{GP}, \mathrm{MMDSC}, \mathrm{MO}, \mathrm{GMP}) \quad (13)$$

where the red, green and blue intensities are a function of the fraction of the population which differentiated into granulocytes progenitors (GP), M-MDSCs, and monocytes (MO), respectively, over the size of the largest population category (including undifferentiated GMP cells).

For those interested in exploring our model further, our code is available online at https://github.com/bronsonweston/GMP-Modeling. This includes a stochastic simulation function and a user friendly MATLAB script, 'MainScript.m', to produce time course simulations and figures as well as stochastic simulations under user specified conditions. Additionally, 'FigureGenerating.m' can be used to easily reproduce any of our results. This code can also be used as an example script to conduct alternative simulations not explored in this study.

2.3.4 Assumptions

As with any model, we have made several simplifying assumptions to avoid unnecessary complexity. First, we ignore autocrine feedback loops of the GMP lineage. We maintain constant cytokine concentration(s) in order to evaluate the effects of the stimulus input, rather than accounting for how the cell may change external conditions. We assume that the cytokine production of an individual cell has a negligible impact on the initial decision-making process of GMP differentiation. Additionally, we assume that all protein isoforms function similarly in the context of our network. For example G-CSFR has seven isoforms, four of which are involved in

granulopoiesis [87]. We assume that [G-CSFR] is the sum of these isoforms, weighted according to the contribution of each to granulopoiesis.

The GMP differentiation network has many mechanisms for generating sigmoidal nonlinearities, such as dimerization of receptor subunits and cooperativity of transcription factor binding to DNA promoter sites. We assume that our sigmoidal functions, $H(W_i) = 1/(1+e^{-\sigma W_i})$, adequately capture the cumulative non-linear effects of these molecular mechanisms.

In addition, we assume that all transcription factors function at the same time scale, and all receptors function at the same, ten-fold slower time scale ($\rho_R = \rho_{TF}/10$). It is hard to know for sure what timescales these proteins are functioning on. While transcription factors are often functional immediately after synthesis, receptors must be trafficked to the periphery of the cell, diffuse within the cell membrane, assemble with other subunits, and bind to cytokines before a signal can be transduced back into the cell, after which the signal itself may take some time to get to its downstream target. At the very least, we would expect a significant time delay between production of the receptor and its impact on the expression of down-stream genes. For these reasons, we justify using a slower timescale for receptors than for transcription factors.

Finally, we assume that receptor activation does not have a significant negative feedback mechanism. Although it has been observed that the level of a receptor, such as M-CSFR and GM-CSFR, is reduced after stimulation by its own ligand [88], we choose to ignore these feedback loops, as we are interested in the initial aspects of cell differentiation, which are dominated by the positive feedback loops included in our model.

2.4 Results

2.4.1 A motif for GMP cell differentiation

The primary objective of this paper is to construct and analyze a dynamic model of the differentiation of GMP cells into monocyte and granulocyte lineages. Before describing the results derived from our model, we compare it briefly to the work of Laslo et al. who proposed a simple, symmetric model of the interactions among C/EBPα, PU.1, Gfi-1, and Egr [9]. The

purpose of their model was to demonstrate that mutual antagonism between Gfi-1 and Egr can be a mechanism for inducing commitment of the monocytic and granulocytic lineages. While achieving its intended purpose, the model's forced symmetry and its neglect of critical regulatory mechanisms limit its predictive capacity and its ability to explain more complex phenomena of myelopoiesis. We improve upon the Laslo model with new, biologically relevant interactions, including a fifth transcription factor, IRF8, as well as new signaling pathways, CSF receptors, and regulatory mechanisms for these receptors. These additional interactions break the symmetry of Laslo's model but extend the range of behaviors we can capture. Rather than modifying the equations of Laslo's model, we derive a new set of equations based on our standard-component modeling approach. Justification for these changes can be found in the methods section.

Our motif for GMP cell differentiation is depicted in Figure 2.2B. We convert this signaling network into a set of non-linear ODEs (Table A.1) with parameter values specified in Table A.2. Sample simulations for monocyte and granulocyte differentiation are presented in Figure 2.3. To gain some insight into these simulations, we use the notion of a "phase plane" from dynamical systems theory [89]–[91]. Although our system of eight nonlinear ODEs defines an eight-dimensional phase space, we can reduce it to a two-dimensional phase plane by making pseudo-steady state approximations on six of the eight variables, leaving the concentrations of "master regulators" PU.1 and C/EBP as the fundamental state variables. The method by which we affect this reduction is explained in the section on "computational methods".

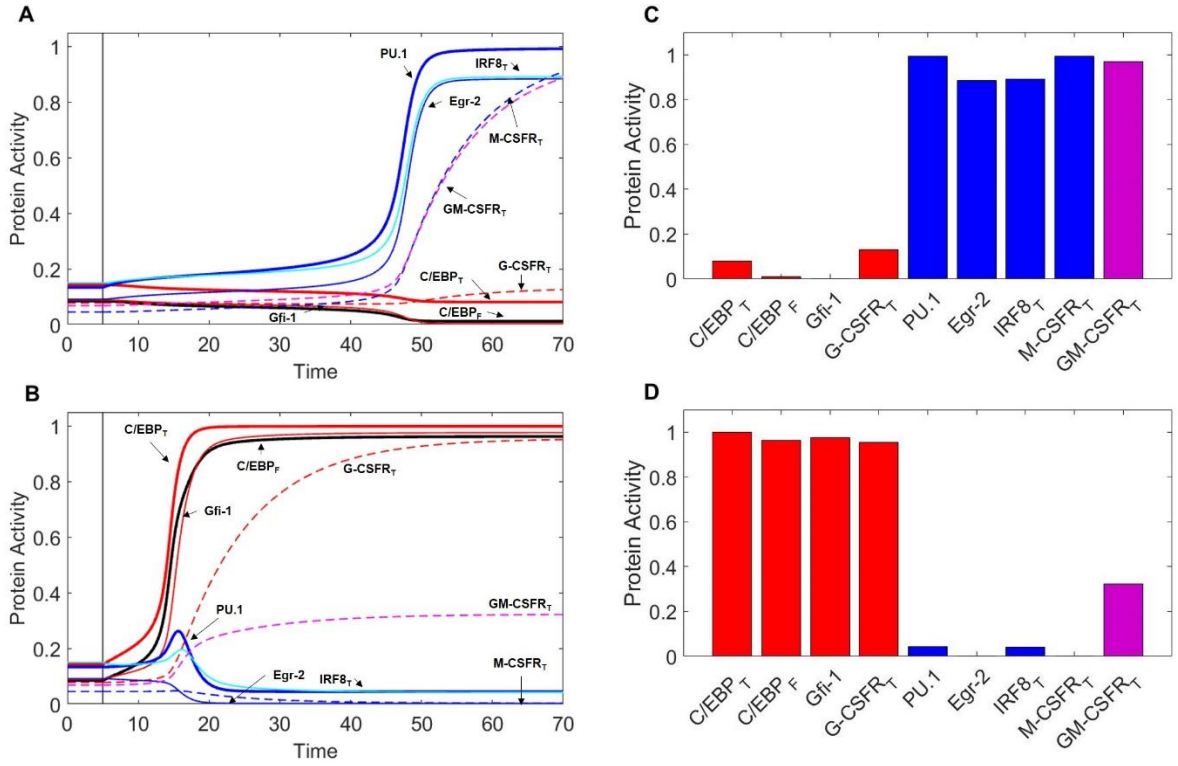

Figure 2.3) Protein activity over time during M-CSF and G-CSF induced differentiation.
For $t \leq 5$, there is no cytokine stimulation. When $t > 5$, [MCSF]=1 in (A), and [GCSF]=1 in (B). Under M-CSF stimulation, the GMP cell differentiates into a monocyte ($PU.1^{high}$, C/EBP_{low}) while under G-CSF stimulation the cell differentiates into a granulocyte progenitor ($PU.1_{low}$, C/EBP^{high}). Thick red line=$[C/EBP]_T$, black line=$[C/EBP]_F$, thick blue line=[PU.1], thin red line=[Gfi-1], thin blue line=[Egr-2],cyan line=$[IRF8]_T$, dashed red line=$[G\text{-}CSFR]_T$, dashed blue line=$[M\text{-}CSFR]_T$, dashed magenta line=$[GM\text{-}CSFR]_T$. One time unit=2h. (C) Final protein activity levels for simulation A indicate that M-CSF induces monopoiesis. (D) Final protein activity levels for simulation B indicate that G-CSF induces granulopoiesis.

On the phase plane (Figure 2.4A), we plot nullclines for the state variables PU.1 and C/EBP in the case of no cytokine stimulation. The PU.1 nullcline is the locus of points where $d[PU.1]/dt = 0$, and the C/EBP nullcline is the locus of points where $d[C/EBP]_T/dt = 0$. Where these nullclines intersect lie steady states of the full eight-dimensional set of ODEs. With no cytokine stimulation, these nullclines intersect five times to form three stable steady states (nodes) and two saddle points. The stable steady state with low levels of both C/EBP and PU.1 corresponds to a naïve GMP cell, whereas the other two stable steady states correspond to granulocyte and monocyte progenitor cells, depending on whether C/EBP or PU.1 is elevated, respectively. For the case of no cytokine stimulation, the GMP cell will sit indefinitely in the naïve state.

It is important to recognize that, in our model, "low" and "high" are relative. GMP cells are not typically described as having low concentrations of PU.1 and C/EBP, since both transcription

factors are required for the transition of a common myeloid progenitor into a GMP cell [32], [54]. In the framework of our model, however, it is appropriate to describe the GMP state as ($PU.1_{low}$, C/EBP_{low}), the granulocyte progenitor state as ($PU.1_{low}$, C/EBP^{high}), and the monocyte state as ($PU.1^{high}$, C/EBP_{low}). It is also important to note that, while PU.1 expression is elevated in neutrophils, PU.1 remains low in early granulocyte progenitors [92].

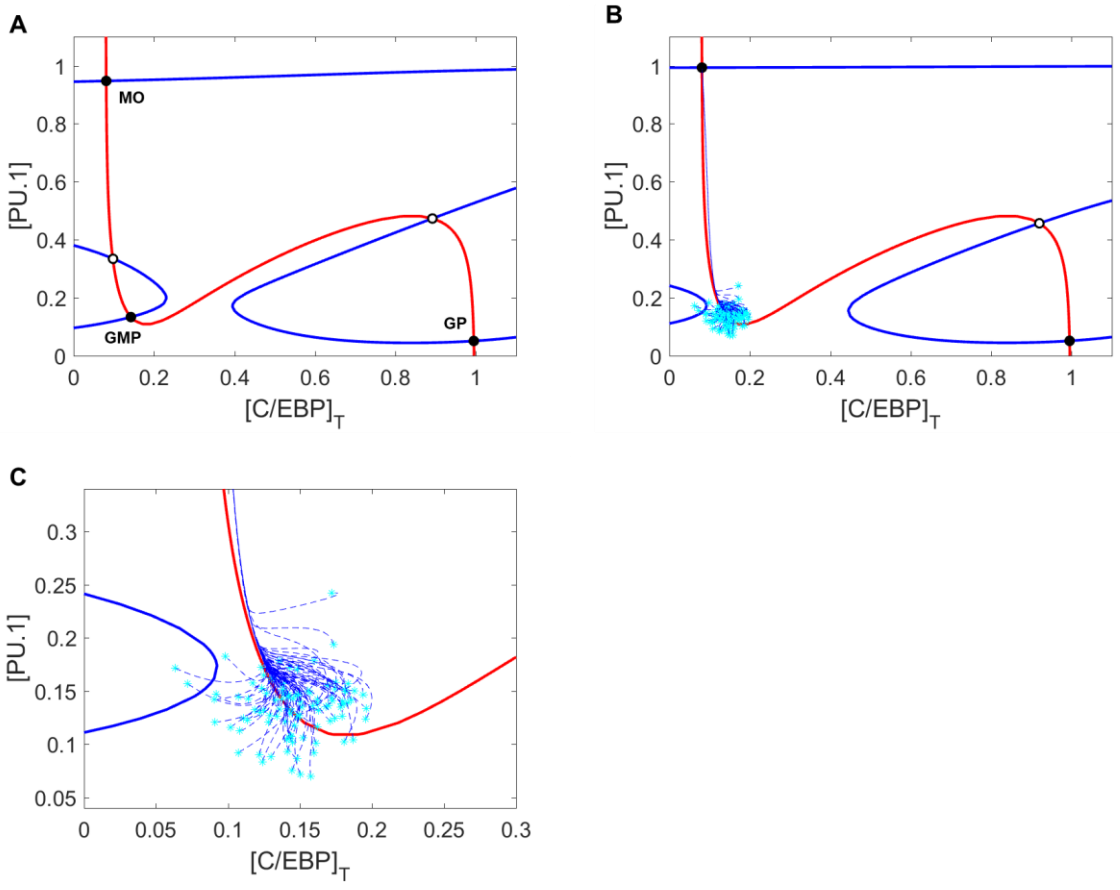

Figure 2.4) Nullcline movement due to M-CSF eliminates the GMP state and induces differentiation into the monocyte lineage.
Blue and red lines are the PU.1 and C/EBP nullclines, respectively. Black circles and white circles designate stable and unstable steady states, respectively. Cyan asterisks represent stochastically generated initial conditions, while blue dashed lines represent the cellular trajectories of monopoiesis from these initial conditions. (**A**) Nullclines with no cytokine stimulus. Of the five intersection points, three represent stable steady states: MO, GMP and GP mark the monocyte, naïve GMP and granulocyte progenitor (GP) states, respectively. Without cytokine stimulation, GMP cells will remain in the stable naïve state, even though monocyte and granulocyte progenitor cell states are also stable nodes of attraction. (**B**) Nullclines with M-CSF stimulation ([MCSF]=1). Only the PU.1 nullcline moves in response to M-CSF, resulting in loss of the GMP state. Cells starting in the neighborhood of the GMP state that has disappeared find themselves in the domain of attraction of the stable monocyte-progenitor cell state. (**C**) A closer look at the initial trajectories of stochastically generated cells reveals that they converge along the same path towards the monocyte state despite different initial conditions.

2.4.2 M-CSF induces monopoiesis

We begin our investigation of external signaling by exploring how nullclines shift in response to M-CSF stimulation. Comparing Figures 2.4A and 2.4B, we see that, in response to M-CSF, the PU.1-nullcline moves and the naïve GMP state is lost. Although both the monocyte ($PU.1^{high}$, C/EBP_{low}) and granulocyte progenitor ($PU.1_{low}$, C/EBP^{high}) states remain, Figures 2.4B and 2.4C show that GMP cells under M-CSF stimulation preferentially differentiate into the monocyte state.

Bifurcation diagrams with respect to M-CSF (Figure 2.5) illustrate how the cytokine affects the stability of GMP cells. We show (Figure 2.5C) how M-CSF concentration can destabilize the GMP state, resulting in differentiation into the monocyte state, and why this differentiation is irreversible. For cytokine concentrations less than ~0.5, there are three stable steady states, including one at $[PU.1] \approx 0.15$, $[C/EBP]_T \approx 0.15$ (the naïve GMP cell), whereas, for [MCSF] > 0.5, there are only two stable steady states, corresponding to monocytes and granulocyte progenitors. Thus, M-CSF induced monopoiesis is irreversible, as the monocyte state remains stable even if the M-CSF concentration is decreased to zero after the transition is made (see the black arrows in Figure 2.5C).

Although we use $[C/EBP]_T$ and [PU.1] as primary markers of cell type, temporal changes in the other transcription factors (Figure 2.3A) give a more complete picture of the dynamics of the system. In the early stages of monopoiesis, we see an immediate increase in PU.1, IRF8, and Egr-2. IRF8 binds to C/EBP resulting in a slight decrease in C/EBP activity while Egr-2 represses Gfi-1, relieving suppression of PU.1. Furthermore, PU.1 upregulates itself, resulting in the switch-like behavior that is demonstrated in Figure 2.5C. Receptors such as GM-CSFR and M-CSFR are heavily upregulated while G-CSFR remains at a lower level (Figure 2.3C).

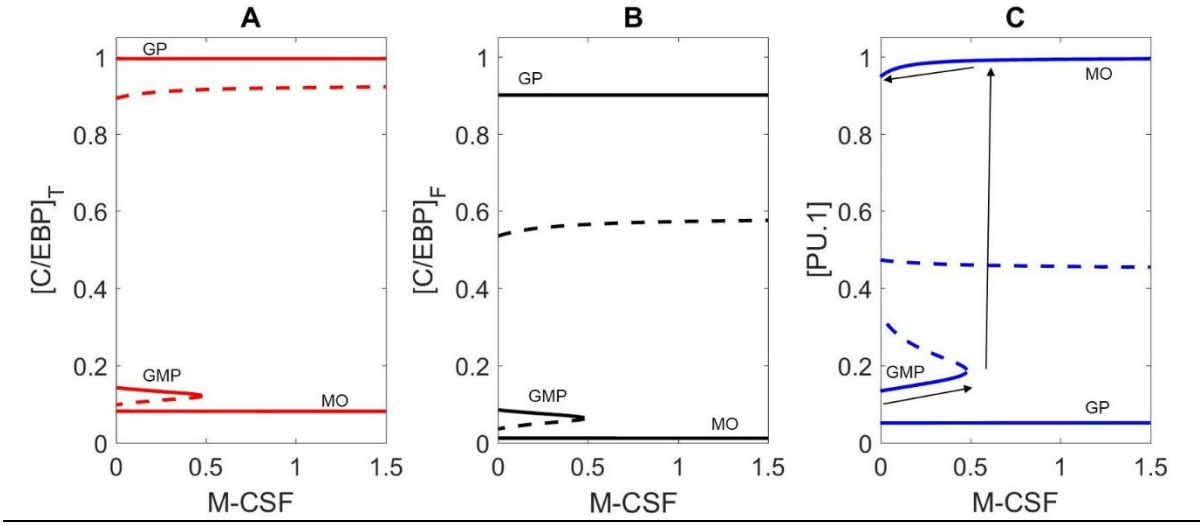

Figure 2.5) Bifurcation diagram with respect to M-CSF concentration.
Three representations of the same bifurcation diagram, in terms of (A) $[C/EBP]_T$, (B) $[C/EBP]_F$, and (C) [PU.1]. Stable steady states are represented by solid lines and unstable states by dashed lines. The dynamical system undergoes a saddle-node bifurcation at [MCSF] ≈ 0.5, where the stable GMP state is lost. Black arrows on (C) demonstrates the irreversible switch of M-CSF induced monopoieses. The bottom line represents the change in the GMP state as [M-CSF] increases, the second arrow (pointing up) represents the "switch" in state and the third arrow (top) demonstrates that decreasing the M-CSF concentration does not return the cell to the GMP state.

2.4.3 G-CSF induces granulopoiesis

G-CSF stimulation changes the landscape of the (PU.1, C/EBP) phase plane (Figure 2.6A) more drastically than M-CSF stimulation. Surprisingly, the PU.1 nullcline is more sensitive to changes in G-CSF than the C/EBP nullcline. As a result, there remain five intersection points, but only two are stable (the monocyte and granulocyte progenitor states). The other three steady states are two saddle points and an unstable node. There appear to be two additional intersection points of these nullclines; however, the apparent intersections are an artifact of projecting the nullclines onto the (PU.1, C/EBP) phase plane. By plotting the nullclines in a three-dimensional phase space in Figure 2.6B, we show that the nullclines intersect only five times.

The bifurcation diagram (Figure 2.6C) is in agreement with our nullclines, and shows that the GMP state disappears at [GCSF] ≈ 0.21, with only two stable steady states remaining (monocyte and granulocyte progenitor) and three unstable steady states. Despite the bistable nature of the system under G-CSF stimulation, GMP cells preferentially differentiate into granulocytes due to the locations of the basins of attraction of the two stable steady states (Figure 2.6A).

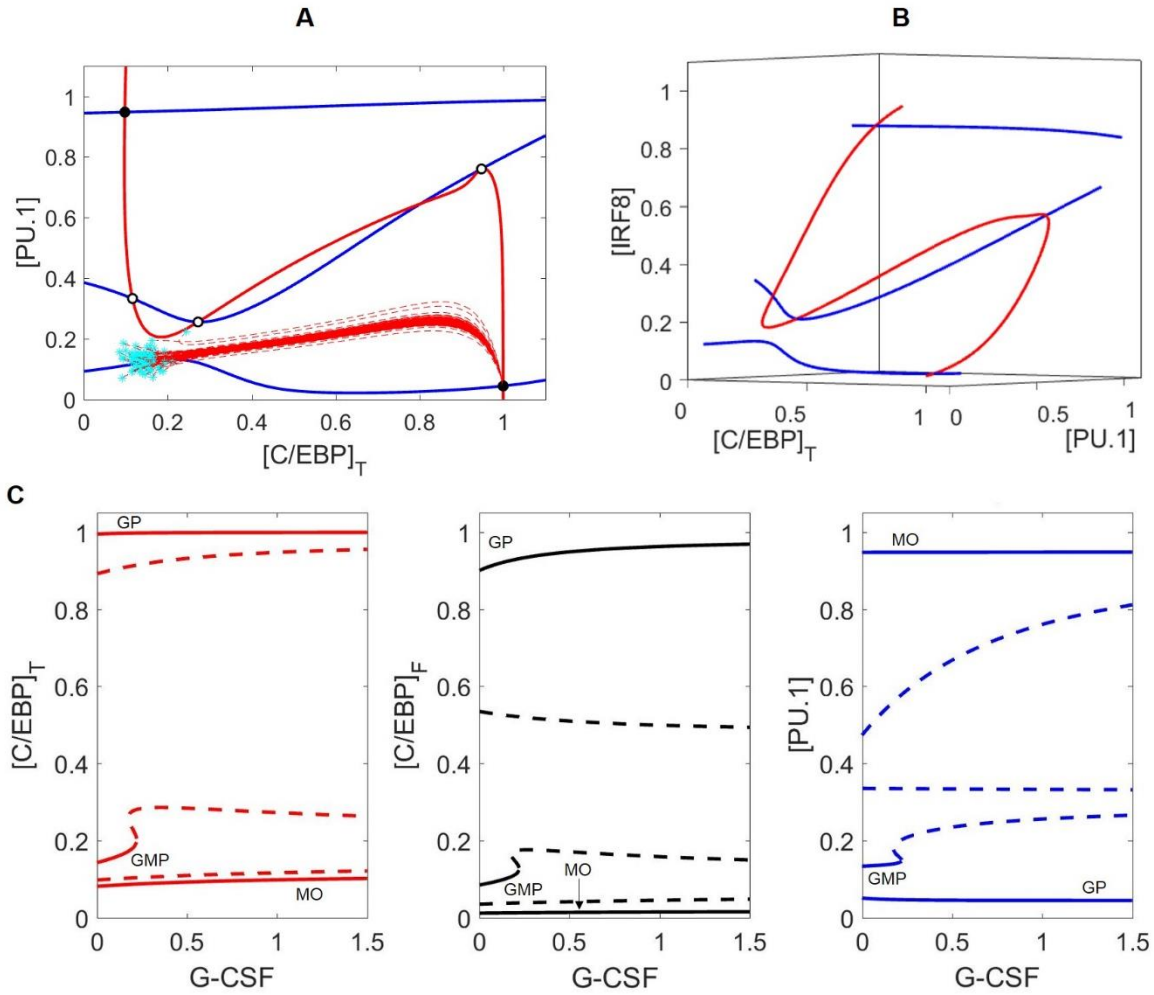

Figure 2.6) Phase plane and bifurcation in response to G-CSF.
(**A**) Nullclines and trajectories as in figure 4; [GCSF]=1. Both PU.1 and C/EBP nullclines move in response to G-CSF, and only two stable steady states remain: the granulocyte state (bottom right) and the monocyte state (top left). GMP cells preferentially differentiate to the granulocyte state under G-CSF stimulation, as indicated by the dashed red lines**.** (**B**) Nullclines in a three-dimensional phase space ([PU.1], $[C/EBP]_T$, and [IRF8]) reveal that there are only five steady states. The two other apparent nullcline intersections in panel A are artefacts of the projection onto a two-dimensional phase plane. (**C**) As in Figure 5, we show three different views of the same bifurcation diagram. Stable states are represented by solid lines and unstable states by dashed lines. For [GCSF] ≤ 0.2, the control system has three stable steady states (GMP, GP, MO) and two (or four) unstable steady states. For larger values of [GCSF], the GMP state is lost and only two stable steady states remain (GP and MO states).

While experiments suggest that G-CSF induces granulopoiesis, the dynamical changes during this process of differentiation are not well documented. Our model (Figure 2.3B) suggests that G-CSF stimulation results in an initial increase of PU.1 expression, due to increased C/EBP activity, before PU.1 is eventually suppressed by Gfi-1. Egr-2 is also suppressed directly by Gfi-

1, and IRF8 is suppressed when PU.1 activity decreases. The system reaches steady state as a granulocyte progenitor cell with high expression of C/EBP, Gfi-1 and G-CSFR, as well as moderate expression of GM-CSFR (Figure 2.3D).

Interestingly, when comparing the differentiation time of M-CSF induced monopoiesis and G-CSF induced granulopoiesis (Figure 2.3A&B), we find that GMP cells commit to the granulocyte progenitor state more quickly than to the monocyte state. This is likely a result of the fact that the auto-activation of C/EBP is stronger in our model than that of PU.1. It is known that it can take approximately 6 days for a monoblast (the earliest stage of monopoiesis) to mature into a monocyte, while it takes a GMP cell 1.5-2 days to mature into a promyelocyte.[93], [94] As the transcription factor expression levels of our granulocyte progenitor state are similar with those of the promyelocyte state, we find that these temporal ratios are consistent with our simulations [92]. However, we must note that, while these times are consistent with the literature, our model suggests that the differentiation time is concentration dependent (Figure A.2).

2.4.4 Low concentrations of GM-CSF favor monopoiesis while higher concentrations favor granulopoiesis

An important question we wish to address in this paper is: what possible mechanism can explain the concentration-dependent behavior of GM-CSF induced differentiation? GM-CSF signals upregulate C/EBP, which in turn promotes PU.1 and Gfi-1 transcription. However, Gfi-1 and PU.1 are mutually antagonistic, and PU.1 suppresses C/EBP activity via IRF8 (Figure 2.2B). Thus, C/EBP can inhibit PU.1 through Gfi-1, or suppress itself and Gfi-1 via activation of PU.1. We propose that this combination of positive and negative interactions that C/EBP has with PU.1, and the asymmetrical nature of the system, manifests itself in the concentration-dependent outcomes of GM-CSF induced GMP differentiation.

At low levels of GM-CSF (Figure 2.7A&C), both C/EBP and PU.1 rise swiftly. PU.1's positive autoregulation drives it to increase faster than Gfi-1, promoting IRF8 and Egr-2 production in the process. IRF8 binds to and suppresses C/EBP, preventing C/EBP-induced expression of Gfi-1, while Egr-2 directly suppresses Gfi-1. Eventually, Gfi-1 is irreversibly suppressed and PU.1 is dominant. The resulting phenotype resembles that of the monocyte lineage. Thus our model

agrees with experimental observations, that low concentrations of GM-CSF encourage monopoiesis [11]. When we compare M-CSF and GM-CSF induced monopoiesis (Figure 2.3A & 2.7A), we find that the final expression patterns are very similar, however the evolution of transcription factor expression is different. Notably, during GM-CSF induced monopoiesis, C/EBP levels and Gfi-1 levels rise substantially prior to being suppressed, while C/EBP and Gfi-1 remain low in M-CSF induced monopoiesis. Our model also suggests that GM-CSF induced monopoiesis is more rapid than M-CSF induced monopoiesis (Figure A.2).

At higher concentrations of GM-CSF (Figure 2.7B&D), C/EBP increases more rapidly due to a combination of stronger GM-CSF stimulation, suppression of IRF8, and C/EBP positive autoregulation. The rapid increase in C/EBP results in acceleration of Gfi-1 production. While PU.1 expression is also enhanced, PU.1 relies heavily on its own capacity to auto-activate. Therefore, when C/EBP is increased, there is a delay before PU.1 reaches its maximum production rate; however, Gfi-1 reaches its maximum production rate immediately. Thus, Gfi-1 is more responsive to a change in C/EBP than PU.1. Furthermore, Gfi-1 directly suppresses PU.1 and Egr-2, while PU.1 must upregulate Egr-2 to inhibit Gfi-1. If Gfi-1 increases faster than PU.1, it halts PU.1-induced Egr-2 expression and establishes dominance over PU.1. In this way, our model predicts that high concentrations of GM-CSF will induce granulopoiesis over monopoiesis, a result which is consistent with experimental observations [11].

We find that, even though the differentiation times of GM-CSF and G-CSF induced granulopoiesis are very similar (Figure A.2), during GM-CSF induced granulopoiesis the PU.1 and IRF8 levels spike considerably higher than during G-CSF induced granulopoiesis (Figure 2.3B & 2.7B). This is likely due to greater Gfi-1 activity during earlier stages of G-CSF induced granulopoiesis.

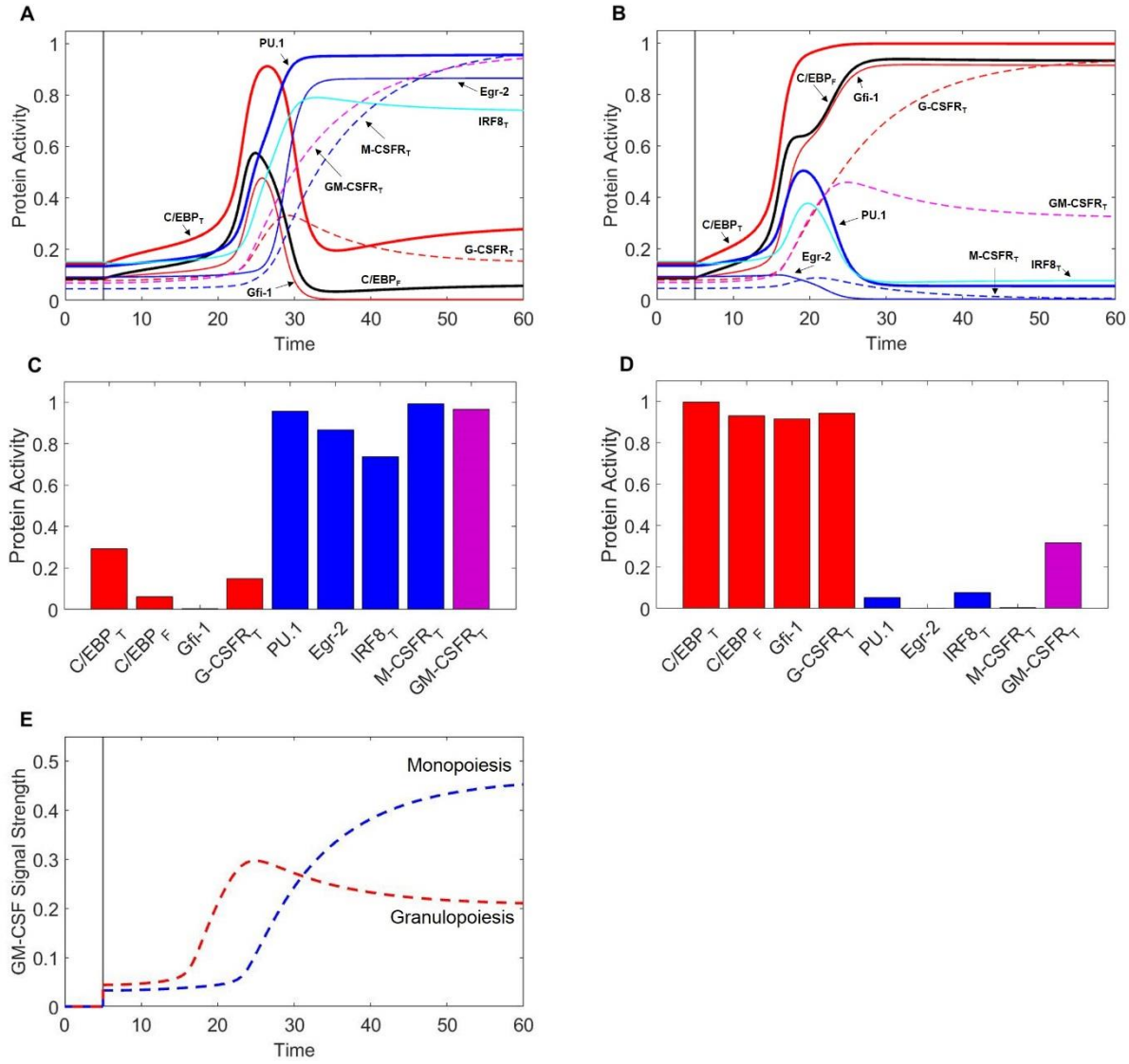

Figure 2.7) GM-CSF induces monopoiesis and granulopoiesis at low and high concentrations, respectively. When $t \leq 5$, [GMCSF] = 0. When $t > 5$, [GMCSF] = 0.6 for low concentration (panel **A**) and 1.2 for high concentration (panel **B**). Thick red line = $[C/EBP]_T$, black line = $[C/EBP]_F$, thick blue line = [PU.1], thin red line = [Gfi-1], thin blue line = [Egr-2], cyan line = $[IRF8]_T$, dashed red line = $[G\text{-}CSFR]_T$, dashed blue line = $[M\text{-}CSFR]_T$, dashed magenta line = $[GM\text{-}CSFR]_T$. (**C**) Final protein activity levels for simulation A indicate that low concentrations of GM-CSF induce monopoiesis. (**D**) Final protein activity levels for simulation B indicate that high concentrations of GM-CSF induce granulopoiesis. (**E**) GM-CSF signal strength during GM-CSF induced granulopoiesis and monopoiesis**.** Signal strength is proportional to and reported as [GMCSFR:GMCSF]. Blue dashed line represents a cell developing into a monocyte for [GMCSF] = 0.6. Red dashed line represents a cell developing into a granulocyte for [GMCSF] = 1.2. We find that higher concentrations of GM-CSF result in a higher initial signal to stimulate granulopoiesis; however, the signal decreases and levels off after the cell has committed to the granulocyte lineage. Lower concentrations of GM-CSF initially have lower signal strengths to initialize monopoiesis; however, GM-CSFR is upregulated to high levels after monocytic commitment, resulting in a greater GM-CSF signal strength in the monocytic lineage.

Intriguingly, our model suggests that GM-CSFR expression decreases slightly after granulocytic commitment, and remains at lower levels than the monocytic lineage. Experimental evidence shows that, indeed, GM-CSFR expression is higher in monocytes than in granulocytes, despite the fact that higher concentrations of GM-CSF favor granulopoiesis over monopoiesis [11], [95], [96]. To explore why, we examine the incoming signal strength of GM-CSF over time with high and low GM-CSF concentrations (Figure 2.7E). We find that the incoming GM-CSF signal is stronger in the short term under high-dose conditions (granulopoiesis), however the signal strength begins to decrease after ~24 time units due to reduced GM-CSFR expression. In contrast, at lower doses of GM-CSF (monopoiesis), the signal strength remains low until ~24 time units, when it increases substantially in a hyperbolic fashion to levels much higher than in granulopoiesis. We propose that the sudden increase in signal is due to a switch-like mechanism, resulting from the positive feedback loop involving GM-CSFR, C/EBP and PU.1. As a result of this mechanism, we observe that the lower the GM-CSF concentration, the longer it takes for the switch to kick in. We ascertain that, at low GM-CSF concentrations, the delay in the switch event permits PU.1 to establish dominance over Gfi-1 and C/EBP, and commit to the monocyte lineage. The signal strength of GM-CSF is half-maximal at ~30 time units after stimulation. At this point in monopoiesis (Figure 2.7A), Gfi-1 is subdued, C/EBP is on a steep decline, and monocytic transcription factors are highly expressed. Thus, by the time the GM-CSF signal is strong, the cell is already committed to the monocyte lineage. Similarly, with higher levels of GM-CSF, the cell has decisively committed to the granulocytic lineage at the point of maximum signal strength (~24 time units in Figure 2.7B).

Our results suggest that in both monopoiesis and granulopoiesis the GM-CSFR signaling capacity changes significantly after the cell has already committed to one lineage over another. If this is true, then the high concentration of GM-CSFR in monocytes relative to granulocytes must serve an alternative function than lineage commitment. One possibility is that GM-CSFR signaling, or lack thereof, is crucial for regulating proteins not accounted for by this model. Alternatively, GM-CSF signaling may function to upregulate C/EBP in the monocytic lineage, since it is necessary for AP-1 to bind with C/EBP to promote monocytic genes [97]. It is also possible that downregulation of GM-CSFR is crucial for proper granulocyte development, as C/EBPα is downregulated in later stages of granulopoiesis [98]. While future experimental

studies may clarify these issues, our model does lead us to an additional conclusion that we will discuss in the subsequent section.

2.4.5 GM-CSF induces M-MDSC differentiation

If low levels of GM-CSF induce monopoiesis and high levels induce granulopoiesis, what happens when we try something in the middle? Remarkably, our model predicts that moderate exposure to GM-CSF can induce GMP differentiation into a hybrid state: $PU.1^{high}$ C/EBP^{high} (Figure 2.8A&B). Moreover, we find that the dynamics of this process are strikingly similar to GM-CSF-induced monopoiesis. While C/EBP and PU.1 both rise swiftly early in the process, there is a lag in GM-CSFR expression, allowing PU.1 to establish dominance over C/EBP and Gfi-1. Thus, the cell begins to resemble the monocytic phenotype. However, when GM-CSFR approaches maximum expression, the signal becomes strong enough to induce a switch in C/EBP behavior, resulting in high C/EBP expression. Furthermore, a large fraction of C/EBP binds with IRF8, restricting its capacity to activate granulocytic genes. As a result of this and high levels of Egr-2, Gfi-1 remains repressed. The outcome is a new hybrid state ($PU.1^{high}$, C/EBP^{high}). Naturally, the question arises, is there a myeloid cell that fits this description? Indeed, M-MDSCs fit this profile, as these monocytic cells presumably express high levels of PU.1 and are known to highly express C/EBPβ [99]. Furthermore, M-MDSCs highly express IRF8 relative to granulocytes, and are likely to express high levels of Egr-2 and low levels of Gfi-1 as these are mutually antagonistic master regulators of the monocytic and granulocytic lineages, respectively [9], [82]. Because the hybrid state fits the expected expression profile of M-MDSCs and displays behavioral characteristic observed in M-MDSC experiments (as discussed below), we propose that this hybrid state is representative of M-MDSCs and refer to this state as the M-MDSC state for the remainder of the paper.

We have described three distinct expression profiles that result from different GM-CSF concentrations, but it is still unclear which phenotypes are favored over the entire range of GM-CSF concentrations. To evaluate this "favorability spectrum", we simulated 10,000 stochastically generated cells under different GM-CSF conditions (Table 2.1). The results confirm that the monocytic state is heavily favored at lower concentrations of GM-CSF. However, the population ratio shifts towards granulocytes as the dose of GM-CSF is increased. We also observe a distinct

dichotomy in the expression of monocytes and M-MDSCs, suggesting that GM-CSF induces some kind of toggle switch.

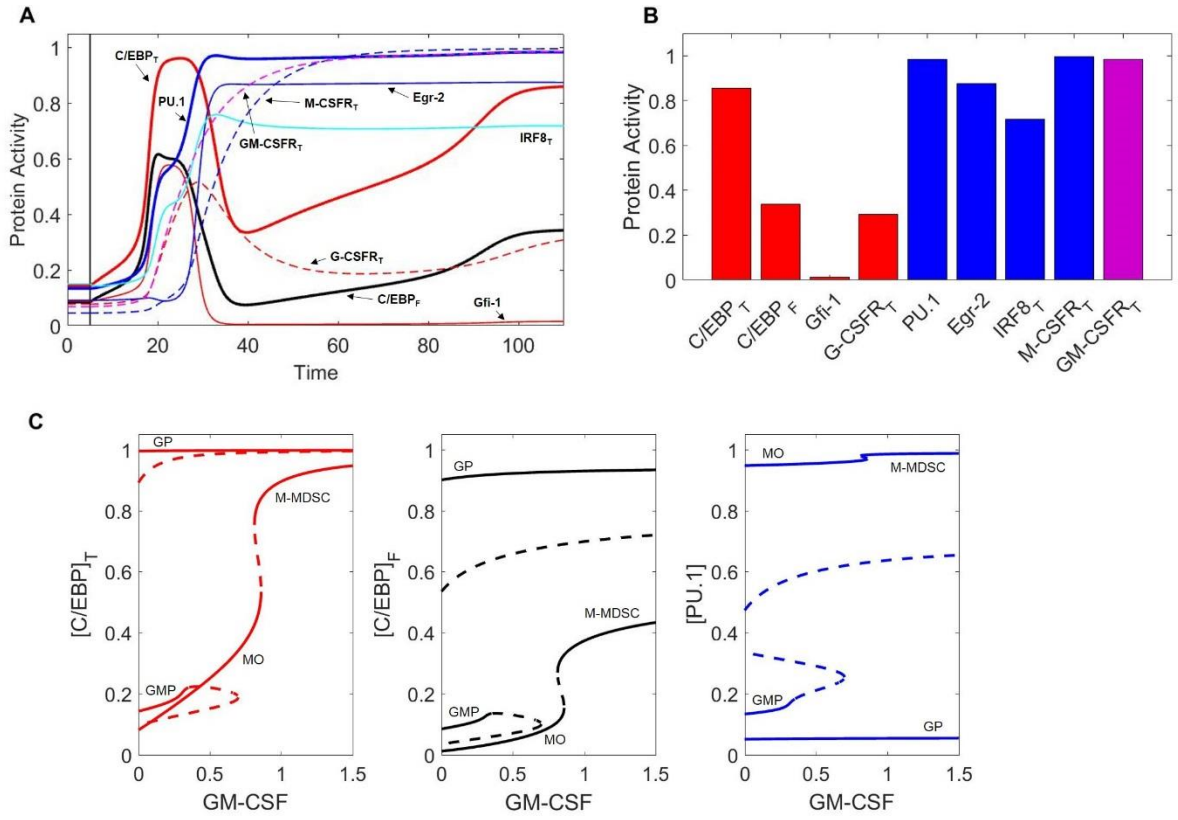

Figure 2.8) GM-CSF induces M-MDSC differentiation.
(**A**) Protein activity over time (*t*) during GM-CSF induction of the M-MDSC phenotype. When $t < 5$, [GMCSF] = 0 units. When $t > 5$, [GMCSF] = 0.9. Line descriptions are the same as Figure 3 and Figures 7A and 7B. (**B**) Final protein activity levels for simulation A indicate that moderate concentrations of GM-CSF can induce the M-MDSC phenotype. (**C**) Three views of the same bifurcation diagram. Stable states are represented by solid lines and unstable states by dashed lines. At [GMCSF] = 0, the system exhibits three stable nodes (GMP, granulocyte progenitor and monocyte) and two unstable saddle points. At [GMCSF] ≈ 0.35, the GMP state is destabilized, and it briefly re-stabilizes for 0.66 < [GMCSF] < 0.69. The MO state ($PU.1^{high}$, C/EBP_{low}) is stable until [GMCSF] ≈ 0.86, at which point it switches to the M-MDSC state ($PU.1^{high}$, C/EBP^{high}).

To explore these effects further, we computed one-parameter bifurcation diagrams with respect to GM-CSF concentration (Figure 2.8C). Indeed, we find that a toggle switch (saddle-node bifurcation) does occur from the monocyte state to the hybrid state when [GMCSF] ≈ 0.86. This suggests that the monocyte state is unstable at high GM-CSF concentrations, while the M-MDSC state is dependent on significant cytokine stimulation.

To better understand the dynamics of cell differentiation at varying GM-CSF concentrations, it is helpful to consider the phase planes and cell trajectories in Figure 2.9. We find that the PU.1

nullcline does not respond to GM-CSF; however, the C/EBP nullcline moves in such a way that the granulocyte state remains fixed in position and the monocyte state shifts substantially. In agreement with the bifurcation diagrams, the nullclines show that, as [GMCSF] increases, the monocyte state moves towards higher concentrations of C/EBP. Furthermore, with this changing nullcline landscape, the basins of attraction alter, resulting in a shift of favorability towards the granulocyte progenitor state. The representative cell trajectories (dashed lines in Figure 2.9) are good indicators of how the nullcline shifts affect cell differentiation. At [GMCSF] ≈ 0.86, the C/EBP nullcline lifts away from the PU.1 nullcline, so that the monocyte state disappears and the M-MDSC state is revealed.

Table 2.1) Population ratios over a range of GM-CSF concentrations.
We simulated the differentiation of 10,000 stochastically generated cells at increasing GM-CSF concentrations over a time period of 150 time units (~150 h). We classified the final state as "naïve GMP", "granulocyte progenitor", "monocyte" or "M-MDSC". The results show that monocytes are heavily favored at low concentrations of GM-CSF, while granulocytes are favored at high concentrations. Monocyte differentiation yields to the M-MDSC phenotype at higher GM-CSF concentrations.

[GMCSF]	% Naïve GMP	% Granulocyte Prog.	% Monocyte	% M-MDSC
0	99.79	0.2	0.01	0
0.2	99.21	0.48	0.31	0
0.4	0	4.15	95.85	0
0.6	0	18.21	81.79	0
0.8	0	38.57	61.43	0
1.0	0	53.97	0	46.03
1.2	0	62.88	0	37.12
1.4	0	68.20	0	31.80

Figure 2.9 shows that M-MDSC differentiation follows a similar trajectory as GM-CSF induced monopoiesis, as we observed before when comparing Figures 2.7A and 2.8A. The pattern of monocyte differentiation is particularly interesting. The differentiating cells move in an arching fashion, first towards states of high PU.1 and C/EBP and then toward states of high PU.1 and low C/EBP; overshooting the monocyte steady state, they make a second turn-around, involving increasing concentration of C/EBP, as they approach the stable monocyte steady state. This

pattern is seen in Figures 2.7A and 2.8A as well, where the C/EBP concentration rises (the arching phase), plummets (the passing phase) and then begins to rise again (the second-turn phase). Differentiation dynamics of the M-MDSC phenotype are quite similar, the critical difference being that the final steady state has much larger concentrations of C/EBP than is typical of monocyte cells.

These results suggest that the stability of the monocyte and M-MDSC states is dependent on the extracellular GM-CSF concentration. Thus, a monocyte exposed subsequently to higher levels of GM-CSF should transition into the M-MDSC state. This result is consistent with experiments that suggest tumor-conditioned media can convert monocytes into M-MDSCs and that GM-CSF can induce M-MDSC differentiation from myeloid progenitors [52], [100], [101]. Similarly, the model suggests that M-MDSCs that are removed from GM-CSF stimulus should be destabilized. Figure A.3 explicitly shows how these transitions can occur. We find that the ability of GM-CSF to convert monocytes into M-MDSCs is partially due to high expression of GM-CSFR within the monocyte lineage, as the signal strength must be sufficiently high to induce this transformation. This suggests one possible biological motivation for monocytes to express such high levels of the receptor, as this monocytic plasticity may be useful in a variety of pathological conditions.

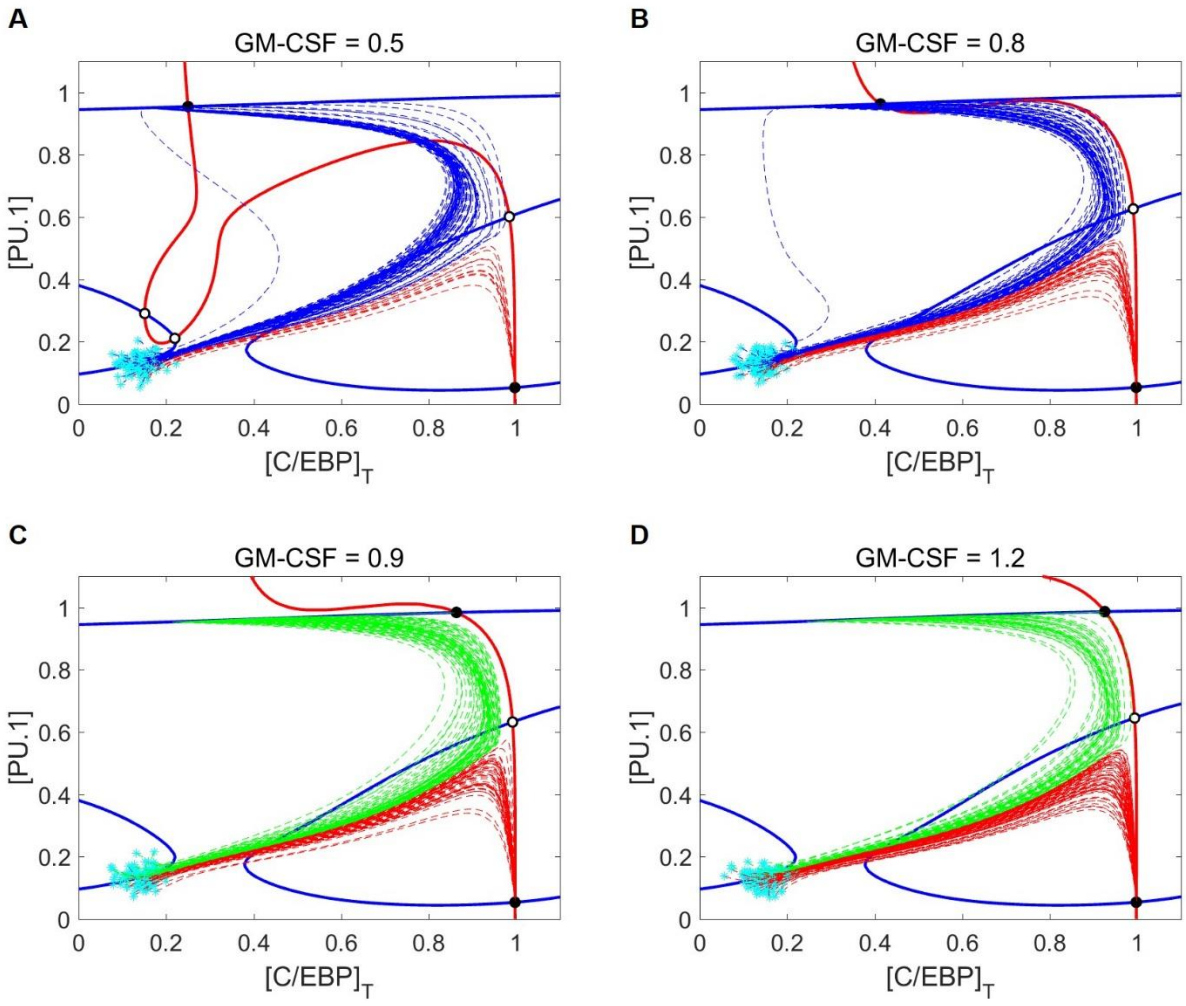

Figure 2.9) Nullcline shifts, in response to changes in GM-CSF concentration, illustrate the switch from monocyte state to M-MDSC.

(**A-D**) Phase planes at four different concentrations of GM-CSF: 0.5, 0.8, 0.9 and 1.2. Solid blue and red lines denote the PU.1 and C/EBP nullclines, respectively. Black and white circles designate stable and unstable steady states, respectively. Cyan asterisks represent stochastically generated initial conditions for a population of simulated cells. After stimulation by GM-CSF, the cells follow the dotted lines (trajectories of the full eight-dimensional system of ODEs projected onto the two-dimensional phase plane). Blue dotted lines end up at a monocyte steady state, red lines at a granulocyte progenitor steady state, and green lines at an M-MDSC steady state. As [GMCSF] increases, the C/EBP nullcline moves in such a way that the monocyte state gives way to a new M-MDSC state.

2.4.6 Combined treatment with G-CSF and M-CSF results in a heterogeneous population of granulocytes and monocytes

If G-CSF and M-CSF promote granulopoiesis and monopoiesis, respectively, what happens when we expose a cell to both simultaneously? A heat map of M-CSF and G-CSF stimulation

(Figure 2.10A) suggests that M-CSF may inhibit granulopoiesis at lower concentrations of G-CSF. However, when both cytokines are introduced at higher levels, our model suggests that the resulting population will be a heterogeneous mix of both granulocytes and monocytes, a result in agreement with experimental observations [10]. Surprisingly, the model suggests that GMP cells stimulated by both G-CSF and M-CSF never differentiate into M-MDSCs. Phase plane analysis suggests that the M-MDSC state does not exist under such conditions (Figure A.4).

2.4.7 G-CSF can push cells towards monopoiesis in low signaling conditions

An intriguing phenomena occurs when G-CSF is paired with low doses of M-CSF. Figure A.5 (an alternative view of the lower-left corner of Figure 2.10A) shows that G-CSF can induce monopoiesis at M-CSF concentrations too weak to stimulate differentiation alone. Although several cells differentiate into granulocytes under these conditions, the fact remains that a larger percent of GMP cells differentiate into monocytes than if G-CSF were absent. G-CSF has a similar effect when paired with GM-CSF. Figure A.6 (an expanded view of the lower-left corner of Figure 2.10B) shows that low concentrations of G-CSF can actually lower the GM-CSF dose required to induce monopoiesis. When [GCSF] = 0, significant monocytic development is not triggered until [GMCSF] > 0.35; however, with [GCSF] = 0.05, the required minimal dose of GM-CSF decreases to 0.2. When the concentration of G-CSF is increased further, however, it pushes the system towards granulopoiesis. Ultimately, these results suggest that, for cells that are primed for the monocyte lineage but do not have quite enough stimulus to initiate the process, G-CSF can provide the small push that is necessary to initiate monopoiesis. However, if G-CSF is introduced at higher concentrations, it will induce granulopoiesis at the expense of monopoiesis.

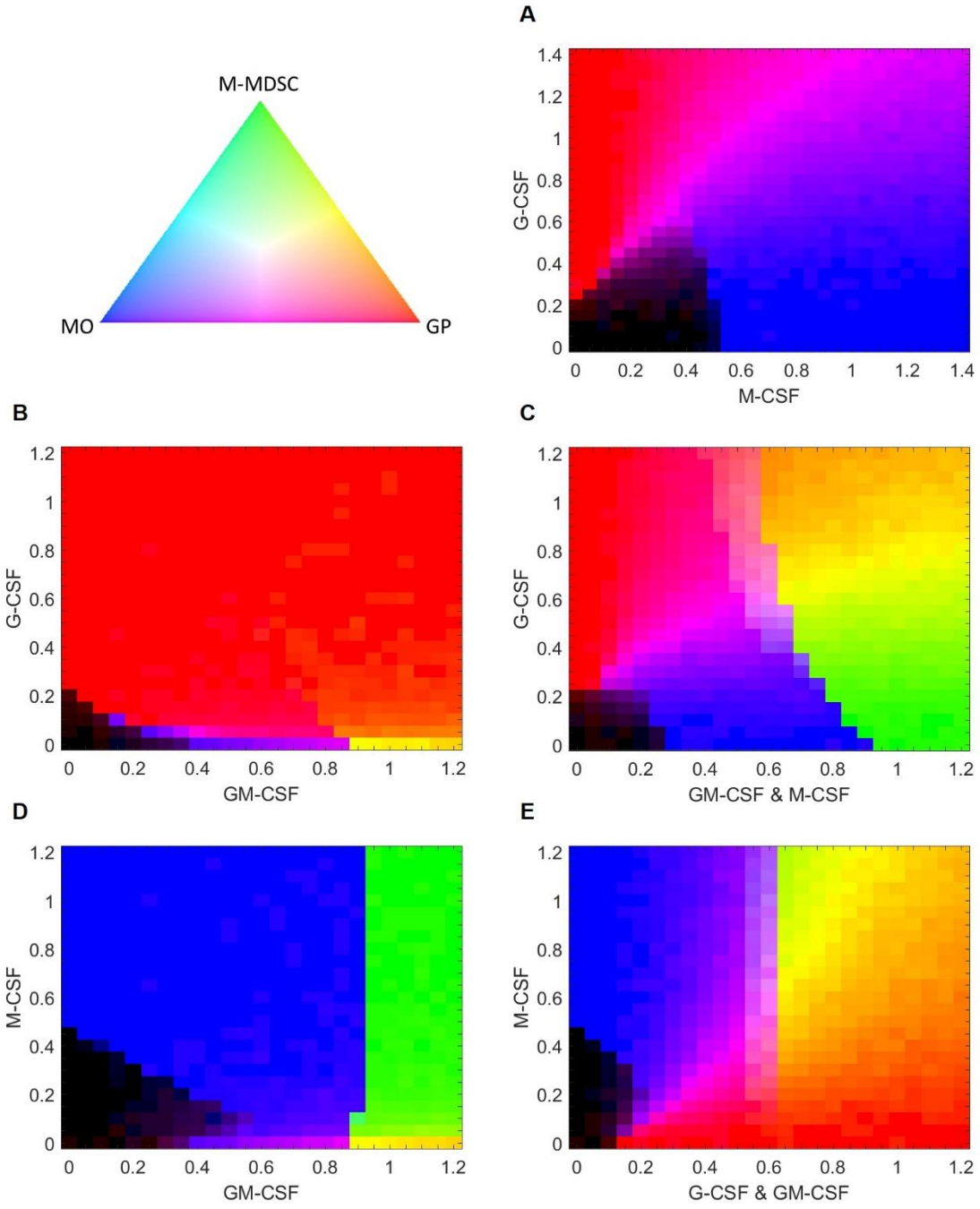

Figure 2.10) Simulated composition of stochastically generated populations of cells in response to various combinations of cytokines.

Each cytokine combination is simulated with 500 stochastically generated cells. The color gradient triangle on the top left correlates to population composition. Populations containing all M-MDSCs, granulocyte progenitors (GP), or monocytes (MO) are represented by green, red and blue, respectively. Black represents populations of undifferentiated cells. The mathematical relationship between population ratios and pixel color is discussed in "computational methods". (**A,B**) G-CSF paired with M-CSF or GM-CSF. (**C**) G-CSF paired with equal concentrations of GM-CSF and M-CSF. (**D,E**) M-CSF paired with GM-CSF or with equal concentrations of G-CSF and GM-CSF.

2.4.8 G-CSF can inhibit or encourage M-MDSC development when paired with M-CSF and GM-CSF

Having evaluated the effects of G-CSF coupled with M-CSF and GM-CSF individually, we naturally progress to evaluate G-CSF effects when paired with equal signals from GM-CSF and M-CSF (GM/M-CSF). As one might expect, our model predicts that, when paired with low levels of GM/M-CSF, G-CSF can induce GMP cells to favor granulopoiesis over monopoiesis (Figure 2.10C). However, at higher levels of GM/M-CSF that still favor the monocyte phenotype (the interval [0.65, 0.9] in Figure 2.10C), G-CSF can push the system in favor of M-MDSC development. In fact, the closer the GM/M-CSF signal is to the M-MDSC switch threshold (≈0.9), the less G-CSF is required to induce the M-MDSC phenotype. The capacity for G-CSF to induce GMPs to differentiate into M-MDSCs suggests that already differentiated monocytes in similar conditions (with GM-CSF) can also be pushed into the M-MDSC state by G-CSF. These results are intriguing, as G-CSF is typically associated with its effects on granulopoiesis and PMN-MDSCs, rather than M-MDSCs.[52], [102] Furthermore, we find that, in conditions that favor M-MDSCs, additional G-CSF can push GMP cells in favor of granulopoiesis. Therefore, our model predicts that G-CSF can either promote or inhibit the production of M-MDSCs, depending on the extracellular conditions.

2.4.9 M-CSF can induce M-MDSC differentiation when mixed with GM-CSF

It has been well documented that both M-CSF and GM-CSF can contribute to M-MDSC development.[103], [104] Since our model indicates that M-CSF alone cannot induce the M-MDSC phenotype, we test to see what effect it has when coupled with GM-CSF (Figure 2.10D). We find that a GM-CSF primed system is hyper-sensitive to M-CSF, as even very low doses of M-CSF can arrest granulopoiesis to favor M-MDSCs. (For detailed effects on granulopoiesis, see Figure A.7.) This suggests that the effects of M-CSF are minimally concentration-dependent. We suspect that this extreme sensitivity is unrealistic for real-life conditions, as the sensitive behavior would likely be washed out by other disturbances, such as other cytokines *in vivo* or in growth serums. Regardless, this calculation suggests that M-CSF paired with GM-CSF makes for a much stronger inducer of the M-MDSC phenotype than either cytokine alone.

Finally, we evaluate GMP behavior when M-CSF is paired with equal concentrations of G-CSF and GM-CSF (GM/G-CSF) (Figure 2.10E). We find that, under conditions that would otherwise encourage granulopoiesis, M-CSF can induce both monocytes and M-MDSCs. In contrast, when M-CSF was exclusively paired with G-CSF, M-MDSCs are not produced (Figure 2.10A). Furthermore, Figure 2.10E is at odds with Figure 2.10D, where the effects of M-CSF with GM-CSF alone are not concentration dependent. However, as M-CSF is increased in a GM/G-CSF system, the proportion of M-MDSCs increases in a concentration-dependent manner. We suggest that the situation in Figure 2.10E is more realistic for experimental and biological settings than Figure 2.10D, as the concentration-dependent behavior is likely more robust to biological disturbances.

2.5 Discussion

In consideration of the crucial roles played by cells of the GMP lineage in human health and disease, we have proposed a molecular regulatory network for the differentiation of GMP cells (Figure 2.2B), based on known facts about the underlying molecular controls of this aspect of hematopoiesis. From our proposed network we have constructed a dynamical model of GMP cell lineage commitment (see Table A.1 for a complete specification of the mathematical model), and we have used numerical simulations and bifurcation analysis to reveal the dynamical consequences of the model. The simulated responses of the model to cytokine stimuli are in good agreement with the fundamental characteristics of GMP differentiation: that G-CSF and high concentrations of GM-CSF favor granulopoiesis, while M-CSF and lower concentrations of GM-CSF favor monopoiesis [10]–[12]. Furthermore, the model makes several intriguing predictions concerning progenitor cell responses to CSF signals. For an itemized list of model predictions, see the Appendix A.2.

2.5.1 Concentration-dependent effects of GM-CSF signaling on GMP differentiation

Investigating the concentration-dependent response of GMP cells to GM-CSF, we uncovered three main features of the response. First: the dual regulatory effects of C/EBP on PU.1; C/EBP

induces PU.1 directly by promoter stimulation and inhibits PU.1 indirectly through stimulation of Gfi-1 [61]–[64]. The balance of these effects is dependent on the concentration of GM-CSF. At high concentrations of GM-CSF, C/EBP increases quickly, resulting in a swift rise in Gfi-1 and repression of PU.1, thereby inducing granulopoiesis. The result, that C/EBP is an antagonist of PU.1 in granulopoiesis, is in agreement with Wang et al. [105], who showed that induction of an isoform of C/EBPα downregulates the *SPI1* gene (encoding PU.1) to promote granulopoiesis. Alternatively, our model predicts that C/EBP has a positive impact on PU.1 in GM-CSF induced monopoiesis, as a result of a slower increase in C/EBP, allowing PU.1 enough time to upregulate itself and establish dominance. Second: PU.1's indirect antagonism of C/EBP and Gfi-1 is essential to commit the cell towards monopoiesis. Third: GM-CSFR signaling forms positive feedback loops with PU.1 and C/EBP. When stimulated, GM-CSFR transmits a signal to C/EBP to increase both C/EBP and PU.1 expression. These proteins, in turn, upregulate GM-CSFR resulting in a stronger GM-CSF signal, which results in even greater stimulation of C/EBP.

These feedback loops create a sensitive, switch-like response of gene expression to GM-CSFR stimulation. We find that the lower the GM-CSF concentration is the longer it takes for the switch to kick in. In GM-CSF-induced granulopoiesis, the switch kicks in early, to allow sufficient upregulation of C/EBP and Gfi-1. In GM-CSF-induced monopoiesis, the switch is delayed, to allow PU.1 to upregulate itself and repress C/EBP and Gfi-1. In this way, we propose that these three dynamic features of the control system work synergistically to produce the unique behaviors associated with GM-CSF-induced differentiation.

2.5.2 Differences among CSF-induced differentiation processes

Given that our model successfully captures the endpoints of GMP differentiation induced by G-, M- and GM-CSF, we propose that our model can also offer significant insights into the different temporal patterns of protein concentrations during the differentiation processes. For example, GM-CSF induced monopoiesis exhibits a significant spike in C/EBP and Gfi-1 concentrations in its early stages, followed by suppression of both proteins, whereas M-CSF induced monopoiesis does not exhibit such a spike. It is possible that these differences could influence downstream transcription factors not accounted for in our model, perhaps resulting in different subtypes of monocytes. (Alternatively, these incongruences may be short-lived, making no difference on the final phenotype.) Nonetheless, our model predicts that the final concentration of C/EBP in

monocytes is dependent on the signaling strength of GM-CSF (see the MO branch in Figure 2.8C). Since the subtype of the monocyte may well depend upon its level of expression of C/EBP, the concentration of GM-CSF in the micro-environment of a differentiated monocyte may have immediate implications on the phenotype of the cell. Intriguingly, it has been shown that GM-CSF induced monocyte-derived macrophages are distinctly different in genetic expression from M-CSF induced monocyte-derived macrophages [106], [107]. Perhaps GM-CSF's influence on C/EBP concentration in this lineage plays some role in the differences observed in these macrophages. In addition, our model suggests that monopoiesis may be induced more quickly by GM-CSF than by M-CSF. If true, GM-CSF may be better suited for emergency monopoiesis than M-CSF.

Similarly, we find that GM-CSF induced granulopoiesis exhibits a larger spike in PU.1 and IRF8 concentrations in its early stages than G-CSF induced granulopoiesis. Although these differences are not as dramatic as the differences between M-CSF and GM-CSF induced monopoiesis, we cannot dismiss the possibility that these differences may effect downstream transcription factors and prime the cells for different subtypes of granulocytes. For example, it has been shown that GM-CSF has a higher propensity for inducing eosinophils than G-CSF [10], [108].

2.5.3 GM-CSFR expression patterns of myeloid cells

An unexpected finding of our model, which agrees with experimental data, is that cells of the granulocyte lineage express lower concentrations of GM-CSFR than monocytes [95], [96]. This is counter-intuitive, as granulocytic differentiation is favored over monocytes at higher concentrations of GM-CSF [11]. Our model suggests that the signal strength of GM-CSFR is stronger in the initial commitment step of GM-CSF-induced granulopoiesis when compared to monopoiesis. However, after the lineage fate is fixed, the concentration of GM-CSFR continues to increase in monopoiesis, but decreases slightly in granulopoiesis (Figure 2.7E). We suspect that these conditions may be crucial for cellular maturation. It is possible that lower levels of GM-CSFR are required to prevent excessive stimulation of C/EBPα, as C/EBPα is downregulated in later stages of granulopoiesis [98]. It is also possible that high GM-CSFR expression is important in later stages of monopoiesis, to stimulate C/EBP. It is known that C/EBP not only stimulates PU.1, but forms a complex with AP-1 in monocytes to activate monocytic genes rather than granulocyte genes [61], [97]. Thus, the capacity to receive a strong

GM-CSF signal may be important for gene regulation within the monocytic lineage. In agreement with this hypothesis, our results suggest that expression of C/EBP in monocytes increases as the GM-CSF concentration increases.

2.5.4 Dynamics of the monocytic myeloid-derived suppressor cell

Our model predicts that the differentiation dynamics of M-MDSCs is very similar to typical monopoiesis; however, once the cell has committed to the monocytic lineage, there is a substantial upregulation of C/EBP. Since M-MDSCs have been shown to express high concentrations of C/EBPβ, but not C/EBPα, we suspect that some mechanism not captured by our model selectively suppresses C/EBPα [99]. We get by without this mechanism, as the function of C/EBPβ and C/EBPα are redundant in hematopoiesis [56]. Our model suggests that a significant fraction of C/EBP in M-MDCSs (and monocytes) is bound to IRF8, suggesting that its impact on granulocytic genes is diminished in these cells. Just like monocytes, the model suggests that PU.1, IRF8, Egr-2, M-CSFR, and GM-CSFR are all expressed at high levels in M-MDSCs as well, while G-CSFR is expressed at levels somewhere between a monocyte and a granulocyte progenitor. Thus, the G-CSFR is potentially a usable marker to distinguish between monocytes and M-MDSCs. Of course, if the variance of G-CSFR expression is large in monocytes or M-MDSCs, G-CSFR will not be an effective marker. Regardless, this suggests that G-CSF may have a stronger influence on M-MDSCs than on monocytes.

Intriguingly, our model suggests that high GM-CSF concentrations can induce a monocyte to morph into an M-MDSC. This behavior is a consequence of high expression of GM-CSFR in monocytes. Additionally, our results suggest that the stability of this M-MDSC state is dependent on GM-CSF stimulation. Thus, if an M-MDSC is removed from cytokine stimulation, the phenotype of the cell will change. These results agree with the literature, as monocytes can be programmed into M-MDSCs in tumor microenvironments, and terminally differentiate into macrophages and dendritic cells when removed from stimulatory conditions [52], [53]. However, as our model is not designed to simulate terminal differentiation into macrophages and dendritic cells, it predicts that M-MDSCs will revert back into monocytes when GM-CSF is withdrawn. We hypothesize that M-MDSCs can be destabilized via the mechanism of our model, but rather than reverting back to a monocyte, will terminally differentiate due to other variables not accounted for in our model.

2.5.5 CSF synergies and crosstalks

We find that G-CSF may play a more dynamic role in GMP differentiation than has been previously proposed. G-CSF is typically thought of as an inducer of the granulocyte lineage, but our model suggests that GMP cells likely exhibit an entire spectrum of differentiation behaviors in response to G-CSF due to signaling crosstalk. We find that, at concentrations of M-CSF not quite sufficient to induce monopoiesis, small concentrations of G-CSF can provide the nudge necessary to initiate monocytic differentiation. We see a similar phenomenon when G-CSF is introduced with GM-CSF: if a cell is primed for monopoiesis, a small concentration of G-CSF may provide the stimulus needed to induce monopoiesis. However, when G-CSF is increased to higher concentrations, monopoiesis is arrested in favor of granulopoiesis. The model also predicts that G-CSF can induce M-MDSC development under the right conditions. Our simulations suggest that normal monopoiesis, in response to simultaneous stimulation by a combination of moderate levels of M- and GM-CSFs, can be skewed in favor of M-MDSCs if paired with G-CSF (see Figure 2.10C). This also suggests that G-CSF can induce monocytes in such conditions to differentiate into M-MDSCs. On the other hand, under conditions that normally favor M-MDSC development, higher G-CSF concentrations will push differentiation in favor of granulopoiesis. Therefore, our model suggests that G-CSF can either promote or inhibit M-MDSC differentiation, depending on extracellular conditions. These predictions should be tested in a laboratory environment, as the implications are far reaching. It is possible that low levels of G-CSF may be utilized *in vivo* to aid monopoiesis and M-MDSC development.

Contrary to the dynamic role of G-CSF, our model suggests that M-CSF plays an exclusively antagonistic role in granulopoiesis. We predict that, under conditions of low G-CSF concentration, M-CSF can interfere with granulopoiesis to arrest GMP differentiation. We also find that M-CSF may drive M-MDSC differentiation under conditions that would normally favor granulopoiesis, depending on the relative concentrations of GM-CSF and G-CSF. Furthermore, our model suggests that pairing high concentrations of M-CSF and GM-CSF may be a potent inducer of M-MDSCs.

2.5.6 CSFs as clinical targets

Cumulatively, our results suggest that M-CSF, GM-CSF, and G-CSF can all favor M-MDSC development, depending on extracellular conditions. We suspect that high concentrations of M-CSF and GM-CSF, as well as lower concentrations of G-CSF, may be present in some biological environments that support M-MDSC development, such as a tumor micro-environment. Indeed, several tumors associated with MDSCs have been reported to express M-CSF, GM-CSF, and/or G-CSF.[39] We propose that a model such as ours can be used to explore the effects of tumor-specific conditions on hematopoiesis. For instance, our model suggests that G-CSF may contribute to M-MDSC differentiation under some, but not all, conditions that are otherwise favorable to monocyte differentiation. Thus, inhibiting G-CSF may be a successful strategy to destabilize the M-MDSC state in a tumor micro-environment where G-CSF is expressed alongside M-CSF and GM-CSF. However, while G-CSF's role in M-MDSC development is more context dependent, our results suggest that M-CSF and especially GM-CSF signaling act as much stronger inducers of M-MDSCs. Interestingly, while GM-CSF may induce M-MDSCs independent of other CSFs, the model suggests that G-CSF and M-CSF are reliant on GM-CSF to induce the M-MDSC state. Therefore, we propose that, among the CSFs, GM-CSF is the most promising therapy target for M-MDSC-associated tumors, while M-CSF may be an excellent alternative. In agreement with our results, knockdown of tumor-released GM-CSF in mice significantly reduced M-MDSC populations, and resulted in increased anti-tumor suppressive immunity.[100] In another study, inhibiting M-CSFR signaling suppressed M-MDSC populations, while making no difference to the PMN-MDSC population. Furthermore, when paired with the VEGFR-2 antibody, blocking M-CSFR signaling resulted in a significant reduction in tumor angiogenesis [46]. In both instances, the ratio of PMN-MDSCs to M-MDSCs increased, suggesting that these effects are due, in part, to altered differentiation rather than proliferation.

Alternatively, since MDSCs may be useful in a variety of pathological conditions, such as sepsis and burns [43], [109], an effective therapeutic strategy may be to upregulate M-MDSCs by administering a combination of GM-CSF and M-CSF (see Figure 2.10C&D). We acknowledge that *in vivo* other cytokines that are similar to GM-CSF (such as IL-3) may play comparable roles in M-MDSC differentiation [110]. Thus, M-CSF and G-CSF may still influence M-MDSC differentiation under conditions where GM-CSF is absent, increasing their value as therapeutic targets.

2.5.7 Network Topology

Ultimately, the behavior of the model is a consequence of the network topology, i.e., multiple feedback and feedforward loops in the reaction mechanism (Figure 2.2B) and the relative strengths of these interactions (e.g., the $\omega_{i,j}$'s in our mathematical model). For example, direct positive feedback loops of C/EBP and PU.1 are crucial for switch-like behavior and are required for the stability of the granulocyte and monocyte phenotypes, respectively. Additional positive feedbacks loops exist within the mutually antagonistic architecture of the network. As C/EBP can antagonize PU.1 through Gfi-1, PU.1 forms two positive feedback loops by inhibiting C/EBP through IRF8 and by inhibiting Gfi-1 through Egr-2. These positive feedback loops are crucial to the stability of the monocytic phenotype. In contrast, C/EBP forms a positive feedback loop by activating Gfi-1, which in turn prevents PU.1 from upregulating IRF8 and inhibiting C/EBP. Thus C/EBP can exist at high concentrations by suppressing PU.1 through this positive feedback loop. Furthermore, Gfi-1 has a positive feedback mechanism by inhibiting PU.1 and Egr-2, which in turn would inhibit Gfi-1. These feedback loops are critical to the irreversibility of the granulocyte phenotype. More positive feedback mechanisms exist between receptors and transcription factors. For example, activated M-CSFR stimulates PU.1 and PU.1 stimulates the expression of M-CSFR. These types of positive feedback loops make the system more responsive to cytokine stimuli. Finally, C/EBP forms a negative feedback loop by activating PU.1 which in turn activates IRF8. This negative feedback loop is necessary for GM-CSF induced monopoiesis, as C/EBP must be suppressed, but only after it has activated PU.1.

Feedforward loops also make significant contributions to the behavior of the system. For instance, GM-CSFR activates C/EBP both directly and indirectly (by inhibiting IRF8), thus forming a coherent-feedforward loop. The inhibition of IRF8 by GM-CSF is important for GM-CSF induced differentiation of GMPs into M-MDSCs (analysis not shown). Another example is the incoherent-feedforward loop by which C/EBP activates PU.1 directly and inhibits PU.1 indirectly through Gfi-1. This incoherent-feedforward loop is crucial to the concentration dependent nature of GM-CSF induced differentiation, as we discussed previously.

2.5.8 Limitations of model

While our model makes several intriguing predictions, we acknowledge that the model neglects many genes and proteins that play important roles in hematopoiesis. Therefore, in interpreting our models results, we must be aware of its limitations. We designed the model specifically to capture the initial decision-making stages of GMP differentiation, rather than the terminal stages of granulopoiesis and monopoiesis. We propose that transcription factors downstream of our network will play large roles in the maturation of granulocyte progenitor and monocyte cells, but only subtly effect the initial dynamics of lineage commitment.

Additionally, our model is limited to qualitative predictions. Although experiments often report quantitative measurements, it is impossible to compare these quantitative experimental results with our simulations for a variety of reasons. First of all, our calculations are made in dimensionless units, and the "real life" equivalent of 1 unit of M-CSF is not necessarily equivalent to 1 unit of G-CSF. Secondly, laboratory experiments typically utilize cytokine-enriched serum, with undefined serum components apparently necessary for cell survival and growth. These serum components are not accounted for in our model and may drastically impact how cells differentiate [108]. Furthermore, cell-to-cell signaling, unaccounted in our model, may impact differentiation dynamics in experimental cultures. Finally, and perhaps the most important limitation of all, our model does not consider the impact of cytokine signaling on cellular responses such as proliferation and apoptosis. These responses may drastically impact the ratios of differentiated cells in experimental cultures. For example, while granulopoiesis may be favored under some conditions, rapid monocyte proliferation may skew experimental results in favor of a larger monocyte fraction.

2.5.9 Summary

We have presented a novel model of GMP cell differentiation and explored the molecular control system's dynamics to provide insight into experimental observations and to make new predictions. We investigated the concentration-dependent nature of GM-CSF-induced differentiation, and proposed a mechanism that can explain its mysterious behavior. We explored the dynamics of CSF signaling crosstalk and found that, while G-CSF may encourage monopoiesis under some conditions, it is likely that M-CSF always has an inhibitory effect on granulopoiesis. Furthermore, our model demonstrates how both GMP cells and monocytes may differentiate into M-MDSCs, providing new insight into how this bizarre phenotype fits into

classical GMP cell differentiation. We found that G-CSF, M-CSF, and GM-CSF may all favor M-MDSC development under different conditions. Moreover, we proposed that, among the CSFs, GM-CSF is the most potent inducer of this phenotype.

As for any “model” of a cellular control system, our model has limitations and potential sources of inaccuracy. For example, our model is not suitable for making quantitative predictions or capturing terminal states of GMP differentiation. Nonetheless, we are confident that our results have utility, as the dynamic processes captured by our model align with numerous experimental observations. Therefore, we welcome experimental evaluation of any of the qualitative predictions we have made.

Chapter 3 : Deriving a Mathematical Model of the *Caulobacter* cell cycle

Bronson R. Weston[1], Young Cao[2*], and John J. Tyson[3]

[1] Program in Genetics, Bioinformatics, and Computational Biology, Virginia Tech, Blacksburg VA, USA

[2] Department of Computer Science, Virginia Tech, Blacksburg, VA, USA

[3] Department of Biological Sciences, Virginia Tech, Blacksburg, VA, USA

The asymmetrical cell cycle of *Caulobacter crescentus* is a consequence of a numerous molecular mechanisms that interact to form one cohesive machine. To model the behavior of the *Caulobacter* cell cycle utilizing mathematics, it is necessary to derive equations that capture the behavior of each of these molecular mechanisms. Here we describe the methodology used to write these equations, we discuss the underlying biological mechanisms of the *C. crescentus* cell cycle and we discuss the methods used to parameterized our model.

3.1 Model Derivation

3.1.1 Modeling Genetic Regulation

To quantify the activity of a promoter site, we utilize mass action kinetics, where a transcription factor (TF) and a DNA binding site interact such that TF + DNA ↔ TF:DNA. If the TF concentration is assumed to be much larger than the concentration of DNA binding sites (a very reasonable assumption), the steady state ratio ($[\mathrm{TF{:}DNA}]_\mathrm{R}$) of TF:DNA to the total concentration of DNA binding sites ($[\mathrm{DNA}]_\mathrm{T}$) takes the following form:

$$[\mathrm{TF{:}\,DNA}]_\mathrm{R} = \frac{[\mathrm{TF{:}\,DNA}]}{[\mathrm{DNA}]_\mathrm{T}} = \frac{[\mathrm{TF}]}{[\mathrm{TF}] + K_\mathrm{d}}\ , \qquad \textit{Eq.}\ 1$$

where K_d is the dissociation constant. Similarly, if a promoter has multiple binding sites for TF and binding is highly cooperative, the following expression is a reasonable estimate for $[\mathrm{TF{:}DNA}]_\mathrm{R}$:

$$[\mathrm{TF{:}\,DNA}]_{\mathrm{R}} = \frac{[\mathrm{TF}]^n}{[\mathrm{TF}]^n + K_{\mathrm{d}}^n}\ , \qquad \textit{Eq.}\ 2$$

where *n*, the Hill exponent, can be approximated by the number of binding-sites [111]. Unless the literature suggests otherwise, we assume that each transcription factor only has one binding site on a given promoter. However, promoter sites targeted by CtrA often have two binding sites. Such binding motifs are considered "full", while promoters with only one CtrA binding site are considered "half" [112]. The CauloBrowser online database designates each promoter site as a "full" or "half" motif [113], and we designated n=1 and n=2 for "half" and "full" motifs, respectively.

Since there may only be one binding site for a given promoter, it may not be entirely intuitive why $[\mathrm{TF{:}\,DNA}]_{\mathrm{R}}$ is capable of existing at all values between zero and one. A more practical way to interpret $[\mathrm{TF{:}DNA}]_{\mathrm{R}}$ is the fraction of the time (or the probability) that the promoter is bound by the transcription factor. As such, the rate of change of mRNA for a given gene can be modeled by

$$\frac{d[\mathrm{mRNA}]}{dt} = k_{\mathrm{s,mRNA}}[\mathrm{TF{:}\,DNA}]_{\mathrm{R}} - (k_{\mathrm{d,mRNA}} + \mu)[\mathrm{mRNA}]. \qquad \textit{Eq.}\ 3$$

Kinetic constants in the form k_{s} and k_{d} designate the synthesis and degradation rate constants, respectively. The dilution coefficient, μ, indicates the specific rate of dilution due to cell growth, where the volume, V, of the cell changes at the rate

$$\frac{dV}{dt} = \mu V. \qquad \textit{Eq.}\ 4$$

The differential equation for the rate of change of a protein takes the standard form:

$$\frac{d[\mathrm{P}]}{dt} = \hat{k}_{\mathrm{s,P}}[\mathrm{mRNA}] - \left(k_{\mathrm{d,P}} + \mu\right)[\mathrm{P}] + f\ , \qquad \textit{Eq.}\ 5$$

where f represents all other interactions that influence the production and removal of the protein. If we assume that the mRNA concentration is always at steady state and that μ is significantly less than $k_{\mathrm{d,mRNA}}$ (a reasonable assumption given that the average mRNA half-life in prokaryotes is ~3 min[114]), then we arrive at the following equation:

$$\frac{d[\mathrm{P}]}{dt} = k_{\mathrm{s,P}}[\mathrm{TF{:}\,DNA}]_{\mathrm{R}} - \left(k_{\mathrm{d,P}} + \mu\right)[\mathrm{P}] + f. \qquad \textit{Eq.}\ 6$$

It is possible that some transcription factors do not have complete control over a gene's transcription. Partial influence can be captured by introducing the parameter, ϵ, such that:

$$\frac{d[\mathrm{P}]}{dt} = k_{\mathrm{s,P}}(\epsilon + (1-\epsilon)\cdot[\mathrm{TF{:}\,DNA}]_{\mathrm{R}}) - \left(k_{\mathrm{d,P}} + \mu\right)[\mathrm{P}] + f, \qquad \textit{Eq.}\ 7$$

where $0 \leq \epsilon \leq 1$. Substituting in Eq. 2 into Eq.7, we get:

$$\frac{d[\mathrm{P}]}{dt} = k_{\mathrm{s,P}}\frac{[\mathrm{TF}]^n + \epsilon\cdot K_{\mathrm{d}}^n}{[\mathrm{TF}]^n + K_{\mathrm{d}}^n} - \left(k_{\mathrm{d,P}} + \mu\right)[\mathrm{P}] + f. \qquad \textit{Eq.}\ 8$$

Alternatively, if a gene is turned off by the binding of a transcription factor, the rate for protein synthesis (Eq. 6) takes the form:

$$\frac{d[\mathrm{P}]}{dt} = k_{\mathrm{s,P}}\,(1 - [\mathrm{TF{:}\,DNA}]_{\mathrm{R}}) - \left(k_{\mathrm{d,P}} + \mu\right)[\mathrm{P}] + f, \qquad \textit{Eq.}\ 9$$

and the expression for partial inhibition by the transcription factor takes the form:

$$\frac{d[\mathrm{P}]}{dt} = k_{\mathrm{s,P}}\frac{\epsilon\cdot[\mathrm{TF}]^n + K_{\mathrm{d}}^n}{[\mathrm{TF}]^n + K_{\mathrm{d}}^n} - \left(k_{\mathrm{d,P}} + \mu\right)[\mathrm{P}] + f. \qquad \textit{Eq.}\ 10$$

We gather information on the promoters of each gene from the online database, CauloBrowser[113]. Since CauloBrowser indicates whether a protein binds to a promoter site, but often does not specify the nature of the protein's influence over the gene's activity, we determine the nature of a given gene-protein interaction by comparing the expression of mRNA (via the CauloBrowser tool) with the expression of proteins that influence the gene of interest. It is often straightforward to determine if a transcription factor inhibits or activates a gene.

When several different proteins interact at a promoter site, we assume that the total promoter activity is the product of individual protein contributions (AND logic rather than OR logic) such that the rate of change of a protein is:

$$\frac{d[\mathrm{P}]}{dt} = k_{\mathrm{s,P}}\left(\prod_{\mathrm{a}\,\epsilon\,\mathrm{A}} \frac{[\mathrm{TF}]_{\mathrm{a}}^{n} + \epsilon_{\mathrm{a}} \cdot K_{\mathrm{d,a}}^{n}}{[\mathrm{TF}]_{\mathrm{a}}^{n} + K_{\mathrm{d,a}}^{n}}\right)\left(\prod_{\mathrm{i}\,\epsilon\,\mathrm{I}} \frac{\epsilon_{\mathrm{i}} \cdot [\mathrm{TF}]_{\mathrm{i}}^{n} + K_{\mathrm{d,i}}^{n}}{[\mathrm{TF}]_{\mathrm{i}}^{n} + K_{\mathrm{d,i}}^{n}}\right) - \left(k_{\mathrm{d,P}} + \mu\right)[\mathrm{P}] + f\ , \qquad \textit{Eq.}\ 11$$

where A and I are sets of transcription factors that activate and inhibit the promoter, respectively.

In *C. crescentus*, several genes are regulated via methylation [115]. The variable, h_{P}, indicates the methylation state of a given gene where h_{P} equals ½ or 1 if the gene is hemi-methylated or fully-methylated, respectively. A typical implementation of h_{P} is demonstrated here:

$$\frac{d[\mathrm{P}]}{dt} = k_{\mathrm{s,P}}[\mathrm{TF{:}\,DNA}]_{\mathrm{R}} \cdot (2 - 2 \cdot h_{\mathrm{P}}) - \left(k_{\mathrm{d,P}} + \mu\right)[\mathrm{P}] + f\ , \qquad \textit{Eq.}\ 12$$

where the gene is active when hemi-methylated and inactive when fully methylated. Alternatively, genes that are active when fully methylated and inactive when hemi-methylated (such as *dnaA* [116]) are modeled as:

$$\frac{d[\mathrm{P}]}{dt} = k_{\mathrm{s,P}}[\mathrm{TF{:}\,DNA}]_{\mathrm{R}} \cdot (2 \cdot h_{\mathrm{P}} - 1) - \left(k_{\mathrm{d,P}} + \mu\right)[\mathrm{P}] + f. \qquad \textit{Eq.}\ 13$$

We introduce a parameter *m* to control the degree of influence that the methylation state has over promoter activity. Hence, when incorporating partial influence of methylation, Eq. 12 and 13 become Eq. 14 and 15, respectively:

$$\frac{d[\mathrm{P}]}{dt} = k_{\mathrm{s,P}}[\mathrm{TF{:}\,DNA}]_{\mathrm{R}} \cdot \left(1 - m_{\mathrm{P}}(2h_{\mathrm{P}} - 1)\right) - \left(k_{\mathrm{d,P}} + \mu\right)[\mathrm{P}] + f, \qquad \textit{Eq.}\ 14$$

$$\frac{d[\mathrm{P}]}{dt} = k_{\mathrm{s,P}}[\mathrm{TF{:}\,DNA}]_{\mathrm{R}} \cdot \left(1 + 2m_{\mathrm{P}}(h_{\mathrm{P}} - 1)\right) - \left(k_{\mathrm{d,P}} + \mu\right)[\mathrm{P}] + f. \qquad \textit{Eq.}\ 15$$

Importantly, the methylation state of h_{P} acts like a switch. When CcrM is sufficiently active ([CcrM]=0.65 in our simulations), all hemi-methylated genes become methylated. Because genes transition from fully methylated to hemi-methylated when the chromosome replication fork passes through the gene [117], we must keep track of the progression of the replication fork, by means of the variable, Elong, where:

$$\frac{d[\mathrm{Elong}]}{dt} = k_{\mathrm{Elong}} \cdot \mathrm{RepSwitch}\ , \qquad \textit{Eq.}\ 16$$

and RepSwitch is equal to one or zero when the chromosome is replicating or not replicating, respectively. Elong also ranges from 0 to 1, representing the fraction of the chromosome that has been replicated. Thus, when [Elong] = 1, RepSwitch and Elong are reset to 0 as chromosome replication has been completed. Utilizing the CauloBrowser database [113], we note the location of each gene containing a methylation site. Each location corresponds to a value, L_G, that indicates the fractional location of gene G along the chromosome. When [Elong] = L_G, the methylation status of the gene changes from 1 to ½.

3.1.2 Protein Complexes and Phosphorylation

Protein binding and phosphotransferase reactions are modeled with mass action kinetics. We assume that such reactions are at pseudo-steady state, as these reactions are much faster than those pertaining to genetic regulation and protein synthesis. Enzymatic reactions, such as phosphorylation and proteolysis, are typically described by:

$$\mathrm{S} + \mathrm{E} \underset{k_{-1}}{\overset{k_1}{\rightleftarrows}} \mathrm{S{:}\,E} \xrightarrow{k_{\mathrm{cat}}} \mathrm{E} + \mathrm{P},$$

where S is the substrate, E is the enzyme, and P is the product (although there is often no product worth tracking for proteolysis). If the substrate concentration is much greater than the enzyme concentration, then the rate of this reaction is given by the Michaelis-Menten equation,

$$\frac{d[\mathrm{P}]}{dt} = k_{\mathrm{s,P}} \frac{[\mathrm{E}]_{\mathrm{T}}[\mathrm{S}]}{[\mathrm{S}] + K_{\mathrm{M}}}. \qquad \textit{Eq.}\ 17$$

The Michaelis constant, $K_M = (k_{-1} + k_{cat})/k_1$, is defined in terms of the forward and reverse rate constants for the enzyme-substrate binding reaction, and the catalytic rate constant for the step S:E → E+P. In Eq. 17, $k_{s,P} = k_{cat}$. However, in the context of several protein-protein reactions in the Caulobacter cell cycle control network, the concentrations of the 'substrate' and the 'enzyme' are similar, and the Michaelis-Menten rate law cannot be used [118]. To simplify things, we assume that, in this context, the catalytic rate constant is much greater than the enzyme-substrate dissociation constant, $k_{cat} >> k_1 >> k_{-1}$, in which case

$$\frac{d[\mathrm{P}]}{dt} = k_{\mathrm{s,P}}[\mathrm{E}][\mathrm{S}], \qquad \textit{Eq.}\ 18$$

where $k_{s,P} = k_1$, i.e., the reaction is rate-limited by the enzyme-substrate binding step. An advantage of this assumption is that we can model different reactions independently, even if the same substrate is targeted by multiple enzymes or if the same enzyme targets multiple substrates. We use this approach for modeling DivJ and PleC phosphorylation/dephosphorylation of DivK and PleD.

Phosphotransferase kinetics take the form:

$$\mathrm{A{\sim}P} + \mathrm{B} \leftrightarrow \mathrm{A} + \mathrm{B{\sim}P}.$$

If A is a histidine kinase, such as CckA kinase, we can assume that the reaction is not reversible, and A is immediately re-phosphorylated by ATP after offering its phosphate group to B. In this scenario, [B~P] accumulates at a rate of:

$$\frac{\mathrm{d}[\mathrm{B{\sim}P}]}{\mathrm{d}t} = k_{\mathrm{f}}\rho[\mathrm{A}]_{\mathrm{T}}[\mathrm{B}], \qquad \textit{Eq.}\ 19$$

where k_f is the forward reaction rate constant and $[\mathrm{A}]_T = [\mathrm{A{\sim}P}]+[\mathrm{A}]$, and

$$\rho = \frac{[\mathrm{A{\sim}P}]}{[\mathrm{A}]_{\mathrm{T}}}.$$

Similarly, if A is a histidine phosphatase, such as CckA phosphatase, we assume that A~P is dephosphorylated as quickly as it is phosphorylated and the reaction is non-reversible such that:

$$\frac{\mathrm{d}[\mathrm{B}]}{\mathrm{d}t} = k_{\mathrm{r}}(1-\rho)[\mathrm{A}]_{\mathrm{T}}[\mathrm{B{\sim}P}], \qquad \textit{Eq.}\ 20$$

To model protein complexes, $\mathrm{A} + \mathrm{B} \leftrightarrow \mathrm{C}$, we utilize two approaches. 1) If the binding is very strong, then the more dilute protein (say, B) is negligible in the free form compared to the bound form, such that:

$$[\mathrm{C}] = \min([\mathrm{A}]_{\mathrm{T}}, [\mathrm{B}]_{\mathrm{T}}) = [\mathrm{B}]_{\mathrm{T}},$$
$$[\mathrm{A}]_{\mathrm{F}} = [\mathrm{A}]_{\mathrm{T}} - [\mathrm{B}]_{\mathrm{T}}, \qquad \textit{Eq.}\ 21$$

$$[\mathrm{B}]_\mathrm{F} = 0\,.$$

Here, [C] is the protein complex concentration, while $[A]_F$ and $[B]_F$ are the concentration of the free form of A and B, respectively. We utilize this method for modeling the interaction of DgcB with PdeA. Alternatively, 2) we solve for the equilibrium concentrations of the reaction

$$\mathrm{A} + \mathrm{B} \leftrightarrow \mathrm{C}\,,$$

where $[A] = [A]_T - [C]$ and $B = [B]_T - [C]$. The solution for this system at equilibrium is given by the equation:

$$[\mathrm{C}] = \frac{[\mathrm{A}]_\mathrm{T} + [\mathrm{B}]_\mathrm{T} + \frac{1}{K_\mathrm{C}} - \sqrt{\left([\mathrm{A}]_\mathrm{T} + [\mathrm{B}]_\mathrm{T} + \frac{1}{K_\mathrm{C}}\right)^2 - 4 \cdot [\mathrm{A}]_\mathrm{T} \cdot [\mathrm{B}]_\mathrm{T}}}{2}, \qquad \textit{Eq.}\ 22$$

where $K_C = k_f/k_r$, is the equilibrium dissociation constant of C. While this approach is more complicated than the previous approach, it is capable of capturing a range of system behaviors. Thus, we use it to model interactions that are key to regulating master regulator CtrA, such as [RcdA:PopA] and [CckA:DivL].

3.1.3 Localization

In many instances, enzymes localize to the poles of *C. crescentus*, while their substrates are freely diffusing. Although we utilize an ordinary differential equation (ODE) model, rather than a partial differential equation model, we are still able to capture the effects of polar localization if we assume that diffusion within the cytoplasm is very fast. For a given Michaelis-Menten reaction (Eq. 17), we can consider the concentrations of the enzyme, product and substrate in two different volumes. V, designates the volume of the entire cell, while V_L designates a local volume. For a given molecule, X, the local concentration $[X]_L$ is related to the cellular concentration [X] such that $[X]=[X]_L$ if X is freely diffusing and $[X]=V_L[X]_L/V$ if X is entirely localized to V_L. The rate that a product accumulates in the local volume is defined as

$$\frac{d[\mathrm{P}]_\mathrm{L}}{dt} = k_{\mathrm{s,P}} \frac{[\mathrm{E}]_\mathrm{L}[\mathrm{S}]_\mathrm{L}}{[\mathrm{S}]_\mathrm{L} + K_\mathrm{M}}. \qquad \textit{Eq.}\ 23$$

If the substrate, [S], is freely diffusing but the enzyme, [E], is localized to V_L, then

$$\frac{d[\mathrm{P}]_{\mathrm{L}}}{dt} = k_{\mathrm{s,P}} \cdot [\mathrm{E}] \cdot \left(\frac{V}{V_{\mathrm{L}}}\right) \cdot \frac{[\mathrm{S}]}{[\mathrm{S}] + K_{\mathrm{M}}} \ , \qquad \textit{Eq.}\ 24$$

and therefore

$$\frac{d[\mathrm{P}]}{dt} = k_{\mathrm{s,P}} \cdot [\mathrm{E}] \cdot \frac{[\mathrm{S}]}{[\mathrm{S}] + K_{\mathrm{M}}} . \qquad \textit{Eq.}\ 25$$

Thus, *d*[P]/*dt* is independent of enzyme localization and cell volume. Therefore, in scenarios that the enzyme is localized and the substrate is freely diffusing, we can model as if there were no localization. An exception to this rule is the case where the local concentration of enzyme is similar or greater than the local concentration of the substrate, because the Michaelis-Menten rate law would no longer be valid. For simplicity, we assume that this is not the case for all such scenarios.

If we reverse the roles of the substrate and enzyme in the last scenario such that the substrate is the localizing agent and the enzyme is freely diffusing, then we get:

$$\frac{d[\mathrm{P}]}{dt} = k_{\mathrm{s,P}} \cdot [\mathrm{E}] \cdot \frac{[\mathrm{S}]}{[\mathrm{S}] \cdot \left(\frac{V}{V_{\mathrm{L}}}\right) + K_{\mathrm{M}}} . \qquad \textit{Eq.}\ 26$$

Since V_{L} is a constant, the equation works out to:

$$\frac{d[\mathrm{P}]}{dt} = \hat{k}_{\mathrm{s,P}} \cdot [\mathrm{E}] \cdot \frac{[\mathrm{S}]}{[\mathrm{S}] \cdot V + \widehat{K}} . \qquad \textit{Eq.}\ 27$$

where $\widehat{K} = K_{\mathrm{M}} \cdot V_{\mathrm{L}}$ and $\hat{k}_{\mathrm{s,P}} = k_{\mathrm{s,P}} \cdot V_{\mathrm{L}}$.

Finally, by the same logic, if both the enzyme and the substrate are localized, then

$$\frac{d[\mathrm{P}]}{dt} = k_{\mathrm{s,P}} \cdot [\mathrm{E}] \cdot \frac{[\mathrm{S}]}{[\mathrm{S}] + \frac{\widehat{K}}{V}} . \qquad \textit{Eq.}\ 28$$

3.1.4 Swarmer vs. Stalked Simulations

While swarmer and stalked cells have different phenotypes, the fundamental kinetics of molecular interactions remain the same within both cell types. Thus, we model both types of cells with the same set of governing ODEs. This small feature represents a large improvement over other ODE models of the *C. crescentus* cell cycle, which attempt to simulate stalked and swarmer cells with fundamentally different ODEs [119], [120]. Instead, we keep track of the localized proteins of the cell, and where they end up after cytokinesis. Simulations designated SW or ST follow the swarmer or stalked cell, respectively, at the time of cell division.

Upon cytokinesis, the volume of the parent cell is divided between two daughter cells. For a given molecular species localized to a pole, the local concentration ($[C]_L$) and volume (V_L) will remain the same, but the cellular concentration ([C]) will shift as the volume, V, changes. The following expression details the shift in concentration after cytokinesis:

$$[C]_{new} = [C]_{old} \cdot \left(\chi_{dif} + \chi_{pole} \left(\frac{V_{old}}{V_{new}} \right) \right), \qquad Eq.\ 29$$

where $[C]_{old}$ is the concentration prior to cytokinesis and $[C]_{new}$ is the concentration in the cell of interest (ST or SW) after cytokinesis. χ_{pole} and χ_{dif} represent the fraction of the molecular species, C, that is located at the pole of interest and that is freely diffusing, respectively. V_{old} is the original volume of the cell and V_{new} is the volume of the daughter cell of interest. Given the characteristics of *Caulobacter* growth, we assume that the volume shift after cytokinesis is proportional to the change in length after cytokinesis. It is reported that the stalked cell length after cytokinesis is approximately 54% of the original cell length [121]. Therefore, $V_{new} = 0.54 \cdot V_{old}$ when following the stalked cell and $V_{new} = 0.46 \cdot V_{old}$ when following the swarmer cell.

3.1.5 CtrA/*Cori* Binding

CtrA~P interacts with five binding sites at the chromosome origin (*Cori*), designated [a]-[e], to inhibit chromosome replication [122]. CtrA molecules recognize the nucleotide motif, TTAA (half-site); however, *Cori* binding sites [a]-[e] have nucleotides in the arrangement of TTAA-N7-TTAA (full-site) [123]. As such, each CtrA binding site may recruit two CtrA molecules and

experiments suggest that pairs of CtrA molecules interact cooperatively to enhance their affinity for *Cori*[123], [124]. While CtrA~P seems to have a higher affinity than unphosphorylated CtrA for sites [a]-[e], mutant experiments on site d suggest that unphosphorylated CtrA ($CtrA_u$) interacts with individual TTAA recognition sites with equal affinity as CtrA~P [123]; this suggests that the differences in affinity between unphosphorylated and phosphorylated forms of CtrA to sites [a]-[e] are a consequence of cooperativity. To investigate this mechanism further, we developed a mathematical model of CtrA interactions with DNA at site [d]. Table 3.1 presents binding/unbinding reactions at site d and corresponding steady-state kinetic expressions. In Table 3.1 we assume that the fraction of CtrA that is bound to DNA is negligible compared to freely diffusing CtrA. This assumption simplifies the model and Importantly, we also assume that the cooperativity between $CtrA_u$ and CtrA~P when bound to DNA is equivalent to the cooperativity between two $CtrA_u$ molecules.

Table 3.1) Kinetics of DNA/CtrA binding.

Binding/Unbinding Reaction	Steady-State Balance	Equilibrium Expression*
$\mathbf{CtrA_U + DNA \leftrightarrow\ DNA{:}\ CtrA_U}$	$\mathbf{2 \cdot k_{+1} \cdot [CtrA_U] \cdot [DNA]_F = k_{-1} \cdot [DNA{:}\ CtrA_U]}$	$\mathbf{[DNA{:}\ CtrA_U] = 2 \cdot \frac{[CtrA_U] \cdot [DNA]_F}{K_{d1}}}$
$\mathbf{CtrA{\sim}P + DNA \leftrightarrow\ DNA{:}\ CtrA{\sim}P}$	$\mathbf{2 \cdot k_{+1} \cdot [CtrA{\sim}P] \cdot [DNA]_F = k_{-1} \cdot [DNA{:}\ CtrA{\sim}P]}$	$\mathbf{[DNA{:}\ CtrA{\sim}P] = 2 \cdot \frac{[CtrA{\sim}P] \cdot [DNA]_F}{K_{d1}}}$
$\mathbf{CtrA_U + DNA{:}\ CtrA_U \leftrightarrow\ DNA{:}\ CtrA_{U_2}}$	$\mathbf{k_{+2} \cdot [CtrA_U] \cdot [DNA{:}\ CtrA_U] = 2 \cdot k_{-2} \cdot [DNA{:}\ CtrA_{U_2}]}$	$\mathbf{[DNA{:}\ CtrA_{U_2}] = \frac{[CtrA_U]^2 \cdot [DNA]_F}{K_{d1} \cdot K_{d2}}}$
$\mathbf{CtrA{\sim}P + DNA{:}\ CtrA_U \leftrightarrow\ DNA{:}\ CtrA{\sim}P{:}\ CtrA_U}$	$\mathbf{k_{+2} \cdot [CtrA{\sim}P] \cdot [DNA{:}\ CtrA_U] = k_{-2} \cdot [DNA{:}\ CtrA{\sim}P{:}\ CtrA_U]}$	$\mathbf{[DNA{:}\ CtrA{\sim}P{:}\ CtrA_U] = 2 \cdot \frac{[CtrA_U] \cdot [CtrA{\sim}P] \cdot [DNA]_F}{K_{d1} \cdot K_{d2}}}$
$\mathbf{CtrA_U + DNA{:}\ CtrA{\sim}P \leftrightarrow\ DNA{:}\ CtrA{\sim}P{:}\ CtrA_U}$	$\mathbf{k_{+2} \cdot [CtrA_U] \cdot [DNA{:}\ CtrA{\sim}P] = k_{-2} \cdot [DNA{:}\ CtrA{\sim}P{:}\ CtrA_U]}$	$\mathbf{[DNA{:}\ CtrA{\sim}P{:}\ CtrA_U] = 2 \cdot \frac{[CtrA_U] \cdot [CtrA{\sim}P] \cdot [DNA]_F}{K_{d1} \cdot K_{d2}}}$
$\mathbf{CtrA{\sim}P + DNA{:}\ CtrA{\sim}P \leftrightarrow\ DNA{:}\ CtrA{\sim}P_2}$	$\mathbf{k_{+3} \cdot [CtrA{\sim}P] \cdot [DNA{:}\ CtrA{\sim}P] = 2 \cdot k_{-3} \cdot [DNA{:}\ CtrA{\sim}P_2]}$	$\mathbf{[DNA{:}\ CtrA{\sim}P_2] = \frac{[CtrA{\sim}P]^2 \cdot [DNA]_F}{K_{d1} \cdot K_{d3}}}$

*$K_{d1} = {}^{k_{-1}}/_{k_{+1}}, K_{d2} = {}^{k_{-2}}/_{k_{+2}}, K_{d3} = {}^{k_{-3}}/_{k_{+3}}$

The concentration of Cori sites is normalized so that:

$$[\mathrm{DNA}]_{\mathrm{Total}} = [\mathrm{DNA}]_{\mathrm{F}} + [\mathrm{DNA{:}\,CtrA_U}] + \left[\mathrm{DNA{:}\,CtrA_{U_2}}\right] + [\mathrm{DNA{:}\,CtrA{\sim}P}] + [\mathrm{DNA{:}\,CtrA{\sim}P_2}] + [\mathrm{DNA{:}\,CtrA{\sim}P{:}\,CtrA_U}] = 1\,. \qquad \textit{Eq.}\ 30$$

By plugging the equilibrium expressions from Table 1 into Eq. 30, we attain the expression:

$$[\mathrm{DNA}]_{\mathrm{F}} + 2\cdot\frac{[\mathrm{CtrA_U}]\cdot[\mathrm{DNA}]_{\mathrm{F}}}{K_{\mathrm{d1}}} + \frac{[\mathrm{CtrA_U}]^2\cdot[\mathrm{DNA}]_{\mathrm{F}}}{K_{\mathrm{d1}}\cdot K_{\mathrm{d2}}} + 2\cdot\frac{[\mathrm{CtrA{\sim}P}]\cdot[\mathrm{DNA}]_{\mathrm{F}}}{K_{\mathrm{d1}}} + \frac{[\mathrm{CtrA{\sim}P}]^2\cdot[\mathrm{DNA}]_{\mathrm{F}}}{K_{\mathrm{d1}}\cdot K_{\mathrm{d3}}} + 2\cdot\frac{[\mathrm{CtrA_U}]\cdot[\mathrm{CtrA{\sim}P}]\cdot[\mathrm{DNA}]_{\mathrm{F}}}{K_{\mathrm{d1}}\cdot K_{\mathrm{d2}}} = 1, \qquad \textit{Eq.}\ 31$$

and therefore:

$$[\mathrm{DNA}]_{\mathrm{F}} = K_{\mathrm{d1}}\cdot\left(K_{\mathrm{d1}} + 2\cdot[\mathrm{CtrA_U}] + 2\cdot[\mathrm{CtrA{\sim}P}] + \frac{[\mathrm{CtrA_U}]^2}{K_{\mathrm{d2}}} + \frac{[\mathrm{CtrA{\sim}P}]^2}{K_{\mathrm{d3}}} + 2\cdot\frac{[\mathrm{CtrA_U}]\cdot[\mathrm{CtrA{\sim}P}]}{K_{\mathrm{d2}}}\right)^{-1}. \qquad \textit{Eq.}\ 32$$

Thus, for any combination of [$CtrA_U$] and [CtrA~P], the fraction of DNA in each state depicted in Fig. 2A (main text) and Table 1 can be calculated. However, reasonable estimates for these states rely on reasonable parameter estimates for K_{d1}, K_{d2} and K_{d3}. To acquire these estimates, we compared our model simulations with experiments published by Siam and Marczynski [123], who measured how DNA footprinting band intensities vary over different concentrations of $CtrA_u$ and CtrA~P. As Siam and Marczynski utilized excess CtrA (relative to DNA binding sites) in their experiments, our model's assumption that concentrations of free CtrA is unaffected by DNA binding is appropriate for parameterization.

First we consider $CtrA_U$ binding to a site [d] mutant that has only one TTAA recognition sequence [123]. In this scenario, the only two states possible are $[DNA]_F$ and [DNA:$CtrA_U$]. Thus, the solution becomes:

$$Intensity = [\mathrm{DNA}]_{\mathrm{F}} = \frac{K_{\mathrm{d1}}}{K_{\mathrm{d1}} + [\mathrm{CtrA_U}]} \qquad \textit{Eq.}\ 33$$

Fitting Eq. 33 to the band intensity depicted in Fig. 4A of Siam and Marczynski, we estimate the value of K_{d1} = 1.06 µM.

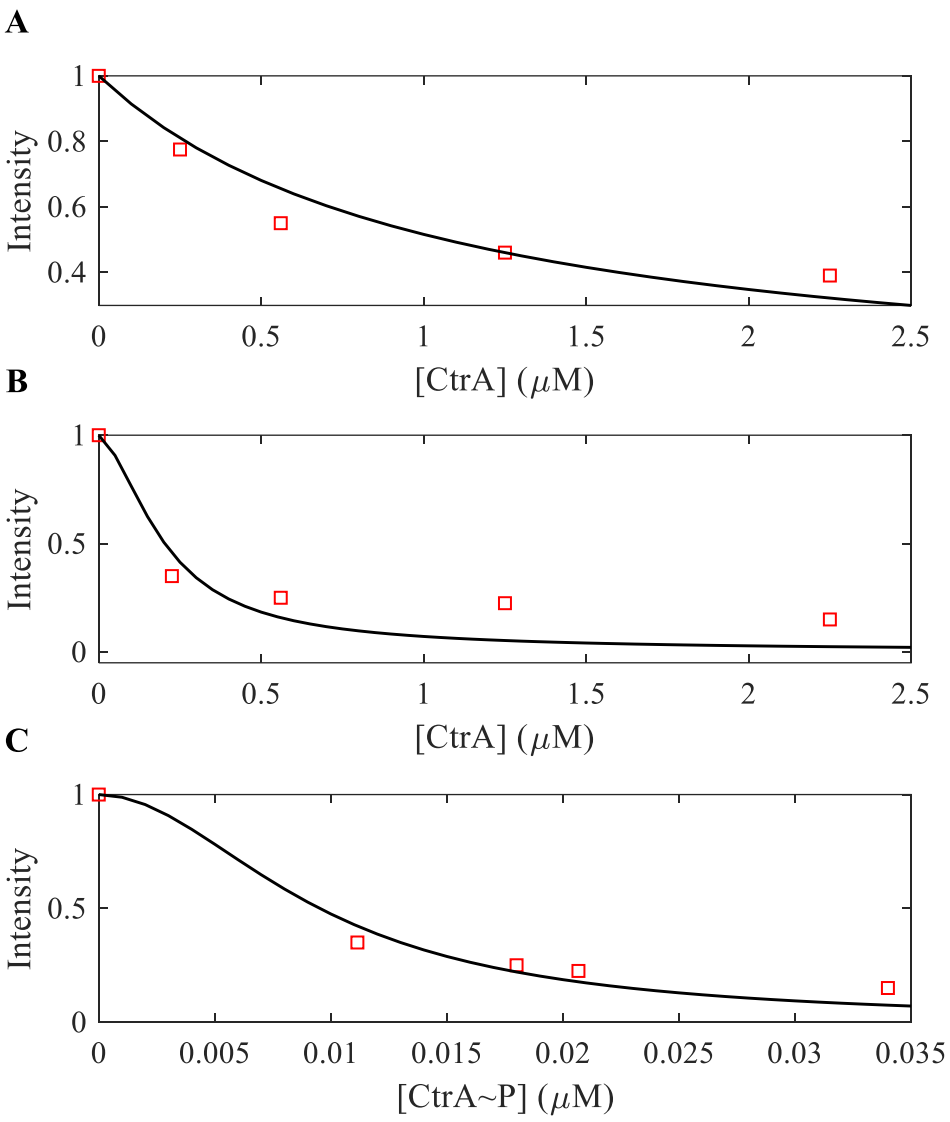

Figure 3.1) Calibrating DNA binding parameters with data from Siam and Marczynski, 2000.
Band intensities of DNase I footprinting assays were measured for CtrA site d by Siam and Marczynski. Data points from Figure 4A and 4B of Siam and Marczynski are replotted as red squares in A and B, respectively. Data points of C were reproduced using a Michaelis-Menten function with K_d = 6 nM as indicated in Siam and Marczynski [123] A) Mutated site d has only one binding sequence for CtrA. Black line illustrates fit of Eq. 33 with K_{d1}=1.06 µM. B) WT site d data retrieved for left hand CtrA binding sequence. Black line illustrates fit using Eq. 35, with K_{d1}=1.06 µM and K_{d2} = 39 nM. C) WT site d binding with CtrA~P. Black line illustrates fit using Eq. 36, with K_{d1}=1.06 µM and K_{d3} = 0.085 nM.

Next, we investigate Fig. 4B of Siam and Marczynski, which displays the intensity of the DNase I footprinting assay on WT site d. As no CtrA~P was present in the experiment, Eq. 34 and 35 were derived to describe this scenario:

$$[\mathrm{DNA}]_\mathrm{F} = \frac{K_{\mathrm{d1}}}{K_{\mathrm{d1}} + 2 \cdot [\mathrm{CtrA_U}] + \frac{[\mathrm{CtrA_U}]^2}{K_{\mathrm{d2}}}}, \qquad \textit{Eq.}\ 34$$

$$Intensity = [\mathrm{DNA}]_\mathrm{F} + \frac{[\mathrm{DNA{:}\ CtrA_U}]}{2},$$

$$= \frac{K_{\mathrm{d1}} + [\mathrm{CtrA_U}]}{K_{\mathrm{d1}} + 2 \cdot [\mathrm{CtrA_U}] + \frac{[\mathrm{CtrA_U}]^2}{K_{\mathrm{d2}}}}. \qquad \textit{Eq.}\ 35$$

In Fig. S2B, we fit the corresponding data in Siam and Marczynski to acquire a K_{d2} of 0.039 μM. Similarly, when modeling [CtrA~P] (with no $CtrA_u$ present), the readings for band intensity should be proportional to:

$$Intensity = [\mathrm{DNA}]_\mathrm{F} + \frac{[\mathrm{DNA{:}\ CtrA{\sim}P}]}{2},$$

$$= \frac{K_{\mathrm{d1}} + [\mathrm{CtrA{\sim}P}]}{K_{\mathrm{d1}} + 2 \cdot [\mathrm{CtrA{\sim}P}] + \frac{[\mathrm{CtrA{\sim}P}]^2}{K_{\mathrm{d3}}}}. \qquad \textit{Eq.}\ 36$$

While the authors do not provide data on [CtrA~P], they do provide a K_d value that they determined by hyperbolic function (K_d/(K_d + [CtrA~P]). We utilize their K_d value to generate artificial data points and fit our Eq. 36 accordingly, as shown in Figure 3.1. We derive a K_{d3} value of 0.085 nM.

3.1.6 Considering Increased Complexity of CtrA:DNA binding

There are three complications that we must consider when extending our model from the experiments of Siam and Marczynski to an *in vivo* system. First, the concentration of free CtrA may not be close to the total concentration of CtrA (i.e. DNA bound CtrA is non-negligible). Second, there are CtrA binding sites on DNA other than *Cori* sites [a]-[e], and these sites may compete with *Cori* for CtrA binding. Third, *Cori* sites [a]-[e] may compete with each other for

CtrA. To investigate these concerns, we developed a set of ODEs to describe these interactions. We call this ODE model the "complex" model and the algebraic equation model (described previously) the "simple" model.

CtrA binds to 183 transcriptional start sites in Caulobacter. 54 of these sites are full-sites bind two CtrA molecules) and the other 124 are half-sites (bind one CtrA molecule) [112]. Information on binding strength to these sites is extremely limited. We assume that the average dissociation constant at the half-sites (K_{dHS}) is equal to K_{d1}, as K_{d1} is an estimate for the affinity of a single CtrA molecule for the TTAA motif. The dissociation constants for the full-motif promoters of *fliQ* and *ccrM* have been estimated to be 0.2 μM and 3.5 μM, respectively [125]. We choose the stronger of the two, K_{dFS} = 0.2 μM. For the sake of simplicity, we also assume that binding at sites [a]-[e] is identical to binding at site d. The four ODEs and two algebraic equations that comprise this "complex" model are summarized by Table 3.2, to simulate binding of CtrA~P molecules to DNA (binding of unphosphorylated CtrA is not considered). Here, DNA_{HS} represents DNA half-sites, DNA_{FS} represents DNA full-sites, and DNA_{Cori} represents *Cori* binding sites. For a given species, X, the concentration of free (unbound) X is represented as $[X]_F$ and $[X]_T$ is the total concentration of X (sum of bound and unbound).

Table 3.2) Complex DNA/CtrA~P binding model

$\frac{d[\mathrm{DNA_{HS}{:}\,CtrA{\sim}P}]}{dt} = ([\mathrm{DNA_{HS}}]_T - [\mathrm{DNA_{HS}{:}\,CtrA{\sim}P}]) \cdot [\mathrm{CtrA{\sim}P}]_F - K_{dHS} \cdot [\mathrm{DNA_{HS}{:}\,CtrA{\sim}P}]$
$\frac{d[\mathrm{DNA_{FS}{:}\,CtrA{\sim}P_2}]}{dt} = ([\mathrm{DNA_{FS}}]_T - [\mathrm{DNA_{FS}{:}\,CtrA{\sim}P_2}]) \cdot [\mathrm{CtrA{\sim}P}]_F^{\,2} - K_{dFS} \cdot [\mathrm{DNA_{FS}{:}\,CtrA{\sim}P_2}]$
$\frac{d[\mathrm{DNA_{Cori}{:}\,CtrA{\sim}P}]}{dt} = 2 \cdot [\mathrm{DNA_{Cori}}]_F \cdot [\mathrm{CtrA{\sim}P}]_F - K_{d1} \cdot [\mathrm{DNA_{Cori}{:}\,CtrA{\sim}P}]$
$\frac{d[\mathrm{DNA_{Cori}{:}\,CtrA{\sim}P_2}]}{dt} = [\mathrm{DNA_{Cori}{:}\,CtrA{\sim}P}] \cdot [\mathrm{CtrA{\sim}P}]_F - 2 \cdot K_{d3} \cdot [\mathrm{DNA_{Cori}{:}\,CtrA{\sim}P_2}]$
$[\mathrm{CtrA{\sim}P}]_F = [\mathrm{CtrA{\sim}P}]_T - [\mathrm{DNA_{HS}{:}\,CtrA{\sim}P}] - 2 \cdot [\mathrm{DNA_{FS}{:}\,CtrA{\sim}P_2}] - [\mathrm{DNA_{Cori}{:}\,CtrA{\sim}P}] - 2 \cdot [\mathrm{DNA_{Cori}{:}\,CtrA{\sim}P_2}]$
$[\mathrm{DNA_{Cori}}]_F = [\mathrm{DNA_{Cori}}]_T - [\mathrm{DNA_{Cori}{:}\,CtrA{\sim}P}] - [\mathrm{DNA_{Cori}{:}\,CtrA{\sim}P_2}]$

$[\mathrm{DNA_{HS}}]_\mathrm{T} = 0.21\ \mu\mathrm{M}$; $[\mathrm{DNA_{FS}}]_\mathrm{T} = 0.09\ \mu\mathrm{M}$; $[\mathrm{DNA}_{Cori}]_\mathrm{T} = 0.0083\ \mu\mathrm{M}$;

We solve for the steady state solution of these equations (utilizing MATLAB solver ode15s) over a range of CtrA~P concentrations. We find that at steady state (i.e., at chemical equilibrium), $[\mathrm{CtrA{\sim}P}]_\mathrm{F}$ values deviate significantly from $[\mathrm{CtrA{\sim}P}]_\mathrm{T}$ concentrations when total concentrations are low (Figure 3.2A). However, when we plot the fraction of $[\mathrm{DNA}_{Cori}{:}\mathrm{CtrA{\sim}P_2}]/[\mathrm{DNA}_{Cori}]_\mathrm{T}$ against $[\mathrm{CtrA{\sim}P}]_\mathrm{T}$, the shape of the curve is extremely similar to that of Figure 4.2D, which describes binding of CtrA~P to *Cori* in the simple model. The only distinguishing difference between the two figures (4.2D and 3.2B) is the CtrA concentration at half-maximal saturation of *Cori*. The simple model and complex models predict 50% *Cori* saturation at CtrA~P concentrations corresponding to 6 and 12 molecules per cell, respectively. Considering that there are ~9,000 CtrA molecules per a swarmer cell [126], the difference between the two models seems to be negligible in consideration of the G1-S transition. Thus, we conclude that the simple model is sufficient for studying the dynamics of CtrA:*Cori* binding and for use in our larger model of the *C. crescentus* cell cycle.

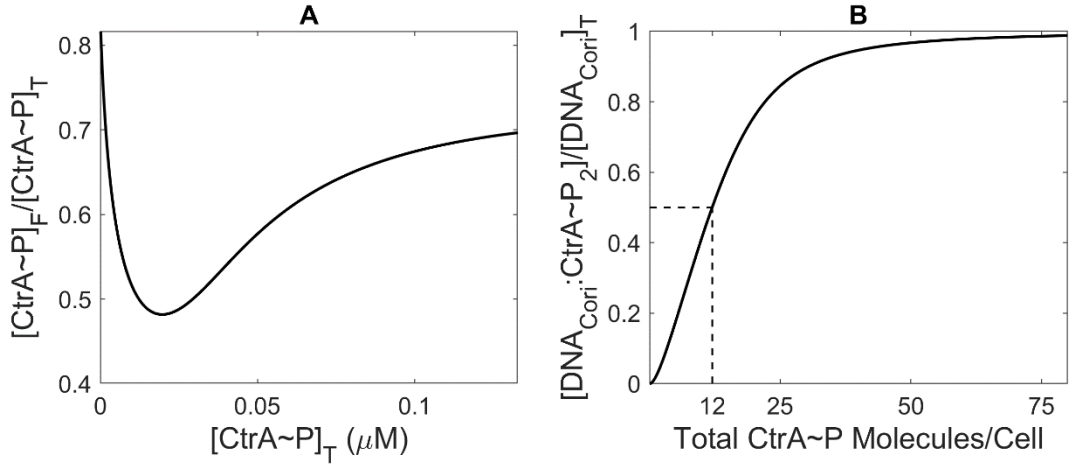

Figure 3.2) Investigating behavior of complex CtrA:DNA binding model.
(A) The ratio of freely diffusing CtrA~P to total CtrA~P ($[\mathrm{CtrA{\sim}P}]_\mathrm{F}$) /$[\mathrm{CtrA{\sim}P}]_\mathrm{T}$) varies with the total concentration of CtrA~P, reaching a minimum value of ~0.48.
(B) The ratio of $[\mathrm{DNA}_{Cori}{:}\mathrm{CtrA{\sim}P_2}]$ to $[\mathrm{DNA}_{Cori}]_\mathrm{T}$ is half-maximal at CtrA~P concentrations (0.02 μM) corresponding to 12 CtrA~P molecules per a cell. The x-axis is the same as "A" but is converted into molecules/cell.

3.1.7 Chromosome Replication

The initiation of chromosome replication is modeled with the variable, Ini, which considers the

influence of DnaA, CtrA, and methylation on *Cori* activity. A detailed description of *Cori* regulation is provided in the main text. Given that the mechanistic details of CtrA inhibition and DnaA activation of *Cori* are complex and not completely understood, attempting to create a detailed model of *Cori* activity would be challenging and likely inaccurate. Therefore, we take a simplistic approach to modeling DNA replication. First, we assume that [DNA:CtrA~P_2] is the only relevant species to inhibit chromosome replication, as levels of [DNA:CtrA~P] and [DNA:CtrA~P:CtrAP] are negligible compared to [DNA:CtrA~P2], as shown in Figure 3.2B (main text). Next, we assume that all five CtrA binding sites cooperatively work together to impair chromosome replication. Thus, assume that the inhibition of Ini by CtrA~P is proportional to (1-[CtrA:CtrA~P_2])^5. DnaA-ATP binds with moderate affinity to two 'G' boxes and binds weakly to five 'W' boxes. Binding to the 'W' boxes is dependent on cooperative interactions with DnaA bound to 'G' boxes. Thus, we assume that if DnaA-ATP binds to the 'G' boxes, the 'W' boxes will follow. We further assume that DnaA-ATP binding at each 'G' box is independent, but DnaA works cooperatively at each G site to initiate chromosome replication. We model the binding of DnaA-ATP as a hyperbolic function, and square the function to capture cooperativity. As for methylation, it was shown that the Δ*ccrM* strain is viable [127], so *Cori* methylation is not required for DNA replication. Therefore, we model the influence of methylation as we specified for Eq. 15. The equation governing the initiation of chromosome replication (Ini) takes the form:

$$\frac{\mathrm{d[Ini]}}{\mathrm{dt}} = \left(1 - 2\,m_{\mathrm{Ini}} \cdot (1 - [\mathrm{M_{Ini}}])\right) \cdot (1 - [\mathrm{DNA{:}\,CtrA{\sim}P_2}])^5 \cdot \left(\frac{[\mathrm{DnaA{\sim}ATP}]}{[\mathrm{DnaA{\sim}ATP}] + J_{\mathrm{a,Ini-DnaA}}}\right)^2 - k_{\mathrm{d,Ini}} \cdot [\mathrm{Ini}] \qquad \textit{Eq.}\ 37$$

where M_{Cori} represents the methylation state of *Cori* and m_{Ini} specifies the degree of influence that methylation has on *Cori* activity. $J_{\mathrm{IniCtrA\sim P}}$ indicates the value of [DNA:CtrA~P2] that results in 50% inhibition of *Cori* activity and $J_{\mathrm{Ini\text{-}DnaA}}$ indicates the concentration of DnaA-ATP that results in 50% *Cori* saturation when [DNA:CtrA~P2] is equal to zero. We assume that chromosome replication begins when [Ini] is equal to 1. Subsequently, Ini is reset to 0. DNA elongation is modeled with the variable, Elong, as mentioned previously (Eq. 16).

3.2 Biological Mechanisms

Progression through the *Caulobacter crescentus* cell cycle is controlled by a complex molecular mechanism that involves genetic regulation, proteolysis, protein-protein interactions, protein phosphorylation and dephosphorylation, and protein localization. To capture the dynamics of these processes, we derived a set of nonlinear ODEs based on observed biological facts. In this section, we will discuss the molecular mechanisms behind the model.

3.2.1 Methylation of DNA

Many genes in *C. crescentus* are regulated by methylation, including master regulators *ctrA* and *dnaA* [115], [122]. Genes transition between a hemi-methylated state and a fully methylated state based on the activity of the DNA methyltransferase, CcrM, and DNA replication. Immediately prior to the initiation of DNA synthesis, the DNA is fully methylated. Genes become hemi-methylated during chromosome replication, as the newly synthesized DNA strands are not methylated, resulting in two hemi-methylated chromosomes. As a consequence, genes that are closer to the origin of replication will become hemi-methylated earlier than genes that are further away, resulting in a timer-like mechanism for gene activity. Later in the cycle (G2 phase), when CcrM level is increasing, CcrM binds to its targeting sequence and adds a methyl-group to the hemi-methylated site, resulting in a fully-methylated gene [115].

The *ccrM* promoter has a methylation site of its own, and is upregulated by CtrA~P and downregulated by DnaA [113], [116]. As *ccrM* is more active transcriptionally when hemi-methylated, chromosome replication primes the cell for CcrM expression. In G2, CtrA~P levels accumulate, and DnaA levels depreciate resulting in CcrM synthesis. When CcrM levels are high enough to methylate DNA, the gene shuts off until G2 of the next cell cycle. Additionally, CcrM is rapidly degraded by Lon protease. As a result of these regulatory mechanisms, the window of CcrM expression is very short [128], [129]. Given that Lon is reported to be constantly active [129], we model the degradation of CcrM as a simple first-order reaction with Lon activity folded into the rate constant.

3.2.2 Regulation of CtrA

CtrA is regulated primarily by three processes: phosphorylation, proteolysis and transcription[130]. Transcription of *ctrA* is controlled by two promoter sites. The first promoter site, P1, is inhibited by CtrA and activated by GcrA. *ctrA* P1 is essential in S phase to induce *ctrA* activity when the CtrA concentration is very low [131], [132]. The P1 promoter is inactive when fully methylated (in G1 phase). This ensures that after CtrA degradation during the G1-S transition, CtrA production does not immediately turn back on. CtrA will not be produced again until after DNA replication has been initiated and the *CtrA* gene has been duplicated, resulting in two hemi-methylated genes. At this point, *ctrA* P1 is active again, and transcription will resume [131].

The *CtrA* gene also has a second promoter site, P2, which is activated by CtrA. Importantly, this promoter has no methylation site and is not influenced by the methylation of P1 [131]. Thus, when CtrA~P is high, CtrA transcription will remain high, regardless of the levels of CcrM. Importantly, unlike many other genes, both the unphosphorylated and phosphorylated forms of CtrA bind with similar affinity to the P1 and P2 promoters [126].

As previously mentioned, CtrA is proteolytically degraded at the G1-S transition. Effective proteolysis of CtrA requires the collaboration of several proteins, including ClpX, ClpP, CpdR, RcdA, and PopA. While unphosphorylated CpdR binds directly to ClpXP and localizes the protease to the old pole, RcdA interacts with both CpdR and PopA. PopA, however, does not recruit CtrA unless it is activated by two cyclic-di-guanosine monophosphate (cdG) molecules. Furthermore, PopA localization to the pole is dependent on cdG, but PopA can interact with RcdA independently of cdG [133]. When these components all come together, they form a complex that effectively targets and degrades CtrA over other ClpXP substrates [134]. Since the concentration of ClpX and ClpP do not fluctuate with the cell cycle [135], we do not explicitly model ClpXP. We also assume that unphosphorylated CpdR is always localized and bound to ClpXP at the old pole. Similarly, we assume that the PopA:cdG_2:RcdA complex is always localized at the old pole. Since PopA interacts with RcdA independently of cdG and vice versa [133], the concentration of the localized PopA:cdG_2:RcdA complex is equal to the total amount of RcdA bound to PopA times the fraction of PopA that is bound by cdG:

$$[\mathrm{PopA{:}\,cdG_2{:}\,RcdA}] = \frac{[\mathrm{PopA{:}\,cdG_2}] \cdot [\mathrm{RcdA{:}\,PopA}]_\mathrm{T}}{[\mathrm{PopA{:}\,cdG_2}] + [\mathrm{PopA}]} \qquad \textit{Eq.}\ 38$$

and $[\mathrm{RcdA{:}PopA}]_\mathrm{T}$ is given by Eq. 22. We assume that the PopA:cdG$_2$:RcdA complex interacts with the localized CpdR:ClpXP complex (simply denoted by CpdR) by simple mass action kinetics, so the rate of change for the entire CtrA proteolytic complex, denoted as $[\mathrm{ClpXP}]_\mathrm{Complex}$ takes the form:

$$\frac{\mathrm{d}[\mathrm{ClpXP}]_\mathrm{Complex}}{\mathrm{dt}} = \frac{V_2}{\mathrm{V}}\left(-k_1\frac{V}{V_2}[\mathrm{ClpXP}]_\mathrm{Complex} + k_2\left(\frac{V}{V_2}\right)^2[\mathrm{CpdR}][\mathrm{PopA{:}\,cdG_2{:}\,RcdA}]_\mathrm{F}\right), \qquad \textit{Eq.}\ 39$$

where $[\mathrm{PopA{:}cdG_2{:}RcdA}]_\mathrm{F}$ designates the concentration of [PopA:cdG$_2$:RcdA] that is not bound to CpdR. As all participating complexes in this interaction are localized to the old pole, we must account for the changes in local concentration on the kinetics by incorporating volume conversions (see Eq. 28 for reference). Importantly, in Eq. 39 we assume that the concentration of CpdR is much larger the PopA:cdG$_2$:RcdA complex. Thus, $[\mathrm{PopA{:}cdG_2{:}RcdA}]_\mathrm{F} = [\mathrm{PopA{:}cdG_2{:}RcdA}] - [\mathrm{ClpXP}]_\mathrm{Complex}$, and the steady state solution for $[\mathrm{ClpXP}]_\mathrm{Complex}$ is:

$$[\mathrm{ClpXP}]_\mathrm{Complex} = \frac{[\mathrm{CpdR}]}{[\mathrm{CpdR}] + \frac{J_{ClpXP:CpdR}}{V}} \cdot \frac{[\mathrm{PopA{:}\,2cdG}] \cdot [\mathrm{RcdA{:}\,PopA}]_\mathrm{T}}{[\mathrm{PopA{:}\,2dG}] + [\mathrm{PopA}]}, \qquad \textit{Eq.}\ 40$$

where $J_{\mathrm{ClpXP:CpdR}} = V_2 \cdot k_1/k_2$.

Phosphorylation of CtrA is regulated by the bi-functional histidine kinase/phosphatase, CckA. CckA interacts with CtrA via the phosphotransferase enzyme, ChpT [136]. As ChpT levels are relatively constant throughout the cell cycle [137], we assume that ChpT does not fluctuate and instantaneously passes a phosphate from CtrA to CckA and vice versa. Given these assumptions, we can model the phosphorylation and dephosphorylation of CtrA in the form of Eq. 19 and 20, respectively. The activity of CckA as a bi-functional phosphatase/kinase is regulated by a variety of mechanisms discussed in the next section.

3.2.3 CckA kinase/phosphatase regulation

CckA, which functions as both a kinase and a phosphatase, is regulated by several mechanisms. First, when CckA is unperturbed by regulatory factors, it acts as a kinase [138]. The tyrosine kinase, DivL, binds with the CckA PAS-B domain and is generally implicated in maintaining the kinase state of CckA [136], [139]. However, phosphorylated DivK (DivK~P) can bind to DivL likely causing a change in conformation of DivL's PAS domains [140]. As a result, the DivK~P:DivL complex binds with CckA to induce phosphatase activity over kinase activity. Importantly, DivK (unphosphorylated) has a weak affinity for DivL [138], [140], and on this basis we assume that unphosphorylated DivK does not interact with DivL in our model. Alternatively, CckA is regulated by the signaling molecule, cdG, which binds to CckA's PAS-B domain to induce the phosphatase state [138], [141].

With these assumptions, we calculate the total CckA phosphatase concentration ($[\mathrm{CckA}]_\mathrm{P}$) as:

$$[\mathrm{CckA}]_\mathrm{P} = \frac{[\mathrm{CckA{:}\ DivL}]_\mathrm{T} \cdot [\mathrm{DivL{:}\ DivK{\sim}P}]}{[\mathrm{DivL}]_\mathrm{T}} + [\mathrm{CckA{:}\ cdG}] - \frac{[\mathrm{CckA{:}\ cdG}] \cdot \frac{[\mathrm{CckA{:}\ DivL}]_\mathrm{T} \cdot [\mathrm{DivL{:}\ DivK{\sim}P}]}{[\mathrm{DivL}]_\mathrm{T}}}{[\mathrm{CckA}]_\mathrm{T}}, \qquad \textit{Eq.}\ 41$$

where the first term represents the fraction of CckA that is bound by DivL:DivK~P and the second term represents the total amount of CckA bound by cdG. As the amount of CckA bound by both cdG and DivL:DivK~P ([cdG:CckA:DivL:DivK~P]) is count twice by the first two terms, the third term subtracts by [cdG:CckA:DivL:DivK~P]. Finally, the difference between $[\mathrm{CckA}]_\mathrm{P}$ and $[\mathrm{CckA}]_\mathrm{T}$ is used to compute $[\mathrm{CckA}]_\mathrm{K}$.

$$[\mathrm{CckA}]_\mathrm{K} = [\mathrm{CckA}]_\mathrm{T} - [\mathrm{CckA}]_\mathrm{P}\,. \qquad \textit{Eq.}\ 42$$

3.2.4 Regulation of DnaA and GcrA

As a crucial DNA replication initiation factor, DnaA is subject to various modes of regulation. First, DnaA binds with ATP and ADP to produce DnaA-ATP and DnaA-ADP. Typically

considered the “active-form”, DnaA-ATP is the only form of DnaA that can promote chromosome replication [142]. Once chromosome replication is initiated, DnaA-ATP is hydrolyzed to DnaA-ADP by the enzyme HdaA. Activity of HdaA is restricted to S-phase, as it binds with the functioning beta-clamp of DNA polymerase to induce hydrolase activity [143]. In this way, HdaA helps restrict DnaA from initiating multiple rounds of chromosome replication within one cell cycle. Indeed, mutants of DnaA that do not interact with HdaA have an excessive accumulation of chromosomes [144]. We could not find any data on temporal regulation of HdaA; however, DnaA-ATP and DnaA-ADP activate the *hdaA* promoter [144]. Since DnaA levels are at their peak at the timing of chromosome replication, it is reasonable to assume that HdaA levels would also be sufficiently high to hydrolyze DnaA at this time as well. Therefore we do not model HdaA explicitly but rather model DnaA-ATP hydrolysis as a function of the variable, RepSwitch, which is set to 1 during chromosome replication and 0 when DNA synthesis is complete.

The influence of DnaA-ATP and DnaA-ADP on DnaA-targeted genes seems to differ depending on the gene. As mentioned, *hdaA* is targeted by both DnaA-ATP and DnaA-ADP; however, DnaA mutant studies suggest that *gcrA, mipZ* and *ftsZ* may be influenced more strongly by DnaA-ADP [144]. Thus, in our model only DnaA-ADP can stimulate *gcrA* activity. Given the uncertainty of regulation at other DnaA targets, we assume equivalent activity of DnaA-ATP and DnaA-ADP.

The *dnaA* promoter is primarily inhibited by GcrA and is most active when fully methylated. Since *dnaA* is located very close to *Cori*, transcription activity decreases once chromosome replication begins. Thus, DnaA levels will decrease from the beginning of S phase, until CcrM accumulates in the G2 phase [116]. Additionally, DnaA proteolysis is targeted by both the ClpAP and Lon proteases [145], [146]. However, because our model can fit DnaA expression data well without explicitly modeling mechanisms regulating DnaA proteolysis, we assume that DnaA turnover as a simple first-order reaction.

Intracellular concentrations of the master regulator GcrA are regulated by transcriptional controls and by proteolysis. The *gcrA* promoter is activated by DnaA and inhibited by CtrA [113], [116]. The CtrA binding motif is full, meaning that it has two CtrA binding recognition sequences [113]. Cell cycle-dependent turnover rates of GcrA also suggest that GcrA is targeted for

proteolysis; however, the mechanism of GcrA proteolysis has not been identified [147], [148]. In the absence of this information, we use a simple linear degradation rate to model GcrA turnover.

3.2.5 PleC and DivJ

DivJ, which accumulates during the swarmer-to-stalked transition, is a histidine kinase that serves to phosphorylate both DivK and PleD [149]. As previously discussed, the phosphorylated state of DivK modulates CckA activity, which in turn influences CpdR and CtrA. In this way, DivJ indirectly drives both the dephosphorylation and proteolysis of CtrA [150]. DivJ further promotes CtrA proteolysis via phosphorylation of PleD [149], as PleD must be phosphorylated to drive cdG synthesis [151] (see section on cdG for further discussion). DivJ activation is regulated primarily by SpmX and DivK. DivK and DivK~P bind to DivJ allosterically to induce its kinase activity [140], [149], while SpmX activates DivJ by directly binding with the protein and recruiting it to the cell pole [152]. We assume that DivJ likely has some activity independent of SpmX, and thus model the activity of DivJ as

$$[\mathrm{DivJ}]_{\mathrm{A}} = ([\mathrm{DivJ{:}\,DivK{\sim}P}] + [\mathrm{DivJ{:}\,DivK}]) \cdot \left([\mathrm{SpmX}] + \theta_{\mathrm{DivJ}}\right) \qquad \textit{Eq.}\ 43$$

where θ_{DivJ} represents the activity of DivJ without localization, and [SpmX] has a maximum activity of 1- θ_{DivJ}. Thus, [SpmX] represents the contribution of SpmX to activating DivJ. Factors that influence *spmX* promoter activity and mRNA translation are complex and not fully understood [25], [152]. Therefore, we develop a function for [SpmX] that is not derived from the biochemistry, but is convenient for our modeling methodology:

$$\frac{\mathrm{d}[\mathrm{SpmX}]}{\mathrm{dt}} = k_{\mathrm{s,SpmX}} \left(\frac{[\mathrm{SpmX}]^3}{c^3 + [\mathrm{SpmX}]^3} \right) (X_{\mathrm{cap}} - [\mathrm{SpmX}]) \qquad \textit{Eq.}\ 44$$

where X_{cap} represents the non-zero steady state [SpmX] value and is set to 1- θ_{DivJ} in all simulations unless otherwise stated. The parameter *c* regulates the inflection point at which [SpmX] begins to accumulate rapidly. The parameter $k_{\mathrm{s,SpmX}}$ is the inversed time scale, regulating the overall rate of [SpmX] accumulation. Because SpmX localizes to the old pole, upon cytokinesis the [SpmX] value remains constant in the stalked cell, but is reset to 0.01 in the swarmer cell. Importantly, [SpmX] is not set to 0, because this would be a stable state of [SpmX] and therefore [SpmX] would never accumulate in the swarmer cell.

PleC acts as the primary antagonist to DivJ, as it can act as a phosphatase on DivK~P. Interestingly, DivK~P can also allosterically bind to PleC to induce its kinase state [153], [154]. Thus, we assume that PleC operates as a phosphatase when not bound to DivK~P, but otherwise operates as a kinase. Additionally, PleC regulates PleD activity [155], as discussed further in the cdG discussion.

PleC is recruited to the new pole by PodJ in the pre-divisional phase of the cell cycle [156], however the mechanism of localization is unclear. We propose that the PleC and PodJ localization reaction takes the form, PleC + PodJ ↔ PodJ:PleC → $PleC_{pole}$ + PodJ, which is identical to the structure of Michaelis-Menten kinetics. The overall assumptions leading to the development of the Michaelis-Menten equation are that the substrate-enzyme complex bind and unbind much faster than product formation and that the substrate concentration is much greater than the enzyme concentration. In parallel, we assume that the rate that PodJ and PleC bind/ unbind is much faster than [PleC] is converted to $[PleC]_{pole}$, and we assume that the localized concentration of PodJ is much greater than local [PleC]. Therefore, the PleC rate of localization takes on the form of Eq. 27.

There are two forms of PodJ: $PodJ_L$ and $PodJ_S$. $PodJ_L$ is the active form of PodJ and is responsible for polar recruiting of PleC. PodJ is synthesized in the $PodJ_L$ form [157], and the *podJ* promoter is regulated by GcrA, DnaA and methylation [113]. $PodJ_L$ is converted to $PodJ_S$ by PerP [158], which has a promoter regulated by methylation and CtrA [113]. Thus, PerP accumulates in the late pre-divisional cell to impair PodJ activity [158]. In our model we do not track $PodJ_S$, and $PodJ_L$ is represented by the variable, [PodJ].

The localizations of DivJ, SpmX and PleC drive swarmer and stalked cell specific behavior. Upon cytokinesis, DivJ becomes dominant over PleC phosphatase in the stalked compartment, as PleC levels decrease dramatically. As a result, PleD and DivK are phosphorylated rapidly, driving CtrA~P depletion and transition into S phase. In contrast, the high level of PleC phosphatase and low level of SpmX/DivJ in the swarmer cell favor CtrA activity. However, PleC concentration decreases as SpmX and DivJ levels increase in G1, until eventually CtrA is degraded and the cell transitions into S phase [152], [159].

3.2.6 cdG

Cyclic-di-GMP (cdG) is an important second messenger of *C. crescentus* that directly influences the G1-S transition. As mentioned previously, cdG regulates CtrA proteolysis by binding to PopA, which forms a complex with RcdA, CpdR and ClpXP [133]. Additionally, cdG binds with CckA to induce phosphatase activity [141], [160]. cdG level is low in swarmer cells but increases rapidly in late G1 to deplete CtrA~P (by dephosphorylation and proteolysis) and thereby induces chromosome replication [160], [161]. Additionally, the spike in cdG prompts the release of the flagellum and production of the stalk and holdfast, thereby inducing the swarmer-stalk transition at the same time as the G1-S transition [162]. As the cell cycle proceeds, cdG level steadily decreases until the following cell cycle [161].

Diguanylate cyclase (DGC) enzymes, including PleD and DgcB, synthesize cdG from two GTP molecules. cdG, in turn, binds allosterically to the I-site of the DGC domain to inhibit activity [151], which contributes to the steady decrease in cdG following the rapid spike during the G1-S transition. While it has been demonstrated that cdG binds to PleD allosterically[163], no experiments (to our knowledge) have investigated binding with DgcB. Since the I-site is highly conserved in DGC enzymes [164], we assume that cdG allosterically inhibits DgcB as well.

PleD can only synthesize cdG in its phosphorylated state. Furthermore, PleD~P localizes to the stalked pole, while the unphosphorylated form does not [148], [165]. The phosphorylation state of PleD is regulated by PleC phosphatase and DivJ kinase [148], [166]. Given that PleC phosphatase interacts with PleD~P, but that these proteins localize to opposite poles, we assume that 10% of PleD~P is freely diffusing and able to interact with PleC phosphatase at the swarmer pole, while the other 90% localizes at the stalked pole.

Phosphodiesterase (PDE) enzymes convert cdG to pGpG [151]. PdeA, the best studied PDE enzyme in *C. crescentus*, also regulates cdG by binding to and inhibiting DgcB [165], [167]. PdeA synthesis is induced by CtrA and PdeA is degraded by the CpdR-ClpXP complex [165]. Thus, unphosphorylated CpdR contributes to CtrA proteolysis directly as well as contributing to the accumulation of cdG via proteolysis of PdeA.

3.2.7 Z-ring

The construction and contraction of the Z-ring are highly coordinated events, involving numerous proteins and steps of regulation [168]. FtsZ makes up the scaffold of the Z-ring, forming polymers responsible for constriction [169], [170] and recruiting other Z-ring proteins active in cytokinesis [171], [172]. Once the Z-ring is formed, it constricts in late G2 phase, leaving polymerized FtsZ localized at the new cell poles. The Z-ring will not re-localize to the mid-cell until FtsZ is depolymerized by MipZ, which binds near the chromosome origin of replication (*Cori*). During the process of chromosome replication, as the *Cori* site of the new chromosome moves towards the new pole, its MipZ factor initiates the depolymerization and re-localization of FtsZ. In this way, *C. crescentus* ensures that the Z-ring cannot re-assemble at mid-cell until after the replicating chromosome is well along in the segregation process [173].

Z-ring assembly and mechanics are complicated, and several models have been published on the dynamics of FtsZ and the Z-ring [174]–[177]. Given that the Z-ring is just one small piece of our model, we want to keep the Z-ring component of the model as simple as possible, while accurately predicting the timing of cytokinesis. First, we note that the synthesis of FtsZ does not correspond with cytokinesis, as FtsZ synthesis rate peaks in the S phase [178]. Thus, a detailed model of FtsZ dynamics will not help much with accurately predicting the timing of cytokinesis. However, we find that the activities of several other Z-ring proteins are temporally relevant to cytokinesis. Figure S4 illustrates how normalized mRNA expression levels of Z-ring relevant genes peak around 120 minutes of a 150-minute cell cycle. In comparison, the Z-ring should completely close around the 130 minute mark of a 150 minute cell cycle [179]. Thus, many Z-ring proteins reach peak expression right around the time of Z-ring constriction. Furthermore, many of these genes are activated by CtrA [113]. Thus, we decided to model Z-ring proteins as a general variable, [Zproteins], whose synthesis is induced by CtrA~P. To improve precision of our model, we designed our rate equation for [Zproteins] after a crucial Z-ring protein, FtsA, which is responsible for anchoring FtsZ polymers to the cytoplasmic membrane and recruiting downstream Z-ring proteins [180]–[182]. Cytokinesis is blocked by both overexpression and destabilizing/disrupting FtsA [183]–[186], which implies that functional cytokinesis requires precise regulation of FtsA. The *ftsA* promoter is upregulated by CtrA[113] and FtsA is quickly

degraded in a ClpAP-dependent manner immediately after cytokinesis[168], [184]. Taking these facts into account, we write the following differential equation for [Zproteins]:

$$\frac{\mathrm{d[Zproteins]}}{\mathrm{dt}} = k_{\mathrm{s,Zp}} \cdot \frac{[\mathrm{CtrA{\sim}P}]^2}{{J_{\mathrm{a,Zp-CtrA}}}^2 + [\mathrm{CtrA{\sim}P}]^2} - \left(\mu + k_{\mathrm{d,Zp}} + k_{\mathrm{d,ZP2}} \cdot [\mathrm{ClpAP}]\right) \cdot [\mathrm{Zproteins}]\,. \qquad \textit{Eq.}\ 45$$

[ClpAP] is a binary variable such that [ClpAP] = 0 for the majority of the cell cycle, but is set to one from the point of Z-ring closure to the point of daughter cell segregation.

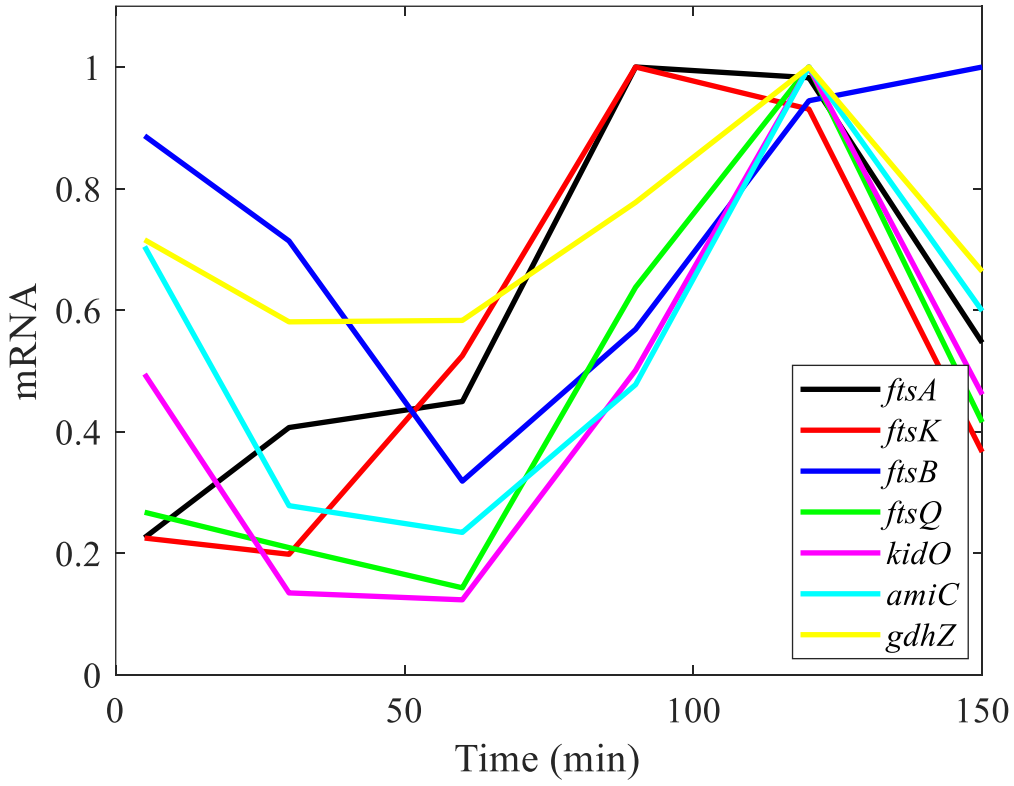

Figure 3.3) Normalized mRNA expression of Z-ring relevant genes.

Experiment conducted by Schrader et al. 2016 [187] and data retrieved via the CauloBrowser web tool [113]. While expression levels are diverse at the beginning of the cell cycle, the expression of each gene peaks around 120 min, corresponding with the timing of cytokinesis.

Given that multiple Z-ring proteins work together to form a functional Z-ring, it is reasonable to assume that Z-ring assembly and constriction is a cooperative process. Thus, we use a Hill function to model constriction of the Z-ring:

$$\frac{\mathrm{d}[\mathrm{Zring}]}{\mathrm{dt}} = -k_{\mathrm{zconstrict}} \cdot [\mathrm{MipZ\ switch}] \cdot \frac{[\mathrm{Zproteins}]^5}{\left(J_{\mathrm{Zring}} + \theta_{\mathrm{Z}}[\mathrm{Zring}]\right)^5 + [\mathrm{Zproteins}]^5}, \quad \textit{Eq.}\ 46$$

where [Zring] is equal to one when the Z-ring is fully open and is equal to zero when closed. Notably, the half-maximal rate of Z-ring constriction occurs when [ZProteins] is equal to $J_{\mathrm{Zring}} + \theta_{\mathrm{Z}}\cdot$[Zring]. Here, $J_{\mathrm{Zring}} + \theta_{\mathrm{Z}}$ dictates the resources needed to initiate cytokinesis (when [Zring] = 1) and J_{Zring} dictates the minimum resources needed to complete cytokinesis (when [Zring] ≈ 0). This feature was introduced for two reasons: 1) A detailed mathematical model of Z-ring constriction in *E. Coli* provides evidence that the force required for Z-ring constriction is greatest at the beginning of cytokinesis, and gradually decreases from 8pN to 3pN as the Z-ring closes [176]. 2) Local concentration of Z-ring proteins should increase as the circumference of the Z-ring decreases, which should further facilitate constriction. Thus, we assume that as the Z-ring closes, less total resources are required to maintain constriction. To account for the activity of MipZ on FtsZ depolymerization and relocalization to the mid-cell, we introduce a binary variable, [MipZ switch], that turns on ([MipZ switch] = 1) after the chromosome has been replicated and the *Cori* locus of the new chromosome relocates to the new pole. The switch turns off ([MipZ switch] = 0) after cytokinesis.

3.2.8 Cell growth

Cells grown in PYE and M2G media have the same average cell length and width despite having significantly different cell cycle times[188]. Thus, the growth rate and cell cycle time must be interrelated in *Caulobacter* to maintain consistent cell size in different conditions. Since the molecular mechanism of cell size control in *Caulobacter* has not been elucidated and is outside the scope of this model, we do not attempt to accurately model the biology of cell growth and size control. However, because cell volume is a variable influencing several equations in our model, we must estimate changes in volume. We use the exponential growth function, Eq. 4, to model volume growth, and adjust the growth rate, μ, after each cell division such that:

$$\mu = T^{-1} \cdot \ln\frac{V_{\mathrm{div}}}{V_{\mathrm{birth}}}, \quad \textit{Eq.}\ 47$$

where T is the time of the previous cell cycle and V_{birth} is the cell volume at birth and V_{div} is the targeted volume at division ($V_{\mathrm{div}} = 2$). When we run our parameter optimization algorithms,

utilizing this method ensures that μ adjusts accordingly. Furthermore, it ensures that the volume of mutant cells does not go to zero or infinity in mutants that have cell cycle times different from a WT cell. Because some mutants do become elongated, we put a limit on μ such that:

$$0.0038 \leq \mu \leq 0.007 .$$

If Eq. 47 calculates μ to be a value outside of these bounds, μ is set to the corresponding limit.

It has been observed in *C. crescentus* that daughter cells separate approximately 18 minutes after the Z-ring closes[179]. Synchronization experiments in *Caulobacter* isolate swarmer cells from the rest of the population and would not capture these unsegregated cells. Therefore, we mark the beginning of the cell cycle as 18 minutes after the Z-ring closes.

3.3 Parameter Estimation

Parameter values were initially estimated from published experimental sources whenever possible, and the remainder were assigned by educated guesswork. To improve the model's performance, we implemented a random-walk algorithm to generate new sets of parameter values and to evaluate each set's performance based on certain criteria built into a 'cost function'. We implement the random-walk algorithm with two goals in mind. The first is to identify a 'best' parameter set with a dramatically smaller cost than the original parameter set. The second is to develop a collection of parameter sets that serve as a sample around a local cost minimum. In this section, we first explain how we implemented the random-walk algorithm and then we discuss the details of our cost function.

3.3.1 Random-walk algorithm

To find improved parameter sets, we utilized the Monte-Carlo Markov-Chain/Simulated Annealing approach. We start with a 'current' parameter set,

$$\mathrm{p} = \begin{pmatrix} p_1 \\ p_2 \\ \vdots \\ p_x \end{pmatrix}, \qquad \textit{Eq.}\ 48$$

of length *x* and perturb it to generate a 'temporary' parameter set **p'**, such that:

$$p_i' = p_i\left(1 + \delta_i \cdot N(0,\sigma)\right), \qquad \textit{Eq.}\ 49$$

where $N(0,\sigma)$ is a random number drawn from a normal distribution with mean zero and standard deviation σ. δ_i is a Boolean variable (i.e., $\delta_i = 0$ or 1) that dictates whether or not a given parameter p_i will be subjected to random perturbation. To determine the values of δ_i, we randomly choose n parameters without replacement using MATLAB's built in function, randsample. If p_i is selected, then δ_i is set to 1. Otherwise $\delta_i = 0$. Additionally, any p_i' that evaluates to a negative number is set to 0.

For a given iteration of the algorithm, the probability that the temporary parameter set replaces the 'current' parameter set is defined as:

$$\mathrm{p} = \mathrm{p}' \text{ if } g \le Pr,$$
$$Pr = \min\left(\exp\left(\frac{f(\mathrm{p}) - f(\mathrm{p}')}{\tau}\right), 1\right), \qquad \textit{Eq.}\ 50$$

where g is a random number selected from a uniform distribution between 0 and 1, f is the cost function for the parameter set, and τ is the 'cooling factor' for simulated annealing. Thus, any temporary parameter set that has a lower cost than the 'current' parameter set replaces the 'current' parameter set. Any temporary parameter set that has a higher cost than the 'current' parameter set has a probability Pr of replacing the current parameter set. This process of generating a new (temporary) parameter set and evaluating it compared to the current parameter set is considered one iteration (one step) of the random walk.

Ultimately, the efficiency of the algorithm is tied to the parameters σ, τ and n. A smaller σ corresponds to smaller perturbations from a given parameter set. If σ is very small, it is more likely to generate a **p**' that is an improvement over **p**. However, it may take much longer to make larger improvements. τ dictates the probability that a **p**' that has a higher cost than **p** will be accepted as the new **p**. A larger τ improves the algorithm's chances of escaping a local minimum but decreases the probability of identifying a new local minimum. When n is large, more parameters are perturbed in each iteration. As a result, each **p**' will be further away (in parameter space) from **p**. The advantage to a large n is that less steps are needed to make a larger change; however, the chances that **p**' is an improvement over **p** decreases.

We use this algorithm to develop three collections of parameter sets: SLOW, QUICK and CORI⁻. SLOW and QUICK parameter sets are parameterized to different CtrA expression patterns (Table S3), while CORI⁻ is parameterized under the assumption that $CtrA_u$ does not bind to *Cori*. Each collection of parameter sets is intended to contain diverse sets of parameter values that adequately fit the biological constraints of the cost function. To create each collection, we first identified a 'best' or 'seed' parameter set for each collection. Starting from a parameter set that we obtained by manually fitting the model to some desired properties, we searched for a seed parameter set in three stages. First, pursue a local minimum using large perturbations and a moderate cooling temperature; second, hone in on a local minimum by making smaller perturbations at a cooler temperature; and third, escape the local minimum (in hopes of finding a radically new parameter set) by making large perturbations at high temperature. Table S2 describes the parameter search procedure in each stage and the number of iterations within each stage. Finally, we repeated this process in a cyclical fashion (stage 1, stage 2, stage 3, stage 1, etc.) until the algorithm stops improving over two cycles. At that point, the parameter set with the best score is defined as the seed parameter set for deriving an entire collection of 'acceptable' parameter sets.

Table 3.3) Details on parameter estimation stages.

Stage #	*n*	*σ*	*τ*	*Iterations*
1	3	35	2.5	250
2	20	5	0.7	750
3	10	15	25	250

Once the seed parameter set is identified, the parameterization algorithm is run five separate times for 1500 iterations (with the seed parameter set as the initial **p** for each run) under the following conditions: n = 10, σ = 5, τ = 6. Here, we save each accepted, or 'current', parameter set to develop the parameter set collection. The small perturbations and medium cooling factor ensure that the algorithm stays close to the local minimum, yet frequently accepts randomly generated temporary parameter sets. Running the algorithm five separate times dramatically increases the diversity of the parameter sets within the collection, as each run of the algorithm takes a different randomized path.

3.3.2 Cost Function

The cost function $f(\mathbf{p})$ is a sum of the scores S of individual simulations of wild-type cells and a selection of mutant strains, simulated for both swarmer (SW) and stalked (ST) cells:

$$f(\mathrm{p}) = 4 \cdot \left(S_{\mathrm{WT,ST}} + S_{\mathrm{WT,SW}}\right) + \sum_{\mathrm{m} \in \mathrm{M}} \left(S_{\mathrm{m,ST}} + S_{\mathrm{m,SW}}\right), \qquad \textit{Eq.}\ 51$$

where M is the set of mutant strains {Δ*pdeA*, Δ*pleD*, Δ*ccrM*, Δ*gcrA*, Δ*popA*&P*divK*::Tn, P*pleC*::Tn, *divL*A601L, LS1, *ctrA*D51E, *ctrA*Δ3Ω, $\mathrm{cdG_0}$} that contribute to the cost function. S_{m} is the score (defined below) for a given strain simulation. Each simulation was run for 1600 minutes and scores were calculated over the last three cycles of the simulation (discussed below). Both swarmer and stalked cells were simulated for each strain. Wild type (WT) simulation scores are multiplied by four to increase their weight in the parameter estimation process.

The score for a WT cell, SW and ST simulations, is defined as the average score of the last three cell cycles plus the standard deviation of the scores:

$$S_{\mathrm{WT,CT}} = \sum_{c=1}^{3} \frac{S^{c}_{\mathrm{WT,CT}}}{3} + \sigma_{S_{\mathrm{WT,CT}}}. \qquad \textit{Eq.}\ 52$$

where CT is the cell type and *c* indicates the cell cycle (of the last three cycles in the simulation) being scored. We track the last 3 cell cycles because the system's limit cycle may take more than one cell cycle to complete. In other words, the oscillatory cycle of the system may take more than one cell cycle to return to its starting point. Therefore, we average the scores of the last three cell cycles and penalize for a larger standard deviation among the individual scores. The penalty is implemented because parameter sets with consistent cell cycle oscillations tend to be more robust to parameter perturbations.

For WT simulations, we score an individual swarmer cell cycle as follows:

$$S^{c}_{\mathrm{WT,SW}} = w_{\mathrm{rep}} \left(\frac{t_{\mathrm{rep},c} - 20}{2}\right)^{2} + w_{\mathrm{div}} \left(\frac{t_{\mathrm{div},c} - 140}{8}\right)^{2} + \sum_{j \in \mathrm{J}} w_j \cdot S_{j,c}\,, \qquad \textit{Eq.}\ 53$$

where w_{rep} and $t_{\mathrm{rep},c}$ are the weight and time of chromosome replication, respectively; w_{div} and $t_{\mathrm{div},c}$ are the weight and time of cell division, respectively. The targeted time of 20 min for

chromosome replication and 140 min for cell division is consistent with experimental observations[189]–[193]. J is a collection of experimental time course data and *j* is an index for a given experiment. The data in set J is usually collected from western blots of synchronized populations and quantified using ImageJ (exceptions include cdG and Replication). See Table S3 for a list experiments and the corresponding protein of interest. The score, $S_{j,c}$, measures the agreement between the simulation and the experimental data. We calculate $S_{j,c}$ as:

$$S_{j,c} = \sum_{t \in T} \frac{(d_{j,t} - \lambda_j \cdot y_{j,t})^2}{n}, \qquad Eq.\ 54$$

where *t* is the time for a given experimental data point, T is the set of all experimental time points, $d_{j,t}$ is the normalized observed concentration in the *j*th experiment at time *t*, and $y_{j,t}$ is the simulated value for the corresponding variable at time *t*. We note that *t* is normalized to the length of the simulated cell cycle, as cell cycle times vary between experiments. Additionally, *n* is the number of data points and λ_j is the scaling coefficient that minimizes the score,

$$S_j(\lambda_j) = \min\left(S_{j*}(\lambda_{j*})\right), \qquad Eq.\ 55$$

where S_{j*} is the score for an arbitrary scaling coefficient, λ_{j*}. We find λ_j using the MATLAB algorithm, fminsearch.

Table 3.4) Sources of data used for parameterization of WT cells.

Variable	Source	Variable	Source
CtrA~P	Jacobs et al. 2003 [22]	DivJ	Sanselicio et al. 2015 [194]
CtrA Total (SLOW and CORI⁻)	Collier et al. 2006 [147]	CckA kinase	Jacobs et al. 2003 [22]
CtrA Total (QUICK)	Mcgrath et al. 2006 [195]	CcrM	Grunenfelder et al. 2001[196]
DnaA	Cheng and Keiler 2009 [23]	CpdR Total	Iniesta et al. 2006 [197]
GcrA	Holtzendorff et al. 2004 [21]	CpdR	Iniesta et al. 2006 [197]
PleC Total	Viollier et al. 2002 [198]	cdG	Abel et al. 2013 [161]
PleC pole	Christen et al. 2010 [199]	RcdA	Mcgrath et al. 2006 [195]
PodJ	Chen et al. 2006 [158]	PdeA	Abel et al. 2011 [167]
PodJ	Viollier et al. 2002 [200]	FtsA	Martin et al. 2004 [184]
DivJ	Wheeler and Shapiro 1999 [24]	PerP	Chen et al. 2006 [158]

In contrast to WT swarmer simulations, we do not score WT stalked simulations in accordance with experimental time-course data because there is no relevant time-course data (to the best of our knowledge) for the stalked cell cycles in *C. crescentus*. For stalked WT simulations, the score is calculated as:

$$S^{c}_{\mathrm{WT,ST}} = \left(\frac{E_{\mathrm{rep},c}}{4}\right)^{2} + \left(\frac{t_{\mathrm{div},c} - 110}{6}\right)^{2}, \qquad \textit{Eq.}\ 56.1$$

$$E_{\mathrm{rep},c} = \min\left(\mathrm{abs}(t_{\mathrm{div},c} - 10 - t_{\mathrm{rep},c}),\ t_{\mathrm{rep},c}{+}10\right). \qquad \textit{Eq.}\ 56.2$$

$E_{\mathrm{rep},c}$ is the error in timing associated with initiation of chromosomal replication. As far as we know, the timing of chromosome replication has not been measured in the stalked cell, so we assume that the stalk cell should resemble the swarmer cell 30 minutes into the cell cycle (because the swarmer cell cycle is ~30 minutes longer than the stalked cell cycle[201]). Given that chromosome replication begins approximately 20 minutes into the swarmer cycle[192], we estimate that the chromosome should begin replication in the stalked cell approximately 10 minutes before cell division (which occurs 8 minutes after the Z-ring is completely closed).

Similar to WT simulations, we simulate mutant strains for 1600 minutes and calculate a score from the last three cell cycles:

$$S_{\mathrm{m,CT}} = \sum_{c}^{3} \frac{S^{c}_{\mathrm{m,CT}}}{3} + \sigma_{S_{\mathrm{m,CT}}}. \qquad \textit{Eq.}\ 57$$

If the cell cycle is arrested, we use a different scoring methodology depending on the strain (discussed in more detail later). We designate the cell cycle as arrested if the cell does not divide within the last 300 minutes of the simulation.

For strains Δ*pdeA*, Δ*popA*&P*divK*::Tn, *ctrA*D51E, *ctrA*Δ3Ω, and P*pleC*::Tn, the cell cycles are scored as:

$$S^{c}_{\mathrm{m,SW}} = \left(\frac{t_{\mathrm{div},c} - 145}{5}\right)^2 + \left(\frac{t_{\mathrm{rep},c} - 20}{4}\right)^2 \text{ if cell cycle not arrested,} \qquad \textit{Eq.}\ 58.1$$

$$S^{c}_{\mathrm{m,ST}} = \left(\frac{t_{\mathrm{div},c} - 115}{5}\right)^2 \text{ if cell cycle not arrested,} \qquad \textit{Eq.}\ 58.2$$

$$S_{\mathrm{m,CT}} = \left(\frac{150}{N_{\mathrm{cycles}}}\right)^2 \text{ if cell cycle arrested.} \qquad \textit{Eq.}\ 58.3$$

These mutants are described as having 'normal' cell cycles in the literature, meaning that they have relatively normal morphology and cell cycle timing. Eq. 58.1 and 58.2 ensure that the cell cycle time of these strains remains close to the WT. Eq. 58.3 accounts for the total score for mutant, m, if the cell cycle is arrested. Here, N_{cycles} is the number of cell cycles completed successfully prior to cell cycle arrest. We observe that arrested simulations often complete several rounds of successful cell cycles prior to arrest. A reasonable comparison would be a dampened oscillator. Eq. 58.3 favors parameter sets that complete more successful cell cycles before cell cycle arrest, until the cell successfully replicates for 1600 minutes. Parameter sets that might have cell cycle arrest after 1600 minutes would likely exhibit instability in their cell cycles. Thus, the standard deviation of cell cycle scores in Eq. 57 ensures that, when the algorithm finds viable parameter sets for a mutant strain, the robustness of these simulations continue to improve.

Mutant strains LS1, ΔccrM, ΔgcrA, cdG_0, Δ*pdeA*, Δ*pleD* and *divL(*A601L) each have unique characteristics or observations, and therefore have unique scoring functions. The following text describes how each mutant is scored and the reasoning behind their scoring functions.

The LS1 mutant strain, characterized by constitutive expression of *ccrM*, is a mutant of the WT LS176 strain rather than the conventional WT NA1000 strain of *C. crescentus*. The strain exhibits several defects such as elongation and the accumulation of additional chromosomes; nonetheless, the cell is viable [202]. Given that the cell is a mutant of LS176 rather than the NA1000 strain, which the rest of our model data is based on, we do not specify any details other than that the cell cycle is not arrested. Similarly, the cdG_0 mutant strains are observed to be viable yet elongated and lacking polar organelles [161]. Without any information regarding the

average cell cycle time in cdG$_0$ mutants, we only score this strain based on viability. Thus, the LS1 and cdG$_0$ mutants are scored as follows:

$$S_{\mathrm{m,CT}} = \left(\frac{150}{N_{\mathrm{cycles}}}\right)^2 \text{ if cell cycle arrested,} \qquad \textit{Eq.}\ 59.1$$

$$S^c_{\mathrm{m,ST}} = 0 \text{ if cell cycle not arrested.} \qquad \textit{Eq.}\ 59.2$$

The *ccrM* knock-out mutant, Δ*ccrM*, is viable in M2G medium, but the cells exhibit large deviations in cell cycle length with the average cell being 1.5x larger than WT [127]. Δ*ccrM* mutants in PYE medium have decreased viability, but one experiment observed a 3 hour cell cycle in PYE medium [203]. Therefore, we score the cell cycle time against 180 minutes, but leave a larger denominator in Eq. 60.2 than Eq. 58.1, due to the large deviations in observed cell cycle length. If the stalked cell cycle is not arrested, we assign a score of zero as the literature does not distinguish between the characteristics of the swarmer and stalked cell cycles of Δ*ccrM* mutants.

$$S_{\Delta ccrM,\mathrm{CT}} = \left(\frac{150}{N_{\mathrm{cycles}}}\right)^2 \text{ if cell cycle arrested,} \qquad \textit{Eq.}\ 60.1$$

$$S^c_{\Delta\mathrm{ccrM,SW}} = \left(\frac{t_{\mathrm{div},c} - 180}{15}\right)^2 \text{ if cell cycle not arrested,} \qquad \textit{Eq.}\ 60.2$$

$$S^c_{\Delta\mathrm{ccrM,ST}} = 0 \text{ if cell cycle not arrested.} \qquad \textit{Eq.}\ 60.3$$

Δ*gcrA* mutants are observed to have a 180 minute swarmer cell cycle in M2G medium [120]. As the timing of the stalked cell cycle is not clear, the Δ*gcrA* mutants are scored as:

$$S_{\Delta gcrA,\mathrm{CT}} = \left(\frac{150}{N_{\mathrm{cycles}}}\right)^2 \text{ if cell cycle arrested,} \qquad \textit{Eq.}\ 61.1$$

$$S^c_{\Delta gcrA,\mathrm{SW}} = \left(\frac{T - 180}{8}\right)^2 \text{ if cell cycle not arrested,} \qquad \textit{Eq.}\ 61.2$$

$$S^{c}_{\Delta gcrA,\mathrm{ST}} = 0 \text{ if cell cycle not arrested.} \qquad \textit{Eq.}\ 61.3$$

The *divL(*A601L) mutant strain, defined by disrupted binding between DivK and DivL, exhibits cell cycle arrest in G1 [204]. Thus, we score the mutant as:

$$S^{c}_{divL(\mathrm{A601L}),\mathrm{CT}} = \frac{5\mathrm{x}10^{4}}{t_{\mathrm{div},c}} \text{ if cell cycle not arrested,} \qquad \textit{Eq.}\ 62.1$$

$$S_{divL(\mathrm{A601L}),\mathrm{CT}} = 5 \cdot (N_{\mathrm{cycles}} - 1) \text{ if cell cycle arrested.} \qquad \textit{Eq.}\ 62.2$$

This method ensures that, if the cell cycle is not arrested, the algorithm pushes the system in favor of longer *divL(*A601L) cell cycles, until the cell cycle is eventually arrested.

Δ*pleD* and Δ*pdeA* have observed average cdG levels of 70% and 123% of WT, respectively, while exhibiting no indication of perturbed cell cycle behavior [160], [161], [167]. Thus, we score these mutants as follows:

$$S^{c}_{\Delta pleD,\mathrm{SW}} = \left(\frac{t_{\mathrm{div},c} - 145}{5}\right)^{2} + \left(\frac{t_{\mathrm{rep},c} - 20}{4}\right)^{2} + 100 \cdot \left(\frac{cdG_{\Delta pleD,\mathrm{SW}}}{cdG_{\mathrm{WT,SW}}} - 0.7\right)^{2} \text{ if cell cycle not arrested,} \qquad \textit{Eq.}\ 63.1$$

$$S^{c}_{\Delta pleD,\mathrm{ST}} = \left(\frac{t_{\mathrm{div},c} - 115}{5}\right)^{2} + +100 \cdot \left(\frac{cdG_{\Delta pleD,\mathrm{ST}}}{cdG_{\mathrm{WT,ST}}} - 0.7\right)^{2} \text{ if cell cycle not arrested,} \qquad \textit{Eq.}\ 63.2$$

$$S^{c}_{\Delta pdeA,\mathrm{SW}} = \left(\frac{t_{\mathrm{div},c} - 145}{5}\right)^{2} + \left(\frac{t_{\mathrm{rep},c} - 20}{4}\right)^{2} + 100 \cdot \left(\frac{cdG_{\mathrm{WT,SW}}}{cdG_{\Delta \mathrm{pdeA,SW}}} - 0.81\right)^{2} \text{ if cell cycle not arrested,} \qquad \textit{Eq.}\ 63.3$$

$$S^{c}_{\Delta pdeA,\mathrm{ST}} = \left(\frac{t_{\mathrm{div},c} - 115}{5}\right)^2 + 100 \cdot \left(\frac{cdG_{\mathrm{WT,ST}}}{cdG_{\Delta\mathrm{pdeA,ST}}} - 0.81\right)^2 \text{ if cell cycle not arrested,} \quad \textit{Eq.}\ 63.4$$

$$S_{\mathrm{m,CT}} = \left(\frac{150}{N_{\mathrm{cycles}}}\right)^2 \text{ if cell cycle arrested,} \quad \textit{Eq.}\ 63.5$$

where $cdG_{\mathrm{m,CT}}$ indicates the average cdG levels in strain m in cell type CT.

Chapter 4 : Computational Investigation of CtrA:*Cori* Binding Suggests a New Role for Unphosphorylated CtrA in the *Caulobacter crescentus* Cell Cycle

Bronson R. Weston[1], Young Cao[2*], and John J. Tyson[3]

[1] Program in Genetics, Bioinformatics, and Computational Biology, Virginia Tech, Blacksburg VA, USA

[2] Department of Computer Science, Virginia Tech, Blacksburg, VA, USA

[3] Department of Biological Sciences, Virginia Tech, Blacksburg, VA, USA

4.1 Abstract

In the alpha-proteobacterium, *Caulobacter crescentus*, a master regulatory protein CtrA, in its phosphorylated form (CtrA~P), binds directly to the chromosome origin (*Cori*) to inhibit DNA replication. Using a mathematical model of CtrA binding at *Cori* site [d], we provide computational evidence that the unphosphorylated form of CtrA ($CtrA_U$) acts as a competitive inhibitor of CtrA~P to promote chromosome replication. These dynamics suggest that CckA phosphatase may clear *Cori* of CtrA~P by altering the $CtrA_U$:CtrA~P ratio rather than completely depleting CtrA~P at the G1-S transition. Incorporating these interactions into a detailed model of the *C. crescentus* cell cycle, we demonstrate that $CtrA_U$ stabilizes the timing of chromosome replication, allows for a speedier transition into S phase, and is essential for a dephosphorylation-dependent transition into S phase. Analysis of mutant simulations indicate that the $CtrA_U$:*Cori* interaction contributes to the viability of numerous mutant strains. Overall, these results suggest that $CtrA_U$ enhances the robustness of chromosome replication.

4.2 Introduction

The accurate duplication of chromosomes and their exact partitioning to daughter cells are foundational to the perpetuation of life. In the freshwater bacterium, *Caulobacter crescentus*, the cycle of chromosome replication and partitioning is inextricably linked to an asymmetric division

process that buds off a motile ‘swarmer’ cell from its parental, sessile ‘stalked’ cell. The processes of DNA replication, cell differentiation and division are managed by four master regulators: CtrA, GcrA, CcrM and DnaA [19]. These proteins interact with each other and with the chromosome origin (*Cori*) to coordinate progression through the cell cycle (Figure 4.1A). Specifically, CtrA~P binds to *Cori* to inhibit the initiation of DNA replication [192], [205], whereas DnaA-ATP binds to *Cori* to activate DNA replication [142]. DnaA and CtrA are indispensable for proper regulation of DNA synthesis. CcrM methylates *Cori* to increase its activity, although this interaction is not essential for chromosome replication [115]. The fourth master regulator, GcrA, does not directly interact with *Cori*, but regulates numerous genes involved with replication machinery [21]. While GcrA is also not essential for viability, Δ*gcrA* mutants have significantly slower cell cycles [120].

The activities of DnaA and CtrA are tightly regulated by three mechanisms: gene expression, post-translational modifications, and proteolysis. First of all, the promoters of *ctrA* and *dnaA* are regulated, in part, by DNA replication via methylation sites. Upon DNA replication, the chromosome becomes hemi-methylated resulting in reduced activity of *dnaA* and increased activity of *ctrA* P1 [19], [131]. CcrM, in turn, re-methylates these genes in G2 [206]. Additionally, GcrA directly interacts with the *ctrA* P1 promoter to activate transcription [21] and with the *dnaA* promoter to inhibit transcription [21]. CtrA, in turn, binds to its own P1 promoter to inhibit transcription, but activates transcription of its P2 promoter [207]. Secondly, both CtrA and DnaA have active (CtrA~P and DnaA-ATP) and inactive ($CtrA_U$ and DnaA-ADP) states. DnaA-ATP induces chromosome replication [142]; and, promptly after replication is initiated, the active DNA polymerase complex recruits an enzyme, HdaA, that hydrolyzes DnaA-ATP to DnaA-ADP to ensure that the chromosome is replicated only once per cell cycle [143], [144]. In the pre-replicative phase, CtrA~P binds with *Cori* to block chromosome replication [125], [192]. At the G1-S transition, a bifunctional kinase/phosphatase, CckA, dephosphorylates CtrA~P to enable chromosome replication [137]. The third strategy by which *Caulobacter* regulates DnaA and CtrA is proteolysis. DnaA is degraded by Lon and ClpP proteases [145], [208], while CtrA is degraded by ClpXP with the help of its associated adaptors, cyclic-di-GMP (cdG),PopA, RcdA, and CpdR [133].

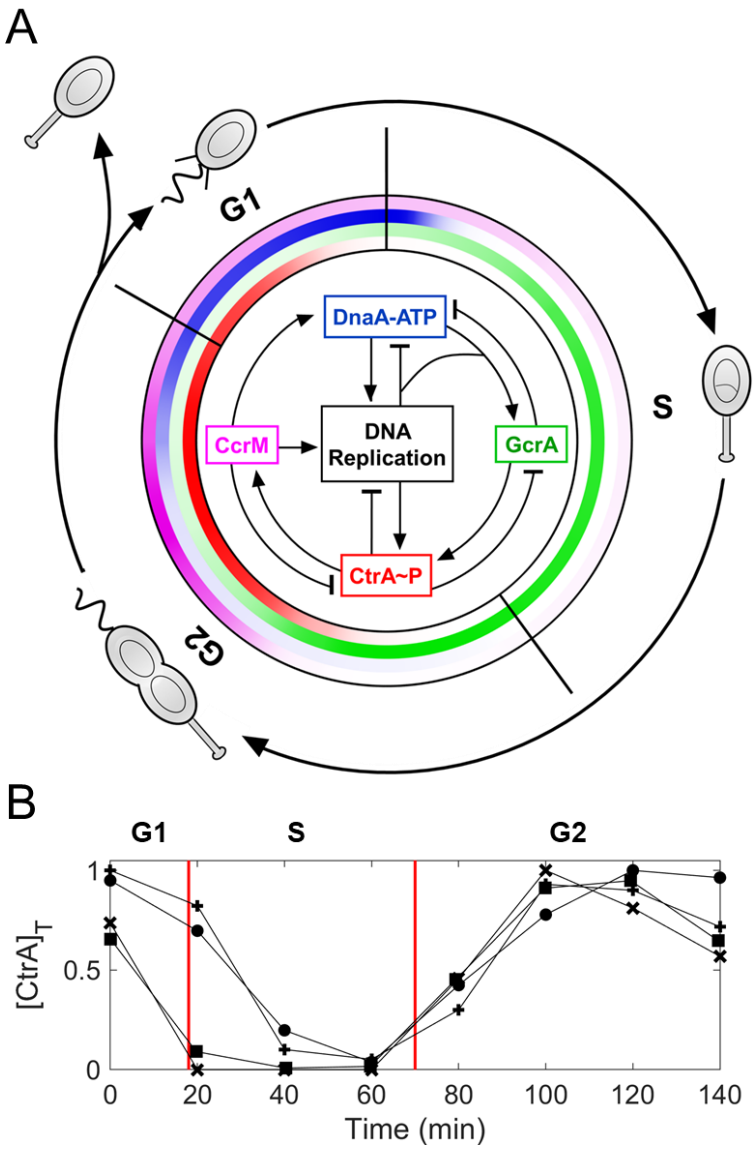

Figure 4.1) Master regulators control progression through the C. crescentus cell cycle.
(A) The dimorphic lifestyle of C. crescentus is divided into three phases (G1, S and G2). G1 is characterized by a swarmer phenotype, expressing a flagellum and pili. When DNA replication is initiated, the cell transitions into S phase, simultaneously releasing its swarmer organelles and synthesizing a stalk. As the cell completes DNA replication, the cell transitions into G2 and synthesizes a flagellum at the new pole. When the cell divides, the stalked daughter cell immediately enters S phase and the swarmer cell enters G1. This process is orchestrated by the cyclical expression and interactions of four master regulators (DnaA, GcrA, CcrM and CtrA) with each other and with DNA. Arrows designate positive interactions and bars represent inhibition. The inner circle indicates the timing of expression of each master regulator (color corresponds to the respective master regulator).
(B) The expression pattern of normalized CtrA levels at the G1-S transition varies significantly between experiments, but not much at the S-G2 transition. Vertical red lines separate phases of the cell cycle. Data points represent western blot data from synchronized populations, quantified with ImageJ. (x, Collier et al. 2006, Fig 5A); (■, Holtzendorff et al. 2004, Fig 3B); (●, McGrath et al. 2006, Fig 3A); (+, Domian et al. 1997, Fig 1A).

Given the variety of regulatory mechanisms governing DnaA and CtrA activities, one might expect consistent, tight control over DnaA and CtrA levels. While this is true for DnaA, it seems not to be so for CtrA. Comparison of CtrA western blots from different synchronization experiments (Figure 4.1B) reveals that CtrA expression at the G1-S transition varies dramatically between populations. While some synchronized populations show that CtrA is mostly cleared by 20 minutes [21], [147], [209], others suggest that it is not cleared until 40—60 minutes after the birth of a swarmer cell [152], [195], [210]. Importantly, these experiments all report similar timing in the re-accumulation of CtrA (~80 minutes), in the timing of swarmer to stalk differentiation (~30-40 min), and total cell cycle times of ~140-160 minutes, suggesting consistency in the timing of chromosome replication despite inconsistency in CtrA levels at the G1-S transition. It appears that chromosome replication may be initiated at CtrA concentrations ranging from 0—80% of maximal expression. Assuming a swarmer cell volume of 1 μm^3 [121], [126], [211], and peak CtrA expression levels of ~20,000 molecules [126], [179], this corresponds to a range of 0-24 μM. In agreement with this conclusion, an experiment that simultaneously tracked DNA methylation and CtrA concentration in a synchronized population showed that chromosome replication was initiated when the CtrA concentration was approximately 50% of maximal [192]. These observations contradict the typical narrative of *Caulobacter* cell-cycle progression, which assumes rapid and complete proteolysis of CtrA at the G1-S transition [210], [212]–[214].

Various studies report chromosome replication approximately 15 minutes into the swarmer cell cycle [192], [215], [216]. The fact that great consistency in the timing of the G1-S transitions is observed, yet inconsistency in proteolysis is also observed, suggests that consistency in the G1-S transition is primarily a consequence of CtrA~P dephosphorylation rather than proteolysis. However, CtrA~P has an extremely strong affinity for *Cori*, $K_d \approx 0.006$ μM [123], which suggests that extreme phosphatase activity would be required to clear CtrA~P from *Cori*. For example, If CtrA concentrations were half maximal (~15 μM), then 50% occupancy of *Cori* binding sites by CtrA~P would correspond to a 1:2500 ratio of CtrA~P to $CtrA_U$. While the threshold occupancy required to inhibit DNA replication is unclear, one study suggests that it may lie anywhere between 57% and 13% [191]. Thus, under prior conceptions of *Cori* regulation, this would imply that CckA phosphatase would consistently have to achieve a CtrA~P:$CtrA_U$ ratio of 1:2500 (and this is a modest estimate). Such an intense demand on CckA phosphatase seems far-fetched for three reasons. First, CckA is a bifunctional kinase/phosphatase, and it is unlikely that CckA could be

partitioned so completely towards the phosphatase form to result in such an extreme CtrA~P:$CtrA_U$ ratio. In agreement with this conclusion, evidence suggests that CckA kinase activity persists at significant levels at the G1-S transition [22]. Second, assuming a swarmer cell volume of 1 μm^3 [121], [126], [211], a concentration of 0.006 μM corresponds to 3 or 4 CtrA~P molecules per cell. However, there are five CtrA binding sites on *Cori*, each of which has two CtrA binding sequences (a total of 10 CtrA binding recognition sequences) [123], so the *Cori* binding sites would be less than half-occupied at 0.006 μM even if the binding were infinitely strong. In other words, the physiology of the *Cori* locus suggests that CtrA~P levels greater than 0.006 μM are required to saturate *Cori*. Third, if CtrA~P must be depleted to such low levels to clear *Cori*, we would likely observe highly stochastic timing of chromosome replication, especially considering the variability in the expression pattern of CtrA between experiments, as even one CtrA~P molecule would make a significant difference in *Cori* binding. However, as mentioned earlier, the initiation of chromosome replication seems to be quite tightly regulated.

The incongruences among these experimental observations merit a closer look into the regulation of CtrA and its interaction with *Cori*. In this paper, we build a mathematical model to simulate the interactions of CtrA at *Cori* site [d] (one of the five CtrA binding sites). We identify a new role for the unphosphorylated form of CtrA ($CtrA_U$) in the G1-S transition; specifically, we propose that $CtrA_U$ interacts with *Cori* (dubbed $CtrA_U$:*Cori* binding) to interfere with CtrA~P:*Cori* binding. Our simulations suggest that this competitive inhibition would substantially alleviate the demand on CckA phosphatase (by ~70 fold) at the G1-S transition. We extend our study by developing a detailed mathematical model of the *Caulobacter* cell cycle to investigate how the interaction of $CtrA_U$ with *Cori* might impact cell cycle progression. Our model suggests that the $CtrA_U$:*Cori* interaction (1) enables a more prompt entry into S phase, (2) ensures consistent timing of chromosome replication given variations in CtrA proteolysis rates, and (3) enhances the robustness of the cell cycle to various mutations.

4.3 Materials and Methods

4.3.1 General Simulation Methodology

All simulations and quantitative analysis were conducting with MATLAB R2019a utilizing customized scripts unless otherwise stated. Each cell cycle simulation was carried out utilizing

MATLAB's ode15s for 1600 simulated minutes. A full list of equations governing the cell cycle model are specified in Appendix B.1. In Chapter 3, we specify the biology and methodology behind the derivation of our cell cycle equations. As the vast majority of protein concentrations are unidentified in *Caulobacter*, we do not attempt to assign specific concentration units to each variable; The notable exceptions of CtrA and cdG, which do have experimentally measured concentrations.

4.3.2 Quantification and Statistical Analysis

All western blots retrieved from the literature were quantified utilizing ImageJ to produce normalized, quantitative data for protein expression levels over time. Simulations were determined to be arrested if the cell did not initiate chromosome replication or did not divide in the last 300 minutes of the simulation. All statistical analysis was performed utilizing built in MATLAB functions. The distribution of scores for each parameter set collection is plotted utilizing MATLAB's boxplot function (https://www.mathworks.com/help/stats/boxplot.html), which automatically calculates the median and interquartile range (IQR) while defining outliers as scores that deviate from the median by more than 1.5 times the IQR. We note that all parameter sets of each collection are included in simulating results, regardless of their score. For our analysis on the timing of cell cycle events (i.e. t^{cr} and t^{div}), we removed outliers utilizing the MATLAB function, rmoutliers (https://www.mathworks.com/help/matlab/ref/rmoutliers.html), which defines an outlier as any time point that is more than three scaled median absolute deviations from the median time. Standard deviations are calculated utilizing the MATLAB function, std (https://www.mathworks.com/help/matlab/ref/std.html).

4.4 Results

While CtrA~P is known to repress chromosome replication, how unphosphorylated CtrA fits into the regulatory picture is not clear. Mutant cells that express non-proteolizable CtrA from the *ctrA* locus, such as the *ctrAΔ3Ω* and the *ctrA*Δ3M2 strain, proceed normally through the cell cycle [210]. Thus, these strains seem to navigate the G1-S transition via dephosphorylation of CtrA. Siam and Marczynski (2000) studied the association of $CtrA_U$ and CtrA~P with the five *Cori* binding sites, [a-e], measuring K_d values of 0.2—0.6 μM for $CtrA_U$ and 0.003—0.015 μM for

CtrA~P, both of which are extremely low in comparison with typical CtrA expression levels which reach ~25 μM in pre-divisional cells and ~12.5 μM in swarmer cells [121], [126], [179], [211]. As CtrAΔ3Ω and CtrAΔ3M2 levels must be similar to WT CtrA expression levels in their respective mutants, since there are no observable differences in cell morphology or cell cycle timing, unphosphorylated CtrA should occupy *Cori* binding sites during the G1-S transition in *ctrAΔ3Ω* and *ctrA*Δ3M2 strains (for a more in depth discussion, see section 4.5). Thus, $CtrA_U$ must not impair chromosome replication when bound to *Cori*.

As discussed previously, we find it unlikely that CckA phosphatase could reduce CtrA~P to concentrations relevant to the experimentally measured dissociation constant in the absence of proteolysis. However, given that $CtrA_U$:*Cori* binding does not impair chromosome replication and that CckA phosphatase activity must somehow be sufficient for the G1-S transition in CtrA proteolysis-null mutants, we hypothesized that unphosphorylated CtrA competes with CtrA~P for *Cori* binding sites to promote chromosome replication. To investigate this hypothesis, we first created a detailed model for CtrA binding to *Cori* at site [d] (Figure 4.2A), based on the experiments of Siam and Marczynski (2000).

4.4.1 CtrA competes with CtrA~P for *Cori* binding sites.

CtrA recognizes the nucleic acid sequence TTAA. Each *Cori* binding site has two CtrA recognition sequences, characterized as TTAA-N7-TTAA. Mutation experiments on site [d] indicate that the affinity of a single CtrA molecule for a single *Cori* binding site is not affected by phosphorylation, but the cooperative binding of CtrA molecules to bipartite sites is affected by phosphorylation [123]. Figure 4.2A demonstrates the different possibilities of CtrA binding to a TTAA-N7-TTAA motif, and the corresponding equilibrium relationships. Note that we assume that the number of CtrA molecules bound to DNA relative to freely diffusing molecules is negligible, as justified in Chapter 3.1.6.

Using Siam and Marczynski's experiments on site [d] to parameterize our *Cori* binding model (see Chapter 3), the resulting model agrees quite well with their data (Figure 3.1). We find that the first binding step of CtrA molecules to site [d] is weak ($K_{d1} \approx 1.06$ μM) and independent of phosphorylation. In the scenario that the first occupant is $CtrA_U$, binding of a second molecule of $CtrA_U$ is weakly cooperative ($K_{d2} \approx 39$ nM); however if both occupants are CtrA~P, binding of the

second molecule is strongly cooperative ($K_{d3} \approx 0.085$ nM). That is to say, the level of cooperativity between CtrA~P molecules is ~460x stronger than between $CtrA_U$ molecules (K_{d2} vs. K_{d3}). As data was not available to determine the cooperativity between CtrA~P and $CtrA_U$ for bipartite sites, we assume that the cooperativity is equivalent to the binding between two $CtrA_U$ molecules (K_{d2}).

Although K_{d3} is significantly greater than K_{d2}, we proceed to investigate our hypothesis that $CtrA_U$ might compete with CtrA~P for *Cori* binding sites at the G1-S transition. Using a range of physiologically relevant concentrations of $CtrA_U$ and CtrA~P, we simulate the ratio of *Cori* site [d] that is associated with the states depicted in Figure 4.2A. The patterns of the resulting heat maps (Figure 4.2B) show that the concentration of *Cori* site [d] saturated by CtrA~P, [DNA:CtrA~P_2], decreases as the concentration of $CtrA_U$ increases. Meanwhile, the concentration of $CtrA_U$ bound DNA, [DNA:$CtrA_{U2}$], increases; The concentrations of the other forms (e.g. [DNA:CtrA~P:$CtrA_U$]) are negligible. These results support our hypothesis that CtrA can displace CtrA~P at *Cori* binding sites at physiologically relevant concentrations.

To further investigate how the ratio of $CtrA_U$ to CtrA~P, [$CtrA_U$]:[CtrA~P], impacts *Cori*, we simulate site [d] binding over a range of CtrA~P concentrations ([CtrA~P]) while holding the ratio constant (Figure 4.2C, left panel). We find that [DNA:CtrA~P_2] is relatively independent of [CtrA~P] but is highly dependent on [$CtrA_U$]:[CtrA~P]. This statement remains true until concentrations of CtrA~P are very low (< 0.02 μM), at which point *Cori* is rapidly freed from CtrA binding. This result is consistent with the patterns in Figure 4.2B, as the shading is relatively constant when moving away from the graph origin in a radial direction. This behavior emphasizes the importance of $CtrA_U$:*Cori* binding. While decreasing CtrA~P concentration (short of complete depletion) has a negligible impact on CtrA~P binding to *Cori*, adjusting the $CtrA_U$:CtrA~P ratio has a large effect, due to the competition between $CtrA_U$ and CtrA~P for *Cori* binding sites.

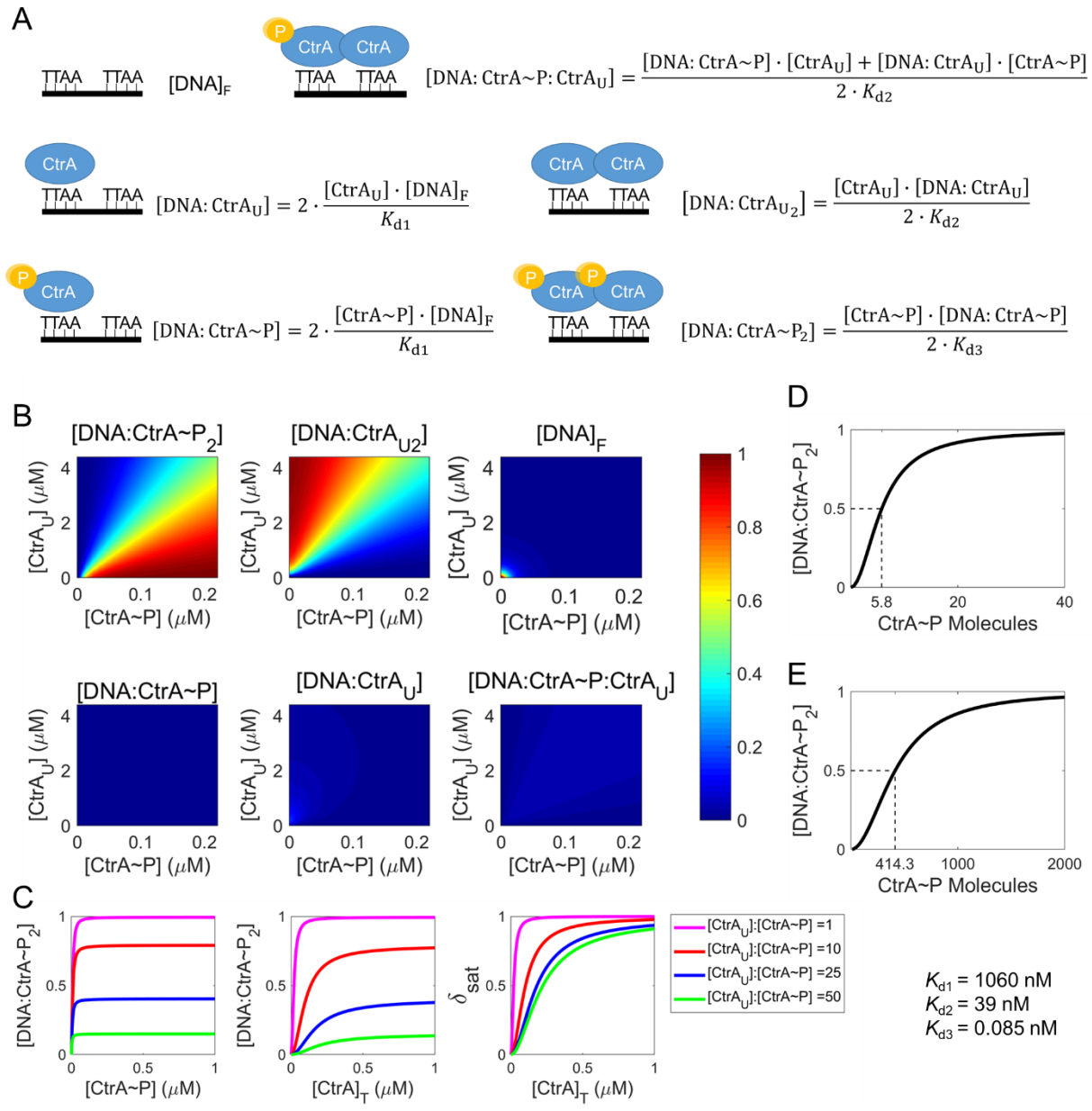

Figure 4.2) Unphosphorylated CtrA competes with CtrA~P for Cori binding sites.
(A) CtrA (unphosphorylated) and CtrA~P bind to Cori site [d] in different combinations. Each combination (or state) is defined by an equilibrium expression, and the sum of all the different occupation states of *Cori* = $[DNA]_T$ = 1 (by definition). Estimated values for the dissociation constants are presented in the lower-right corner.
(B) The probability of each possible state (from A) was calculated over a range of concentrations, $[CtrA_U]$ and [CtrA~P]. Results are represented by a heat map, where the color corresponds to the fractional occupancy of the state, as depicted by the color bar on the right.
(C) $[DNA:CtrA\sim P_2]$ is a function of the $[CtrA_U]$:[CtrA~P] ratio and the concentration of <u>all</u> CtrA species (unphosphorylated and phosphorylated), $[CtrA]_T = [CtrA_U] + [CtrA\sim P]$. δ_{sat} reflects the current concentration of $DNA:CtrA\sim P_2$ divided by the maximum level possible at the given $[CtrA_U]$:[CtrA~P].
(D) Simulation of the $[DNA:CtrA\sim P_2]$ state as a function of CtrA~P molecules per cell when all CtrA molecules are phosphorylated. Assumed volume of cell is 1 μm^3.
(E) Simulation of $[DNA:CtrA\sim P_2]$ as a function of CtrA~P molecules per cell when unphosphorylated CtrA

molecules are present. In these calculations, $[CtrA]_T$ = 15 μM. For an assumed volume of cell of 1 μm^3, the number of unphosphorylated CtrA molecules = 10,000 – number of CtrA~P molecules.

Next, we compare how [DNA:CtrA~P_2] depends on total CtrA levels ($[CtrA]_T$) at several fixed [$CtrA_U$]:[CtrA~P] ratios (Figure 4.2C middle panel). Similar to the [DNA:CtrA~P_2] vs [CtrA~P] curve (Figure 4.2C left panel), [DNA:CtrA~P_2] saturates with increasing $[CtrA]_T$, and the saturation limit (or maximum) of [DNA:CtrA~P_2] decreases as [$CtrA_U$]:[CtrA~P] increases. However, we find that the [DNA:CtrA~P_2] curve begins to deviate significantly from the maximum [DNA:CtrA~P_2] at higher $[CtrA]_T$ concentrations when [$CtrA_U$]:[CtrA~P] is higher. The observed drop-off in [DNA:CtrA~P_2] is due to the fact that [CtrA~P] reaches very low levels (< 0.02 μM) more quickly at higher ratios of $CtrA_U$ to CtrA~P. However, correct interpretation of these curves is difficult by the fact that the maximum value of [DNA:CtrA~P_2] depends on the [$CtrA_U$]:[CtrA~P] ratio. To resolve this complication, we define a new metric, δ_{sat}, which measures [DNA:CtrA~P_2] relative to the maximum [DNA:CtrA~P_2] for a given [$CtrA_U$]:[CtrA~P] ratio:

$$\delta_{\mathrm{sat}} = \frac{[\mathrm{DNA{:}\ CtrA{\sim}P_2}]}{\max\left([\mathrm{DNA{:}\ CtrA{\sim}P_2}]\right)}$$

where max([DNA:CtrA~P_2]) is the limiting concentration of DNA:CtrA~P_2 at sufficiently large $[CtrA]_T$ and fixed [$CtrA_U$]:[CtrA~P] ratio. We estimate the max([DNA:CtrA~P_2]) by calculating [DNA:CtrA~P_2] when $[CtrA]_T$ = 100 μM. The δ_{sat} vs $[CtrA]_T$ curve (Figure 4.2C right panel) clearly shows that, as $[CtrA]_T$ decreases, CtrA~P saturation of *Cori* binding sites (relative to the maximum possible saturation) is cleared at a faster rate at higher [$CtrA_U$]:[CtrA~P] ratios. Given that max([DNA:CtrA~P_2]) is also much lower at higher ratios, there is a clear synergy between proteolysis and dephosphorylation in determining CtrA~P binding to *Cori*.

Next, we compare our results to those of Siam and Marczynski, who estimated dissociation constants by fitting hyperbolic curves, i.e., $K_d/(K_d + [CtrA])$, to their experimental data. As mentioned, they estimated that CtrA~P interacts with site [d] with K_d = 0.006 μM, which translates to 3 - 4 CtrA~P molecules per cell, given a cell volume of 1 μm^3. The estimation produced by our model is very similar when $CtrA_U$ is absent, suggesting that site [d] is 50% saturated by CtrA~P at concentrations corresponding to approximately 6-12 molecules per cell (Figure 4.2D and Figure S2). However, when we fix $[CtrA]_T$ = 15 μM = 10^4 molecules per cell, and vary CtrA~P level (Figure 4.2E), we find that site [d] is ~50% occupied at CtrA~P ≈ 414 molecules per cell (~0.7

μM). This translates to a CtrA~P:$CtrA_U$ ratio of approximately 1:20, which seems far more achievable for the bifunctional CckA kinase/ phosphatase than the ratio of 1:2500 estimated earlier.

4.4.2 Caulobacter Cell Cycle Model

In consideration of our findings in the previous section, we now investigate the potential roles of $CtrA_U$:*Cori* binding on cell cycle progression in *C. crescentus*. Inspired by earlier computational models of Li et al., 2009 and Subramanian et al., 2013, we develop a new mathematical model, based on ordinary differential equations (ODEs), to capture the dynamics of the molecular mechanism governing progression through the *Caulobacter* cell cycle. As with Li's model, our model encompasses protein-protein interactions, protein phosphorylation, DNA methylation, protein-DNA interactions, genetic expression, proteolysis, cytokinesis, and chromosome replication. We also introduce bifunctionality to the histidine kinase/phosphatase enzymes, PleC and CckA, as was done previously by Subramanian. We improve the model's representation of CtrA degradation by adding important molecular components, most notably the second-messenger molecule, cdG, which is an essential component to the CtrA proteolysis complex and interacts with CckA to induce its phosphatase state. Figure 4.3 details the regulatory interactions of the model. For a full description of the model, see Chapter 3.

In light of the experimental diversity of CtrA expression (Figure 4.1B), we study two different parameterizations of our model: a "SLOW" parameter set, characterized by sluggish CtrA proteolysis extending well into S phase (Figure 4.4A, top panel), and a "QUICK" parameter set, characterized by rapid proteolysis of CtrA at the G1-S transition (Figure 4.4B, top panel). These parameter sets were optimized by fitting simulations of seventeen variables (Table 3.4) to time-course data for wild-type (WT) swarmer cells, plotted in Figure 4.4A and B and Figure B.1A and B.2A, and to the phenotypes (viable or arrested) of swarmer and stalked cells in a collection of 11 mutant strains (red font in Figure 4.5A). Using the fitting procedure explained in Chapter 3, we obtained 918 and 1,151 sets of SLOW and QUICK parameters, respectively. In Figure 4.4, we plot the range of time courses predicted by 100 randomly selected parameter sets in each case, to show how well the model agrees with experimental observations of WT swarmer cells.

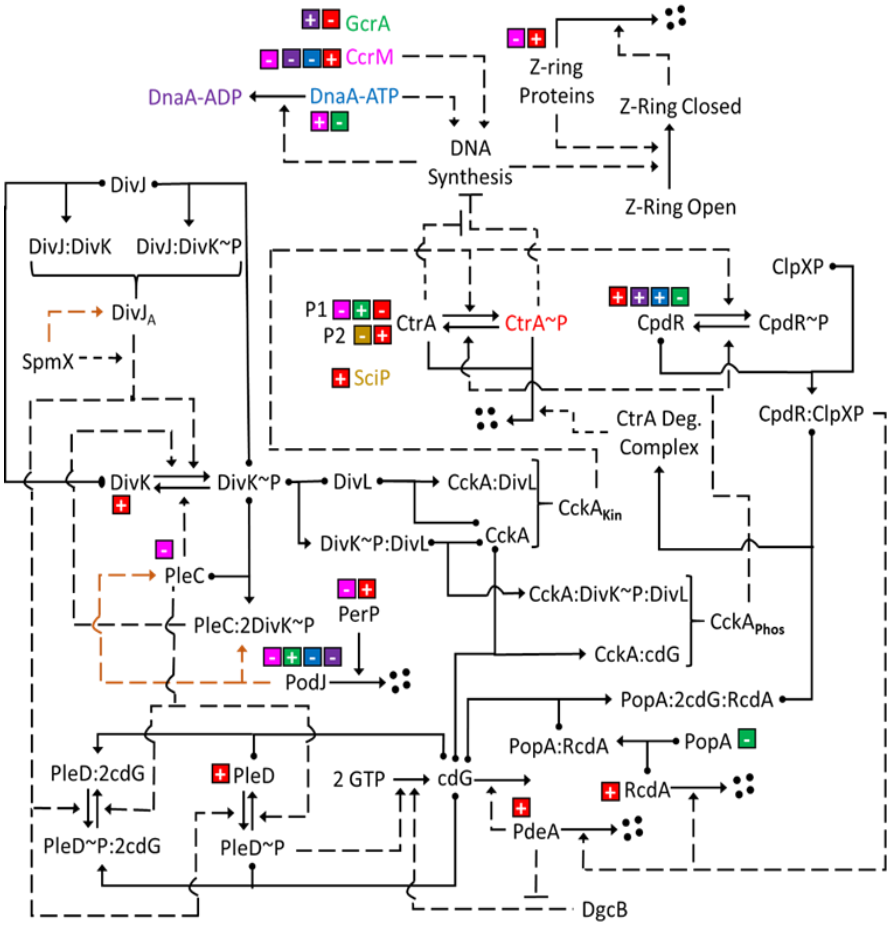

Figure 4.3) Wiring diagram of the molecular mechanisms underlying the cell cycle model of C. crescentus. Genetic regulation is depicted by a color-coded scheme: for each protein that interacts with a promoter, a box with a plus or minus sign indicates whether the protein activates or inhibits expression of the gene, and the color of the box identifies the regulatory protein (e.g., green = GcrA). Proteins that combine to form complexes are marked by solid dots on the arms of a T-shaped arrow pointing to the resulting complex (e.g., PopA and RcdA form the PopA:RcdA complex). The chemical conversion of one molecular species to another is indicated by an arrow (e.g., CtrA to CtrA~P). Proteolysis is depicted by an arrow from a protein to four black circles. Dashed arrows indicate an 'influence' (e.g., catalysis) of a protein on a chemical reaction (e.g., PleC dephosphorylates DivK~P). A dashed orange arrow indicates that one molecule influences the localization of another (e.g., PodJ affects the location of PleC).

To assess the predictive power of our model, we simulated swarmer and stalked phenotypes for 23 additional mutant strains (black font in Figure 4.5A) and evaluated whether our model correctly predicts the cell cycle to be viable or arrested. Details of each mutant strain are found in Table B.2. Figure 4.5A reports the fraction of failed simulations for each mutant strain. Considering simulations that fail less than 25% of the time to be successful predictions, we find that the QUICK and SLOW parameter sets perform equally well (88.6% success rate in Figure 4.5B).

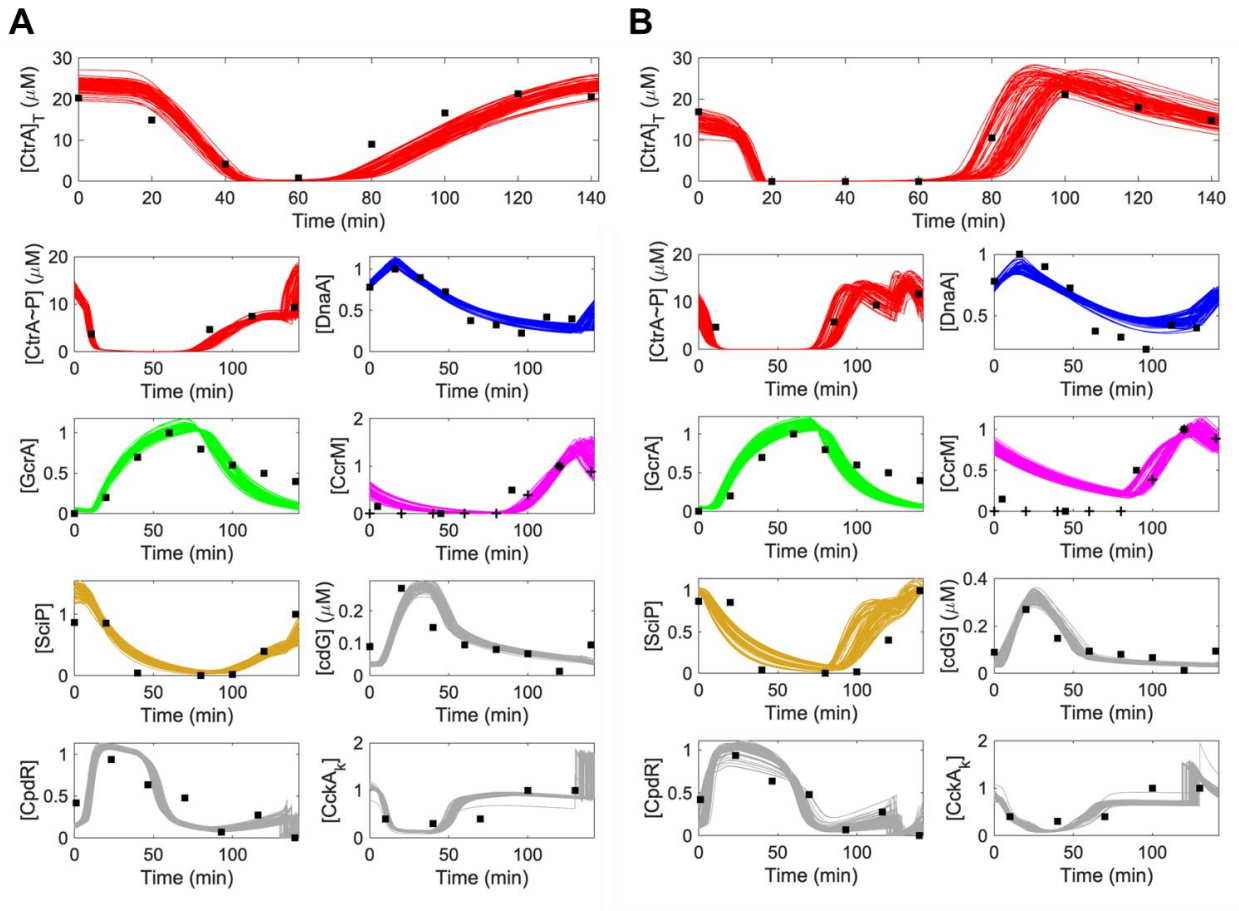

Figure 4.4) SLOW and QUICK swarmer cell simulations fit experimental data well.
(A) For 100 randomly selected SLOW parameter sets, we plot swarmer-cell simulations in comparison to experimental data, using the same color code as in Figure 4.3. The large spikes in [$CckA_K$] and [CpdR] near the end of the cell cycle (when the Z-ring closes) are artifacts of our modeling methodology (see Chapter 3 for details). Data collected as follows: [$CckA_K$]: Jacobs et al. 2003, Fig 3A; [CpdR]: Iniesta et al. 2006, Fig 5A; [cdG]: Abel et al. 2013, Fig 7; [SciP]: Tan et al. 2010, Fig 1B; [CcrM]:+, Zhou and Shapiro 2018, Fig 2A; [CcrM]: ■, Grunenfelder et al. 2001, Fig 2; [GcrA]: Holtzendorff et al. 2004, Fig 3B; [DnaA]: Cheng and Keiler 2009, Fig 2C; [CtrA~P]: Jacobs et al. 2003, Fig 3A; [$CtrA]_T$: Mcgrath et al. 2006, Fig 2C. In all plots except [cdG], [$CtrA]_T$ and [CtrA~P], concentrations are unitless and normalized to the experimental data, which predict relative concentrations at each time point are normalized to one. [$CtrA]_T$ and [CtrA~P] experimental data are also unitless, however absolute CtrA concentrations in our model are a prediction and therefore the data is normalized to the simulation output. cdG levels are not normalized in any way, as absolute concentration is quantified from the source of the data.
(B) Same as (A), for 100 QUICK parameter sets. Experimental data are the same, except for [$CtrA]_T$ acquired from Collier et al. 2006, Fig 5A.

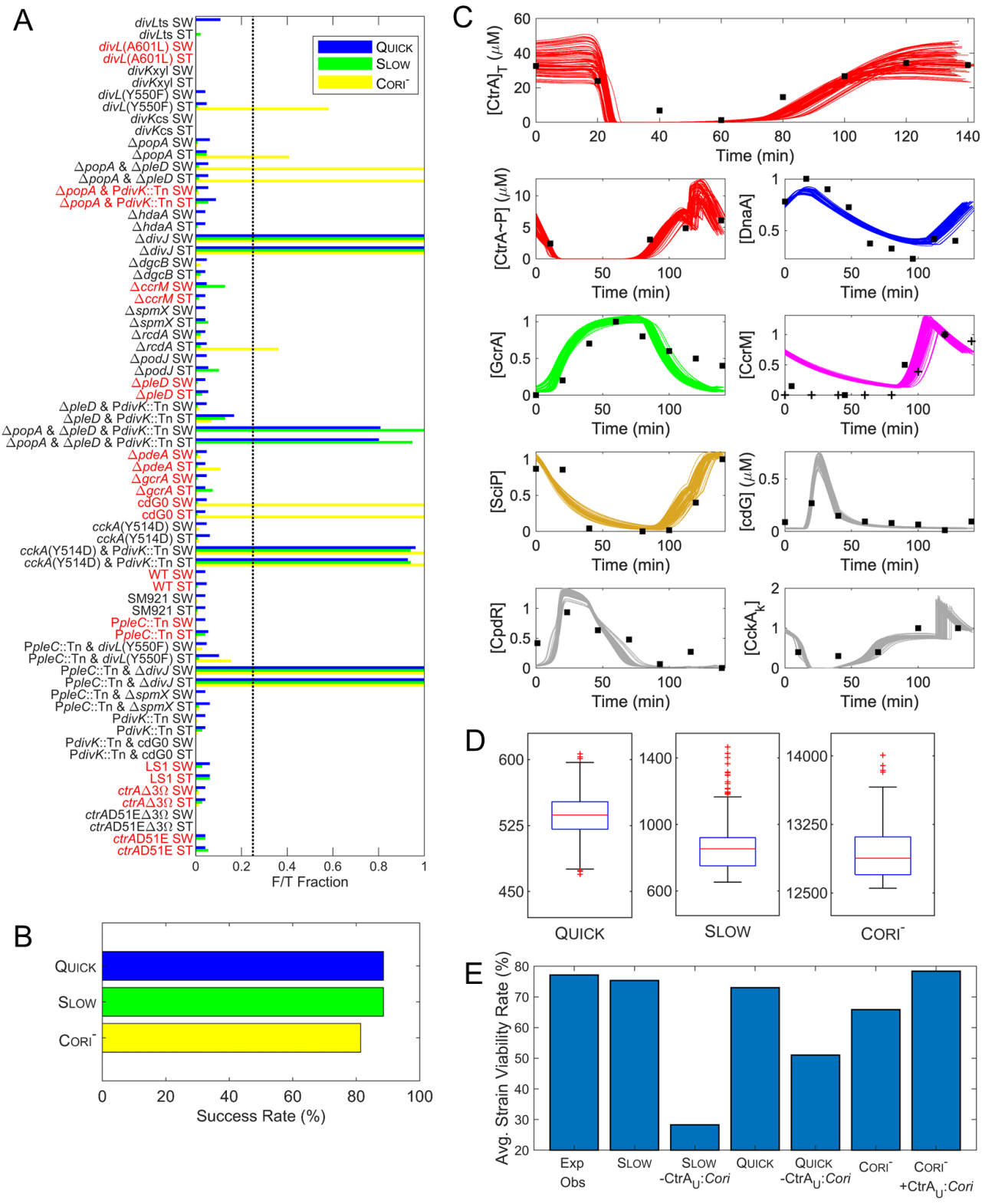

Figure 4.5) Parameter sets agree well with experimentally observed strain viability.
(A) The fraction of total simulations that failed (F/T fraction) is plotted for each mutant case. A simulation is considered to have 'failed' if it predicts cell cycle arrest when experimental observations report a viable cell cycle,

or vice versa. See Table B.2 for details on mutant simulations. For each mutant, 150 parameter sets were chosen at random from each parameter set collection and simulated for both swarmer cell (SW) and stalked cell (ST). The yellow bar corresponds to an arbitrary threshold (25%) that we use to compute the success rate of strain for the QUICK, SLOW and CORI⁻ parameter sets. Strains labeled with red font were included in the parameterization cost function.
(B) QUICK and SLOW parameter sets successfully capture strain viability behavior in ~88.6% of all simulated strains. CORI⁻ parameter sets successfully capture strain viability behavior in ~81.4% of all simulated strains. A strain simulation is considered successful if 75% or more of simulations agree with experimental observations on cell cycle arrest behavior.
(C) Plot of 100 swarmer cell simulations from the CORI⁻ parameter sets. Experimental data and methodology is the same as Figure 4.4A.
(D) Box plot of cost distribution for each parameter set collection. Red horizontal line indicates median, blue box indicates the interquartile range (IQR), whiskers are set to 1.5xIQR and outliers are indicated by red '+' markers. We note that the range of the x-axis of SLOW and CORI⁻ boxplots hide some outliers to enhance visibility. The greatest costing outliers are ~3,600 and ~15,700 for the SLOW and CORI⁻ parameter sets, respectively. Medians values are approximately 540, 850, and 12,900 for the QUICK, SLOW and CORI⁻ parameter sets, respectively.
(E) The average strain viability rate is calculated as the sum of all viable simulations divided by the total number of simulations for each strain in (A). Simulations were run with and without the :$CtrA_U$:*Cori* interaction as indicated. The fraction of strains that are reported as viable experimentally (Exp Obs) is reported for comparison.

4.4.3 Unphosphorylated CtrA interacts with *Cori* to ensure timely initiation of chromosome replication

To investigate the impact of $CtrA_U$:*Cori* binding on cell cycle progression, we examine the effects of removing the $CtrA_U$:Cori interaction from WT cells (referred to as a "WT -$CtrA_U$:*Cori*" simulation). First, we observe significant differences in the timing of chromosome replication (t^{cr}) between our WT and WT -$CtrA_U$:*Cori* simulations (Figure 4.6A&C). SLOW and QUICK parameter sets predict average delays (Δt^{cr}) of approximately 23 and 2 minutes, respectively. These delays indicate that $CtrA_U$:*Cori* binding facilitates a more rapid G1-S transition. In consideration that the t^{cr} of WT simulations is relatively consistent between SLOW and QUICK parameter sets (Figure 4.6A), the significant difference in Δt^{cr} between these parameter sets suggests that without $CtrA_U$:*Cori* binding, the timing of the G1-S transition is highly dependent on the rate of proteolysis of CtrA. As we demonstrated earlier (Figure 4.2), *Cori* occupancy by CtrA~P is dramatically affected by competitive inhibition from $CtrA_U$. Therefore, it is likely that CckA phosphatase activity is insufficient to deplete CtrA~P to the minute concentrations required to initiate chromosome replication in the absence of $CtrA_U$:*Cori* binding.

With these results in mind, we investigate how the $CtrA_U$:*Cori* interaction influences timing of chromosome replication in the event that proteolysis is slowed down. Adjusting the rate of proteolysis in the QUICK parameter sets makes very little difference in t^{cr} in WT simulations (Figure 4.6D). However, in the WT - $CtrA_U$:*Cori* simulations, t^{cr} increases substantially as the

proteolysis rate decreases. This suggests that $CtrA_U$:*Cori* binding stabilizes the timing of chromosome replication when proteolysis is perturbed.

Next, we investigate the timing of cell division (t^{div}) of WT and WT - $CtrA_U$:*Cori* simulations. We find that SLOW and QUICK parameter sets predict average delays (Δt^{div}) of approximately 15 and 0.53 minutes, respectively (Figure 4.6C). The fact that delays in cell division are not equivalent to delays in chromosome replication (Δt^{cr}) suggests that delays in the G1-S transition can be partially compensated in the S and G2 stages of the cell cycle. Upon inspection, we found that no single interaction of the model is responsible for this compensation, and we attribute it to synergies within the molecular mechanism driving cell cycle progression and its inherent robustness.

Given that perturbing $CtrA_U$:*Cori* binding results in heightened dependency of t^{cr} on the CtrA proteolysis rate, we speculate that removing $CtrA_U$:*Cori* interactions will induce G1 arrest in mutants that impair CtrA proteolysis. To evaluate this hypothesis, we simulate each mutant strain without $CtrA_U$:*Cori* binding and calculate strain-specific viability and the average viability of all strains (Figure 5E). While normal SLOW and QUICK simulations have average strain viability rates of 75% and 73%, respectively, removal of $CtrA_U$:*Cori* binding results in average strain viability rates of 28% and 51%, respectively. Thus, our simulations suggest that $CtrA_U$:*Cori* binding contributes significantly to mutant strain viability. Closer inspection (Table B.3 and B.4) reveals that cell cycle arrest is consistently induced in mutant strains that directly influence CtrA proteolysis, such as Δ*popA*, *ctrA*Δ3Ω and cdG^0 (a mutant strain depleted of cdG). However, the SLOW parameters also exhibit cell cycle arrest in several mutants that do not directly influence CtrA proteolysis, such as Δ*pleD* and P*pleC*:Tn. Further investigation revealed that these mutants influence CtrA proteolysis indirectly, resulting in G1 arrest (Table B.3 and B.4). The observation that QUICK - $CtrA_U$:*Cori* simulations are more stable than SLOW - $CtrA_U$:*Cori* simulations is likely a consequence of a more robust CtrA proteolysis response in QUICK parameter sets. Overall, these results suggest that the $CtrA_U$:*Cori* interaction makes the cell cycle more robust to mutations that influence proteolysis, both directly and indirectly, and therefore contributes to the stability of the cell cycle control mechanism.

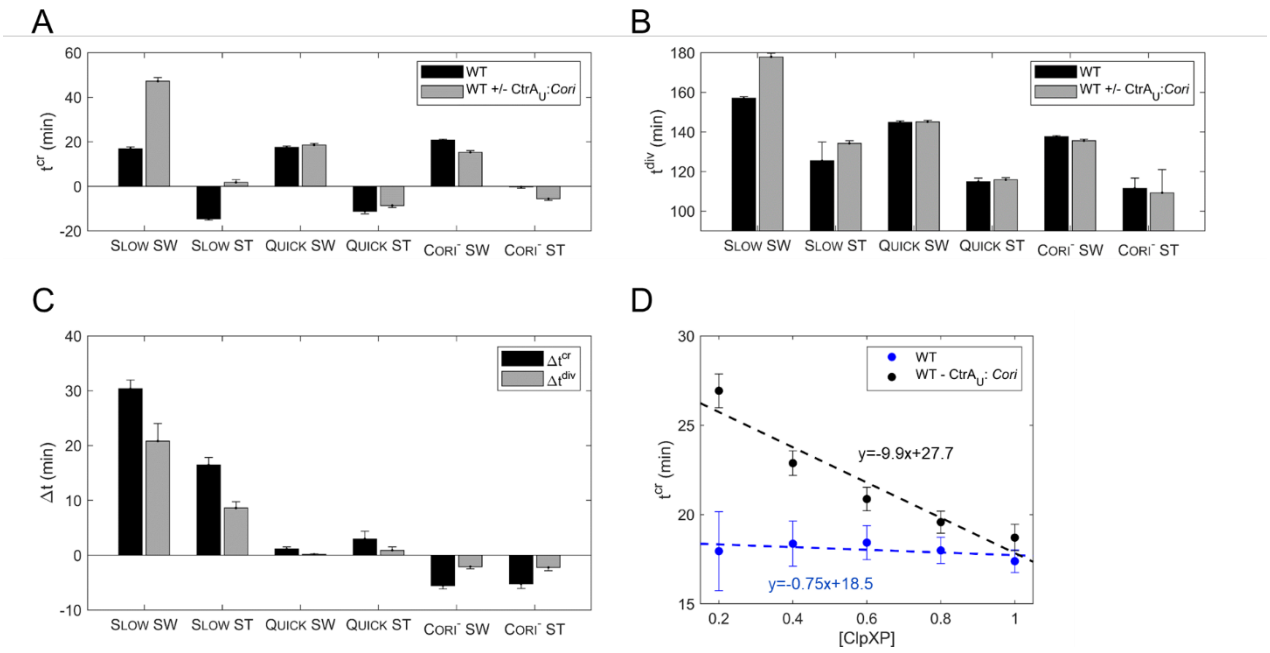

Figure 4.6) Chromosome replication and cell division times are influenced by the interaction of unphosphorylated CtrA with Cori binding sites.
(A and B) Bar graphs report the average time from cell division to the initiation of chromosome replication (t^{cr}) and to cell division (t^{div}) in simulations of WT cells, with and without the CtrA$_U$:*Cori* interaction. Grey bars represent WT – CtrA$_U$:*Cori* for SLOW and QUICK parameter sets and represent WT + CtrA$_U$:*Cori* for CORI⁻ parameter sets. t^{cr} and t^{div} are calculated as the time difference between the end of the previous cell cycle and the corresponding event time. Negative times for t^{cr} indicates that chromosome replication begins after the Z-ring closes but before the daughter cells separate. The error bars indicate standard deviations.
(C) For each cell we compare the WT and WT +/- CtrA$_U$:*Cori* simulations (as indicated in A and B) and plot the average differences in chromosome replication time and cell division. Error bars indicate the standard deviations.
(D) Timing of chromosome replication was recorded for 150 random QUICK parameter sets under different ClpXP activity levels for WT and WT - CtrA$_U$:*Cori* simulations. [ClpXP] = 1 represents the basal level in simulations of WT cells. Simulations were performed by adjusting $k_{d,CtrA1}$ in accordance with the basal ClpXP activity. Dashed lines and corresponding equations illustrate the line of best fit for the simulated data points. Error bars indicate the standard deviation in t^{cr} of each simulation.

4.4.4 Parameter sets tuned without the CtrA$_U$:*Cori* interaction alleviate high rates of cell cycle arrest but deviate from experimental observations

As CtrA$_U$:*Cori* binding makes a significant difference for the timing of chromosome replication and the stability of the G1-S transition in QUICK and SLOW mutant strain simulations, we decided to investigate how the model might behave if we parameterized it without CtrA$_U$:*Cori* binding. Thus, we created a new collection of parameter sets, dubbed the CORI⁻ parameter sets, that are selected with the same cost function as the SLOW parameter sets but without the CtrA$_U$:*Cori*

interaction. In Figure 4.5C, we plot simulations of WT swarmer cells using 100 parameter sets randomly chosen from the CORI⁻ collection. We find that, while the CORI⁻ parameter sets fit the experimental data reasonably well, the cost of CORI⁻ parameter sets are ~10 to 30 times higher than the cost of QUICK and SLOW parameter sets (Figure 4.5D). Indeed investigation of CORI⁻ simulations reveal some unusual characteristics.

First, we observe that the CORI⁻ parameter sets express high levels of total CtrA, with an average peak concentration of 36 μM in swarmer simulations (Figure 4.5C and B.4A). In comparison, SLOW and QUICK parameter sets have an average swarmer cell peak of 24 μM and 25 μM, respectively (Figures 4.4A,4.4B and B.4A). As experimental observations report peak CtrA levels approaching 20-30 μM [126], CORI⁻ parameter sets do not perform quite as well as the SLOW and QUICK parameter sets, especially when considering that the cost function's targeted peak concentration for $[CtrA]_T$ was 25 μM for swarmer cell simulations. While SLOW and QUICK parameter sets, on average, come within 1 μM of the targeted concentration, the average CORI⁻ simulation is approximately 11 μM (~44%) higher than the target concentration. Despite having higher total CtrA levels, CtrA~P concentrations are lower in CORI⁻ simulations than in QUICK and SLOW simulations (Figure B.4B). These discrepancies suggest that the CORI⁻ parameter sets struggle to sufficiently phosphorylate CtrA, and therefore require exaggerated expression of total CtrA to increase the levels of CtrA~P. If true, this would suggest that phosphatase activity of the bifunctional CckA kinase/phosphatase is overly emphasized in CORI⁻ parameter sets. This concern is validated by two observations. (1) Comparing parameter values among the three parameter set collections (Table B.1), we find that the activity of CckA phosphatase on CtrA~P is far stronger (by 4- to 8-fold) in the CORI⁻ parameter sets than in the QUICK and SLOW parameter sets. (2) The level of CckA kinase, i.e., $[CckA_K]$, is completely depleted at the G1-S transition in CORI⁻ simulations (Fig. 6B), which contradicts experimental observations(Figure 4.5C). In contrast, QUICK and SLOW simulations show detectable levels of $[CckA_K]$ throughout the G1-S transition (Figure 4.4A&B).

We further observe that CORI⁻ simulations exhibit an intense spike in cdG at the G1-S transition, with an average peak of 0.67 μM in swarmer cell simulations (Figure 4.5C and Figure B.4D). In contrast, QUICK and SLOW parameter sets have average swarmer simulation peaks of 0.32 μM and 0.28 μM at the G1-S transition, respectively (Figure 4.4A&B and Figure B.4D). As swarmer cell

peak cdG concentrations reach approximately 0.27 μM at the G1-S transition [161], it is clear that CORI⁻ parameter sets over emphasize cdG synthesis.

The last discrepancy we observe is that the concentration of CtrA ($[CtrA]_T$) depletes far faster in the CORI⁻ simulations than in the SLOW simulations (Figure 4.5C vs. Figure 4.4A), despite being parameterized against the same experimental data. We conclude that this is a consequence of the dramatic cdG response in CORI⁻ parameter sets, which results in extreme partitioning of CckA towards the phosphatase state, causing rapid accumulation of unphosphorylated CpdR (the active form of CpdR [133]). As levels of RcdA and PopA are already sufficiently high in G1 (Figure B.3), the exaggerated synthesis of cdG in CORI⁻ simulations results in rapid accumulation of the CtrA degradation complex (Figure 4.3 & Figure B.3) and speedy proteolysis of CtrA.

Next we investigate the performance of CORI⁻ parameter sets on mutant strains. We find that 81% of simulated strains agree with experimentally observed behavior on cell cycle viability (Figure 4.5B). In comparison, SLOW parameter sets had an 89% success rate. Notably, virtually all of the CORI⁻ parameter sets predict cell cycle arrest of the cdG^0 mutant (Figure 4.5A), i.e. cells that lack cdG. As cdG^0 is a penalized strain of the cost function (see Chapter 3), this indicates that the large penalty associated with cell cycle arrest in cdG^0 simulations is less than the penalty would be if the cell cycle was not dependent on cdG in CORI⁻ parameter sets. In other words, cdG acts as an essential crutch to compensate for the absence of the $CtrA_U$:*Cori* interaction in CORI⁻ parameter sets. Additional investigation of Δ*rcdA* and Δ*popA* (Figure 4.5A), suggests that, when CtrA proteolysis is impaired, the CORI⁻ parameter sets have difficulty (failure rates > 25%) simulating the cell cycle of stalked cells but not of swarmer cells. Moreover, for the Δ*popA* & Δ*pleD* strain, the CORI⁻ parameter sets fail completely (100%) for both swarmer and stalked simulations. We conclude that, when proteolysis is impaired, the G1-S transition of CORI⁻ simulations depends on excessive cdG synthesis (via PleD) to induce a dramatic CckA phosphatase response to sufficiently dephosphorylate CtrA.

In summary, the same parameterization algorithm that provided high-quality parameter sets for the QUICK and SLOW collections was unable to train the model to fit all of the biological constraints when the $CtrA_U$:*Cori* interaction was removed. The incongruencies between experimental observations and CORI⁻ simulations point to a dependency on a supraphysiological shift in the ratio of CckA kinase to CckA phosphatase to sufficiently deplete CtrA~P at the G1-S transition. This

result supports our previous conclusion that the competition between $CtrA_U$ and CtrA~P for *Cori* binding sites is an essential interaction for robust regulation of the G1-S transition.

4.4.5 Introducing $CtrA_U$:*Cori* interactions improves the behavior of CORI$^-$ simulations

We extend our study by introducing the $CtrA_U$:*Cori* interaction to the CORI$^-$ parameter sets, and find that the interaction increases overall strain viability from 66.8% to 78.4% (Figure 4.5E). Closer investigation reveals that adding the $CtrA_U$:*Cori* interaction to CORI$^-$ simulations results in 100% cdG^0 rescue from G1 arrest. We further find that the previously mentioned strains, Δ*rcdA,* Δ*popA* and Δ*popA* & Δ*pleD* are all rescued from G1 arrest as well (Table B.5). These results support our previous findings, that the $CtrA_U$:*Cori* interaction makes a significant contribution towards the robustness of the G1-S transition. Because the CORI$^-$ parameter sets were parameterized without the $CtrA_U$:*Cori* interaction, the fact that these results agree with our previous findings indicates that our results are unlikely to be a consequence of parameter choice but are a consequence of the fundamental biology.

Next, we evaluate the timing of chromosome replication in CORI$^-$ simulations with the addition of $CtrA_U$:*Cori* (Figure 4.6A&C). We find that chromosome replication begins approximately 5-6 minutes earlier in the presence of $CtrA_U$:*Cori* binding than in its absence. The cell cycle was also ~2 minutes shorter in CORI$^-$ + $CtrA_U$:*Cori* simulations (Figure 4.6B&C). These results also agree with our findings from the QUICK and SLOW parameter sets, that the $CtrA_U$:*Cori* interaction enables an earlier transition into S phase and a quicker cell cycle; however, the difference in cell cycle times is not as large as the difference in G1 times ($\Delta t^{div} < \Delta t^{cr}$).

4.5 Discussion

The chromosome origin of replication in *Caulobacter crescentus*, *Cori*, is highly regulated (Figure 4.7). CcrM methylates *Cori* at five sites to enhance activity [116], [217] while DnaA-ATP interacts with two moderately strong ‘G’ boxes and five weak ‘W’ boxes to unwind DNA and recruit other proteins (e.g. helicase) to initiate chromosome replication [191]. Meanwhile, CtrA~P inhibits chromosome replication by binding to five sites, [a]-[e] [192]. While *Cori* regulation is relatively well studied, how unphosphorylated CtrA affects *Cori* activity has not gathered much attention. Utilizing a mathematical model, trained by experimental data, we demonstrate that $CtrA_U$ can

interact with *Cori* binding site [d] to displace CtrA~P at physiologically relevant concentrations. Given that CtrA binding dynamics at sites [c] and [e] are very similar site to [d], our results for site [d] should apply to sites [c] and [e] as well. Binding to site [a] and [b] are a bit different, as CtrA~P interacts cooperatively between these two binding sites. However, an 'ab' mutation separating sites [a] from [b] by 14 bp disrupts this cooperativity and reveals that site [b] has very similar binding dynamics as sites [c]-[e], while binding at site [a] was not detectable. Indeed, sites [b]-[e] all match the TTAA-N7-TTAA consensus, while site [a] differs by 1bp [123]. These facts suggest that binding dynamics at site [b]-[e] are very similar and CtrA binding at site [a] is dependent on the binding dynamics of site [b]. Thus, our findings that $CtrA_U$ disrupts CtrA~P binding at site [d] also implies that it disrupts CtrA~P binding at all *Cori* binding sites.

What then is the significance of this interaction? One scenario to consider is that *Cori* activity is identical when bound by $CtrA_U$ as when bound by CtrA~P, attributing no significance to this interaction. The alternative scenario is that $CtrA_U$ bound *Cori* is substantially more active than CtrA~P bound *Cori*, which would attribute great significance to this competitive interaction. From an evolutionary perspective, it seems highly unlikely to us that *Caulobacter* would have evolved to have two forms of a master regulator compete for *Cori* binding sites with no regulatory significance. When considering the collective *Caulobacter* literature, we raise four main points that cumulatively suggests that $CtrA_U$ does not impair chromosome replication. 1) CtrAU binds very strongly to Cori ($K_d \approx$ 0.5-0.6 µM) when compared to typical CtrA expression levels of approximately 10-15 µM in swarmer cells [123], [126]. 2) Mutant strains expressing non-proteolizable CtrA from the ctrA locus (i.e. *ctrA*Δ3Ω, *ctrA*Δ3M2 and *ctrA*DD) demonstrate relatively constant CtrA levels throughout the cell cycle and exhibit normal cell morphology and timing of chromosome replication [210]. This suggests that these cells express CtrA at levels comparable to WT cells (~20-30 µM) and that they navigate the G1-S transition via dephosphorylation of CtrA. 3) A study investigating the mutant strain, PxylX::*ctrA*Δ3Ω, which overexpresses CtrAΔ3Ω from a xylose induced promoter, were slightly filamentous and had slower cell cycles than WT. However, flow cytometry revealed that the distribution of cells exhibiting 1 and 2 chromosomes was indistinguishable from pXylX::*ctrA* cells (which express WT CtrA from a plasmid promoter and have no morphological defects). In comparison, PxylX::*ctrAD51E*Δ3Ω cells are extremely filamentous and have an extreme bias of cells with only 1 chromosome, showing clear G1 arrest. CtrAD51EΔ3Ω is the conjunction of two CtrA site

mutations [210]. The "Δ3Ω" portion details that it is non-proteolizable while the "D51E" portion details that it is a form of CtrA that is cannot be phosphorylated, yet behaves like active CtrA. Importantly, although behaving like CtrA~P, CtrAD51E was shown to bind with similar affinity to $CtrA_U$ to *Cori* binding sites [124]. Thus, it is fair to conclude that PxylX::*ctrAD51E*Δ3Ω and PxylX::*ctrA*Δ3Ω should have similar CtrA expression levels and similar affinities for *Cori* binding, however the "active" behavior of CtrAD51E leads to G1 arrest while CtrAΔ3Ω does not inhibit chromosome replication as it can be dephosphorylated at the G1-S transition. We note that an additional study also investigated PxylX::*ctrA*Δ3Ω, demonstrating more severe elongation with slightly more cells containing 1 chromosome than 2. However, this study also showed that a significant fraction of cells also exhibited 3 or 4 chromosomes per cell. From these two studies, we conclude that the filamentous characteristics of the PxylX::*ctrA*Δ3Ω mutant is likely unassociated with chromosome replication and may be a result of altered Z-ring or growth regulations. 4) One must also consider that DnaA and CtrA compete for *Cori* binding sites; But it is unlikely that DnaA can displace $CtrA_U$ from *Cori* unless $CtrA_U$ interacts with DnaA in a unique way from CtrA~P. It was shown that somewhere between 0.001 μM and 0.01 μM of GST-CtrA, a dimerized active form of CtrA, is sufficient to displace 0.1 μM of DnaA from *Cori* [191]. GST-CtrA has a similar binding affinity as CtrA~P for *Cori* [126], and our model suggests that $CtrA_U$ can displace the majority of CtrA~P at ratios of 25:1. Therefore, if CtrA~P and $CtrA_U$ interact identically with DnaA, we would expect that 0.1 μM of DnaA can be displaced by 0.025-0.25 μM of $CtrA_U$. While we are not aware of any studies that quantify the in vivo concentrations of DnaA in *Caulobacter*, concentrations are estimated to be ~0.4 μM in E. Coli [218]. Thus, we expect that DnaA concentrations would be within 10 fold of the 0.1 μM used in the experiments of Taylor et al. In contrast, the concentrations of $CtrA_U$ are likely to be greater than 15 μM at the G1-S transition in *ctrA*Δ3Ω mutants, which is 60-600 fold greater than the concentrations we estimate would be needed to displace 0.1 μM of DnaA. Therefore, the cumulative evidence suggests that, in *ctrA*Δ3Ω and similar mutants, $CtrA_U$ must interact with *Cori* at the G1-S transition, yet chromosome replication functions normally.

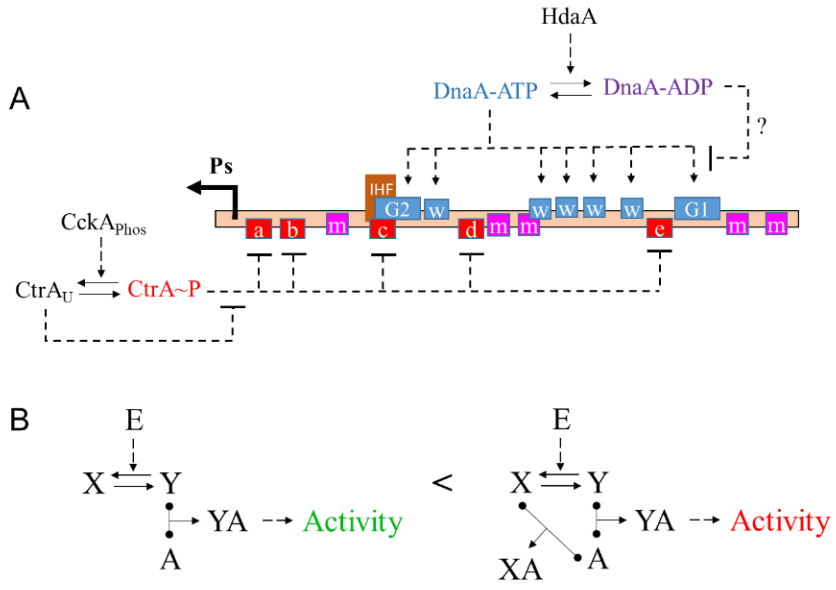

Figure 4.7) *Cori* physiology and regulation.
(A) The *Cori* locus consists of five methylation sites (m), five weak DnaA binding sites (w), two moderate affinity G boxes (G1 and G2), five CtrA binding sites ([a]-[e]) and an IHF binding site overlapping G2 and site [c]. The strong promoter (Ps) is regulated via binding of CtrA~P to sites [a] and [b]. CtrA~P inhibits *Cori* activity while DnaA-ATP promotes activity. Dashed lines indicate influencing interactions, arrow heads designate activation and flat heads designate inhibition. Solid arrows pointing from one molecular species to another designate molecular transformation (or a chemical reaction). HdaA converts DnaA-ATP to DnaA-ADP while CckA phosphatase (CckA$_{Phos}$) converts CtrA~P to CtrA$_U$. We provide computational evidence that CtrA$_U$ likely displaces CtrA~P for *Cori* binding sites to promote chromosome replication. In a similar fashion we suspect that DnaA-ADP displaces DnaA-ATP to inhibit a second round of chromosome replication.
(B) For any pair of species X and Y, where Y binds with A to induces some activity but X does not, enzyme E can inhibit this activity by converting Y to X. Intuitively, the efficiency of E for inhibiting activity is enhanced if X can also bind with A without inducing activity. Thus, E simultaneously reduces the concentration of Y and A to deplete the YA complex. Binding interactions are illustrated as lines with solid bulbs pointing to the binding partners and arrows pointing to the resulting complex. Solid arrows indicate conversion of one species to another and dashed arrows indicate influential interactions

How might CtrA$_U$ bind to *Cori* without disrupting chromosome replication? With regards to sites [a] and [b], CtrA~P inhibits the essential strong promoter, Ps, which controls downstream *hemE* activity [123], [219]; However, CtrA$_U$ must not impair transcription, otherwise the *ctrAΔ3Ω* mutant (and similar mutants) would not be viable. Similar behavior has been documented before. At the *ctrA* promoter, P1, it was shown that CtrA~P binds to inhibit transcription, while CtrA$_U$ binds to P1 with similar affinity without disrupting transcription [126]. Site [c] overlaps with the DnaA G1 box and a binding site for integration host factor (IHF), a protein that presumably promotes chromosome replication . It was shown that active CtrA can displace both IHF and DnaA

from site [c] [220]; However if $CtrA_U$ can displace CtrA~P, intuitively $CtrA_U$ can displace IHF and DnaA which would make it a repressor at site [c]. A study knocking out this site shows that chromosome replication is still possible but the cell cycle/ growth slows down significantly [220], suggesting that IHF and/or DnaA binding at this site are necessary for normal cell cycle behavior. As the *ctrAΔ3Ω* strain has normal cell cycle timing, it is unlikely that $CtrA_U$ impairs site [c]. It is possible that $CtrA_U$ interacts with either DnaA or IHF at site [c], in a way that CtrA~P does not, to allow them to bind. Additionally, mutations at this locus influences the transcription of the distant Ps promoter [220]. As with sites [a] and [b], it is also possible that CtrA~P impairs Ps transcription when bound to site [c], but $CtrA_U$ does not. More research is needed to fully understand the binding dynamics and regulation at site [c]. Site [d] is also a mystery, as the mechanism by which CtrA~P inhibits chromosome replication at site [d] is not documented, to the best of our knowledge. However, *Caulobacter* cells expressing *Cori* cloned plasmids showed significant increases in plasmid replication when site [d] was knocked out [190]. Site [e], is located ~4 bp from the essential DnaA box, G1. It was shown that active CtrA displaces DnaA from G1 and adjacent W sites [191]. As binding of DnaA to G1 is essential for the initiation of chromosome replication, and the *ctrAΔ3Ω* strain has a normal cell cycle, $CtrA_U$ must not impair DnaA binding to G1. Somehow, the phosphorylation of CtrA must cause a conformational change that blocks DnaA from binding to G1, either directly or indirectly.

Regardless of the mechanisms involved, the cumulative evidence from the literature and this work suggests that $CtrA_U$ competes with CtrA~P for *Cori* binding sites at physiologically relevant concentrations to promote chromosome replication. Indeed, we find that the $CtrA_U$:*Cori* interaction dramatically influences CtrA~P:*Cori* binding dynamics. Our model suggests that the fraction of CtrA~P saturated *Cori* binding sites, [DNA:CtrA~P_2], is relatively independent of the cellular concentration of CtrA~P. In contrast, due to the competition with $CtrA_U$ for *Cori* binding sites, [DNA:CtrA~P_2] is strongly dependent on the ratio of $CtrA_U$ to CtrA~P (Figure 4.2C). This result has profound implications regarding the functionality of CckA phosphatase at the G1-S transition. It was previously thought that CtrA dephosphorylation and proteolysis were redundant mechanisms, where the function of CckA phosphatase was simply to clear CtrA~P at the G1-S transition [167], [221]. Yet, our results indicate that the concentration of CtrA~P has a negligible impact on *Cori* binding until concentrations are extremely low (<0.02 μM). We propose that complete dephosphorylation of CtrA would be challenging for CckA, as it is a bifunctional

phosphatase/ kinase and should retain some kinase activity at the G1-S transition. Indeed, one experiment measuring CckA kinase activity found detectable levels at the G1-S transition [22]. Instead, due to the competitive inhibition of $CtrA_U$ with CtrA~P, CckA can dramatically relieve *Cori* from CtrA~P by manipulating the ratio of [$CtrA_U$]:[CtrA~P] and these dynamics are independent of the concentration of CtrA~P. This result further explains why a wide range of CtrA expression patterns are observed at the G1-S transition between *Caulobacter* populations (Figure 4.1B). By manipulating the ratio of CckA kinase to CckA phosphatase, *Caulobacter* can adjust the ratio of $CtrA_U$ to CtrA~P independently of the total concentration of CtrA. Thus, we suspect that the total concentration of CtrA at the G1-S transition makes a negligible impact on the cell cycle when CckA is functioning normally.

To further investigate the implications of $CtrA_U$:*Cori* binding, we developed a detailed mathematical model of the molecular mechanisms driving the *Caulobacter* cell cycle. We parameterized our model to three separate conditions: SLOW and QUICK parameter sets both include $CtrA_U$:*Cori* binding and are tuned to CtrA expression patterns with slow proteolysis and quick proteolysis at the G1-S transition, respectively. The CORI$^-$ parameter sets were parameterize without $CtrA_U$:*Cori* binding and with slow CtrA proteolysis data. Despite being parameterized to the same data, we find that the SLOW parameter sets fit the CtrA expression pattern very well but the CORI$^-$ parameter sets induce rapid proteolysis at the G1-S transition. Additionally, we find that the CORI$^-$ parameter sets express supraphysiological levels of cdG to induce supraphysiological CckA phosphatase activity (Figure 4.4A and 4.5C). These results support our prior conclusion, that the total concentration of CtrA at the G1-S transition has a negligible impact due to $CtrA_U$:*Cori* binding and normal CckA functioning. The fact that CORI$^-$ parameter sets had distinct abnormalities also suggests that the competition of $CtrA_U$ with CtrA~P for *Cori* binding sites is an essential interaction to explain the observed biology of *C. crescentus*.

When we remove $CtrA_U$:*Cori* binding from SLOW and QUICK parameter sets, we find that the timing of chromosome replication is consistently delayed, but these delays are significantly greater in the Slow parameter sets ($\Delta t^{cr} \approx 23$ min) than in QUICK parameter sets ($\Delta t^{cr} \approx 2$ min). We find that the large difference in delays is due to the fact that, without $CtrA_U$:*Cori* binding, the G1-S transition is highly dependent on CtrA proteolysis. However, the fact that QUICK parameter sets, characterized by rapid proteolysis of CtrA, demonstrate consistent delays in chromosome

replication timing when the $CtrA_U$:*Cori* interaction is removed indicates one of two scenarios: (1) $CtrA_U$ displacement of CtrA~P at *Cori* typically precedes proteolysis; (2) The dynamics of CtrA dephosphorylation and proteolysis act cooperatively, in a $CtrA_U$:*Cori* dependent manner, to disrupt CtrA~P:*Cori* binding. Along these lines, our analysis of the *Cori* binding model at site [d] did suggest some cooperativity between reducing total CtrA levels and manipulating the $CtrA_U$:CtrA~P ratio (Figure 4.2C). Importantly, this synergy was a consequence of $CtrA_U$:*Cori* binding. When we decreased the rate of proteolysis in QUICK parameter sets, we found that the timing of chromosome replication gained very mild delays in chromosome replication. Importantly, these delays were less than the delays associated with removing $CtrA_U$:*Cori* binding. This suggests that, while there may be some synergy between CtrA proteolysis and dephosphorylation in speeding up the G1-S transition, *Cori* binding sites are likely freed from CtrA~P more quickly by $CtrA_U$ displacement than by proteolysis. This makes sense when considering the biochemistry of *C. crescentus*. The CckA kinase/ phosphatase dictates the phosphorylation of both CtrA and CpdR [137], [222]. Thus, CtrA~P and CpdR~P are simultaneously dephosphorylated at the G1-S transition. CpdR, in its unphosphorylated state, localizes to the old pole where it interacts with ClpXP [197]. The CpdR:ClpXP complex must then recruit other adaptors (PopA, RcdA and cdG) before CtrA proteolysis can begin [133], [223]. Then CtrA proteolysis takes several minutes before CtrA levels are completely depleted [133], [210]. In contrast, there is no lag between the dephosphorylation of CtrA and its ability to compete with CtrA~P for *Cori* binding sites. Additionally the kinetics of protein binding and unbinding typically occurs on faster time scales than those of proteolytic degradation [86]. Afterall, proteolytic degradation requires protein-protein binding before the proteolysis process even begins. Therefore, since CtrA~P and CpdR~P are dephosphorylated simultaneously, $CtrA_U$ should have ample time to displace CtrA~P from *Cori* binding sites by the time CtrA proteolysis is relevant.

Investigation of mutant simulations of all three parameter sets revealed that the $CtrA_U$:*Cori* interaction was necessary for the viability of several mutant strains, including cdG^0, Δ*popA* and Δ*rcdA*. We report that, when $CtrA_U$:*Cori* binding was removed from simulations, overall strain viability dropped by 43% in SLOW parameter sets and 22% in QUICK parameter sets. Additionally, overall strain viability increased by 13% when adding $CtrA_U$:*Cori* binding to $CORI^-$ simulations (Figure 4.5E). We point out that the SLOW and QUICK results are likely more accurate in terms of predicting viability than the $CORI^-$ parameter sets, given that $CORI^-$ simulations do not fit biological

observations quite as well. Importantly, despite the cdG^0 mutant being a penalized strain of the cost function, 100% of $CORI^-$ parameter sets failed to capture cdG^0 viability. However, simply introducing the $CtrA_U$:*Cori* interaction to $CORI^-$ simulations resulted in recovery from G1 arrest. Closer investigation into other mutant simulations revealed that the absence of the $CtrA_U$:*Cori* interaction frequently led to G1 arrest in mutants that have impaired proteolysis. Conclusively, these results suggest that the $CtrA_U$:*Cori* interaction is necessary to explain observed mutant viability behavior. As pointed out previously, the competition of $CtrA_U$ and CtrA~P for *Cori* binding sites changes the dynamics of CtrA~P:*Cori* binding from being a simple function of CtrA~P concentration to being a function of the $CtrA_U$:CtrA~P ratio. This leads to a greater efficiency of the CckA phosphatase at the G1-S transition, which seems to be necessary for a dephosphorylation dependent G1-S transition. In other words, the interaction of $CtrA_U$:*Cori* is necessary for CckA phosphatase to sufficiently clear *Cori* of CtrA~P in the absence of total proteolysis. Thus, the $CtrA_U$:*Cori* interaction significantly enhances the robustness of the G1-S transition.

In conclusion, here we provide computational evidence that $CtrA_U$ contributes to a speedier and more robust G1-S transition. Moreover, we show that the competitive interaction between $CtrA_U$ and CtrA~P for *Cori* binding sites dramatically increases the efficacy of CckA phosphatase for regulating DNA replication. This behavior fits a general paradigm of systems biology (Figure 4.7B) as follows: a molecule X is converted to molecule Y which can binds with an activator, A, to induce some activity. An enzyme E converts Y back into species X which does not associate with A to induce activity. In such a scenario, enzyme E impairs the activity by depleting Y and reducing the concentration of the YA complex. However, the efficiency of enzyme E to impair activity can be enhanced if molecule X also directly binds with A to compete with Y for A binding sites. In such a scenario, E can deplete the YA complex by simultaneously reducing the availability of Y and A that might bind to induce activity. As biological systems are pruned for efficiency by natural selection, we propose that for any system that has been identified that matches the left panel of Figure 4.7B, the possibility that molecule X inhibits activity by competitive inhibition should be considered. We can think of two additional examples that have not been investigated in *C. crescentus*. First, *ctrA* promoters P1 and P2 have similar binding affinities for CtrA~P and $CtrA_U$, yet $CtrA_U$ does not influence *ctrA* activity in the manner of CtrA~P [126]. No one, to the best of our knowledge, has investigated the dynamics of competition between $CtrA_U$ and CtrA~P

for *ctrA* P1 and P2; But rationally, if we consider that $CtrA_U$ and CtrA~P have similar binding affinities for *ctrA* then they should compete for *ctrA* binding sites. Therefore, if $CtrA_U$ does not directly affect *ctrA* P1 or P2 activity and CtrA~P does, then $CtrA_U$ must be a competitive inhibitor of CtrA~P with regards to *ctrA* regulation. We intend to investigate the nature of this interaction in future works. In a similar vein, it is known that both DnaA-ADP and DnaA-ATP can bind to *Cori* with similar affinity [191], but *Cori* is less active after DnaA-ATP hydrolysis [224], suggesting that DnaA-ADP does not promote chromosome replication. As HdaA hydrolyzes DnaA-ATP to DnaA-ADP immediately after DNA replication is initiated to prevent a second round of replication initiation [224], DnaA-ADP should displace DnaA-ATP as the ratio shifts in favor of DnaA-ADP. Therefore, we suspect that DnaA-ADP may act as a competitive inhibitor to DnaA-ATP at *Cori* just as $CtrA_U$ does with CtrA~P. In our model, we do not simulate DnaA-ADP binding to *Cori*, because we could not find quantitative experiments necessary to estimate kinetic constants. In our model, DnaA-ATP must be hydrolyzed extremely quickly by HdaA to ensure that a second round of chromosome replication does not begin (Figure B.1,B.2&B.3). We suspect that, in reality, DnaA-ATP is not hydrolyzed as quickly as in our model. Just as parameterizing our model without the $CtrA_U$:*Cori* interaction resulted in a dubiously high activity of CckA phosphatase, the improbably high rate of DnaA-ATP hydrolysis in our model may be a consequence of neglecting the DnaA-ADP:*Cori* interaction. The competitive inhibition should increase the efficiency of the HdaA enzyme just as our model suggests that the $CtrA_U$:*Cori* interaction enhances the efficiency of CckA. We urge experimental biologists to more consider such potential interactions in the future, and specifically to investigate the roles of unphosphorylated CtrA in the *Caulobacter* cell cycle.

Chapter 5 : Molecular mechanisms of cell cycle arrest in carbon and nitrogen starved *Caulobacter* populations

Bronson R. Weston[1*], Chunrui Xu[1*], John J. Tyson[2] and Yang Cao

[1] Program in Genetics, Bioinformatics, and Computational Biology, Virginia Tech, Blacksburg VA, USA

[2] Department of Biological Sciences, Virginia Tech, Blacksburg, VA, USA

[3] Department of Computer Science, Virginia Tech, Blacksburg, VA, USA

[*] Equal Contributors

5.1 Abstract

The freshwater bacterium, *Caulobacter crescentus*, has an ingenious solution to thrive in nutrient-poor environments. When the cell divides, it does so asymmetrically to produce two daughter cells of different phenotype and function. The "stalked" cell utilizes a stalk organelle to attach to surfaces in its environment, while the "swarmer" cell utilizes a flagellum to move through the water in search of more favorable environmental conditions. When the swarmer cell is satisfied, it differentiates into a stalked cell, clings to an environmental surface, and proceeds with the cell cycle. The molecular mechanism that manifests in this intriguing behavior is well studied under nutrient rich conditions, however the response of the molecular mechanism to nitrogen and carbon starvation is not so clear. Here we present a mathematical model which is trained by experimental data to capture the dynamics of the molecular mechanism driving the *C. crescentus* cell cycle. We investigate what is known about carbon and nitrogen signaling and find that it is insufficient to explain experimental observations of rapid, robust arrest in swarmer cell populations. We find that the phosphorylation status of cell cycle regulator, DivK, is of utmost importance to G1 arrest and demonstrate that carbon and nitrogen starvation signaling likely influences the activity of a DivK kinase or phosphatase.

5.2 Introduction

Caulobacter species are frequently referred to as ubiquitous [17], [26], [225]–[228], colonizing diverse ecosystems from freshwater habitats such as lakes, streams and tap water, to seawater, and many kinds of soils [17], [229]. The oligotrophic bacteria have evolved a character-defining dimorphic lifestyle as a survival mechanism for nutrient-poor environments [17], [26], [230]. More specifically, the bacterium strategically expresses different organelles in different phases of the cell cycle. In the G1 phase, the bacterium expresses a flagellum and is referred to as a "swarmer" cell. The flagellum permits the cell to navigate its environment in search of sufficient nutrients [26]. If environmental conditions are suitable, the swarmer cell will differentiate into a "stalked" cell by abandoning its flagellum and synthesize a stalk [148] equipped with the strongest biological adhesive ever measured, called a holdfast, to cling to a local surface in its environment [18], [231]. During this differentiation process, *Caulobacter* simultaneously initiates chromosome replication, thus progressing into the S phase of the cell cycle. As the bacterium continues to grow, it will synthesize a new flagellum at the pole opposite to the stalk and assembles a Z-ring at the mid-cell. Thus, upon cytokinesis, the two daughter cells have different morphologies [166]. The stalked daughter cell will remain attached to the environmental surface, while the swarmer cell is free to migrate or differentiate locally depending on environmental conditions.

The asymmetrical cell cycle of *C. crescentus* is well characterized and requires complex coordination of genetic expression, protein phosphorylation, proteolysis, protein localization and second messenger signaling. Master regulators of the cell cycle include transcription factors DnaA, GcrA, and CtrA, as well as the methyltransferase, CcrM [166]. These four proteins interact with each other and other downstream targets to orchestrate the oscillatory behavior of the cell cycle. Detailed mathematical models have been developed to demonstrate and analyze the regulatory paradigm of *C. Crescentus*. Some mathematical models have been used to demonstrate how *Caulobacter* can utilize the bistability of regulatory proteins to navigate the cell cycle [136], [232], while others establish insights into spatial regulation [233], [234], stochastic regulation [235] or mutant behaviors [119], [150] in *C. crescentus*; But none explore how *Caulobacter* responds to starvation. As *Caulobacter* are known oligotrophs, and their defining dimorphic lifestyle evolved out of necessity as a strategy to thrive in nutrient scarce

environments, here we are motivated to utilize mathematical modeling to explore the cell cycle mechanism in the context of nutrient stress.

5.2.1 Molecular Response to Carbon and Nitrogen Starvation in *Caulobacter*

Under circumstances of insufficient carbon or nitrogen, *C. crescentus* arrests its cell cycle, however the details of arrest are a bit controversial. Swarmer cells that are introduced to carbon or nitrogen depleted medium immediately arrest at G1. It is generally thought that swarmer cells arrest and persist in the swarmer state unless introduced into nutrient replete medium [208], [236], [237], however Britos *et al*. observed that 65% of carbon starved swarmer cells developed stalks and only 11% initiate DNA replication after 2 hours [4]. Thus, while there is an agreement in the *Caulobacter* community on G1 arrest in swarmer populations, whether swarmer populations develop stalks or remain in the swarmer state is not entirely clear. Gorbatyuk *et al*. observed that carbon starved stalked cells mostly remain in the pre-divisional phase after 180 min[208]. However results from Ronneau *et al*. suggest that stalked cells demonstrated delays in S phase and cytokinesis, but eventually divide and arrest at G1 after 200-260 min [237]. Overall, these experiments suggest that swarmer populations under nitrogen and carbon starvation immediately arrest in G1 while stalked populations demonstrate significant delays in cell division followed by G1 arrest (Fig 5.1).

Both, nitrogen and carbon starvation influence cell cycle behavior through regulation of second messengers ppGpp, pppGpp, and cdG [237], [238]. ppGpp and pppGpp, collectively referred to as (p)ppGpp, synthesized from GDP and GTP, respectively, by the synthetase form of the bifunctional enzyme, SpoT, in *C. crescentus* [239]. Similarly, the hydrolase form of SpoT converts (p)ppGpp back into GDP/GTP. The switch between synthetase and hydrolase activity of SpoT is regulated by the phosphorylation of a nitrogen Phosphotransferase System (PTS^{Ntr}) [237]. Carbon and nitrogen starvation signal into the PTS^{Ntr} system through modulation of intracellular concentrations of glutamine, pyruvate (Pyr) and phosphoenolpyruvate (PEP). These molecules directly influence phosphate transfer in the PTS^{Ntr} system which modulates SpoT activity. Xu *et al*. developed a mathematical model of the PTS^{Ntr} and secondary messenger pathway, demonstrating that carbon and nitrogen starvation results in a dramatic increase in (p)ppGpp and decreases in GTP and cdG levels [1]. These observations are consistent with experimental observations [237], [238]. Another mechanism by which carbon starvation may

influence SpoT activity is through the carbon PTS system, because PEP and Pyr influence carbon PTS as well which interacts with PTS^{Ntr} through phosphate transfer [240], [241]. However, the mechanisms underlying the crosstalk between carbon PTS and PTS^{Ntr} is not fully investigated.

In response to shifts in second messengers, *C. crescentus* will target cell cycle regulatory proteins to arrest the cell cycle and conserve energy and resources [242]. For the remainder of the paper, unless otherwise stated, we will refer to carbon and nitrogen starvation as simply "starvation", as these pathways mostly rely on the same signaling mechanisms. Master regulator DnaA is targeted and rapidly depleted under starvation due to decreased *dnaA* translation efficiency and constitutive proteolysis by Lon protease [243]. It has been demonstrated that (p)ppGpp, is involved in the depletion of DnaA [208], however the mechanism is yet to be elucidated. This signaling molecule is thought to have several other targets including the cell cycle master regulator, CtrA [244].

Proteolysis of CtrA is inhibited in a SpoT dependent manner under carbon and nitrogen starvation [245]. It was previously postulated the CtrA is stabilized through downstream signaling of (p)ppGpp, however Xu *et al*. demonstrated with a mathematical model that carbon and nitrogen starvation-induced SpoT activity likely leads to reduced GTP and cdG levels. As cdG is an adaptor of CtrA proteolysis, it is more likely that SpoT impairs proteolysis through the reduction of cdG levels. Despite being stabilized, CtrA levels are still reduced to approximately 30% of normal levels under nitrogen and carbon starvation [4]. It is suspected that the decrease in CtrA expression is partially dependent on SigT, however no clear mechanism has been determined [4].

As DnaA and CtrA promote and inhibit chromosome replication, respectively, it is thought that carbon and nitrogen starvation signaling influence CtrA and DnaA stability to induce G1 arrest [245]. However, the mechanisms of this should be further explored. First, the half-life of DnaA under starvation is 16-20 minutes [236], [243], however swarmer cells have typically committed to S phase within 20 minutes under normal conditions (Chapter 4). Furthermore, while CtrA is stabilized under starvation conditions, only the phosphorylated form (CtrA~P) can inhibit chromosome replication and it is unknown whether CtrA remains phosphorylated under starvation.

CtrA phosphorylation is regulated through CckA, the activity of which is manipulated through cdG and DivK. As discussed previously, cdG decreases under starvation, which should reduce CckA phosphatase activity; but the cdG_0 strain, which is depleted of cdG, can navigate through the cell cycle without arrest [161]. In contrast, strains depleted of DivK result in G1 arrest [246]. This suggests that DivK is essential and sufficient to regulate CckA and CtrA activity, while cdG is not. DivK~P inhibits the kinase activity of CckA by binding to DivL, and the DivL:DivK~P interacts with CckA to induce phosphatase activity, which is necessary to deplete CtrA~P levels at the G1-S transition [247]. As stalked and swarmer populations both arrest at G1 under carbon and nitrogen stress, it is likely that DivK regulation is involved in starvation signaling.

Under starvation conditions, DivJ does not localize to the old pole as it typically does during the G1 to S transition [244]. The mechanism underlying delocalization of DivJ likely work through SpmX, the scaffolding protein that localizes DivJ at the old pole [152], as cdG influences SpmX accumulation through a ShkA-ShpT-TacA signaling pathway at the G1 to S transition [248]. cdG is thought to activate TacA which improves the transcription of *spmX*. Importantly, SpmX also increases the activity of DivJ kinase.

Figure 5.1D summarizes how carbon/nitrogen-based SpoT signaling impairs the G1-S transition. However, there is still much to discover regarding nutrient signaling mechanisms. In this paper, we build upon previous mathematical models of the *Caulobacter* cell cycle and analyze the model in the context of carbon and nitrogen starvation. We find that the identified signaling pathways can explain many biological observations, but are not sufficient for robust, rapid G1 arrest of swarmer cell populations. Our analysis reveals that DivK synthesis and DivK kinase/phosphatase activity are likely strategic targets of nutrient signaling, necessary to explain experimental observations.

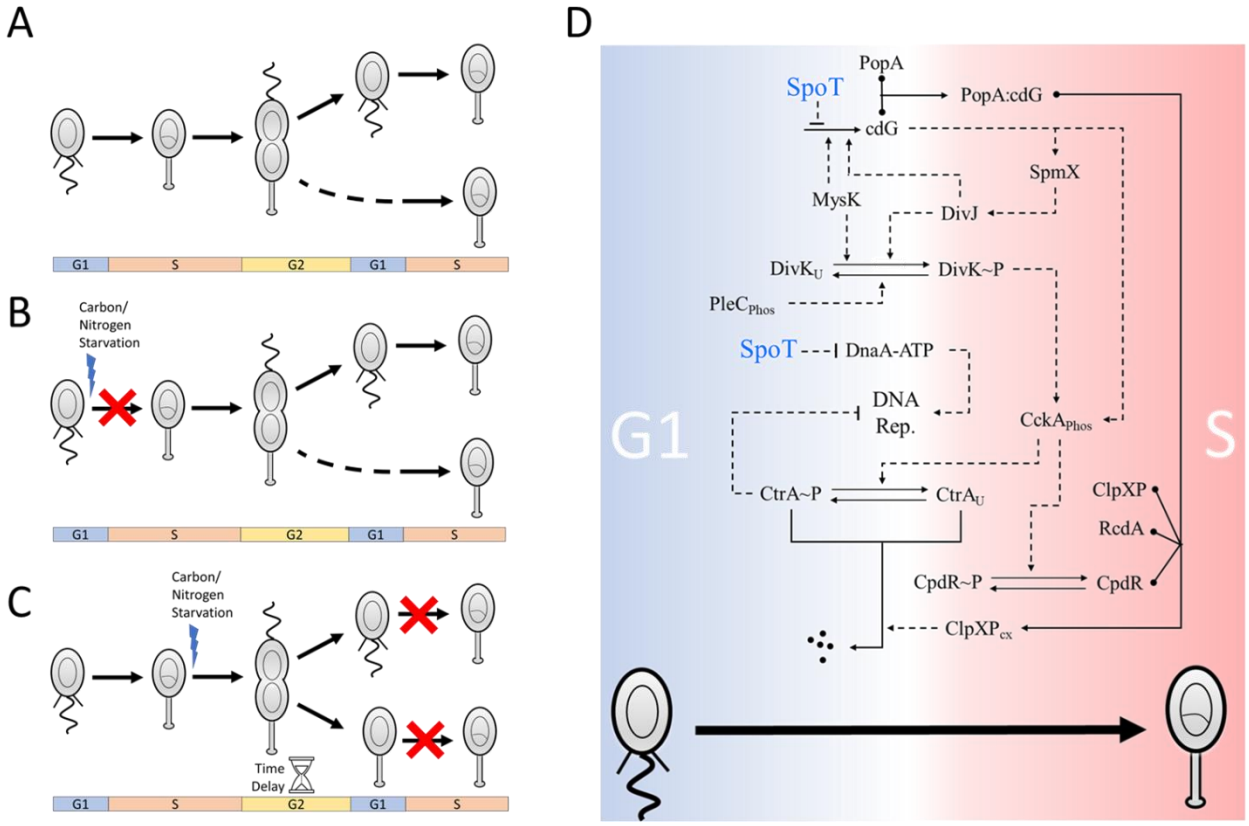

Figure 5.1) Nitrogen/Carbon starvation leads to G1 arrest.
(A) In nutrient rich conditions *C. crescentus* demonstrates an asymmetrical cell cycle. Upon cytokinesis, the stalked daughter cell immediately enters S phase while the swarmer cell delays chromosome replication and enters G1.
(B) Carbon/nitrogen starved swarmer populations exhibit immediate G1 arrest.
(C) Carbon/nitrogen starved stalked populations show delays in S phase and cytokinesis. Eventually cells divide and arrest at G1.
(D) The G1-S transition is dependent on regulation of the active forms of CtrA (CtrA~P) and DnaA (DnaA-ATP), as these master regulators directly inhibit and promote DNA replication, respectively. In G1, levels of PleC phosphatase ($PleC_{phos}$), unphosphorylated DivK ($DivK_U$) and CtrA~P are high. At the G1-S transition, PleC concentrations decrease while DivJ and cdG concentrations increase, leading to accumulation of SpmX, DivK~P and CckA phosphatase. As a result, CtrA~P levels decrease and chromosome replication is initiated. Carbon and nitrogen starvation impair the G1-S transition by targeting the synthesis of DnaA and cdG through SpoT signaling. Here, a solid arrow pointing from one species to another demonstrates the conversion of molecular species. A solid arrow point from nothing to a molecular species (i.e. cdG) or from a molecular species to a series of dots (i.e. CtrA) represents molecular synthesis and proteolysis, respectively. Solid lines point from a molecular species to another line indicates that the molecular species influences a molecular conversion. Dashed lines indicate influential interactions, where an arrowhead indicates a positive influence and a flat head indicates inhibition.

5.3 Methods

In this study, we expand upon the model of Weston *et al*. (Chapter 4) in the interest of capturing

stress signaling in *Caulobacter*. Here we specify the changes made to the original model in Chapter 4 to enhance biological accuracy. All other details of model are the same as in Chapter 4. For a full set of equations, see Appendix C.1.

5.3.1 Improvement to SciP modeling

SciP binds to several genes targeted by CtrA to perturb promoter activity, including the *ctrA* promoter [249]. Meanwhile, CtrA in turn activates expression of *sciP* through the *sciP* promoter. The interaction between SciP and CtrA is essential for the robustness of DNA replication regulation, which is involved in Weston *et al*.'s model (Chapter 4). We build on the SciP equation of Chapter 4, and incorporate the observation that SciP binds to its own promoter to impair transcription [113]. The improved equation of SciP is as follows:

$$\frac{\mathrm{d[SciP]}}{\mathrm{dt}} = k_{\mathrm{s,SciP}} \frac{[\mathrm{CtrA{\sim}P}]^2}{{J_{\mathrm{a,SciP-CtrA}}}^2+[\mathrm{CtrA{\sim}P}]^2} \cdot \frac{{J_{\mathrm{i,SciP-SciP}}}^2}{{J_{\mathrm{i,SciP-SciP}}}^2+[\mathrm{SciP}]^2} - \left(\mu + k_{\mathrm{d,SciP}}\right) \cdot [\mathrm{SciP}]\,,$$

Where $k_{\mathrm{s,SciP}}$ and $k_{\mathrm{d,SciP}}$ are the synthesis rate and degradation rate, respectively. μ indicates the dilution rate due to *C. crescentus* cell growth. $J_{\mathrm{a,SciP\text{-}CtrA}}$ and $J_{\mathrm{i,SciP\text{-}SciP}}$ describe the affinity of CtrA:*sciP*-promoter and SciP:*sciP*-promoter binding, respectively.

5.3.2 Modeling PTS$^{\mathrm{Ntr}}$/SpoT nutrient signaling cascade through cdG:

Previously, we modeled the response of secondary messengers - (p)ppGpp, GTP, and cdG - to starvation signals in *C. cresentus* [1]. We found that the SpoT enzyme dramatically influences GTP levels through conversion into (p)ppGpp and that depleted GTP leads to reduced cdG synthesis. While cdG is converted into pGpG and GMP and eventually back into GTP, we find that cdG synthesis and hydrolysis rates make a negligible impact on GTP and (p)ppGpp levels. This is due to the fact that cdG concentrations are negligible compared to GTP concentrations in *C. crescentus* [161], an observation that is consistent in other bacteria as well [250]. As the secondary messenger model and the larger cell cycle model (from Chapter 4) both capture cdG regulation, we first considered merging the two models to capture nutrient signaling in the cell cycle. However, such a merger would slow down the model simulation time and is unnecessary, as GTP levels influence cdG synthesis, but not the other way around. Thus, we import GTP

levels from Xu *et al.* [1] under normal and starvation conditions and adjust the synthesis rate of cdG such that:

$$\frac{\mathrm{d[cdG]}}{\mathrm{dt}} = \left(k_{\mathrm{s,cdG1}} \cdot [\mathrm{PleD{\sim}P}] + k_{\mathrm{s,cdG2}} \cdot [\mathrm{DgcB}]_{\mathrm{a}}\right) \cdot \frac{[\mathrm{GTP}]^2}{J_{\mathrm{s,cdG}}^2 + [\mathrm{GTP}]^2} - k_{\mathrm{d,cdG}} \cdot ([\mathrm{PdeA}] + PDE) \cdot [\mathrm{cdG}] - \mu \cdot [\mathrm{cdG}] + 2 \cdot \left(-k_{\mathrm{PopACdG}}^{+} \cdot [\mathrm{PopA}] \cdot [\mathrm{cdG}]^2 + \left(k_{\mathrm{XCdG}}^{-} + k_{\mathrm{d,PopA}}\right) \cdot [\mathrm{PopA{:}\,cdG_2}]\right) + 2 \cdot \left(-k_{\mathrm{PleDcdG}}^{+} \cdot ([\mathrm{PleD}] + [\mathrm{PleD{\sim}P}]) \cdot [\mathrm{cdG}]^2 + \left(k_{\mathrm{d,PleD}} + k_{\mathrm{XCdG}}^{-}\right) \cdot ([\mathrm{PleD{:}\,cdG_2}] + [\mathrm{PleD{\sim}P{:}\,cdG_2}])\right) - k_{\mathrm{CckAcdG}}^{+} \cdot [\mathrm{cdG}] \cdot ([\mathrm{CckA}]_{\mathrm{T}} - [\mathrm{CckA{:}\,CdG}]) + k_{\mathrm{CckAcdG}}^{-} \cdot [\mathrm{CckA{:}\,cdG}] + 2 \cdot \left(-k_{\mathrm{DgcBcdG}}^{+} \cdot (DgcB - [\mathrm{DgcB{:}\,cdG_2}]) \cdot [\mathrm{cdG}]^2 + k_{\mathrm{XCdG}}^{-} \cdot [\mathrm{DgcB{:}\,cdG_2}]\right),$$

where the red text highlights the only change made to the cdG differential equation from Chapter 4. Here, $J_{\mathrm{s,cdG}}$ indicates the concentration of GTP corresponding to half maximal synthesis. We input different GTP levels to adjust the synthesis of cdG under normal and starved conditions in this study, where $J_{\mathrm{s,cdG}}$=1500µM, [GTP]=1221µM for normal condition and 227µM for starved condition (obtained from Xu *et al.* [1]).

5.3.3 Modelling other Starvation Signaling Pathways

cdG regulates SpmX accumulation, which recruits DivJ to the old pole, at the G1-S transition [251]. As cdG synthesis is impaired from starvation [1] and DivJ delocalization has been observed in carbon and nitrogen starved *Caulobacter* populations [244], [248], it is evident that SpmX synthesis is shut off under such conditions. Our initial simulations (not shown) did not predict sufficient suppression of *spmX* and therefore include forced SpmX suppression in Signals 1-5 (Table 5.1) in this version of the model. Future iterations will ensure such artificial signals are not necessary.

(p)ppGpp influences numerous other molecules in response to starvation. SpoT is required for the rapid proteolysis of DnaA upon starvation, which is confirmed by Δ*spoT* mutant analysis [236]. We reduce DnaA synthesis ($k_{\mathrm{s,DnaA}}$) in our model to simulate the inhibition of DnaA translation efficiency under stress. (p)ppGpp constrains cell size and slows down cell growth under starvation, where the underlying mechanisms have not been identified [244], [245]. In this study, we reduced the average cell growth rate from normal conditions by 1/3 to capture decreased growth rates under starvation. While evidence suggests that there is no significant

growth in *Caulobacter* colonies after 8 hrs of monitoring starvation [208], we assume that there must be some growth in the initial stages of starvation response as stalked cells continue to proceed through their cell cycle slowly and divide before G1 arrest [237]. If stalked cells did not continue to grow to relatively full size before cytokinesis, surely observations of significantly shorter cell lengths would be reported in starved populations.

Moreover, high-throughput proteome analyses show that DivK levels decrease to 67% of wild type cells upon 60 min carbon deprivation, whereas the levels of DivL and CckA increase to 3.8-fold and 1.8-fold under the same circumstance [4]. However, the mechanisms of these changes are unknown. Here, we introduce the reduced DivK, increased DivL and CckA through their relative synthesis parameters (Signal2 in Table 5.1). In order to capture the immediate robust G1 arrest under starvation, which is observed in experiments [4], [237], we proposed two candidates, PleC and DivJ, regulating the phosphorylation of CtrA through DivK (Signal3&5 in Table 5.1). Moreover, it has been reported that CtrA levels significantly decrease under starvation conditions, while the underlying mechanisms are unknown [4]. We additionally reduce the synthesis rate of CtrA to simulate the reduction upon starvation signaling (Signal 4&5 in Table 5.1).

Table 5.1) Signaling targets and arrest statistics.

Paradigm	Description	Parameters changes	Fractional Arrested*				
				1st G1	2nd G1	1st G2	2nd G2
Signal 1	• Introducing stress response through cdG-dependent pathway. • Inhibiting DnaA synthesis. • Inhibiting SpmX synthesis.	$k_{s,DnaA} = 0$ $k_{s,cdG1} = 0.056 \times k_{s,cdG1}$ $k_{s,cdG2} = 0.056 \times k_{s,cdG2}$ $\mu = 0.0018$ $k_{s,SpmX} = 0$	**SW**	0	100%	0	0
			ST	0	96.9%	0.6%	0

Signal 2	• Introducing stress response through cdG-dependent pathway. • Inhibiting DnaA synthesis. • Inhibiting SpmX synthesis. • decreasing DivK. • increasing DivL. • increasing CckA.	$k_{s,DnaA} = 0$ $k_{s,cdG1} = 0.056 \times k_{s,cdG1}$ $k_{s,cdG2} = 0.056 \times k_{s,cdG2}$ $\mu = 0.0018$ $k_{s,SpmX} = 0$ $k_{s,DivK1} = k_{s,DivK1}/5$ $k_{s,DivK2} = k_{s,DivK2}/5$ $k_{s,CckA} = k_{s,CckA} \times 1.8$ $k_{s,DivL} = k_{s,DivL} \times 3.8$	**SW**	18.2%	80.5%	1.3%	0
			ST	0	96.9%	0.6%	0
Signal 3	• Introducing stress response through cdG-dependent pathway. • Inhibiting DnaA synthesis. • Inhibiting SpmX synthesis. • Decreasing DivK. • Increasing DivL. • Increasing CckA. • Slowing down PleC proteolysis.	$k_{s,DnaA} = 0$ $k_{s,cdG1} = 0.056 \times k_{s,cdG1}$ $k_{s,cdG2} = 0.056 \times k_{s,cdG2}$ $\mu = 0.0018$ $k_{s,SpmX} = 0$ $k_{s,DivK1} = k_{s,DivK1}/5$ $k_{s,DivK2} = k_{s,DivK2}/5$ $k_{s,CckA} = k_{s,CckA} \times 1.8$ $k_{s,DivL} = k_{s,DivL} \times 3.8$ $k_{d,PleC} = k_{d,PleC} \times 0.8$	**SW**	89.3%	10.1%	0.6%	0
			ST	0	96.9%	0.6%	0
Signal 4	• Introducing stress response through cdG-dependent pathway. • Inhibiting DnaA synthesis. • Inhibiting SpmX synthesis. • Decreasing DivK. • Increasing DivL. • Increasing CckA.	$k_{s,DnaA} = 0$ $k_{s,cdG1} = 0.056 \times k_{s,cdG1}$ $k_{s,cdG2} = 0.056 \times k_{s,cdG2}$ $\mu = 0.0018$ $k_{s,SpmX} = 0$ $k_{s,DivK1} = k_{s,DivK1}/5$ $k_{s,DivK2} = k_{s,DivK2}/5$ $k_{s,CckA} = k_{s,CckA} \times 1.8$ $k_{s,DivL} = k_{s,DivL} \times 3.8$	**SW**	96.2%	3.8%	0	0
			ST	0	96.9%	0.6%	0

	• Slowing down PleC proteolysis. • Decreasing CtrA.	$k_{d,PleC} = k_{d,PleC} \times 0.8$ $k_{s,CtrA\text{-}P1} = k_{s,CtrA\text{-}P1}/30$ $k_{s,CtrA\text{-}P2} = k_{s,CtrA\text{-}P2}/30$					
Signal 5	• Introducing stress response through cdG-dependent pathway. • Inhibiting DnaA synthesis. • Inhibiting SpmX synthesis. • Decreasing DivK. • Increasing DivL. • Increasing CckA. • Decreasing CtrA. • Inhibiting DivJ.	$k_{s,DnaA} = 0$ $k_{s,cdG1} = 0.056 \times k_{s,cdG1}$ $k_{s,cdG2} = 0.056 \times k_{s,cdG2}$ $\mu = 0.0018$ $k_{s,SpmX} = 0$ $k_{s,DivK1} = k_{s,DivK1}/5$ $k_{s,DivK2} = k_{s,DivK2}/5$ $k_{s,CckA} = k_{s,CckA} \times 1.8$ $k_{s,DivL} = k_{s,DivL} \times 3.8$ $k_{s,CtrA\text{-}P1} = k_{s,CtrA\text{-}P1}/30$ $k_{s,CtrA\text{-}P2} = k_{s,CtrA\text{-}P2}/30$ $k_{s,DivJ} = 0$	**SW**	100%	0	0	0
			ST	0	96.9%	0.6%	0

*1st G1 corresponds to cells with immediate G1 arrest (no chromosome replication). 2nd G1 corresponds to cells that divide and then arrest at G1. 1st G2 corresponds to cells that initiate chromosome replication but never divide. 2nd G2 corresponds to cells that replicate DNA twice but only divide once.

5.3.4 An unknown Kinase likely contributes to the transition into S phase through phosphorylating the two response regulators - PleD and DivK

As previously mentioned, SpmX is regulated via the cdG-ShkA-TacA pathway. PleD, the primary synthetase of cdG, is active in its phosphorylated form (PleD~P) and is regulated by DivJ kinase and PleC phosphatase [155]. Previous experiments have measured that SpmX is expressed in Δ*divJ* and double mutant Δ*pleC*Δ*divJ* strains, while transcription of *spmX* decreases to 1/4 of wild type cells in Δ*pleD* [248]. These results indicate that PleD is phosphorylated and active in Δ*divJ* and Δ*pleC*Δ*divJ* strains. Therefore, there must be an unknown kinase responsible for phosphorylation of PleD independently of DivJ and PleC. Moreover, significant levels of phosphorylated DivK have been measured in Δ*divJ* and double mutant Δ*divJ* & *pleC*::Tn5 strains [24]. As DivJ and PleC are the only known kinases of DivK, this result indicates that an unknown kinase must regulate DivK as well. Furthermore, in Chapter 4, our simulations of mutants Δ*divJ* and Δ*divJ* & *pleC*::Tn5 support the necessity for an unknown DivK kinase as

well. Wheeler and Shapiro [24] observed that Δ*divJ* and Δ*divJ,pleC*::Tn5 are filamentous but successfully replicate, while Δ*divJ* and Δ*divJ,pleC*::Tn5 simulations in Chapter 4 suggest that the cell cycle should arrest at G1 if an additional DivK kinase is not included. Inclusion of an additional DivK kinase resulted in the rescue of Δ*divJ* and Δ*divJ,pleC*::Tn5 simulations without compromising the quality of model performance. The cumulative evidence suggests that there is at least one unknown kinase acting on DivK and PleD. We speculate that the unknown kinase regulating PleD and DivK are one in the same and name this mystery kinase 'MysK' for short.

In the model presented here, we build on the DivK and PleD equations of Chapter 4 and include MysK activity as an independent parameter. As the Δ*divJ* & *pleC*::Tn5 strain expresses DivK~P at ~27% of WT levels [24], we also justify that DivK~P must have a significant basil rate of hydrolysis relative to MysK activity, otherwise DivK~P levels should be much greater than 27% of WT in the presence of a sufficient kinase. In support of an additional phosphatase, CckN has been identified as a phosphatase for DivK. Furthermore, it was shown that CckN makes little impact on the phosphorylation of DivK in the presence of DivJ and PleC, but makes a profound impact in their absence [252]. Thus, we include a parameter for basil hydrolysis, $k_{\mathrm{hyd,DivK}}$. See Appendix C for updated equations and parameters (Table C.1).

Modifications to modeling the ClpXP and adaptor complex:

In Chapter 4, it was assumed that RcdA and PopA:cdG interact independently before associating with CpdR and ClpXP. However, we did not account for RcdA interacting independently with the CpdR:ClpXP complex independently of PopA. While this interaction was inconsequential in Chapter 4, the degradation of TacA is dependent on the ClpXP:CpdR:RcdA complex (in the absence of PopA and cdG) and therefore this interaction must be accounted for in this version of the model.

We assume that RcdA may interact with CpdR independently of its phosphorylated state, and therefore we define the concentration of the RcdA:CpdR complex as:

$$[\mathrm{RcdA{:}\,CpdR}]_{\mathrm{T}} = \frac{[\mathrm{CpdR}]_{\mathrm{T}} + [\mathrm{RcdA}] + \frac{1}{K_{\mathrm{RcdACpdR}}} - \sqrt{\left([\mathrm{CpdR}]_{\mathrm{T}} + [\mathrm{RcdA}] + \frac{1}{K_{\mathrm{RcdACpdR}}}\right)^2 - 4 \cdot [\mathrm{CpdR}]_{\mathrm{T}} \cdot [\mathrm{RcdA}]}}{2},$$

where K_{RcdACpdR} is the dissociation constant for the RcdA:CpdR complex and $[\mathrm{CpdR}]_{\mathrm{T}} = [\mathrm{CpdR}] + [\mathrm{CpdR{\sim}P}]$. As only unphosphorylated CpdR interacts with the ClpXP complex to catalyze proteolysis [133], we calculate the concentration of RcdA bound to unphosphorylated CpdR such that:

$$[\mathrm{RcdA{:}CpdR}] = [\mathrm{RcdA{:}CpdRT}] \cdot \frac{[\mathrm{CpdR}]}{[\mathrm{CpdR}]_{\mathrm{T}}}.$$

Utilizing the same logic as Chapter 4, we derive then derive the following equation for the fully equipped ClpXP:CpdR:RcdA:PopA:cdG_2 complex:

$$[\mathrm{ClpXP}]_{\mathrm{Complex}} = \frac{[\mathrm{RcdA{:}\,CpdR}]}{[\mathrm{RcdA{:}\,CpdR}] + \frac{K_{\mathrm{ClpXpCpdR}}}{V}} \cdot [\mathrm{PopA{:}\,cdG_2}],$$

where $K_{\mathrm{ClpXpCpdR}}$ is the dissociation constant for the RcdA:CpdR complex with [PopA:cdG_2]. Notably, we assume that the RcdA:CpdR complex is significantly greater than the PopA:cdG_2 complex to arrive at this equation.

Additionally, it was shown that the RcdA adaptor is also a target for proteolysis by the CpdR:ClpXP complex [253], which we capture in Chapter 4; however, *in vivo* expression patterns of RcdA do not reflect significant proteolysis at the timing of CpdR expression [195], [197]. Therefore, we removed this insignificant interaction in our model and get the following differential equation for RcdA:

$$\frac{\mathrm{d}[\mathrm{RcdA}]}{\mathrm{dt}} = k_{\mathrm{s,RcdA}} \cdot \frac{[\mathrm{CtrA{\sim}P}]^2}{{J_{\mathrm{a,RcdACtrA}}}^2 + [\mathrm{CtrA{\sim}P}]^2} - \left(\mu + k_{\mathrm{d,RcdA}}\right) \cdot [\mathrm{RcdA}].$$

where $k_{\mathrm{s,RcdA}}$ and $k_{\mathrm{d,RcdA}}$ are the synthesis and degradation rates, respectively, and $J_{\mathrm{a,RcdACtrA}}$ corresponds to concentration of CtrA~P that leads to half-maximal rates of synthesis of RcdA.

5.3.5 Changes to modeling of active DivJ

DivJ kinase activity is upregulated by interacting with SpmX and DivK. However, it is unclear how much the activity is influenced when DivJ is bound to just SpmX, just DivK, or to both molecules. For simplicity, we assume that DivJ activity is negligible when not bound by either SpmX or DivK, and that DivJ is at 100% activity when bound by both, DivK and SpmX. We

further assume that the phosphorylated and unphosphorylated form of DivK impact DivJ activity to the same degree. Hence, we get the following equation:

$$[\mathrm{DivJ}]_{\mathrm{A}} = ([\mathrm{DivJ{:}\,DivK{\sim}P}] + [\mathrm{DivJ{:}\,DivK}]) \cdot \left((1 - \epsilon_{\text{DivJ-DivK}}) \cdot \left(\frac{\min([\mathrm{SpmX}], [\mathrm{DivJ}]_{\mathrm{T}})}{[\mathrm{DivJ}]_{\mathrm{T}}} \right) + \epsilon_{\text{DivJ-DivK}} \right) + \epsilon_{\text{DivJ-SpmX}} \cdot [\mathrm{DivJ}] \cdot \frac{\min([\mathrm{SpmX}], [\mathrm{DivJ}]_{\mathrm{T}})}{[\mathrm{DivJ}]_{\mathrm{T}}},$$

where $\varepsilon_{\text{DivJ-SpmX}}$ dictates the fraction of activity DivJ has when only bound to SpmX and $\varepsilon_{\text{DivJ-DivK}}$ is the fraction of DivJ activity when only bound to DivK. The function, min([SpmX, $[\mathrm{DivJ}]_{\mathrm{T}}$)/$[\mathrm{DivJ}]_{\mathrm{T}}$ represents the fraction of DivJ bound by SpmX.

cdG regulates morphogenesis through the ShkA-TacA-SpmX pathway:

SpmX accumulates at the G1-S transition to influence the localization and activity of DivJ [194], however DivJ is delocalized under carbon and nitrogen depleted conditions [244]. In Chapter 4 SpmX is captured via a simplistic toy function to minimize model complexity. To effectively capture the molecular biology of carbon and nitrogen signaling in *Caulobacter*, we refurbished the SpmX portion of the model.

cdG controls the expression of *spmX* through the ShkA-TacA pathway. Phosphorylated TacA controls the transcription of SpmX [152], [248], which recruits and activates DivJ at the stalked pole [194]. TacA is activated by a phosphorelay system, including a hybrid histidine kinase ShkA and a phosphotransferase protein ShpA [248]. ShkA is predominantly inactive without cdG, while cdG binds to ShkA to induce the kinase activity of ShkA [246]. ShkA kinase transfers phosphates to a His residue of the phosphotransferase ShpA which are then received by the receiver domain of TacA in sequence [246], [248].

Here, [ShkA] and [ShkA:cdG] are the concentrations of inactive and active ShkA, respectively. We assume that binding and unbinding of cdG with ShkA reaches steady state quickly and that the concentration of cdG is much greater than ShkA. Hence, we model the binding reaction as:

$$[\mathrm{ShkA}]_{\mathrm{T}} = [\mathrm{ShkA}] + [\mathrm{ShkA{:}cdG}],$$

$$[\text{ShkA:cdG}] = [\text{ShkA}]_{\text{T}} \cdot \frac{[\text{cdG}]}{[\text{cdG}] + K_{\text{D,ShkAcdG}}},$$

where $[\text{ShkA}]_{\text{T}}$ is the total concentration of ShkA. $K_{\text{D,ShkAcdG}}$ is the dissociation constant of binding/unbinding reaction.

We were unable to find information regarding temporal regulation of ShpA in the literature. Thus, we turn to the similar CckA-ChpT-CtrA pathway modeled in Chapter 4 for insight. ChpT concentrations are stable throughout the cell cycle [137], and therefore the kinetics of ChpT transfer were collapsed into the transfer of phosphates between CckA and CtrA directly, to simplify the model. Similarly, we assume that ShpA concentrations are constant throughout the cell cycle and model phosphate transfer between ShkA and TacA directly.

CtrA~P directly promotes the expression of *shkA* [113] and *tacA* [248]. Additionally, ShkA and TacA are both proteolyzed by ClpXP, but depend on different arrangements of adaptor molecules [248]. The proteolysis of ShkA requires the adaptors, PopA, cdG, RcdA and CpdR, while TacA proteolysis only requires CpdR and RcdA adaptors [248]. Therefore, the ShkA-TacA pathway includes both cdG-mediated activation and cdG-dependent degradation. We model the ShkA-TacA pathway as follows:

$$\frac{\text{d}[\text{ShkA}]_{\text{T}}}{\text{dt}} = k_{\text{s,ShkA}} \frac{[\text{CtrA}\sim\text{P}]}{[\text{CtrA}\sim\text{P}] + J_{\text{a,ShkA-CtrA}}} - \left(k_{\text{d,ShkA1}} + \mu\right) \cdot [\text{ShkA}]_{\text{T}} - k_{\text{d,ShkA2}} \cdot [\text{ClpXP}]_{\text{Complex}} \cdot \frac{[\text{ShkA}]_{\text{T}}}{[\text{ShkA}]_{\text{T}} + J_{\text{d,ShkA}}},$$

where $k_{\text{s,ShkA}}$ is the synthesis rate of ShkA and $J_{\text{a,CtrA-ShkA}}$ indicates the dissociation constant between CtrA~P with the *shkA* promoter. $k_{\text{d,ShkA1}}$ and $k_{\text{d,ShkA2}}$ represent the basal degradation rate and ClpXP-dependent degradation rate, respectively. $[\text{ClpXP}]_{\text{complex}}$ is the complex of ClpXP, cdG, RcdA and CpdR, as described later. $J_{\text{d,ShkA}}$ is the dissociation constant between ShkA and the ClpXP complex.

Regulation of TacA is described as:

$$\frac{\mathrm{d[TacA]}}{\mathrm{dt}} = k_{\mathrm{s,TacA}} \cdot \frac{[\mathrm{CtrA\sim P}]}{[\mathrm{CtrA\sim P}]+J_{\mathrm{a,CtrA\text{-}TacA}}} - (\mu + k_{\mathrm{d,TacA1}}) \cdot [\mathrm{TacA}] - k_{\mathrm{d,TacA2}} \cdot [\mathrm{RcdA{:}CpdR}] \cdot \frac{[\mathrm{TacA}]}{[\mathrm{TacA}]+J_{\mathrm{d,TacA}}} - k_{\mathrm{phos,TacA}} \cdot [\mathrm{ShkA{:}cdG}] \cdot [\mathrm{TacA}] + k_{\mathrm{dephos,TacA}} \cdot [\mathrm{TacA\sim P}],$$

$$\frac{\mathrm{d[TacA\sim P]}}{\mathrm{dt}} = -k_{\mathrm{d,TacA2}} \cdot [\mathrm{RcdA{:}CpdR}] \cdot \frac{[\mathrm{TacA\sim P}]}{[\mathrm{TacA\sim P}]+J_{\mathrm{d,TacA}}} + k_{\mathrm{phos,TacA}} \cdot [\mathrm{ShkA{:}cdG}] \cdot [\mathrm{TacA}] - (\mu + k_{\mathrm{d,TacA1}} + k_{\mathrm{dephos,TacA}}) \cdot [\mathrm{TacA\sim P}],$$

Where $k_{\mathrm{s,TacA}}$ represents the synthesis rate of TacA. $k_{\mathrm{d,TacA1}}$ and $k_{\mathrm{d,TacA2}}$ indicate the rate of basal degradation and degradation catalyzed by the protease complex, ClpXP:CpdR:RcdA, respectively. $k_{\mathrm{phos,TacA}}$ and $k_{\mathrm{dephos,TacA}}$ indicate the phosphorylation and dephosphorylation constants of TacA, respectively.

The refurbished equation of SpmX is:

$$\frac{\mathrm{d[SpmX]}}{\mathrm{dt}} = k_{\mathrm{s,SpmX}} \frac{[\mathrm{TacA\sim P}]}{[\mathrm{TacA\sim P}] + J_{\mathrm{a,TacA-SpmX}}} - \left(k_{\mathrm{d,SpmX}} + \mu\right) \cdot [\mathrm{SpmX}]$$

where $k_{\mathrm{s,SpmX}}$ and $k_{\mathrm{d,SpmX}}$ represent the synthesis and proteolysis rate of SpmX, respectively. $J_{\mathrm{a,TacA\text{-}SpmX}}$ indicates the binding affinity between TacA~P and *spmX* promoter.

5.3.6 Calculating DivK~P/DivK$_T$ Bifurcation Regions:

To capture DivK phosphorylation activity at fixed concentrations of DivL, PleC and DivJ, we reduced our larger model into a smaller model that captures how these proteins interact with DivK and impact its phosphorylation. See Appendix C.1.2 for a full set of equations for the DivK reduced model.

To calculate the steady-state DivK~P:DivK$_T$ fraction under different conditions, the reduced model was simulated for 300 minutes using MATLAB's ode15s. To find the bistable region, the model was simulated with initial conditions such that DivK~P=DivK$_T$ and DivK$_U$=DivK$_T$. Simulations resulting in identical steady-states indicates monostability while those with two different steady-states indicate bistability. We then capture the bifurcation points by tracing the lines that separate monostability from bistability. The line that separates high DivK~P:DivK$_T$ monostable behavior from bistable behavior we refer to as a PleC threshold.

To predict how the PleC threshold changes under different conditions of DivK and SpmX, we construct hundreds of 2D bifurcation diagrams (PleC vs DivJ concentrations) under various expression levels of SpmX and DivL. By incorporating the data for the resulting thresholds into the MATLAB function, griddata, we then estimate for any DivJ, DivK and SpmX concentration what the corresponding PleC concentration is at the PleC threshold. Thus, when we run our starvation simulations, we can estimate how the PleC threshold evolves over time with respect to the system and reliably estimate when the PleC concentrations cross the PleC threshold.

5.3.7 Deriving Parameter Sets

Given the nature of this chapter, it was necessary to ensure that the new model was relatively reliable at predicting DivK~P levels. Thus, we incorporated mutant DivK~P data into our parameterization algorithm for numerous mutants to guide our model into accurate parameter sets for DivK~P. In general, we utilized the same parameterization algorithm as specified in Chapter 3. However, the full list of mutant strains used is as follows: {Δ*pdeA*, Δ*pleD*, Δ*ccrM*, Δ*gcrA*, Δ*popA*&P*divK*::Tn, P*pleC*::Tn, *divL*A601L, LS1, *ctrA*D51E, *ctrA*Δ3Ω, cdG$_0$, Δ*divJ*, Δ*spmX*}.

Cell cycle scores for Δ*pdeA*, Δ*pleD*, Δ*ccrM*, Δ*gcrA*, Δ*popA*&P*divK*::Tn, *divL*A601L, LS1, *ctrA*D51E, *ctrA*Δ3Ω, and cdG$_0$ were all scored as indicated in Chapter 3.

P*pleC*::Tn, , Δ*divJ*, and Δ*spmX* mutants were scored as follows:

$$S_{\mathrm{m,CT}} = \zeta_{\mathrm{m,CT}} \cdot \left(\frac{1500}{N_{\mathrm{cycles}}}\right)^2 + \frac{S_{\mathrm{m}}^{\mathrm{DivK}}}{2} + \left(1 - \zeta_{\mathrm{m,CT}}\right) \cdot \left(\sum_{c}^{3} \frac{S_{\mathrm{m,CT}}^{c}}{3} + \sigma_{S_{\mathrm{m,CT}}}\right),$$

where $\zeta_{\mathrm{m,CT}}$ is the arrest coefficient for species m of cell type CT and is equal to one if the cell cycle is arrested and zero if not. $S_{\mathrm{m}}^{\mathrm{DivK}}$ is the DivK related score for species m, $S_{\mathrm{m,CT}}^{c}$ is the cell cycle specific score and $\sigma_{S_{\mathrm{m,CT}}}$ is the standared deviation of cell cycle specific scores. For more details and context regarding cell cycle specific scores, see Chapter 3.

Cell cycle specific scores are calculated the same for P*pleC*::Tn, , Δ*divJ*, and Δ*spmX* such that:

$$S_{\mathrm{m,SW}}^{c} = \left(\frac{t_{\mathrm{div},c} - 145}{5}\right)^2 + \left(\frac{t_{\mathrm{rep},c} - 20}{4}\right)^2,$$

$$S_{\mathrm{m,ST}}^{c} = \left(\frac{t_{\mathrm{div},c} - 115}{5}\right)^2,$$

where $t_{\mathrm{div,c}}$ and $t_{\mathrm{rep,c}}$ indicate the time of division and chromosome replication in cell cycle, c.

DivK specific scores are calculated as:

$$S_{\mathrm{P}pleC::\mathrm{Tn}}^{\mathrm{DivK}} = 3500 \cdot \left(\left(\frac{DivKP_{\mathrm{P}pleC::\mathrm{Tn}}}{DivKP_{\mathrm{WT}}} - 1.6\right)^2 + \left(\frac{DivKP_{\mathrm{P}pleC::\mathrm{Tn}} \cdot DivKT_{\mathrm{WT}}}{DivKT_{\mathrm{P}pleC::\mathrm{Tn}} \cdot DivKP_{\mathrm{WT}}} - 2\right)^2\right),$$

$$S_{\Delta divJ}^{\mathrm{DivK}} = \left(500 \cdot \left(\frac{DivKP_{\Delta divJ}}{DivKP_{\mathrm{WT}}} - 0.06\right)\right)^2,$$

$$S_{\Delta spmX,\mathrm{SW}}^{\mathrm{DivK}} = \left(350 \cdot \left(\frac{DivKP_{\Delta spmX} \cdot DivKT_{\mathrm{WT}}}{DivKT_{\Delta spmX} \cdot DivKP_{\mathrm{WT}}} - 0.36\right)\right)^2,$$

where $DivKP_{\mathrm{m}}$ and $DivKT_{\mathrm{m}}$ are the average DivK~P levels and total DivK levels, respectively, for species m.

5.4 Results

5.4.1 Investigating Performance of Model

To model the starvation response of *Caulobacter* we first build on to the model of Chapter 4, as discussed in the Methods section. Our revised network includes additions of the ShkA-TacA-SpmX pathway and several signaling mechanisms (Figure 5.2).

To ensure our new model and parameter sets are in sufficient agreement with experimentally observed behavior, we repeat the analysis of Chapter 4 with the new parameter sets. In Chapter 4, Quick and Slow parameter sets both had an 88.6% success rate in predicting mutant strain viability. Chapter 5 parameter sets perform slightly better, with a 92.9% success rate (Figure 5.3A). When plotting our wild type (WT) swarmer cell simulation to experimental data (Figure 5.3A and Figure C.1), we conclude that our model fits the data relatively well.

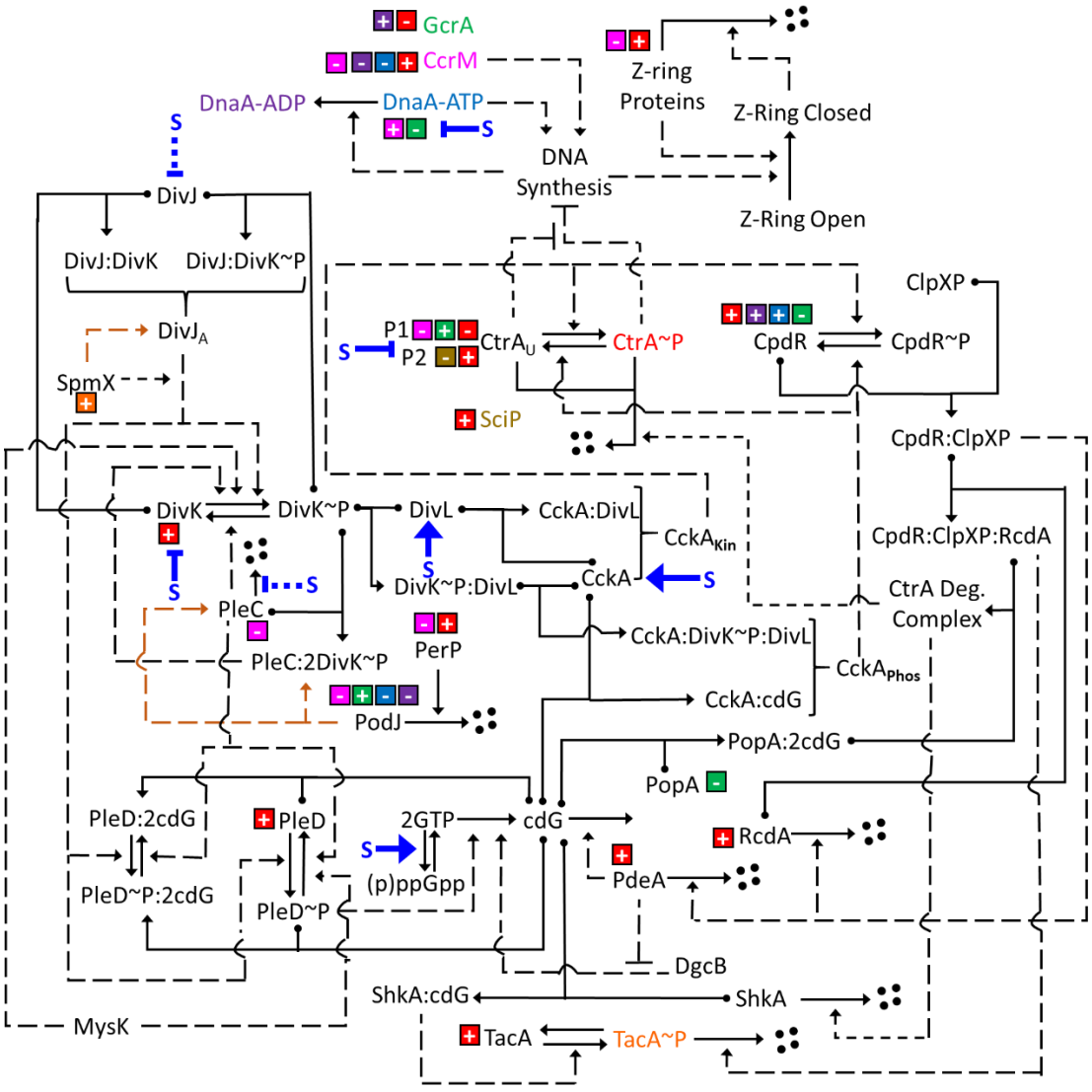

Figure 5.2) Wiring diagram of regulatory interactions captured by the model.
Genetic regulation is depicted by a color-coded scheme: for each protein that interacts with a promoter, a box with a plus or minus sign indicates whether the protein activates or inhibits expression of the gene, and the color of the box identifies the regulatory protein (e.g., green = GcrA). Proteins that combine to form complexes are marked by solid dots on the arms of a T-shaped arrow pointing to the resulting complex (e.g., PopA and RcdA form the PopA:RcdA complex). Chemical conversion of one molecular species to another is indicated by an arrow (e.g., CtrA to CtrA~P). Proteolysis is depicted by an arrow from a protein to four black circles. Dashed arrows indicate an 'influence' (e.g., catalysis) of a protein on a chemical reaction (e.g., PleC dephosphorylates DivK~P). A dashed orange arrow indicates that one molecule influences the localization of another (e.g., PodJ affects the location of PleC). A bright blue S and corresponding interactions indicates an element of starvation signaling (see Table 5.1). Solid blue lines indicate influencing interactions supported by observations, while dashed blue lines indicate hypothetical signals proposed in this study.

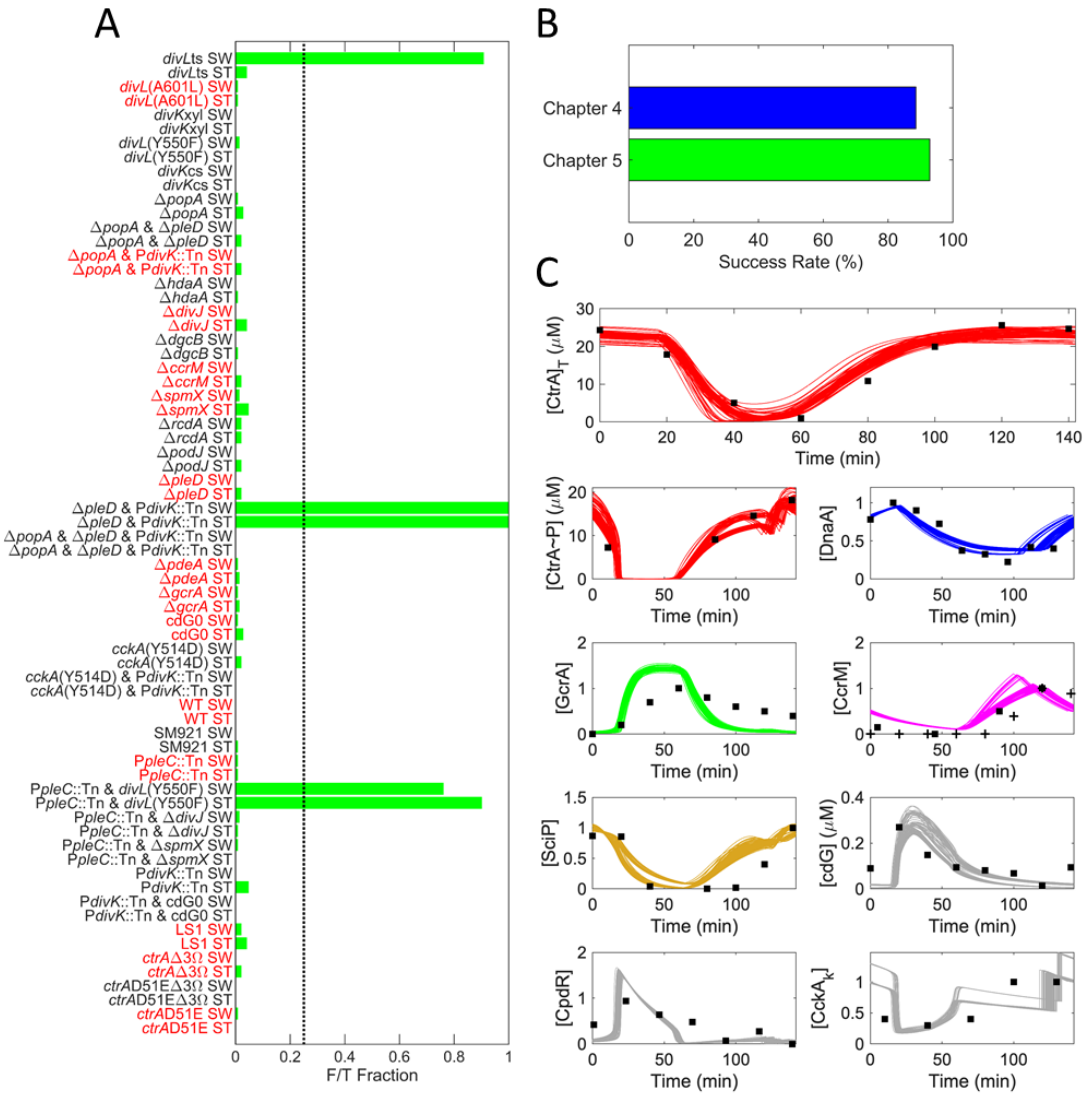

Figure 5.3) Model and parameter sets fit experimental data reasonably well.
(A) The fraction of total simulations that failed (F/T fraction) is plotted for each mutant case. A simulation is considered to have 'failed' if it predicts cell cycle arrest when experimental observations report a viable cell cycle, or vice versa. See Table B.2 for details on mutant simulations. For each mutant, 150 parameter sets were chosen at random from each parameter set collection and simulated for both swarmer cell (SW) and stalked cell (ST). The black dashed line corresponds to an arbitrary threshold (25%) that we use to compute the success rate of strain prediction. Strains labeled with red font were included in the parameterization cost function.
(B) The model presented in here (Chapter 5) performed with a 92.9% success rate. In comparison, models from Chapter 4 (QUICK and SLOW) performed with an 88.6% success rate. A strain simulation is considered successful if 75% or more of simulations agree with experimental observations on cell cycle arrest behavior.
(C) For 100 randomly selected SLOW parameter sets, we plot swarmer-cell simulations in comparison to experimental data, using the same color code as in Figure 5.2. The large spikes in [$CckA_K$] and [CpdR] near the end of the cell cycle (when the Z-ring closes) are artifacts of our modeling methodology (see Chapter 3 for details). Data collected as follows: [$CckA_K$]: Jacobs *et al*. 2003, Fig 3A; [CpdR]: Iniesta *et al*. 2006, Fig 5A; [cdG]: Abel *et al*.

2013, Fig 7; [SciP]: Tan *et al*. 2010, Fig 1B; [CcrM]:+, Zhou and Shapiro 2018, Fig 2A; [CcrM]: ■, Grunenfelder *et al.* 2001, Fig 2; [GcrA]: Holtzendorff *et al.* 2004, Fig 3B; [DnaA]: Cheng and Keiler 2009, Fig 2C; [CtrA~P]: Jacobs *et al*. 2003, Fig 3A; $[CtrA]_T$: Mcgrath *et al*. 2006, Fig 2C. In all plots except [cdG], $[CtrA]_T$ and [CtrA~P], concentrations are unitless and normalized to the experimental data, which predict relative concentrations at each time point are normalized to one. $[CtrA]_T$ and [CtrA~P] experimental data are also unitless, however, absolute CtrA concentrations in our model are a prediction and therefore the data is normalized to the simulation output. cdG levels are not normalized in any way, as absolute concentration is quantified from the source of the data.

Given that *Caulobacter* arrests at G1 under carbon starvation, at CtrA~P regulates the G1-S transition, we conduct further analysis to ensure that our model will accurately capture the regulation of CtrA phosphorylation. CckA is regulated through DivK and cdG [160]. The work of Xu *et al*. suggests that cdG should be depleted due to SpoT activity in starvation conditions [1], but the behavior of DivK phosphorylation has not been investigated, to the best of our knowledge, under carbon or nitrogen stress. To ensure our model can predict DivK~P levels reliably, we evaluate DivK~P levels measured in mutants from two different papers: 1) Wheeler and Shapiro (1999) [24]; 2) Radhakrishnan *et al*. (2008) [152]. Cumulatively, these papers investigated five mutant strains, with only two strains overlapping (Table 5.2). These include a *divJ* knock out (Δ*divJ*) and a *pleC* knock out (Δ*pleC* and P*pleC*::Tn5) strains. We find that the two papers predict similar qualitative results, but report dramatically different levels for DivK~P. For instance, Wheeler and Shapiro report that normalized DivK~P levels were 168% of WT in P*pleC*::Tn5 cells, while Radhakrishnan *et al*. report that the normalized ratio of DivK~P:$DivK_T$ levels are 430% of WT in Δ*pleC* cells. We note that both, P*pleC*::Tn5 and Δ*pleC*, are *pleC* knock out strains and should behave identically. Therefore, if both of these papers reported values were in agreement, $DivK_T$ levels would have to be ~60% lower in WT than in *pleC* knock out strains. Similarly, for the results of the Δ*divJ* strains to be in agreement, $DivK_T$ levels must be ~500% higher than WT. Such dramatic shifts in DivK expression seem unlikely, especially in Δ*divJ*. We therefore conducted our own analysis of the Western blots provided by Wheeler and Shapiro and Radhakrishnan *et al*. utilizing ImageJ software. We found that the results of the two papers were much closer utilizing our independent analysis. We estimate that the normalized DivK~P levels in *pleC* knock out strains are 142% and 179% of WT from the Wheeler and Shapiro and Radhakrishnan *et al*. papers, respectively (Table 5.2). We found similar improvements in the Δ*divJ* analysis.

Next, we investigate how our model performs against DivK expression data and find reasonable agreement with experimental analysis. The one exception was with the performance of the Δ*spmX* & Δ*pleC* double mutant, where our model predicts DivK~P levels to be significantly less than experimental observation. It is possible that our parameter sets can be improved further to fit this behavior, but generally higher DivK~P levels in the *spmX*&Δ*pleC* would require greater MysK activity, decreased basil alternatively it may be that aspects of MysK or CckN activity that are not accounted for in the model are necessary to explain this behavior.

Table 5.2) DivK~P levels in various mutant strains.

	Normalized DivK~P (%)				Normalized Ratio $\frac{\text{DivK~P}}{\text{DivK}_T}$ (%)			
Source of Data	Ref [24]	Ref [24]	Ref [152]	Model Results	Ref [152]	Ref [152]	Ref [24]	Model Results
Source of Analysis	Ref [24]	This study*	This study*	This study	Ref [152]	This study*	This study*	This study
WT	100	100	100	100	100	100	100	100
Δ*spmX*	-	-	36	45	28	36	-	39
Δ*divJ*	44	8	4	8	9	4	7	5
P*pleC*::Tn*5*/Δ*pleC*	168	142	179	152	430	225	170	178
Δ*spmX*&Δ*pleC*	-	-	187	117	388	222	-	126
Δ*divJ*&P*pleC*::Tn	27	7	-	40	-	-	7	35

*: Analysis conducted using ImageJ software.

5.4.2 Introducing Known Signaling Mechanisms of Carbon/Nitrogen Starvation (Signal 1) Results in secondary G1 arrest

Given reasonable agreement of our model with experimental data, we proceed to investigate how our model responds to environmental signals. However, the exact mechanism of nutrient signaling is not clear in many cases. For instance, it is observed that GcrA levels decrease significantly under carbon starvation [113], but whether this is a downstream consequence of shifts in transcription factor activity (e.g. due to shifts in CtrA activity) or due to an independent

signaling mechanism is unclear. Therefore, we take a step by step approach to introducing signals into our network to investigate what elements of starvation might be captured by what signals.

First, we introduce a signal that we define as 'Signal 1' (Table 5.1), which composes of inhibition to translation of *dnaA* and impaired synthesis of cdG due to the response of the PTS^{Ntr}-SpoT pathway [1]. We start with these two pathways because the mechanisms are best defined compared to other starvation observations and we know that these mechanisms operate independently. We note that we also artificially impair the synthesis of SpmX in Signal 1. While inhibition of SpmX should be a downstream effect of inhibiting cdG, the parameter sets described in this paper are unable to reliably capture this behavior. We will address this concern in the next iteration of our model, but for now we forcefully impair SpmX synthesis.

When introducing Signal 1 at t=0 (G1 phase/swarmer cell), we find that cell cycle arrest is not immediate, and that the cell completes one whole round of replication prior to arrest in G1 (Figure 5.4A and Table 5.1). We call this secondary G1 arrest. In contrast, experiments suggest that swarmer cell populations arrest immediately at G1 [208], [236], [237]. When introducing Signal 1 at t=45 (S phase/stalked cell), the cell cycle appears to be relatively unhindered but arrests at after cytokinesis G1 (Figure 5.4B & Table 5.1). However, stalked cells introduced to starvation should exhibit significant delays in cytokinesis [237]. Clearly, signaling through cdG and DnaA is not sufficient to explain experimental observations on cell cycle progression/arrest.

To identify whether or not Signal 1 can adequately explain DnaA and CtrA expression patterns, we plot simulations against temporal protein expression data of from a population of nitrogen starved swarmer cells, retrieved from Gorbatyuk *et al*. [208] (Figure 5.4C&D). Not surprisingly, we find that Signal 1 adequately explains DnaA expression but does not explain CtrA expression. This result suggests that depletion of DnaA in swarmer cells under carbon and nitrogen starvation is not sufficient to prevent chromosome replication. A closer investigation reveals that DnaA levels are about 35-45% of peak levels at the timing of chromosome replication. But should DnaA replication be possible at such levels or is this a consequence of inaccurate parameter choice? Leslie *et al*. 2015 showed that Caulobacter cells in stationary phase have DnaA levels that are ~10-18% of exponential phase [243]. Furthermore, since cells still divide, albeit slowly, in stationary phase, this suggests that 10-18% of typical DnaA levels

(compared to a nutrient rich simulation) should be sufficient for chromosome replication. Altogether, these results suggest that the rate of DnaA depletion is not nearly fast enough to explain G1 arrest without further interventions from starvation signaling; therefore, CtrA~P must remain sufficiently high to inhibit chromosome replication, at least until DnaA can be sufficiently depleted.

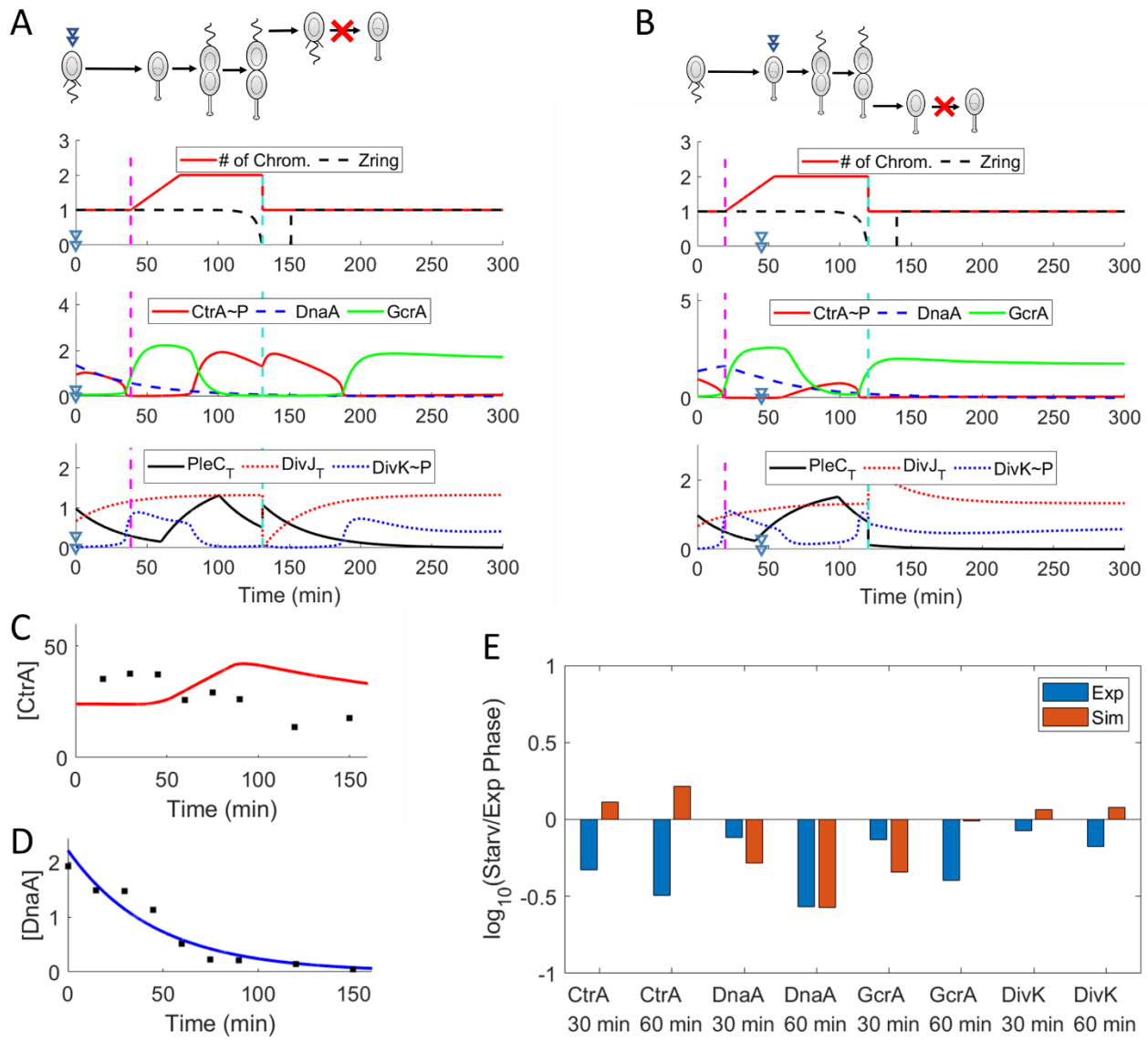

Figure 5.4) Starvation Signal 1 performs poorly.
(A) Swarmer cell simulation of Signal 1 response. Plot of chromosome count and Z-ring constriction (first panel) and select normalized protein concentrations (second and third panel). Concentrations are normalized to average WT expression. When the Zring variable is equal to 1, the Z-ring is fully open. It is closed when Zring is equal to 0. The corresponding position in the cell cycle is indicated in the illustration above. A double arrow indicates when the nutrient signal is introduced. A red "X" indicates that swarmer cells arrest in G1.
(B) Stalked cell simulation of Signal 1 response. Stalked cells arrest at G1 as indicated in the illustration. All other

details are the same as in "A".
(C) CtrA expression levels in swarmer cell simulations relative to normalized data extracted from Gorbatyuk *et al*. [208].
(D) DnaA expression levels in swarmer cell simulations relative to normalized data extracted from Gorbatyuk *et al*. [208].
(E) Protein expression levels 30 and 60 minutes after nutrient depletion relative to nutrient rich conditions. 'Exp' indicates experimental observations from Britos *et al*. [4]. 'Sim' indicates average simulation values from 30 and 60 minutes into simulations of swarmer, stalked and pre-divisional cells.

5.4.3 Introducing signals (Signal 2) that influence CckA, DivL and DivK levels leads to slight improvements in performance

Having identified that nutrient signaling must influence CtrA phosphorylation to induce immediate G1 arrest in swarmer cells, we turn our focus to the regulator of CtrA phosphorylation, the bifunctional kinase/phosphatase, CckA [247]. Unperturbed, CckA typically acts like a kinase, however interactions through DivK and cdG induce phosphatase activity. More specifically, DivK~P forms a complex with DivL which in turn binds to CckA to induce phosphatase activity, while cdG binds to CckA directly [138], [247]. It was demonstrated by Britos *et al*. that concentrations of DivK, CckA, and DivL all significantly shift within 60 minutes after shifting environmental conditions from nutrient-rich to glucose depleted media [4]. However, Signal 1 simulations suggested that DivK levels should increase 60 minutes after the nutrient shift and our equations dictate constant synthesis rates for DivL and CckA as WT mRNA data for *divL* and *cckA* are relatively constant [113], [187]. Thus, we develop Signal 2, which composes of the perturbations from Signal 1 (i.e. impaired cdG synthesis and transcription of *dnaA*) with the addition to increased expression of DivL and CckA and reduced expression of DivK.

First, we simulate swarmer cells with Signal 2 and find that 18.2% of our parameter sets indicate immediate cell cycle arrest at G1 while ~80% complete one full cell cycle and arrest at the second G1 (Table 5.1). While an ideal result would demonstrate 100% arrest at the first G1 phase, this is an improvement over Signal l results. To evaluate which of the three proteins might contribute most to immediate G1 arrest, we next simulated each change individually. We find that individual changes to expression of CckA, DivL and DivK leads to 1st G1 arrest rates of 0%, 0% and 17.6%, respectively (no corresponding figure or table for this result). Thus, the concentration of DivK must be the largest contributing factor to rapid G1 arrest.

5.4.4 Investigation into DivK regulation

To investigate how DivK concentration influences G1 arrest, we develop a reduced model of DivK phosphorylation (see Methods) and begin our analysis by constructing a heat map depicting the steady-state ratio of DivK~P to $DivK_T$ over a range of DivJ and PleC concentrations. First, we find that, for any given DivJ concentration, DivK~P:$DivK_T$ changes dramatically in a switch-like fashion at a corresponding PleC concentration. Second, we find that the PleC concentration corresponding to this "switch" event changes depending on the initial concentration. In Figure 5.5A and B, we show a heat map resulting from simulations with initial conditions of $DivK_U$=$DivK_T$ and DivK~P=$DivK_T$, respectively. This indicates that there is a region of bistability, where the steady-state solution depends on the initial conditions of the simulation.

In Figure 5.5C, we demonstrate this bistable region and illustrate how a cell typically navigates through the two-dimensional grid. A swarmer cell will express high PleC levels and low DivJ levels. This corresponds to a region of low DivK~P. As the cell cycle proceeds, DivJ levels increase and PleC levels decrease, which results in a shift towards high DivK~P, dephosphorylation of CtrA and progression into S phase and a stalked phenotype. Once the chromosome is replicated, PleC levels begin to increase as the cell transitions into G2, and conditions favor DivK~P once again. Finally, when the cell divides, localized DivJ remains in the stalked cell while localized PleC remains in the swarmer cell. This results in immediate transition into S phase for the stalked cell, while S phase does not begin in the swarmer cell until DivJ levels accumulate again and PleC levels decrease.

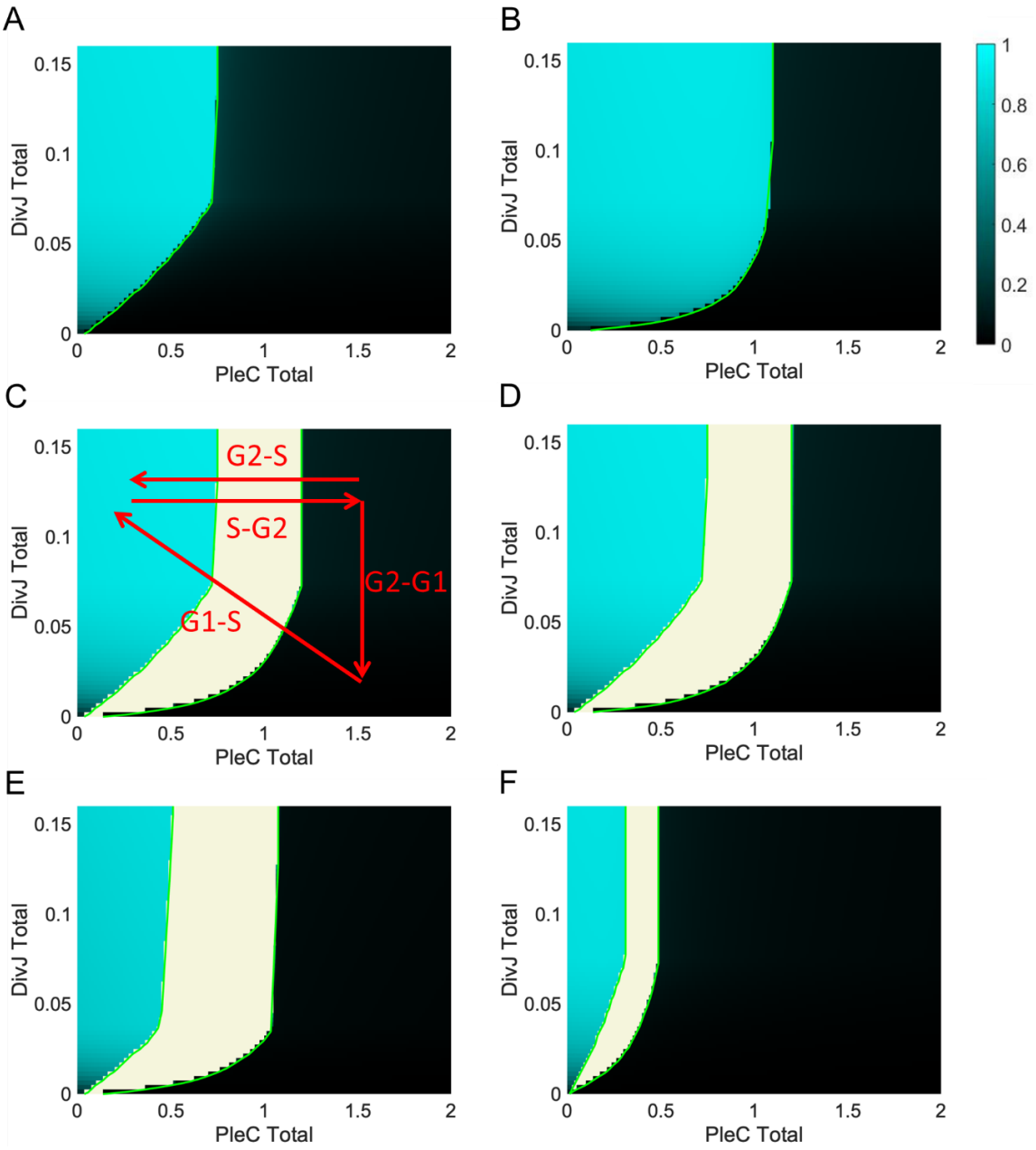

Figure 5.5) DivK~P exhibits bistable behavior over a range of PleC and DivJ concentrations.
Heat map demonstrates DivK~P:$DivK_T$ ratios as indicated by the color bar on the upper right. White regions designate bistability. A green line is plotted to track the edges of the bistable region.
(A) Simulations under SpmX, DivL and DivK total concentrations equivalent to stalked cell expression levels. Initial condition: DivK~P = $DivK_T$.
(B) Simulations under SpmX, DivL and DivK total concentrations equivalent to stalked cell expression levels. Initial condition: DivK~P = $DivK_T$. Initial condition: $DivK_U$ = $DivK_T$
(C) Plot all three stability regions under initial conditions indicated in (A) and (B). White shading indicates the region of bistability. A typical cell cycle moves through all 3 regions in the various stages of the cell cycle.
(D) Same as (C), with $DivL_T$ reduced by 50%.
(E) Same as (C), with SpmX reduced by 50%.
(F) Same as (C), with $DivK_T$ reduced by 50%.

Next, we investigate how SpmX, $DivK_T$ and $DivL_T$ concentrations influence the bifurcation behavior. Note that CckA is not investigated here as it has no influence over DivK bifurcation because its activity is downstream of DivK. First, reducing $DivL_T$ by 50% resulted in very small changes to the bifurcation patterns (Figure 5.5D). However, reducing SpmX levels by 50% lead to a significant reduction in 2-dimensional space corresponding to high DivK~P:$DivK_T$ (Figure 5.5E). Simulations of bifurcation when $DivK_T$ is reduced by half show a dramatic reduction of bistable space (Figure 5.5F), and a strong depreciation in 2-dimensional space associated with high DivK~P:$DivK_T$. In other words, the line that separates the DivK~P:$DivK_T$ high zone from the bistable zone (left-most green line in Figures 5.5C-F) shifts dramatically to the left when SpmX and $DivK_T$ levels are reduced. From this point forward, we will refer to this line as the PleC threshold.

The PleC threshold is significant to the G1-S transition, as it indicates when DivK becomes highly phosphorylated and therefore indicates when CckA phosphatase turns on, which leads to rapid degradation and dephosphorylation of CtrA. In the context of a swarmer cell during carbon and nitrogen starvation, DivK concentration declines over time resulting in constant movement of the PleC threshold. Simultaneously, PleC concentrations decrease and DivJ concentrations increase. We suspect that the timing of intersection between the 2-dimensional trajectory (DivJ and PleC) and the PleC threshold is a contributing factor towards cell cycle arrest, as a larger delay would allow more time for DnaA to be sufficiently proteolyzed to impair chromosome replication. To investigate this hypothesis, we identify one parameter set that exhibits immediate swarmer cell (G1) arrest in response to Signal 2, and another that results in secondary G1 arrest (after one full cell cycle). By computing the concentrations of DivJ, DivK, and SpmX over the course of Signal 2 temporal simulations, we estimate what the PleC concentration must be at each time point to cross the PleC threshold (Figure 5.6). Figure 5.6A demonstrates a cell that exhibits secondary G1 arrest. We observe that the PleC concentration intersects with the PleC threshold at approximately 47 minutes after the nutrient shift. In comparison, the simulation that results in immediate G1 arrest (Figure 5.6B) demonstrates intersection at roughly 59 minutes after the nutrient shift. Additionally, both simulations indicate that the PleC threshold moves away from the PleC concentration over time, resulting in longer delays. We find that, in cells with postponed and immediate G1 arrest, the shift in the PleC threshold delays the timing of the intersection by about 20 minutes and 30 minutes, respectively. This result supports our

hypothesis, that longer delays in the timing of the PleC threshold intersection can lead to immediate G1 arrest.

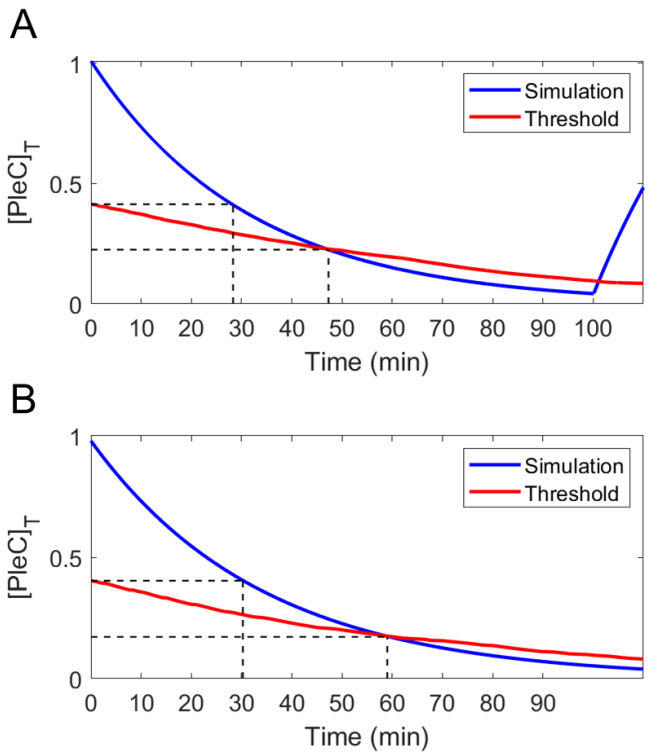

Figure 5.6) Swarmer cells that exhibit secondary G1 arrest cross the PleC threshold faster than those that exhibit immediate G1 arrest.

(A) Simulation of a swarmer cell that exhibits secondary G1 arrest in response to Signal 2. Blue line indicates PleC concentration over time and the red line indicates the PleC threshold. Black dashed lines indicate the concentration and time corresponding to when the simulated PleC concentration crosses the PleC threshold and the time that the lines would have intersected if the threshold did not change over time.

(B) Simulation of a swarmer cell that exhibits immediate G1 arrest in response to Signal 2. Other details are identical to (A).

5.4.5 Simulation of Signal 3 – Impaired PleC proteolysis

In consideration of Signal 2 results, we find it likely that starvation signaling targets variables that can delay the timing of the PleC threshold intersection. Thus, we develop Signal 3 that enhances the stability of PleC by reducing the degradation rate of PleC by 80% while maintaining the mechanisms of Signal 2 (Table 5.1). We find that Signal 3 results in consistent, rapid G1 arrest in swarmer cells and stalked cells (Figure 5.7A&B and Table 5.1). To investigate the system with respect to the PleC threshold, we take the parameter set that exhibited secondary G1 arrest with Signal 2 (Figure 5.6A) and simulate it with Signal 3 (Figure 5.7F). We see that the intersection between the PleC concentration and the PleC threshold occurs at ~67 min, which is roughly 20 minutes longer than we observed for Signal 2. Overall, these results suggest that prolonged DivK phosphatase activity is necessary for robust G1 arrest during carbon and nitrogen starvation.

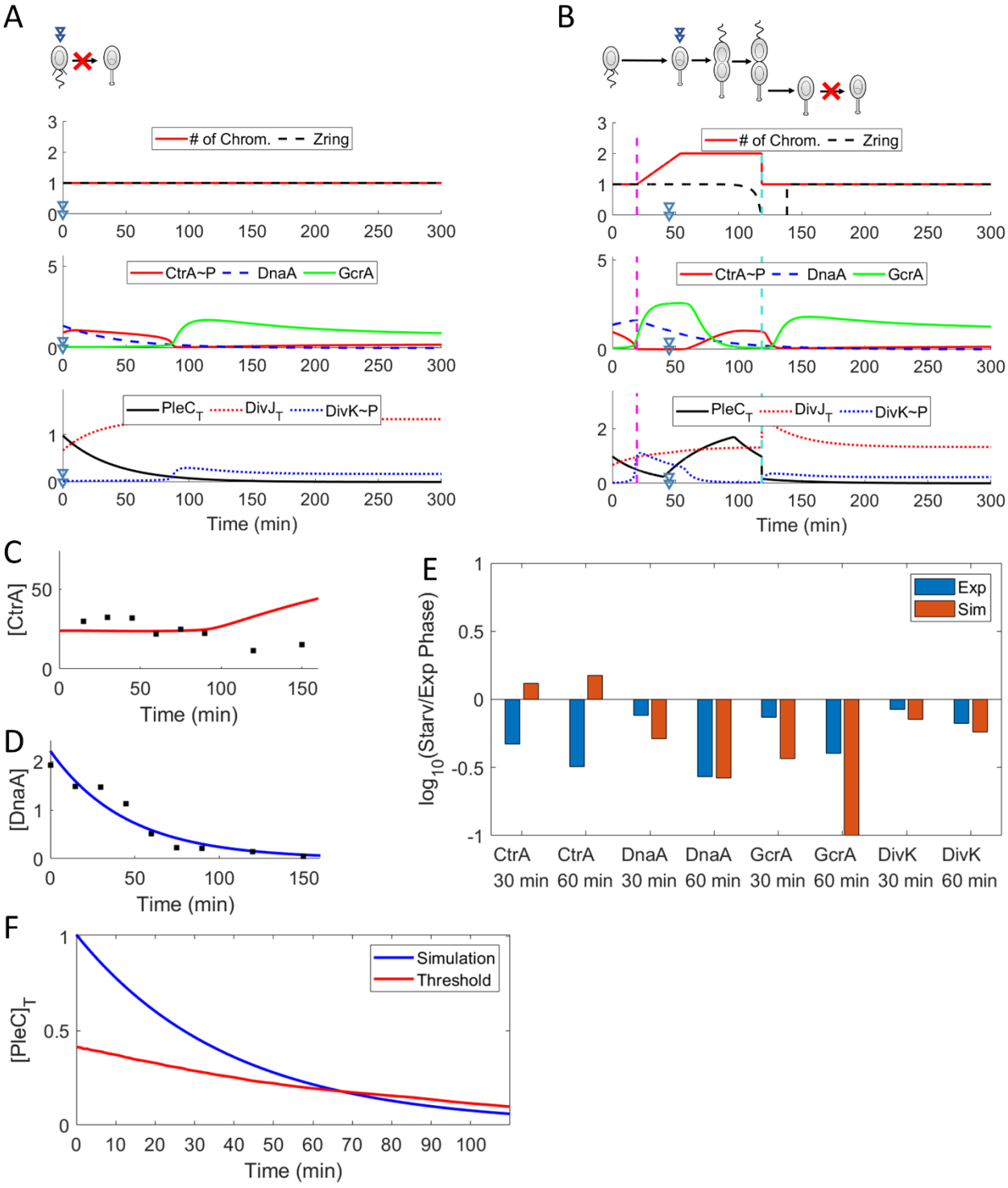

Figure 5.7) Starvation Signal 3 simulations fit experimental observations well with the exception of CtrA expression.

(A) Swarmer cell simulation of Signal 3 response. Red "X" indicates immediate G1 arrest. Other details are identical to Figure 5.4A.

(B) Stalked cell simulation of Signal 3 response. Red "X" indicates G1 arrest in stalked daughter cell. Other details are identical to Figure 5.4A.

(C) CtrA expression levels in swarmer cell simulations relative to normalized data extracted from Gorbatyuk *et al*. [208].
(D) DnaA expression levels in swarmer cell simulations relative to normalized data extracted from Gorbatyuk *et al*. [208].
(E) Protein expression levels 30 and 60 minutes after nutrient depletion relative to nutrient rich conditions. Details specified in Figure 5.4E.
(F) Simulation of swarmer cell response to Signal 3. Parameter set was the same used in Figure 5.6A. See 5.6A for details.

Given that Signal 3 successfully captures *Caulobacter* cell cycle arrest in swarmer and stalked cells, we investigate how well simulations agree with experimentally observed protein expression levels. We find our simulations seem to underestimate GcrA levels but dramatically overestimate CtrA levels. Our Signal 3 simulations suggest that CtrA levels should increase compared to average levels in nutrient-rich conditions, while experiments show that they should decrease significantly. Additionally, levels of CtrA~P influence GcrA levels [113], which may explain why GcrA expression for Signal 1 and Signal 2 differ from experimental observation (Figure 5.4E and C.2E). Collectively, these results suggest that an additional signal not considered here is likely responsible for the downregulation of CtrA. Experiments suggest that CtrA may be impaired by SigT [4]. However, the true mechanism remains unknown. Thus, we build on top of Signal 3 an additional signal to impair CtrA synthesis and call the resulting paradigm Signal 4.

5.4.6 Simulation of Signal 4 – reduced synthesis of CtrA

Simulations with Signal 4 shows good agreement with the experimental CtrA expression pattern from Gorbatyuk *et al*. [208] (Figure 5.8C) and agrees with Britos *et al*. that CtrA expression is reduced at 30 min and 60 min after glucose is removed compared to nutrient-rich conditions; however, CtrA levels are not as low as Britos *et al*. results suggest [4]. Similarly, GcrA levels at 30 and 60 min after glucose depletion are predicted to be below nutrient-rich conditions, but not as low as Britos *et al*. suggest. Additionally, stalked cell simulations (introducing nutrient depletion at t = 45 min) show significant delays in cytokinesis with cell division occurring around 200 min, a finding that is consistent with experimental observations [237]. In comparison, Signal 3 predicted that starved stalked cells would divide around 120 min. Thus, Signal 4 suggests that decreased expression of CtrA contributes to observed delays in cytokinesis of starved stalked cells.

Overall, Signal 4 simulations agree well with experimental observations for *Caulobacter*'s starvation response. However, the most detailed resource for starvation response is Britos *et al.*, who gathered data on protein and mRNA expression levels at 30 min and 60 min after starvation. We find that the expression levels of proteins at 30 min and 60 min is perhaps not a good indicator of long term response. In starved swarmer cell populations, our simulations suggest that a large shift in behavior occurs at approximately 100 minutes after the nutrient shift as a consequence of PleC depletion below the PleC threshold. This results in an increase in GcrA and a shift from high levels of CtrA~P to high levels of $CtrA_U$.

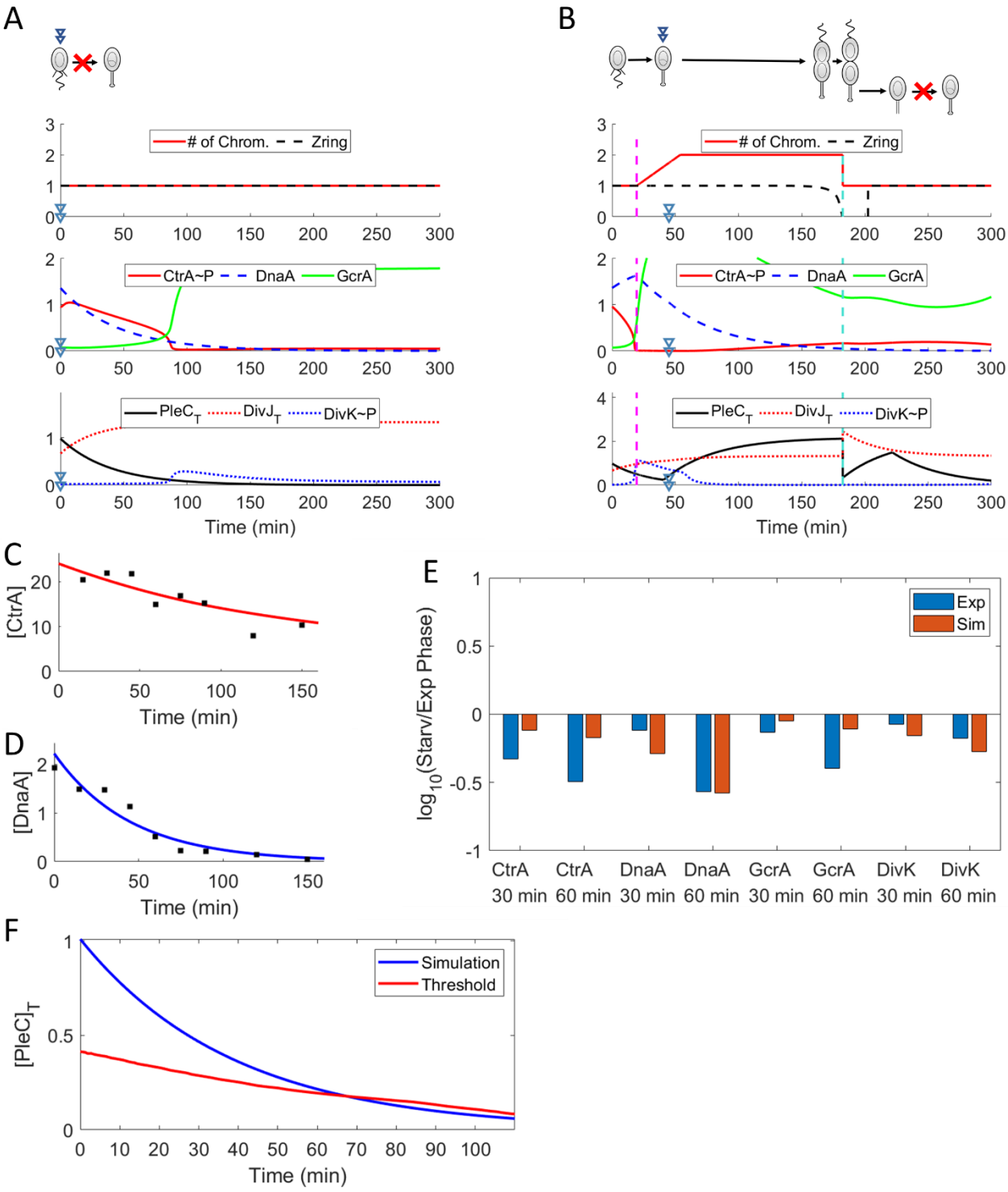

Figure 5.8) Starvation Signal 4 agrees well with experimental observations.
(A) Swarmer cell simulation of Signal 4 response. Red "X" indicates immediate G1 arrest. Other details are identical to Figure 5.4A.
(B) Stalked cell simulation of Signal 3 response. Red "X" indicates G1 arrest in the stalked daughter cell. Other

details are identical to Figure 5.4A.
(C) CtrA expression levels in swarmer cell simulations relative to normalized data extracted from Gorbatyuk *et al*. [208].
(D) DnaA expression levels in swarmer cell simulations relative to normalized data extracted from Gorbatyuk *et al*. [208].
(E) Protein expression levels 30 and 60 minutes after nutrient depletion relative to nutrient-rich conditions. Details specified in Figure 5.4E.
(F) Simulation of swarmer cell response to Signal 4. See 5.6A for details.

5.4.7 Simulation of Signal 5 – Impaired DivJ synthesis

With Signal 3 and 4 we explored PleC stability as a target of starvation signaling to induce immediate G1 arrest in swarmer cell populations. However, alternative signaling mechanisms may exist. In our final signaling paradigm, Signal 5, we include all the aspects of Signal 4 but instead of stabilizing PleC, we destabilize DivJ (Table 5.1). Signal 5 simulations exhibit immediate G1 arrest in swarmer cell populations and delayed cytokinesis followed by G1 arrest in stalked cell populations. Indeed, simulations of PleC concentrations against the PleC threshold show significant delays in the timing of the intersection (Figure 5.9F). Additionally, protein expression patterns are very similar to Signal 4. Overall, these results suggest that starvation may influence DivJ kinase or PleC phosphatase activity for rapid, robust arrest at G1 in swarmer cell populations.

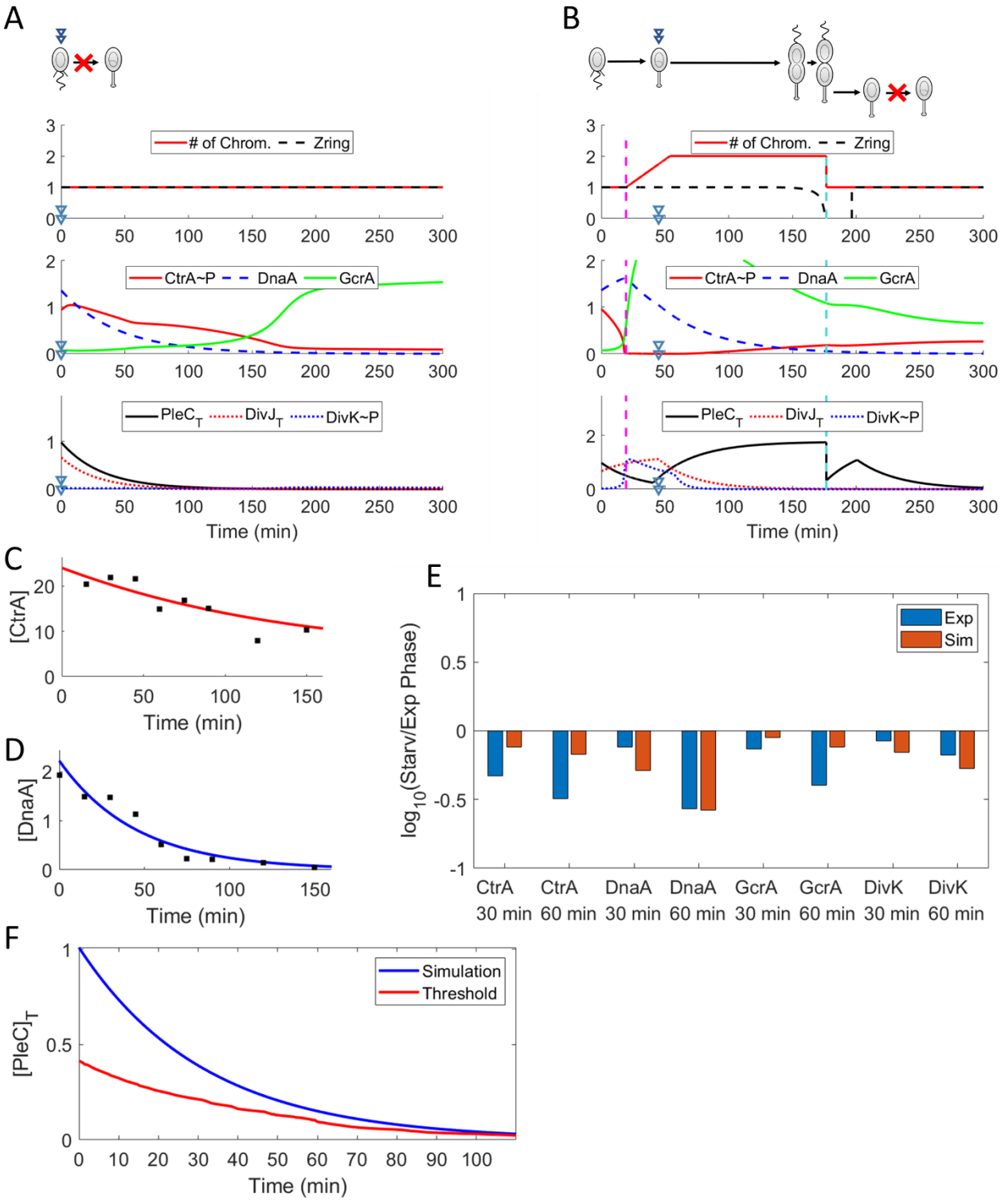

Figure 5.9) Starvation Signal 5 agrees well with experimental observations.
(A) Swarmer cell simulation of Signal 5 response. Red "X" indicates immediate G1 arrest. Other details are identical to Figure 5.4A.
(B) Stalked cell simulation of Signal 5 response. Red "X" indicates G1 arrest in stalked daughter cell. Other details are identical to Figure 5.4A.

(C) CtrA expression levels in swarmer cell simulations relative to normalized data extracted from Gorbatyuk *et al*. [208].
(D) DnaA expression levels in swarmer cell simulations relative to normalized data extracted from Gorbatyuk *et al*. [208].
(E) Protein expression levels 30 and 60 minutes after nutrient depletion relative to nutrient rich conditions. Details specified in Figure 5.4E.
(F) Simulation of swarmer cell response to Signal 5. See 5.6A for details.

5.5 Discussion

In this study, we investigated the molecular mechanism behind *Caulobacter* cell cycle arrest from carbon and nitrogen starvation. First, we probe the contributions of two signaling targets, DnaA transcription and cdG synthesis. We find that these two pathways are insufficient to explain immediate G1 arrest in swarmer cell populations, however they do predict G1 arrest in the second cell cycle when DnaA levels are too low to initiate chromosome replication. Not surprisingly, elimination of cdG lead to stable CtrA levels exceeding that of exponential phase cells. This suggests that nutrient signals must influence CtrA via additional mechanisms to explain reduced CtrA expression under carbon and nitrogen starvation. More importantly, these simulations demonstrated rapid dephosphorylation of CtrA within 40 min in nitrogen/carbon starved swarmer cells, leading to initiation of chromosome replication. Thus, carbon/nitrogen signaling likely influences CtrA phosphorylation to maintain CtrA~P levels and arrest at G1. In agreement with this hypothesis, levels of FliF and PilA were shown to remain stable after 80 minutes in carbon starved swarmer cells, while cells in nutrient-rich medium showed steady depletion of both proteins [236]. As *fliF* and *pilA* are both activated by CtrA~P [113], it stands to reason that CtrA~P levels remain high for at least 80 minutes after starvation conditions are induced.

Next, we turned our attention to proteins that influence CtrA phosphorylation. Britos *et al*. demonstrated that DivK levels decrease while DivL and CckA levels increase within 60 minutes of carbon starvation [4]. When we individually manipulate the expression of each protein, we find that only DivK levels make a difference in cell cycle arrest, with ~18% of parameter sets predicting immediate G1 arrest in carbon/nitrogen starved swarmer cells. Moreover, simulating perturbation to all three proteins simultaneously showed made a negligible impact compared to

only perturbing DivK. Overall, these results suggest that shifts in DivL and CckA concentrations in response to carbon and nitrogen starvation make a negligible impact to cell cycle dynamics, however, shifts in DivK concentration are significant to the starvation signaling pathway. A more rigorous analysis revealed that the *Caulobacter* cellular mechanisms consist of bifurcating behavior with regards to the DivJ and PleC concentrations. We find that the oscillations of DivJ and PleC concentrations influence the DivK~P:$DivK_T$ ratio by navigating through the regions of monostability and bistability. Furthermore, we find that total DivK concentrations and SpmX concentrations both significantly influence the bifurcation pattern such that reducing DivK and SpmX concentration under carbon and nitrogen starvation creates a large lag for the system to favor high DivK~P:$DivK_T$ ratio. This lag translates to a longer period of high CtrA~P levels which may afford DnaA enough time to degrade such that high CtrA~P expression is no longer necessary to inhibit chromosome replication. In other words, our analysis suggests that depletion of DivK and SpmX in response to carbon and nitrogen starvation leans the system in favor of DivK phosphatase/low DivK~P levels. As PleC levels decrease in G1, eventually the system leans in favor of DivK kinase, resulting in a dramatic shift in DivK~P levels leading to depletion of DivK~P. The longer the delay in this shift, the more likely DnaA will be sufficiently depleted to maintain G1 arrest.

As *Caulobacter* is an oligotroph, its response to starvation should be robust. Thus, we suspect that in response to carbon and nitrogen deprivation, *Caulobacter* likely directly signals to influence DivK kinase and/or phosphatase activity. Thus, we took the previously discussed signaling pathway (Signal 2, Table 5.1) and slowed down PleC proteolysis by 20% (Signal 3, Table 5.1) to find that 100% of swarmer cells arrested immediately in G1. As PleC is targeted by ClpXP proteolysis [252], it is possible that carbon or nitrogen signaling could interfere with ClpXP dependent degradation of PleC. Alternatively, it is possible to get similar results by targeting other DivK kinases or phosphatases. We found that impairing DivJ activity works just as well as targeting PleC. Recently, Coppine *et al*. demonstrated that synthesis of CckN, a DivK phosphatase, is elevated in response (p)ppGpp [252]. While CckN is not included in our model, we do have a term for basil DivK~P hydrolysis, $k_{hyd,DivK}$. We find that increasing $k_{hyd,DivK}$ by 5 in combination with Signal 2 is sufficient for 100% swarmer cell arrest. As these results indicate that CckN may be an important player in cell cycle response to carbon and nitrogen starvation, we intend to incorporate CckN into future iterations of the model.

As previously mentioned, our results indicate that additional starvation signals that target CtrA are necessary to explain decreased expression in carbon and nitrogen starved cells. When a signal impairing CtrA synthesis is paired with the previously mentioned signaling cascade, Signal 4 (collectively making Signal 5, Table 5.1), we find that the resulting simulations accurately predict significant delays in cytokinesis in starved stalked cell populations. This result seems to be a consequence of the slowed synthesis of Z-ring relevant proteins due to reduced levels of CtrA~P. While the delays in cytokinesis (~150 min) are not as significant as experimental observations (>200 min), we suspect that sluggish accumulation and assembly of the Z-ring likely contributes partially to the observed delays in cytokinesis.

In previous work, Xu *et al*. demonstrated that cdG levels are likely depleted due to the accumulation of (p)ppGpp, thus providing a link between (p)ppGpp regulation and CtrA proteolysis. cdG is also responsible for the accumulation of SpmX at the G1-S transition [248]. We expanded on this work here and found that the cdG response is not sufficient for cell cycle arrest. However, when we remove signals that impair cdG/SpmX from Signal 4 and 5, we find that immediate G1 arrest in swarmer cells is compromised (Figure C.3, Table C.2). Thus, while the proposed signal from Xu *et al*. is not sufficient on its own to explain starvation response behavior, it is an essential component to the starvation response.

In summary, our results indicate that numerous aspects of the cell cycle machinery are necessary targets of nutrient starvation response. For the first time, in this study we show that depletion of DivK concentration makes a significant contribution to carbon/nitrogen induced swarmer cell arrest. Our results further suggest that carbon/nitrogen starvation likely signals to at least one DivK kinase or phosphatase for robust, rapid G1 arrest in swarmer cells. In future works, we will expand on this model and explore the potential role of CckN in carbon and nitrogen starvation response.

Chapter 6 : Advancements to the field and future work

6.1 Overview of this work and corresponding advancements to the field

In this work, we applied systems biology techniques to study two different kinds of cells: Human granulocyte-monocyte progenitor (GMP) cells and the bacterium, *Caulobacter crescentus*. In both cases, we developed our mathematical models by first considering prior works. Here, we will discuss the works that inspire our models and how our work advances the field.

In 2006, Laslo et al. proposed a simple model composed of four transcription factors to describe how cell fate determination functions at the molecular level in GMP cells. Specifically, Laslo et al. described a symmetrical motif where PU.1 and C/EBPα stimulate Egr and Gfi-1, respectively, and Egr and Gfi-1 are mutually antagonistic [9]. While the proposed model was a reasonable first step in describing the lineage commitment process of GMP cells, it neglected numerous details and had little explanatory power. For instance, it is known that C/EBPα stimulates PU.1 synthesis [61], [62]. Given that these two proteins are essential regulators of GMP lineage commitment [3], [9], such an interactions between these two proteins cannot be ignored. Furthermore, the Laslo et al. model was insufficient to explain complex behavior, such as how GM-CSF can induce different responses at different concentrations [3]. In Chapter 2, we consider the details of molecular interactions in GMP cells to build a more detailed model of the GMP cell differentiation mechanism. We include additional proteins and molecular interactions necessary to explain the lineage commitment process of GMP cells. In this work, we explained the concentration dependent responses of this cell line to GM-CSF, the diverse responses of these cells to combinations of cytokines and we proposed the mechanism by which monocytic-myeloid derived suppressor cells (M-MDSCs) fit into the lineage commitment process. While the predictions of this model must be validated by experiments, the proposed model is a significant advancement in detailing the molecular mechanism of lineage commitment in GMP cells.

In Chapters 3-5, we develop models of the *Caulobacter crescentus* cell cycle. We drew inspiration from the work of Li et al., who published an ordinary differential equation (ODE) model of the *Caulobacter crescentus* cell cycle that considered genetic regulation, protein phosphorylation, DNA replication, cytokinesis and proteolysis [119]. This paper was a major step forward in the development of a comprehensive model of the *Caulobacter* cell cycle. However, it possesses a plethora of significant shortcomings. The most critical issue was that equations do not properly reflect the biology. An example of this is that mass is not conserved between stalked and swarmer cells upon cytokinesis in the simulations. Other issues include, but are not limited to, the inaccurate uses of Michaelis-Menten functions, describing non-linear interactions as linear and the implementation of false assumptions on gene expression activity of methylated and hemi-methylated genes. These issues are all addressed in the new models presented in Chapters 3-5. We also make copious improvements over Li et al. by incorporating several new proteins and regulatory interactions. These include the implementation of bifunctional kinase/phosphatase activity of PleC and CckA, inclusion of cyclic-di-GMP (cdG) and its regulating factors (PleD, DgcB, PdeA, etc.), the influence of cdG over CckA and CtrA proteolysis, significant improvements to the CtrA proteolysis model (in addition to cdG), the addition of SpmX regulation, the inclusion of SciP, improvements to biological accuracy of gene methylation and promoter activity, the inclusion of DnaA-ATP and DnaA-ADP hydrolysis and synthesis, and more. Overall, these improvements provide the scientific community with the most detailed and biologically consistent mathematical model of the *Caulobacter* cell cycle to date.

In Chapter 4, we provide computational evidence that the unphosphorylated form of CtrA ($CtrA_U$) competes with the phosphorylated form (CtrA~P) for *Cori* binding sites at physiologically relevant concentrations. We further provide evidence that this interaction is necessary to explain experimental observations in *Caulobacter* and that it results in substantial improvements to the efficiency of CckA phosphatase and stability over the G1-S transition. We suspect that our results could provide insight into regulatory mechanisms in other alphaproteobacteria as well, as *ctrA* is highly conserved [254]. Moreover, these results suggest that the "inactive form" of CtrA, $CtrA_U$, could serve additional roles that have not been identified by the *Caulobacter* community.

Lastly, in Chapter 5 we extend the reach of our model by applying it to nitrogen and carbon starvation. This marks the first attempt, to the best of our knowledge, for the utilization of systems biology to study stress response in *Caulobacter*. Our results suggest that much of what is known about the molecular mechanism of starvation signaling is insufficient to explain behavioral observations of *Caulobacter*. We find that it is likely that targeted dephosphorylation of DivK is essential to explain immediate G1 arrest in swarmer cell populations. While there is still more to be done, this work is a huge accomplishment and a step forward to understand the molecular carbon/nitrogen starvation response in *Caulobacter*.

6.2 Future work opportunities

This work opens many doors, each with unique paths to answer different questions. Here, we break down the potential directions into three primary categories: GMP related projects, *Caulobacter* ODE projects and *Caulobacter* PDE projects.

6.2.1 GMP related projects

As previously discussed, in Chapter 2 we developed a model to explain and explore the lineage commitment process of GMP cells. There are many plausible directions to proceed with research from here. The most obvious is to test any of the numerous predictions made by the model with "wet-lab" (i.e. anything other than *in silico*) experiments. Since some predictions might be more difficult to test than others, we suggest starting with the prediction that low levels of G-CSF can encourage monopoiesis when paired with M-CSF concentrations that are too low to induce monopoiesis alone. Appendix A.2 provides a comprehensive list of predictions that might be of interest to experimental biologists.

To a systems biologist, there are several productive ways to extend the model presented here. First, one may expand on the current model to include more proteins and complexities. For instance, it is known that other proteins such as c-JUN, c-MYB, RUNX1, GATA-2 and GATA-1 all play roles in the molecular network in GMP cell differentiation [255], but were not explicitly modeled in Chapter 2. Additionally, the specified model significantly simplifies cytokine signaling. Other proteins such as those of the STAT family are involved in cytokine signaling

cascades [5]. Incorporating additional complexities may enhance the power and reliability of the mathematical model.

Alternatively, one might want to expand our model to capture lineage commitment steps downstream of those investigated in this work. For instance, it would be interesting to investigate the decision-making process between monocytes and dendritic cells. Such a model could provide new insight into how signals influence the lineage commitment between these cell lines and could explain why monocytic-myeloid derived suppressor cells differentiate into macrophages and dendritic cells when removed from GM-CSF rich conditions, rather than reverting back to the monocyte state [3]. Similarly, one might extend the network to investigate the lineage decision-making process between neutrophils, eosinophils, basophils and polymorphonuclear-myeloid derived suppressor cells. On the other hand, rather than extending the model downstream of the GMP state, one might extend the model upstream to the common-myeloid progenitor (CMP) cell. CMP cells have to choose between differentiation into GMP cells or megakaryocyte-erythroid progenitors (MEP) cells. Interestingly, C/EBPα and PU.1 are both involved in this lineage commitment step [256], [257], suggesting that the molecular network governing CMP lineage commitment overlaps with the mechanism governing GMP lineage commitment. By extending the model to include CMP differentiation, new insights can be garnered into how hematopoiesis transitions smoothly and intentionally between states in a multi-tiered system. It may further reveal if the process of CMP differentiation has downstream effects on GMP commitment as well.

6.2.2 *Caulobacter* ODE projects

In Chapter 4, we investigated the role that $CtrA_U$ plays in the context of regulating chromosome replication. It would be interesting to extend this project by investigating how competition between $CtrA_U$ and CtrA~P at promoter sites influences the genetic expression of various genes. As our model suggests that the interaction between $CtrA_U$ and *Cori* has significant consequences on cell cycle activity, $CtrA_U$ interactions with other DNA sites likey have significant consequences as well.

In Chapter 5, we investigated nitrogen and carbon starvation in *Caulobacter*. This work can be improved by introducing CckN, a DivK phosphatase that was recently shown to be targeted of

SpoT during carbon starvation [252]. We believe that this may be the "unknown mechanism" influencing DivK~P levels that is necessary to explain immediate G1 arrest in swarmer cells. Utilizing the model to show how this recently discovered mechanism works in synergy with other signaling mechanisms would be a great contribution to the field.

While the work of Chapter 5 focuses primarily on the mechanism by which *Caulobacter* arrests its cell cycle in response to nitrogen and carbon starvation, the model could easily be utilized to investigate the recovery process from starvation conditions to nutrient-rich conditions. Such analysis may provide insight into the advantages of the starvation mechanism over alternative mechanisms. For instance, why does *Caulobacter* slowly proteolyze DnaA under starvation conditions rather than rapid proteolysis? Rapid proteolysis of DnaA would surely contribute to robust G1 arrest in swarmer cell populations, but this is not the evolutionary path *Caulobacter* took. Perhaps slower degradation of DnaA is useful in the context of starvation recovery so that DnaA is still present just in case swarmer cells find nutrient-rich environments relatively quickly (within 30 minutes after birth). This may enable a more swift recovery and progression into S phase.

Lastly, the work of Chapter 5 can be extended by investigating other stress signals in *Caulobacter*, such as sodium stress, ethanol stress or DNA damage. While aspects of these signaling mechanisms have been elucidated [258], it is unclear if the known details are sufficient to explain the experimentally observed behavior. Implementing these identified signals into the model would likely provide new insights into these signaling mechanisms.

6.2.3 *Caulobacter* PDE projects

Caulobacter achieves a dimorphic cell cycle by simultaneously and synergistically regulating concentration, activity and spatial distribution of proteins [259]. While the models presented in Chapters 3-5 detail the molecular mechanisms governing protein activity and expression, they do not capture the molecular mechanisms governing protein localization. These aspects of *Caulobacter* activity have been investigated through partial differential equation (PDE) models in the works of Subramanian et al. [234] and Chen et al. [260]; however, these models did not capture the molecular mechanisms detailing protein expression and activity. In future works, these models can be merged into one larger, comprehensive model that captures the molecular

mechanisms governing protein concentration, activity and spatial distribution. Such a model could be used to provide new insights into how the spatial localization of proteins work in synergy with genetic and post-transcriptional regulatory mechanisms. This type of model could also be applied to investigate questions that would otherwise not be possible to address. For instance, it is known that ClpXP localizes to the stalked pole (i.e. the old pole), resulting in a concentration gradient of CtrA in pre-divisional cells [234]. Considering that the chromosomes of *Caulobacter* are organized spatially along the length of the cell [259], [261] and that CtrA regulates hundreds of genes in *Caulobacter* [112], it is likely that this concentration gradient influences genetic expression in pre-divisional cells. Investigating the impacts of the CtrA concentration gradient on genetic regulation would be interesting from both a biological and computational perspective. Additionally, the localization of ClpXP to the old pole at the G1-S transition is also of interest, as *Cori* is located near the old pole [259]. The colocalization of ClpXP and *Cori* may enable a speedier transition into S phase, as CtrA levels may be significantly lower in the volume that surrounds *Cori* relative to the rest of the cell. Whether or not the localization of ClpXP to the old pole enhances the efficiency of CtrA proteolysis in the context of chromosome replication, and to what degree, are excellent questions that can be investigated with the proposed hybrid model.

Appendix A. Supplementary Material for Chapter 2

A.1 Model Tuning:

In consideration of the lack of time course data for protein concentrations during GMP differentiation, we went about tuning our model to match behavioral characteristics of GMP differentiation. We first defined the concentration profiles we would expect from these myeloid cells relative to each other (outlined below).

Cell Type	Higher Expression of:	Lower Expression of:
GMP	N/A	C/EBP, PU.1, IRF8. Egr-2, Gfi-1, GM-CSFR, M-CSFR, G-CSFR
Granulocyte	C/EBP, Gfi-1, G-CSFR	PU.1, Egr-2, IRF8, M-CSFR
Monocyte	PU.1, IRF8, Egr-2, M-CSFR, GM-CSFR	C/EBP, Gfi-1, G-CSFR
M-MDSC	C/EBP, PU.1, Egr-2, IRF8, M-CSFR, GM-CSFR	Gfi-1, G-CSFR

Next we defined the following characteristics we would expect under different signaling conditions:

- The GMP, granulocyte and monocyte states should all be stable under conditions with no stimuli. We would expect that granulocytes and monocytes, upon migrating out of areas of high CSF concentrations would remain stable and GMP cells should be reliant on the CSFs for differentiation.
- G-CSF should induce granulopoiesis and M-CSF should induce monopoiesis
- GM-CSF should favor monopoiesis at lower concentrations and granulopoiesis at higher concentrations.
- G-CSF and M-CSF, when paired, should yield a heterogeneous population of monocytes and granulocytes.
- GM-CSF alone should produce a heterogeneous population of monocytes and granulocytes

- Monocytes should not be able to convert back into GMPs or granulocytes regardless of cytokine exposure
- Granulocytes should not be able to convert back into GMPs or monocytes regardless of cytokine exposure.
- GM-CSFR should be higher in the monocyte lineage than the granulocyte lineage
- The M-MDSC state should be inducible by GM-CSF

Next we chose weights that would result in the behaviors we defined. This is a lengthy and tedious process, and some weights are more relevant to certain behaviors than others. We will address a few of the weighting parameters, and their impact on the model's dynamics. First, the concentration dependent response of GMP cells to GM-CSF relies on a stronger interaction between C/EBP and Gfi-1 ($\omega_{\text{Gfi1,C/EBP}}$) than between C/EBP and PU.1 ($\omega_{\text{PU.1,C/EBP}}$). PU.1's auto-regulation gives it an advantage over Gfi-1 when C/EBP increases slowly, but if C/EBP increases faster the higher weight of its interaction with C/EBP gives it the upper hand. If the ratios between these weights were much smaller or much larger, GM-CSF would always favor one lineage over the other rather than exhibiting bi-functional behavior. Additionally, GM-CSFR is upregulated more heavily by PU.1 ($\omega_{\text{GMCSFR,PU.1}}$) than by C/EBP ($\omega_{\text{GMCSFR,C/EBP}}$). As a consequence, GM-CSFR is expressed higher in our simulated monocyte than in the granulocyte progenitor. Furthermore, the higher expression of GM-CSFR in monocytes makes them more sensitive to GM-CSF stimulation, and higher levels of GM-CSFR can shift the monocyte phenotype into an M-MDSC state. Receptor time scales (ρ_{R}) were set slower to transcription factor times scales (ρ_{TF}), which allows for a larger range of values for GM-CSF induced monopoiesis as it allows PU.1 more time to self-activate. Furthermore, we justify this distinction as transcription factors are often functional immediately after synthesis, while receptors must diffuse to the periphery of the cell and through the cell membrane, assemble with other subunits and with cytokines before a signal can be transmitted, and then the signal must propagate through multiple proteins for the signal itself to reach its downstream target.

A.2 Model Predictions:

- A combination of positive and negative interactions between C/EBP and PU.1 is responsible for the concentration dependent response of GMPs to GM-CSF.

- In the GMP state, Gfi-1 is more responsive to sudden shifts in C/EBP concentration than PU.1.
- GM-CSFR expression changes significantly after the cell has committed to one lineage in both granulopoiesis and monopoiesis. This suggests an alternative function for GMCSFR than lineage commitment.
- Low levels of G-CSF can push cells towards monopoiesis at M-CSF and GM-CSF concentrations too weak to stimulate differentiation alone.
- M-CSF antagonizes G-CSF induced granulopoiesis.
- GM-CSF induced monopoiesis exhibits a different concentration profile over time than M-CSF induced monopoiesis. In particular C/EBP and Gfi-1 spike in early stages of GM-CSF induced monopoiesis, and remain low in M-CSF induced monopoiesis.
- GM-CSF signal can increase the C/EBP concentration in monocytes.
- GM-CSF induced monopoiesis is likely quicker than M-CSF induced monopoiesis.
- GM-CSF induced granulopoiesis has a larger spike in PU.1 and IRF8 than G-CSF induced granulopoiesis. This is likely due to a slightly quicker rise in the concentration of Gfi-1 in G-CSF induced granulopoiesis.
- High expression of GM-CSFR in the monocyte lineage contributes to the sensitivity of GM-CSF induced M-MDSC differentiation.
- Gfi-1 is suppressed in the M-MDSC phenotype.
- The majority of C/EBP is bound to IRF8 in the monocyte lineage; whereas in M-MDSCs about half of C/EBP is unbound.
- M-MDSC differentiation resembles a monocyte in concentration profile before C/EBP is heavily upregulated.
- The M-MDSC state requires stimulation from cytokines other than M-CSF and G-CSF to remain stable.
- G-CSF can push monocytes into an M-MDSC phenotype in the presence of suitable concentrations of GM-CSF.
- M-CSF paired with GM-CSF makes for a stronger inducer of M-MDSCs than either cytokine alone.

- In M-MDSCs, G-CSFR is expressed at a level intermediate between a monocyte and a granulocyte.

A.3 Figures

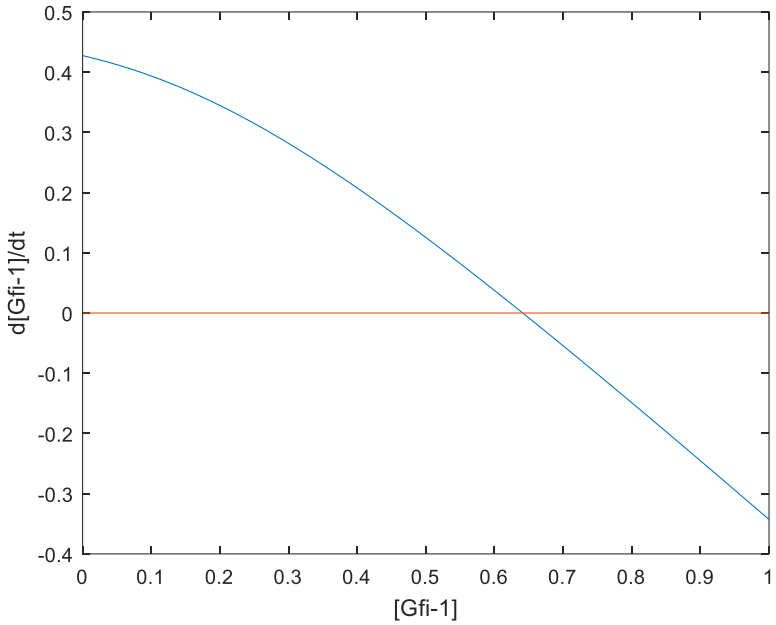

Figure A.1) An iterative search for the Gfi-1 solution.
We search over a range of [Gfi1] values ([Gfi1] ∈ [0,1]) to find the steady state solution of [Gfi1], where the rate of change of [Gfi1] (blue curve) is equal to zero. The point where the blue curve intersects the red line is the location of the solution. When an intersection is found, we "zoom in" to find the solution by repeating the iterative search process with smaller intervals around the intersection until we find a solution that is within our tolerance specifications (10^{-9}). In this simulation, all CSF values = 0, [PU.1]=0.3, and $[C/EBP]_F$=0.6.

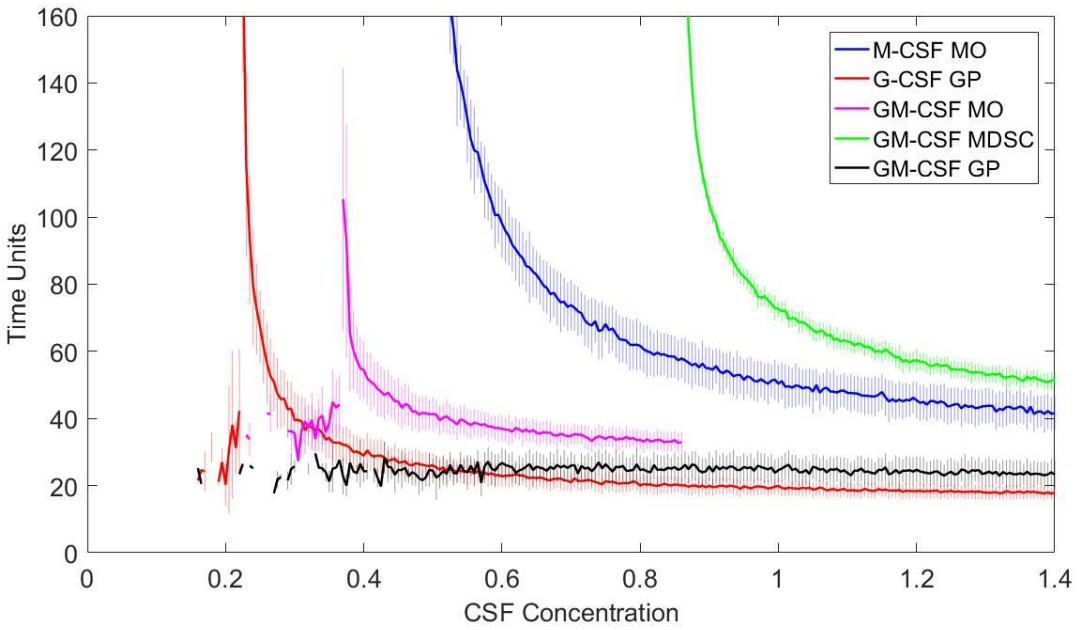

Figure A.2) Differentiation times under different cytokine conditions.
Differentiation times under different cytokine conditions. Thick lines indicate the average time it takes a population of 100 cells to differentiate under the given cytokine concentration. Vertical lines represent the standard deviation of these differentiation times. The time it takes a GMP cell to differentiate decreases as the concentration of its stimulus increases, reaching a plateau at high CSF concentration. Results indicate that GM-CSF induced monopoiesis (magenta line) is quicker than M-CSF induced monopoiesis (blue line). Naturally, differentiation into the M-MDSC state (green line) takes substantially longer than monopoiesis, because the cell must first pass through a monocyte-like state before reaching the M-MDSC steady state. GM-CSF and G-CSF induced granulopoiesis have similar differentiation times. The asymptotic ascending differentiation times appear when the naïve state becomes unstable. The cells that differentiate at concentrations lower than this point are heavily primed to differentiate into the GP or MO phenotypes and thus will differentiate more quickly than the majority of cells.

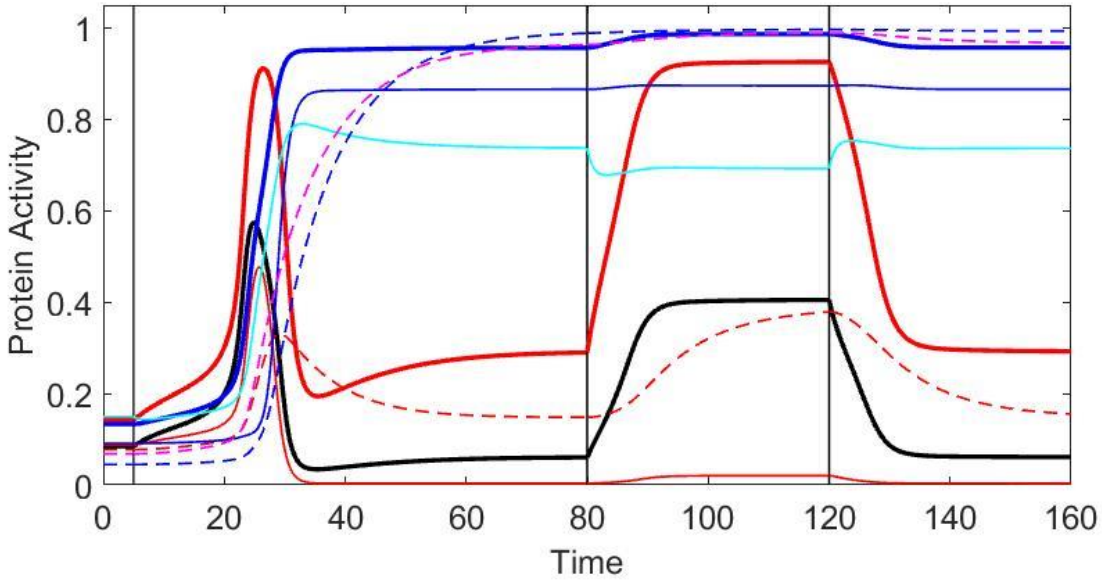

Figure A.3) GM-CSF can induce a monocyte to morph into an M-MDSC phenotype in a reversible process. A GMP cell differentiates into a monocyte when induced by lower concentrations of GM-CSF. However, when the concentration is increased further, the monocyte state destabilizes and the cell settles into the M-MDSC state. Furthermore, when the GM-CSF concentration is decreased again, the M-MDSC state is destabilized and reverts back to a monocyte-like phenotype. [GM-CSF] = 0 when $t < 5$. [GM-CSF] = 0.6 when $5 < t < 80$ and $t > 120$. [GM-CSF] = 1.2 when $80 < t < 120$. Thick red line = $[C/EBP]_T$, black line = $[C/EBP]_F$, thick blue line = [PU.1], thin red line = [Gfi1], thin blue line = [Egr2], cyan line = $[IRF8]_T$, dashed red line = $[G\text{-}CSFR]_T$, dashed blue line = $[M\text{-}CSFR]_T$, dashed magenta line = $[GM\text{-}CSFR]_T$.

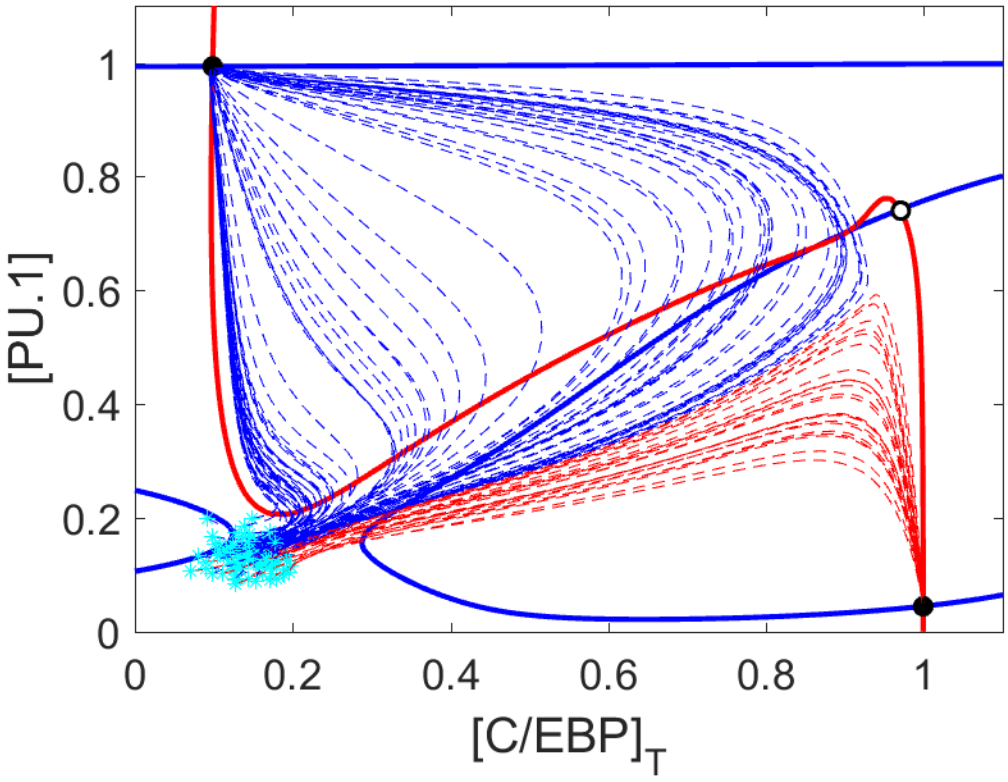

Figure A.4) Phase plane and cell trajectories describe the system under M-CSF and G-CSF stimulation. Thick, solid blue and red lines illustrate the PU.1 and C/EBP nullclines respectively. Cyan asterisks represent stochastically generated cellular initial conditions. Thin, red dashed lines represent the cell trajectory during granulopoiesis, while thin, blue dashed lines represent the cellular trajectories during monopoiesis. M-CSF and G-CSF can be mixed to get a heterogeneous population of both granulocytes and monocytes. As only the monocyte and granulocyte states are stable, M-MDSCs are not acquired under these conditions. [M-CSF] = 1 and [G-CSF] = 1 in this simulation.

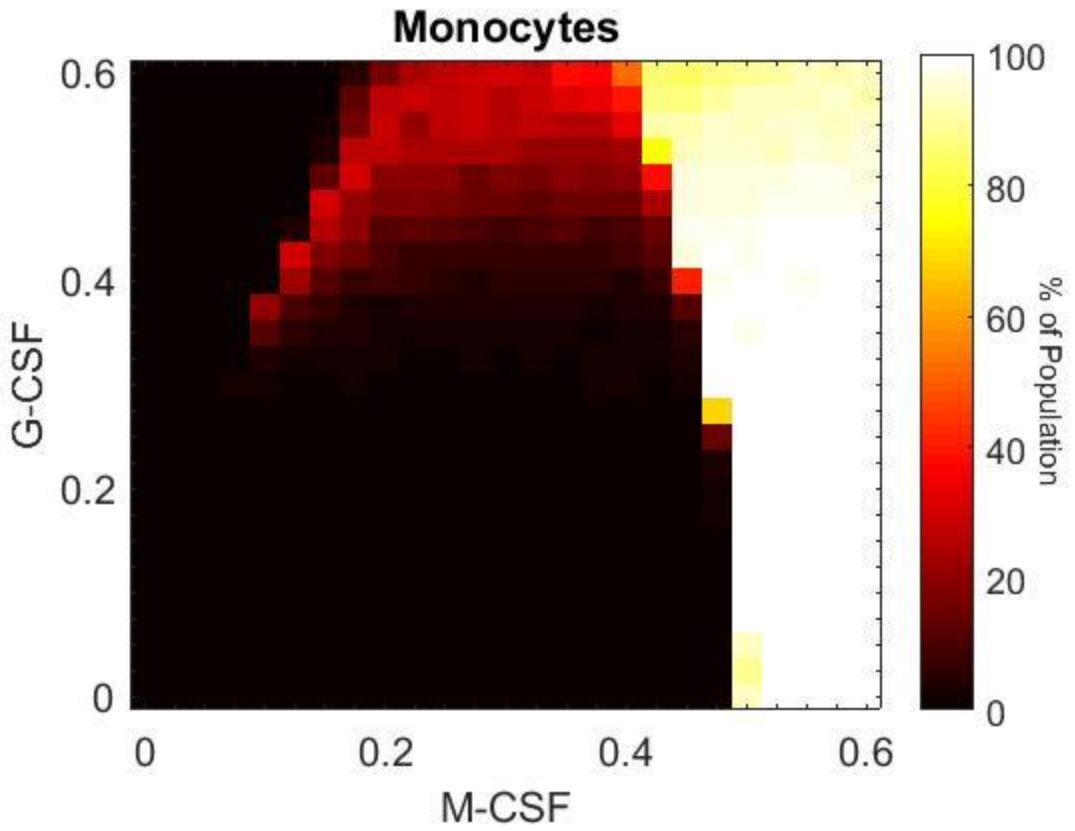

Figure A.5) Heat map of the population fraction that differentiates into monocytes under M-CSF and G-CSF stimulation.

Each cytokine combination is simulated with 500 stochastically generated cells. The color gradient on the right correlates to fraction of cells that differentiate into monocytes. We find G-CSF can lower the required dose of M-CSF to induce monopoiesis. Thus, G-CSF can assist in monopoiesis under some conditions.

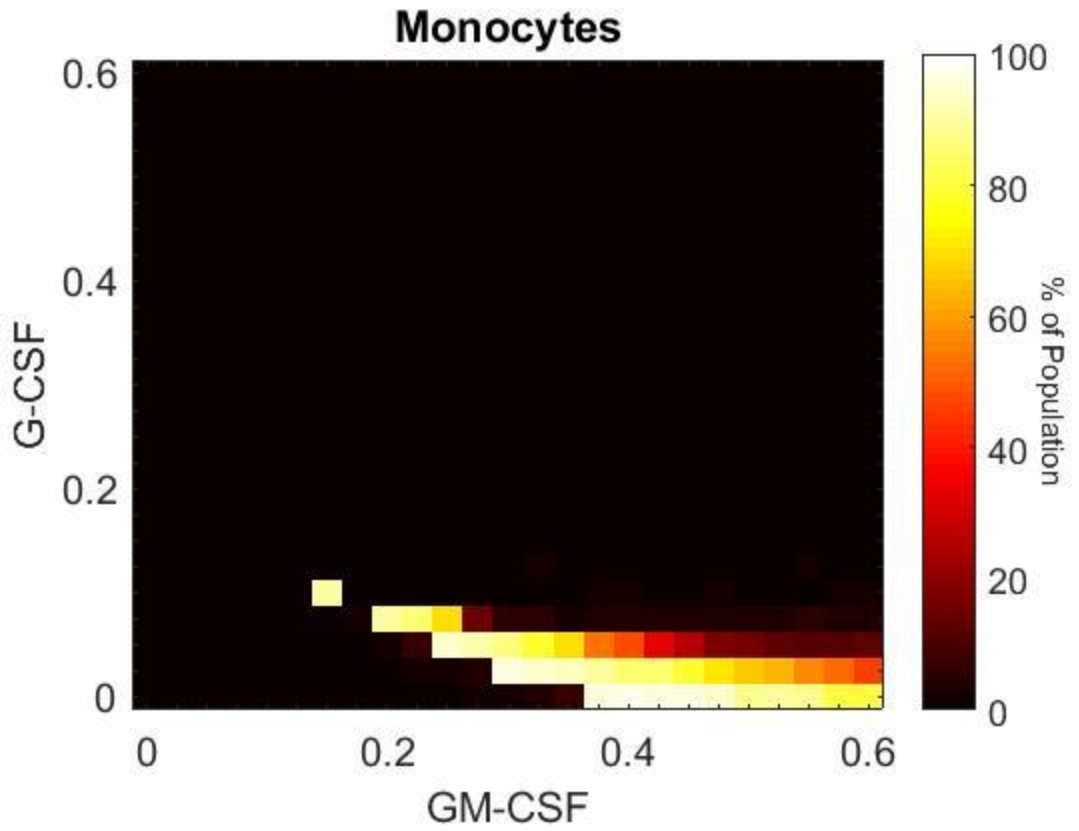

Figure A.6) Heat map of the population fraction that differentiates into monocytes under GM-CSF and G-CSF stimulation.

Each cytokine combination is simulated with 500 stochastically generated cells. The color gradient on the right correlates to fraction of cells that differentiate into monocytes. We find G-CSF can lower the required dose of GM-CSF to induce monopoiesis. Thus, G-CSF can assist in monopoiesis under some conditions. However, when G-CSF is increased further, it arrests monopoiesis in favor of granulopoiesis.

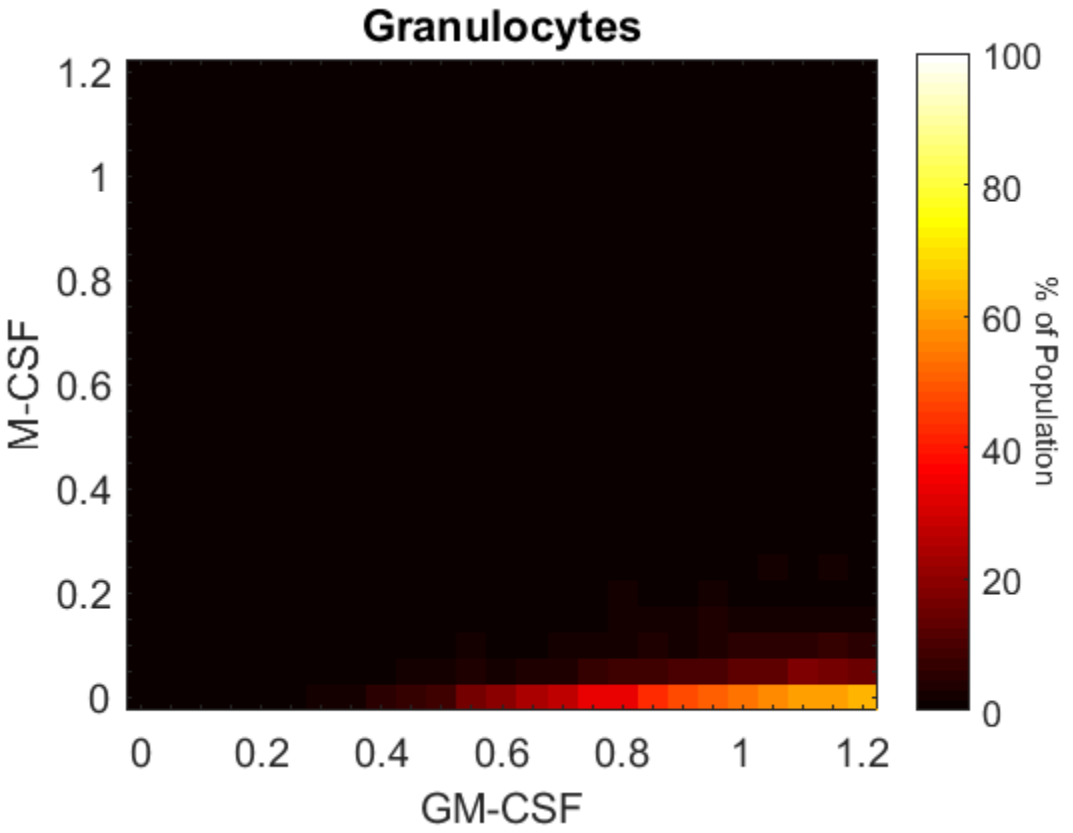

Figure A.7) Heat map of the population fraction that differentiates into granulocytes under GM-CSF and M-CSF stimulation.
Each cytokine combination is simulated with 500 stochastically generated cells. The color gradient on the right correlates to fraction of cells that differentiate into granulocyte progenitors. We find that very low doses of M-CSF are required to arrest GM-CSF induced granulopoiesis.

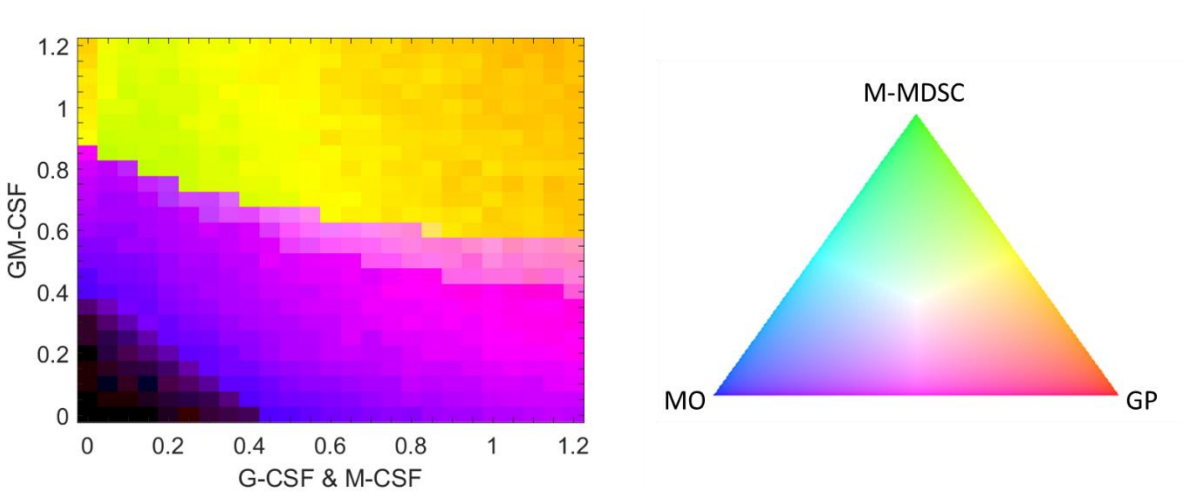

Figure A.8) Heatmap of GMP cell differentiation ratios when GM-CSF is paired with equal stimulation of G-CSF and M-CSF.

Each cytokine combination is simulated with 500 stochastically generated cells. The color gradient triangle on the right correlates to population composition. Populations containing all M-MDSCs, granulocyte progenitors (GP), or monocytes (MO) are represented by green, red and blue, respectively. Black represents populations of undifferentiated cells. We find that as GM-CSF increases, the population ratio switches from being a blend of monocytes and granulocytes, to being composed of M-MDSCs and granulocytes. All three cell types are induced simultaneously under some conditions. As GM-CSF increases further, the ratio of granulocytes to M-MDSCs shifts in favor of granulocytes.

A.4 Tables

Table A.1) Chapter 2 Equations

Differential Equations

1	$\frac{d[\mathbf{PU.1}]}{dt} = \rho_{\mathbf{TF}}\left(\frac{1}{1+e^{-\sigma W_{\mathbf{PU.1}}}} - [\mathbf{PU.1}]\right)$
2	$\frac{d[\mathbf{C/EBP}]_{\mathbf{T}}}{dt} = \rho_{\mathbf{TF}}\left(\frac{1}{1+e^{-\sigma W_{\mathbf{C/EBP}}}} - [\mathbf{C/EBP}]_{\mathbf{T}}\right)$
3	$\frac{d[\mathbf{Gfi1}]}{dt} = \rho_{\mathbf{TF}}\left(\frac{1}{1+e^{-\sigma W_{\mathbf{Gfi1}}}} - [\mathbf{Gfi1}]\right)$
4	$\frac{d[\mathbf{Egr2}]}{dt} = \rho_{\mathbf{TF}}\left(\frac{1}{1+e^{-\sigma W_{\mathbf{Egr2}}}} - [\mathbf{Egr2}]\right)$
5	$\frac{d[\mathbf{IRF8}]_{\mathbf{T}}}{dt} = \rho_{\mathbf{TF}}\left(\frac{1}{1+e^{-\sigma W_{\mathbf{IRF8}}}} - [\mathbf{IRF8}]_{\mathbf{T}}\right)$
6	$\frac{d[\mathbf{GMCSFR}]_{\mathbf{T}}}{dt} = \rho_{\mathbf{R}}\left(\frac{1}{1+e^{-\sigma W_{\mathbf{GMCSFR}}}} - [\mathbf{GMCSFR}]_{\mathbf{T}}\right)$
7	$\frac{d[\mathbf{GCSFR}]_{\mathbf{T}}}{dt} = \rho_{\mathbf{R}}\left(\frac{1}{1+e^{-\sigma W_{\mathbf{GCSFR}}}} - [\mathbf{GCSFR}]_{\mathbf{T}}\right)$
8	$\frac{d[\mathbf{MCSFR}]_{\mathbf{T}}}{dt} = \rho_{\mathbf{R}}\left(\frac{1}{1+e^{-\sigma W_{\mathbf{MCSFR}}}} - [\mathbf{MCSFR}]_{\mathbf{T}}\right)$

W equations

9	$W_{\mathbf{PU.1}} = \omega^{\mathbf{o}}_{\mathbf{PU.1}} + \omega_{\mathbf{PU.1,PU.1}}[\mathbf{PU.1}] + \omega_{\mathbf{PU.1,Gfi1}}[\mathbf{Gfi1}] + \omega_{\mathbf{PU.1,C/EBP}}[\mathbf{C/EBP}]_{\mathbf{F}} + \omega_{\mathbf{PU.1,MCSFR}}[\mathbf{MCSFR:MCSF}]$
10	$W_{\mathbf{C/EBP}} = \omega^{\mathbf{o}}_{\mathbf{C/EBP}} + \omega_{\mathbf{C/EBP,C/EBP}}[\mathbf{C/EBP}]_{\mathbf{F}} + \omega_{\mathbf{C/EBP,GMCSFR}}[\mathbf{GMCSFR:GMCSF}] + \omega_{\mathbf{C/EBP,GCSFR}}[\mathbf{GCSFR:GCSF}]$
11	$W_{\mathbf{Gfi1}} = \omega^{\mathbf{o}}_{\mathbf{Gfi1}} + \omega_{\mathbf{Gfi1,C/EBP}}[\mathbf{C/EBP}]_{\mathbf{F}} + \omega_{\mathbf{Gfi1,Egr2}}[\mathbf{Egr2}] + \omega_{\mathbf{Gfi1,GCSFR}}[\mathbf{GCSFR:GCSF}]$
12	$\mathbf{W}_{\mathbf{Egr2}} = \omega^{\mathbf{o}}_{\mathbf{Egr2}} + \omega_{\mathbf{Egr2,PU.1}}[\mathbf{PU.1}] + \omega_{\mathbf{Egr2,Gfi1}}[\mathbf{Gfi1}]$
13	$W_{\mathbf{IRF8}} = \omega^{\mathbf{o}}_{\mathbf{IRF8}} + \omega_{\mathbf{IRF8,PU.1}}[\mathbf{PU.1}] + \omega_{\mathbf{IRF8,GMCSFR}}[\mathbf{GMCSFR:GMCSF}] + \omega_{\mathbf{IRF8,GCSFR}}[\mathbf{GCSFR:GCSF}]$
14	$W_{\mathbf{GMCSFR}} = \omega^{\mathbf{o}}_{\mathbf{GMCSFR}} + \omega_{\mathbf{GMCSFR,PU.1}}[\mathbf{PU.1}] + \omega_{\mathbf{GMCSFR,C/EBP}}[\mathbf{C/EBP}]_{\mathbf{F}}$

15 $$W_{GCSFR} = \omega^{0}_{GMCSFR} + \omega_{GCSFR,PU.1}[PU.1] + \omega_{GCSFR,C/EBP}[C/EBP]_F + \omega_{GCSFR,Gfi1}[Gfi1]$$

16 $$W_{MCSFR} = \omega^{0}_{MCSFR} + \omega_{MCSFR,PU.1}[PU.1] + \omega_{MCSFR,C/EBP}[C/EBP]_F + \omega_{MCSFR,Gfi1}[Gfi1] + \omega_{MCSFR,Egr2}[Egr2]$$

Protein Binding Equations

17 $$[GMCSFR:GMCSF] = \frac{[GMCSF][GMCSFR]_T}{[GMCSF] + K_{d,GMCSFR}}$$

18 $$[MCSFR:MCSF] = \frac{[MCSF][MCSFR]_T}{[MCSF] + K_{d,MCSFR}}$$

19 $$[GCSFR:GCSF] = \frac{[GCSF][GCSFR]_T}{[GCSF] + K_{d,GCSFR}}$$

20 $$[C/EBP]_F = \frac{1}{2}\left(-b + \sqrt{b^2 + \frac{4[C/EBP]_T}{K_{eq}}}\right)$$

21 $$b = [IRF8]_T + \frac{1}{K_{eq}} - [C/EBP]_T$$

Table A.2) Chapter 2 Parameter Values.
Cytokine concentrations vary from one simulation to another, as specified in the figure legends. The half-life of transcription factors is ~$(0.7/\rho_{TF})\cdot(60\text{ min}) = 42$ min, and for receptors ~420 min.

Targeted Protein	Parameter	Value
General terms	$\boldsymbol{\sigma}$	3.2
	$\boldsymbol{\rho_{TF}}$	1
	$\boldsymbol{\rho_{R}}$	0.1
	[GM-CSF]	adjustable
	[G-CSF]	adjustable
	[M-CSF]	adjustable
C/EBP	$\boldsymbol{\omega^{o}_{C/EBP}}$	- 0.79
	$\boldsymbol{\omega_{C/EBP,C/EBP}}$	2.71
	$\boldsymbol{\omega_{C/EBP,GMCSFR}}$	0.75
	$\boldsymbol{\omega_{C/EBP,GCSFR}}$	0.85
	$\boldsymbol{K_{eq}}$	7.5
PU.1	$\boldsymbol{\omega^{o}_{PU.1}}$	- 0.8
	$\boldsymbol{\omega_{PU.1,PU.1}}$	1.79
	$\boldsymbol{\omega_{PU.1,Gfi1}}$	- 1.22
	$\boldsymbol{\omega_{PU.1,C/EBP}}$	0.99
	$\boldsymbol{\omega_{PU.1,MCSFR}}$	0.85
Gfi-1	$\boldsymbol{\omega^{o}_{Gfi1}}$	- 0.75
	$\boldsymbol{\omega_{Gfi1,C/EBP}}$	1.6
	$\boldsymbol{\omega_{Gfi1,Egr2}}$	- 1.27
	$\boldsymbol{\omega_{Gfi1,GCSFR}}$	0.75
IRF8	$\boldsymbol{\omega^{o}_{IRF8}}$	- 0.73
	$\boldsymbol{\omega_{IRF8,PU.1}}$	1.4
	$\boldsymbol{\omega_{IRF8,GMCSFR}}$	- 0.62

	$\omega_{\mathbf{IRF8,GCSFR}}$	- 0.62
	$\omega^{\mathbf{o}}_{\mathbf{Egr2}}$	- 0.8
Egr2	$\omega_{\mathbf{Egr2,PU.1}}$	1.45
	$\omega_{\mathbf{Egr2,Gfi1}}$	- 1.27
	$\omega^{\mathbf{o}}_{\mathbf{GMCSFR}}$	- 1.2
	$\omega_{\mathbf{GMCSFR,PU.1}}$	2.3
GM-CSFR	$\omega_{\mathbf{GMCSFR,C/EBP}}$	0.9
	$K_{\mathbf{d,GMCSFR}}$	0.65
	$\omega^{\mathbf{o}}_{\mathbf{GMCSFR}}$	- 1.0
	$\omega_{\mathbf{GCSFR,PU.1}}$	0.4
G-CSFR	$\omega_{\mathbf{GCSFR,C/EBP}}$	1.1
	$\omega_{\mathbf{GCSFR,Gfi1}}$	0.9
	$K_{\mathbf{d,GCSFR}}$	0.9
	$\omega^{\mathbf{o}}_{\mathbf{MCSFR}}$	- 1.25
	$\omega_{\mathbf{MCSFR,PU.1}}$	2
	$\omega_{\mathbf{MCSFR,C/EBP}}$	0.5
M-CSFR	$\omega_{\mathbf{MCSFR,Gfi1}}$	- 1.2
	$\omega_{\mathbf{MCSFR,Egr2}}$	1
	$K_{\mathbf{d,MCSFR}}$	0.45

Table A.3) Chapter 2 Initial Simulation Conditions.
All time course simulations, except stochastically generated cells, were run with the following initial conditions:

$[C/EBP]_T = 0.1424$	[PU.1] = 0.1331	[Gfi1] = 0.08803	[GMCSFR] = 0.06807
[IRF8] = 0.1494	[Egr2] = 0.09112	[GCSFR] = 0.07737	[MCSFR] = 0.04482

Appendix B. Supplementary Material for Chapter 4

B.1 Equations and Simulation Events Governing Cell Cycle Model

In this section, we provide a complete list of equations governing the cell cycle model. For details on equation derivations, see Chapter 3. For a list of corresponding parameter values, Table B.1. Alternative parameter values utilized in mutant simulations are found in Table B.2. Parameters designated by red font are specifically included to accommodate mutant simulations, and are always set to zero unless specified otherwise for a given mutant simulation.

B.1.1 Governing Equations

$$\frac{\mathrm{d}[\mathrm{CtrA_U}]}{\mathrm{dt}} = k_{\mathrm{s,CtrA-P1}} \frac{\epsilon_{\mathrm{CtrA-GcrA}} \cdot J_{\mathrm{a,CtrA-GcrA}} + [\mathrm{GcrA}]}{J_{\mathrm{a,CtrA-GcrA}} + [\mathrm{GcrA}]} \cdot \frac{{J_{\mathrm{i,CtrA-CtrA\sim P}}}^2}{{J_{\mathrm{i,CtrA-CtrA}}}^2 + [\mathrm{CtrA\sim P}]^2}$$
$$\cdot \left(1 - m_{\mathrm{CtrA-P1}} \cdot (2M_{\mathrm{ctrA}} - 1)\right) + k_{\mathrm{s,CtrA-P2}} \frac{\epsilon_{\mathrm{CtrA-CtrA}} \cdot {J_{\mathrm{a,CtrA-CtrA\sim P}}}^2 + [\mathrm{CtrA\sim P}]^2}{{J_{\mathrm{a,CtrA-CtrA}}}^2 + [\mathrm{CtrA\sim P}]^2}$$
$$\cdot \frac{{J_{\mathrm{i,CtrA-SciP}}}^2}{{J_{\mathrm{i,CtrA-SciP}}}^2 + [\mathrm{SciP}]^2} - \left(\mu + k_{\mathrm{d,CtrA1}} + k_{\mathrm{d,CtrA2}} \cdot \frac{[\mathrm{ClpXP}]_{\mathrm{Complex}}}{J_{\mathrm{d,CtrA}} + [\mathrm{CtrA_U}] + [\mathrm{CtrA\sim P}]}\right) \cdot [\mathrm{CtrA_U}]$$
$$+ \; k_{\mathrm{dephos,CtrA}} \cdot [\mathrm{CckA}]_{\mathrm{P}} \cdot [\mathrm{CtrA\sim P}] - k_{\mathrm{phos,CtrA}} \cdot [\mathrm{CtrA_U}] \cdot [\mathrm{CckA}]_{\mathrm{K}} + k_{\mathrm{s,CtrA\Delta 3\Omega}}$$

$$\frac{\mathrm{d}[\mathrm{CtrA\sim P}]}{\mathrm{dt}} = -\left(\mu + k_{\mathrm{d,CtrA1}} + k_{\mathrm{d,CtrA2}} \cdot \frac{[\mathrm{ClpXP}]_{\mathrm{Complex}}}{J_{\mathrm{d,CtrA2}} + [\mathrm{CtrA_U}] + [\mathrm{CtrA\sim P}]}\right) \cdot [\mathrm{CtrA\sim P}] - \; k_{\mathrm{dephos,CtrA}} \cdot [\mathrm{CckA}]_{\mathrm{P}}$$
$$\cdot [\mathrm{CtrA\sim P}] + k_{\mathrm{phos,CtrA}} \cdot [\mathrm{CtrA_U}] \cdot [\mathrm{CckA}]_{\mathrm{K}} + k_{\mathrm{s,CtrAD51E}}$$

$$\frac{\mathrm{d}[\mathrm{DnaA}]_{\mathrm{T}}}{\mathrm{dt}} = k_{\mathrm{s,DnaA1}} \frac{J_{\mathrm{i,DnaA-GcrA}}}{J_{\mathrm{i,DnaA-GcrA}} + [\mathrm{GcrA}]} \cdot \left(1 - 2\, m_{\mathrm{DnaA}} \cdot (1 - M_{\mathrm{DnaA}})\right) - \left(\mu + k_{\mathrm{d,DnaA}}\right) \cdot [\mathrm{DnaA}]$$

$$\frac{\mathrm{d}[\mathrm{DnaA\sim ATP}]}{\mathrm{dt}} = k_{\mathrm{s,DnaA}} \frac{J_{\mathrm{i,DnaA-GcrA}}}{J_{\mathrm{i,DnaA-GcrA}} + [\mathrm{GcrA}]} \cdot \left(1 - 2\, m_{\mathrm{DnaA}} \cdot (1 - M_{\mathrm{DnaA}})\right)$$
$$- \left(\mu + k_{\mathrm{d,DnaA}} + k_{\mathrm{d,DnaAatp}} \cdot \mathrm{RepSwitch}\right) \cdot [\mathrm{DnaA\sim ATP}]$$

$$\frac{\mathrm{d}[\mathrm{GcrA}]}{\mathrm{dt}} = k_{\mathrm{s,GcrA}} \frac{\epsilon_{\mathrm{GcrA-DnaA}} \cdot J_{\mathrm{a,GcrA-DnaA}} + ([\mathrm{DnaA}]_{\mathrm{T}} - [\mathrm{DnaA\sim ATP}])}{J_{\mathrm{a,GcrA-DnaA}} + ([\mathrm{DnaA}]_{\mathrm{T}} - [\mathrm{DnaA\sim ATP}])} \cdot \frac{{J_{\mathrm{i,GcrA-CtrA}}}^2}{{J_{\mathrm{i,GcrA-CtrA}}}^2 + [\mathrm{CtrA\sim P}]^2}$$
$$- \left(\mu + k_{\mathrm{d,GcrA}}\right) \cdot [\mathrm{GcrA}]$$

$$\frac{\mathrm{d}[\mathrm{SciP}]}{\mathrm{dt}} = k_{\mathrm{s,SciP}} \frac{[\mathrm{CtrA\sim P}]^2}{{J_{\mathrm{a,SciP-CtrA}}}^2 + [\mathrm{CtrA\sim P}]^2} - \left(\mu + k_{\mathrm{d,SciP}}\right) \cdot [\mathrm{SciP}]$$

$$\frac{\mathrm{d}[\mathrm{DivK}]}{\mathrm{dt}} = k_{\mathrm{s,DivK1}} + k_{\mathrm{s,DivK2}} \cdot \frac{[\mathrm{CtrA{\sim}P}]^2}{J_{\mathrm{a,DivK-CtrA{\sim}P}}{}^2 + [\mathrm{CtrA{\sim}P}]^2} - \left(\mu + k_{\mathrm{d,DivK}}\right) \cdot [\mathrm{DivK}] - k_{\mathrm{phos,DivK1}} \cdot [\mathrm{DivJ}]_{\mathrm{A}} \cdot [\mathrm{DivK}] - k_{\mathrm{phos,DivK2}} \cdot [\mathrm{PleC}]_{\mathrm{K}} \cdot [\mathrm{DivK}] + k_{\mathrm{dephos,DivK}} \cdot [\mathrm{PleC}] \cdot [\mathrm{DivK{\sim}P}] - k^{+}_{\mathrm{DivJDivK}} \cdot [\mathrm{DivJ}] \cdot [\mathrm{DivK}] + \left(k^{-}_{\mathrm{DivJDivK}} + k_{\mathrm{d,DivJ}}\right) \cdot [\mathrm{DivJ{:}\ DivK}]$$

$$\frac{\mathrm{d}[\mathrm{DivK{\sim}P}]}{\mathrm{dt}} = -\left(\mu + \mathrm{k}_{\mathrm{d,DivK}}\right) \cdot [\mathrm{DivK{\sim}P}] + k_{\mathrm{phos,DivK1}} \cdot [\mathrm{DivJ}]_{\mathrm{A}} \cdot [\mathrm{DivK}] + k_{\mathrm{phos,DivK2}} \cdot [\mathrm{PleC}]_{\mathrm{K}} \cdot [\mathrm{DivK}] - k_{\mathrm{dephos,DivKP+}} \cdot [\mathrm{PleC}] \cdot [\mathrm{DivK{\sim}P}] + 2 \cdot \left(\left(k^{-}_{\mathrm{PleCDivKP}} + k_{\mathrm{d,PleC}} + k_{\mathrm{d,DivK}}\right) \cdot [\mathrm{PleC{:}\ DivK{\sim}P_2}] - k^{+}_{\mathrm{PleCDivKP}} \cdot [\mathrm{PleC}] \cdot [\mathrm{DivK{\sim}P}]^2\right) - k^{+}_{\mathrm{DivJDivKP}} \cdot [\mathrm{DivJ}] \cdot [\mathrm{DivK{\sim}P}] + \left(k^{-}_{\mathrm{DivJDivKP}} + \mathrm{k}_{\mathrm{d,DivJ}}\right) \cdot [\mathrm{DivJ{:}\ DivK{\sim}P}] - k^{+}_{\mathrm{DivLDivKP}} \cdot [\mathrm{DivL}] \cdot [\mathrm{DivK{\sim}P}] + \left(k^{-}_{\mathrm{DivLDivKP}} + k_{\mathrm{d,DivL}}\right) \cdot [\mathrm{DivL{:}\ DivK{\sim}P}]$$

$$\frac{\mathrm{d}[\mathrm{DivJ}]}{\mathrm{dt}} = k_{\mathrm{s,DivJ}} - \left(\mu + k_{\mathrm{d,DivJ}}\right) \cdot [\mathrm{DivJ}] - k^{+}_{\mathrm{DivJDivK}} \cdot [\mathrm{DivJ}] \cdot [\mathrm{DivK}] + \left(k^{-}_{\mathrm{DivJDivK}} + k_{\mathrm{d,DivK}}\right) \cdot [\mathrm{DivJ{:}\ DivK}] - k^{+}_{\mathrm{DivJDivKP}} \cdot [\mathrm{DivJ}] \cdot [\mathrm{DivK{\sim}P}] + \left(k^{-}_{\mathrm{DivJDivKP}} + k_{\mathrm{d,DivK}}\right) \cdot [\mathrm{DivJ{:}\ DivK{\sim}P}]$$

$$\frac{\mathrm{d}[\mathrm{DivJ{:}\ DivK}]}{\mathrm{dt}} = k^{+}_{\mathrm{DivJDivK}} \cdot [\mathrm{DivJ}] \cdot [\mathrm{DivK}] - \left(\mu + k^{-}_{\mathrm{DivJDivK}} + \mathrm{k}_{\mathrm{d,DivJ}} + \mathrm{k}_{\mathrm{d,DivK}}\right) \cdot [\mathrm{DivJ{:}\ DivK}]$$

$$\frac{\mathrm{d}[\mathrm{DivJ{:}\ DivK{\sim}P}]}{\mathrm{dt}} = k^{+}_{\mathrm{DivJDivKP}} \cdot [\mathrm{DivJ}] \cdot [\mathrm{DivK{\sim}P}] - \left(\mu + k^{-}_{\mathrm{DivJDivKP}} + k_{\mathrm{d,DivJ}} + k_{\mathrm{d,DivK}}\right) \cdot [\mathrm{DivJ{:}\ DivK{\sim}P}]$$

$$[\mathrm{DivJ}]_{\mathrm{A}} = ([\mathrm{DivJ{:}\ DivK{\sim}P}] + [\mathrm{DivJ{:}\ DivK}]) \cdot \left([\mathrm{SpmX}] + \theta_{\mathrm{DivJA}}\right)$$

$$\frac{\mathrm{d}[\mathrm{DivL}]}{\mathrm{dt}} = k_{\mathrm{s,DivL}} - \left(\mu + k_{\mathrm{d,DivL}}\right) \cdot [\mathrm{DivL}] - k^{+}_{\mathrm{DivLDivKP}} \cdot [\mathrm{DivL}] \cdot [\mathrm{DivK{\sim}P}] + \left(k^{-}_{\mathrm{DivLDivKP}} + k_{\mathrm{d,DivK}}\right) \cdot [\mathrm{DivL{:}\ DivK{\sim}P}]$$

$$\frac{\mathrm{d}[\mathrm{DivL{:}\ DivK{\sim}P}]}{\mathrm{dt}} = k^{+}_{\mathrm{DivLDivKP}} \cdot [\mathrm{DivL}] \cdot [\mathrm{DivK{\sim}P}] - \left(\mu + k^{-}_{\mathrm{DivLDivKP}} + \mathrm{k}_{\mathrm{d,DivK}} + k_{\mathrm{d,DivL}}\right) \cdot [\mathrm{DivL{:}\ DivK{\sim}P}]$$

$$[\mathrm{DivL}]_{\mathrm{T}} = [\mathrm{DivL}] + [\mathrm{DivL{:}\ DivK{\sim}P}]$$

$$\frac{\mathrm{d}[\mathrm{CckA}]_{\mathrm{T}}}{\mathrm{dt}} = k_{\mathrm{s,CckA}} - \left(\mu + k_{\mathrm{d,CckA}}\right) \cdot [\mathrm{CckA}]_{\mathrm{T}}$$

$$\frac{\mathrm{d}[\mathrm{CckA{:}\ CdG}]}{\mathrm{dt}} = k^{+}_{\mathrm{CckAcdG}} \cdot [\mathrm{cdG}] \cdot ([\mathrm{CckA}]_{\mathrm{T}} - [\mathrm{CckA{:}\ CdG}]) - k^{-}_{\mathrm{CckAcdG}} \cdot [\mathrm{CckA{:}\ cdG}] - \left(\mu + k_{\mathrm{d,CckA}}\right) \cdot [\mathrm{CckA{:}\ cdG}]$$

$$[\mathrm{CckA{:}\ DivL}]_{\mathrm{T}} = \frac{[\mathrm{CckA}]_{\mathrm{T}} + [\mathrm{DivL}]_{\mathrm{T}} + \frac{1}{K_{\mathrm{CckADivL}}} - \sqrt{\left([\mathrm{CckA}]_{\mathrm{T}} + [\mathrm{DivL}]_{\mathrm{T}} + \frac{1}{K_{CckA:DivL}}\right)^2 - 4 \cdot [\mathrm{CckA}]_{\mathrm{T}} \cdot [\mathrm{DivL}]_{\mathrm{T}}}}{2}$$

$$[\text{CckA}]_\text{P} = \frac{[\text{CckA: DivL}]_\text{T} \cdot [\text{DivL: DivK}\sim\text{P}]}{[\text{DivL}]_\text{T}} + [\text{CckA: cdG}] - \frac{[\text{CckA: cdG}] \cdot \frac{[\text{CckA: DivL}]_\text{T} \cdot [\text{DivL: DivK}\sim\text{P}]}{[\text{DivL}]_\text{T}}}{[\text{CckA}]_\text{T}}$$

$$[\text{CckA}]_\text{K} = [\text{CckA}]_\text{T} - [\text{CckA}]_\text{P}$$

$$\frac{\text{d}[\text{PleC}]}{\text{dt}} = k_{\text{s,PleC}} \cdot (2 - 2 \cdot M_{\text{PleC}}) - (\mu + k_{\text{d,PleC}}) \cdot [\text{PleC}] + k^{-}_{\text{PleCDivKP}} \cdot [\text{PleC: DivK}\sim\text{P}_2] - k^{+}_{\text{PleCDivKP}} \cdot [\text{PleC}] \cdot [\text{DivK}\sim\text{P}]^{\,2} + 2 \cdot k_{\text{d,DivK}} \cdot [\text{PleC: DivK}\sim\text{P}_2]$$

$$\frac{\text{d}[\text{PleC: DivK}\sim\text{P}_2]}{\text{dt}} = k^{+}_{\text{PleCDivKP}} \cdot [\text{PleC}] \cdot [\text{DivK}\sim\text{P}]^{\,2} - (k_{\text{d,PleC}} + k^{-}_{\text{PleCDivKP}} + 2 \cdot k_{\text{d,DivK}} + \mu) \cdot [\text{PleC: DivK}\sim\text{P}_2]$$

$$[\text{PleC}]_\text{tot} = [\text{PleC}] + [\text{PleC: DivK}\sim\text{P}_2]$$

$$\frac{\text{d}[\text{PleC}]_\text{Pole}}{\text{dt}} = k_{\text{PleCbinding}} \cdot ([\text{PleC}]_\text{tot} - [\text{PleC}]_\text{Pole}) \cdot \frac{[\text{PodJ}]}{[\text{PodJ}] \cdot [\text{V}] + J_{\text{PleCPodJ}}} - (k_{\text{PleCunbinding}} + k_{\text{d,PleC}} + \mu) \cdot [\text{PleC}]_\text{Pole}$$

$$\frac{\text{d}[\text{PodJ}]}{\text{dt}} = k_{\text{s,PodJ}} \cdot \frac{J_{\text{i,PodJ-DnaA}}}{J_{\text{i,PodJ-DnaA}} + [\text{DnaA}]_\text{T}} \cdot \frac{[\text{GcrA}]}{J_{\text{a,PodJ-GcrA}} + [\text{GcrA}]} \cdot (2 - 2 \cdot M_{\text{PodJ}}) - (\mu + k_{\text{d,PodJ1}}) \cdot [\text{PodJ}] - k_{\text{d,PodJ2}} \cdot \frac{[\text{PodJ}]}{J_{\text{d,PodJ}} + [\text{PodJ}]} \cdot [\text{PerP}]$$

$$\frac{\text{d}[\text{PerP}]}{\text{dt}} = k_{\text{s,PerP}} \cdot \frac{[\text{CtrA}\sim\text{P}]^2}{J_{\text{a,PerP-CtrA}}{}^2 + [\text{CtrA}\sim\text{P}]^2} \cdot (2 - 2 \cdot M_{\text{PodJ}}) - (\mu + k_{\text{d,PerP}}) \cdot [\text{PerP}]$$

$$[\text{DNA}]_\text{F} = \frac{K_{\text{d1}}}{K_{\text{d1}} + 2 \cdot [\text{CtrA}\sim\text{P}] + \frac{[\text{CtrA}\sim\text{P}]^2}{K_{\text{d3}}} + (1 - \sigma_{\text{CtrAU:}\mathit{Cori}}) \cdot \left(2 \cdot [\text{CtrA}_\text{U}] + \frac{[\text{CtrA}_\text{U}]^2}{K_{\text{d2}}} + 2 \cdot \frac{[\text{CtrA}_\text{U}] \cdot [\text{CtrA}\sim\text{P}]}{K_{\text{d2}}}\right)}$$

$$[\text{DNA: CtrA}\sim\text{P2}] = \frac{[\text{CtrA}\sim\text{P}]^2 \cdot [\text{DNA}]_\text{F}}{K_{\text{d1}} \cdot K_{\text{d3}}}$$

$$\frac{\text{d}[\text{Ini}]}{\text{dt}} = \left(1 - 2\, m_{\text{Ini}} \cdot (1 - M_{\text{Ini}})\right) \cdot (1 - [\text{DNA: CtrA}\sim\text{P}_2])^5 \cdot \left(\frac{[\text{DnaA}\sim\text{ATP}]}{[\text{DnaA}\sim\text{ATP}] + J_{\text{a,Ini-DnaA}}}\right)^2 - k_{\text{d,Ini}} \cdot [\text{Ini}]$$

$$\frac{\text{d}[\text{Elong}]}{\text{dt}} = k_{\text{elong}} \cdot \mathit{RepSwitch}$$

$$\frac{\text{d}[\text{CcrM}]}{\text{dt}} = k_{\text{s,CcrM}} \cdot \frac{[\text{CtrA}\sim\text{P}]^2}{J_{\text{a,CcrM-CtrA}}{}^2 + [\text{CtrA}\sim\text{P}]^2} \cdot \frac{J_{\text{I,CcrM-DnaA}}}{J_{\text{I,CcrM-DnaA}} + [\text{DnaA}]} \cdot (2 - 2 \cdot M_{\text{CcrM}}) - (\mu + k_{\text{d,CcrM}}) \cdot [\text{CcrM}] + k_{\text{s,LS1}}$$

$$\frac{\text{d}[\text{SpmX}]}{\text{dt}} = k_{\text{s,SpmX}} \frac{[\text{SpmX}]^3}{c^3 + [\text{SpmX}]^3} \cdot \left((1 - \theta_{\text{DivJA}}) \cdot (1 - \sigma_{\Delta\text{SpmX}}) - [\text{SpmX}]\right)$$

$$\frac{\mathrm{d}[\mathrm{Zproteins}]}{\mathrm{dt}} = k_{\mathrm{s,Zp}} \frac{[\mathrm{CtrA{\sim}P}]^2}{{J_{\mathrm{a,Zp-CtrA}}}^2 + [\mathrm{CtrA{\sim}P}]^2} - \left(\mu + k_{\mathrm{d,Zp}} + k_{\mathrm{d,ZP2}} \cdot [\mathrm{ClpAP}]\right) \cdot [\mathrm{Zproteins}]$$

$$\frac{\mathrm{d}[\mathrm{Zring}]}{\mathrm{dt}} = -k_{\mathrm{Zconstrict}} \cdot MipZswitch \cdot \frac{[\mathrm{Zproteins}]^5}{\left(J_{\mathrm{Zring}} + \theta_{\mathrm{Z}} \cdot [\mathrm{Zring}]\right)^5 + [\mathrm{Zproteins}]^5}$$

$$\frac{\mathrm{d}[\mathrm{V}]}{\mathrm{dt}} = \mu \cdot [\mathrm{V}]$$

$$\mu = T^{-1} \cdot \ln \frac{V_{\mathrm{div}}}{V_{\mathrm{birth}}}$$

$$\frac{\mathrm{d}[\mathrm{CpdR}]}{\mathrm{dt}} = k_{\mathrm{s,CpdR}} \frac{\epsilon_{\mathrm{CpdR-DnaA}} \cdot J_{\mathrm{a,CpdR-DnaA}} + [\mathrm{DnaA}]_{\mathrm{T}}}{J_{\mathrm{a,CpdR-DnaA}} + [\mathrm{DnaA}]_{\mathrm{T}}} \cdot \frac{[\mathrm{CtrA{\sim}P}]}{J_{\mathrm{a,CpdR-CtrA}} + [\mathrm{CtrA{\sim}P}]} \cdot \frac{J_{\mathrm{i,CckAGcrA}}}{J_{\mathrm{i,CckAGcrA}} + [\mathrm{GcrA}]}$$
$$+ \ k_{\mathrm{dephos,CpdR}} \cdot \ [\mathrm{CpdR{\sim}P}] \cdot [\mathrm{CckA}]_{\mathrm{P}} - k_{\mathrm{phos,CpdR}} \cdot [\mathrm{CpdR}] \cdot [\mathrm{CckA}]_{\mathrm{K}} \ - (\mu + k_{\mathrm{d,CpdR}}) \cdot [\mathrm{CpdR}]$$

$$\frac{\mathrm{d}[\mathrm{CpdR{\sim}P}]}{\mathrm{dt}} = -k_{\mathrm{dephos,CpdR}} \cdot \ [\mathrm{CpdR{\sim}P}] \cdot [\mathrm{CckA}]_{\mathrm{P}} + k_{\mathrm{phos,CpdR}} \cdot [\mathrm{CpdR}] \cdot [\mathrm{CckA}]_{\mathrm{K}} - (\mu + k_{\mathrm{d,CpdR}}) \cdot [\mathrm{CpdR{\sim}P}]$$

$$\frac{\mathrm{d}[\mathrm{RcdA}]}{\mathrm{dt}} = k_{\mathrm{s,RcdA}} \cdot \frac{[\mathrm{CtrA{\sim}P}]^2}{{J_{\mathrm{a,RcdACtrA}}}^2 + [\mathrm{CtrA{\sim}P}]^2} - \left(\mu + \ k_{\mathrm{d,RcdA}}\right) \cdot [\mathrm{RcdA}] - k_{\mathrm{d,RcdA2}} \cdot ([\mathrm{RcdA}] - [\mathrm{RcdA{:}\ PopA}])$$
$$\cdot \frac{[\mathrm{CpdR}]}{J_{\mathrm{d,CpdR}} + [\mathrm{CpdR}]}$$

$$\frac{\mathrm{d}[\mathrm{PopA}]}{\mathrm{dt}} = k_{\mathrm{s,PopA}} \cdot \frac{J_{\mathrm{i,PopA-GcrA}}}{J_{\mathrm{i,PopA-GcrA}} + [\mathrm{GcrA}]} - (\mu + k_{\mathrm{d,PopA}}) \cdot [\mathrm{PopA}] - \ k^{+}_{\mathrm{PopACdG}} \cdot [\mathrm{PopA}] \cdot [\mathrm{cdG}]^2 + k^{-}_{\mathrm{XCdG}}$$
$$\cdot [\mathrm{PopA{:}\ cdG_2}]$$

$$\frac{\mathrm{d}[\mathrm{PopA{:}\ cdG_2}]}{\mathrm{dt}} = \ k^{+}_{\mathrm{PopACdG}} \cdot [\mathrm{PopA}] \cdot [\mathrm{cdG}]^2 - (\mu + k^{-}_{\mathrm{XCdG}} + k_{\mathrm{d,PopA}}) \cdot [\mathrm{PopA{:}\ cdG_2}]$$

$$[\mathrm{PopA}]_{\mathrm{T}} = [\mathrm{PopA}] + [\mathrm{PopA{:}\ cdG_2}]$$

$$[\mathrm{RcdA{:}\ PopA}] = \frac{[\mathrm{PopA}]_{\mathrm{T}} + [\mathrm{RcdA}] + \frac{1}{K_{\mathrm{RcdAPopA}}} - \sqrt{\left([\mathrm{PopA}]_{\mathrm{T}} + [\mathrm{RcdA}] + \frac{1}{K_{\mathrm{RcdAPopA}}}\right)^2 - 4 \cdot [\mathrm{PopA}]_{\mathrm{T}} \cdot [\mathrm{RcdA}]}}{2}$$

$$[\mathrm{ClpXP}]_{\mathrm{Complex}} = \frac{[\mathrm{CpdR}]}{[\mathrm{CpdR}] + \frac{K_{\mathrm{ClpXpCpdR}}}{V}} \cdot \frac{[\mathrm{PopA{:}\ cdG_2}] \cdot [\mathrm{RcdA{:}\ PopA}]}{[\mathrm{PopA{:}\ cdG_2}] + [\mathrm{PopA}]}$$

$$\frac{\mathrm{d}[\mathrm{PdeA}]}{\mathrm{dt}} = k_{\mathrm{s,PdeA}} \cdot \frac{[\mathrm{CtrA{\sim}P}]}{J_{\mathrm{a,PdeACtrA}} + [\mathrm{CtrA{\sim}P}]} - \ k_{\mathrm{d,PdeA2}} \cdot [\mathrm{CpdR}] \cdot \frac{[\mathrm{PdeA}]}{J_{\mathrm{d,PdeA}} + [\mathrm{PdeA}]} - (\mu + k_{\mathrm{d,PdeA1}}) \cdot [\mathrm{PdeA}]$$

$$[\mathrm{DgcB}]_{\mathrm{a}} = \max(DgcB - [\mathrm{PdeA}], 0) \cdot \frac{DgcB - [\mathrm{DgcB{:}\ cdG_2}]}{DgcB}$$

$$\frac{\mathrm{d}[\mathrm{cdG}]}{\mathrm{dt}} = k_{\mathrm{s,cdG1}} \cdot [\mathrm{PleD{\sim}P}] + k_{\mathrm{s,cdG2}} \cdot [\mathrm{DgcB}]_{\mathrm{a}} - k_{\mathrm{d,cdG}} \cdot ([\mathrm{PdeA}] + PDE) \cdot \frac{[\mathrm{cdG}]}{J_{\mathrm{d,cdG}} + [\mathrm{cdG}]} - \mu \cdot [\mathrm{cdG}] + 2$$
$$\cdot \left(- k^{+}_{\mathrm{PopACdG}} \cdot [\mathrm{PopA}] \cdot [\mathrm{cdG}]^2 + \left(k^{-}_{\mathrm{XCdG}} + k_{\mathrm{d,PopA}}\right) \cdot [\mathrm{PopA{:}\ cdG_2}]\right) + 2$$
$$\cdot \left(-k^{+}_{\mathrm{PleDcdG}} \cdot ([\mathrm{PleD}] + [\mathrm{PleD{\sim}P}]) \cdot [\mathrm{cdG}]^2 + \left(k_{\mathrm{d,PleD}} + k^{-}_{\mathrm{XCdG}}\right)\right.$$
$$\left. \cdot ([\mathrm{PleD{:}\ cdG_2}] + [\mathrm{PleD{\sim}P{:}\ cdG_2}])\right) - k^{+}_{\mathrm{CckAcdG}} \cdot [\mathrm{cdG}] \cdot ([\mathrm{CckA}]_{\mathrm{T}} - [\mathrm{CckA{:}\ CdG}]) + k^{-}_{\mathrm{CckAcdG}}$$
$$\cdot [\mathrm{CckA{:}\ cdG}] + 2 \cdot \left(- k^{+}_{\mathrm{DgcBcdG}} \cdot (DgcB - [\mathrm{DgcB{:}\ cdG_2}]) \cdot [\mathrm{cdG}]^2 + k^{-}_{\mathrm{XCdG}} \cdot [\mathrm{DgcB{:}\ cdG_2}]\right)$$

$$\frac{\mathrm{d}[\mathrm{DgcB{:}\ cdG_2}]}{\mathrm{dt}} = k^{+}_{\mathrm{DgcBcdG}} \cdot (DgcB - [\mathrm{DgcB{:}\ cdG_2}]) \cdot [\mathrm{cdG}]^2 - (\mu + k^{-}_{\mathrm{XCdG}}) \cdot [\mathrm{DgcB{:}\ cdG_2}]$$

$$\frac{\mathrm{d}[\mathrm{PleD}]}{\mathrm{dt}} = k_{\mathrm{s,PleD}} \cdot \frac{[\mathrm{CtrA{\sim}P}]^2}{J_{\mathrm{a,PleD-CtrA}}{}^2 + [\mathrm{CtrA{\sim}P}]^2} - \left(\mu + k_{\mathrm{d,PleD}}\right) \cdot [\mathrm{PleD}] - k_{\mathrm{phos,PleD}} \cdot [\mathrm{DivJ}]_{\mathrm{A}} \cdot [\mathrm{PleD}]$$
$$+ \left(\left(\frac{1}{10}\right) + \left(\frac{9}{10}\right) \cdot \frac{[\mathrm{PleC}]_{\mathrm{tot}} - [\mathrm{PleC}]_{\mathrm{pole}}}{[\mathrm{PleC}]_{\mathrm{tot}}}\right) \cdot k_{\mathrm{dephos,PleD}} \cdot [\mathrm{PleC}] \cdot [\mathrm{PleD{\sim}P}] - k^{+}_{\mathrm{PleDcdG}} \cdot [\mathrm{PleD}]$$
$$\cdot [\mathrm{cdG}]^2 + k^{-}_{\mathrm{XCdG}} \cdot [\mathrm{PleD{:}\ cdG_2}]$$

$$\frac{\mathrm{d}[\mathrm{PleD{\sim}P}]}{\mathrm{dt}} = -\left(\mu + k_{\mathrm{d,PleD}}\right) \cdot [\mathrm{PleD{\sim}P}] + k_{\mathrm{phos,PleD}} \cdot [\mathrm{DivJ}]_{\mathrm{A}} \cdot [\mathrm{PleD}]$$
$$- \left(\left(\frac{1}{10}\right) + \left(\frac{9}{10}\right) \cdot \frac{[\mathrm{PleC}]_{\mathrm{tot}} - [\mathrm{PleC}]_{\mathrm{pole}}}{[\mathrm{PleC}]_{\mathrm{tot}}}\right) \cdot k_{\mathrm{dephos,PleD}} \cdot [\mathrm{PleC}] \cdot [\mathrm{PleD{\sim}P}] - k^{+}_{\mathrm{PleDcdG}} \cdot [\mathrm{PleD{\sim}P}]$$
$$\cdot [\mathrm{cdG}]^2 + k^{-}_{\mathrm{XCdG}} \cdot [\mathrm{PleD{\sim}P{:}\ cdG_2}]$$

$$\frac{\mathrm{d}[\mathrm{PleD{:}\ cdG_2}]}{\mathrm{dt}} = -\left(\mu + k_{\mathrm{d,PleD}}\right) \cdot [\mathrm{PleD{:}\ cdG_2}] - k_{\mathrm{phos,PleD}} \cdot [\mathrm{DivJ}]_{\mathrm{A}} \cdot [\mathrm{PleD{:}\ cdG_2}]$$
$$+ \left(\left(\frac{1}{10}\right) + \left(\frac{9}{10}\right) \cdot \frac{[\mathrm{PleC}]_{\mathrm{tot}} - [\mathrm{PleC}]_{\mathrm{pole}}}{[\mathrm{PleC}]_{\mathrm{tot}}}\right) \cdot k_{\mathrm{dephos,PleD}} \cdot [\mathrm{PleC}] \cdot [\mathrm{PleD{\sim}P{:}\ cdG_2}] + k^{+}_{\mathrm{PleDcdG}}$$
$$\cdot [\mathrm{PleD}] \cdot [\mathrm{cdG}]^2 - k^{-}_{\mathrm{XCdG}} \cdot [\mathrm{PleD{:}\ cdG_2}]$$

$$\frac{\mathrm{d}[\mathrm{PleD{\sim}P{:}\ cdG_2}]}{\mathrm{dt}} = -\left(\mu + k_{\mathrm{d,PleD}}\right) \cdot [\mathrm{PleD{\sim}P{:}\ cdG_2}] + k_{\mathrm{phos,PleD}} \cdot [\mathrm{DivJ}]_{\mathrm{A}} \cdot [\mathrm{PleD{:}\ cdG_2}]$$
$$- \left(\left(\frac{1}{10}\right) + \left(\frac{9}{10}\right) \cdot \frac{[\mathrm{PleC}]_{\mathrm{tot}} - [\mathrm{PleC}]_{\mathrm{pole}}}{[\mathrm{PleC}]_{\mathrm{tot}}}\right) \cdot k_{\mathrm{dephos,PleD}} \cdot [\mathrm{PleC}] \cdot [\mathrm{PleD{\sim}P{:}\ cdG_2}] + k^{+}_{\mathrm{PleDcdG}}$$
$$\cdot [\mathrm{PleD{\sim}P}] \cdot [\mathrm{cdG}]^2 - k^{-}_{\mathrm{XCdG}} \cdot [\mathrm{PleD{\sim}P{:}\ cdG_2}]$$

B.1.2 Events and switches:

1) When [Zring]= 0 the cell volumes are split and protein concentrations shift in accordance with the equations specified below.
2) A new cell cycle begins when daughter cells separate 20 minutes after [Zring]=0.
3) M_i = 0.5 when the replication fork passes through gene i (i.e. [Elong]= 0.36 for *ctrA*, [Elong]=0.01 for *dnaA*, [Elong]= 0.25 for *ccrM*, and [Elong]= 0.75 for *perP*). M_i = 1 when [CcrM]=0.65.

4) [Zring]=1 at beginning of each cell cycle.
5) *MipZswitch*= 0 when [Zring]=0; *MipZswitch*= 1 when [Elong] = 1.
6) [ClpAP] = 1 when [Zring] = 0; [ClpAP] = 0 at beginning of each cell cycle.
7) *RepSwitch* = 1 when [Ini] = 1 and [Ini] is immediately reset to 0.
8) *RepSwitch* = 0 when [Elong]=1
9) [Elong] = 0 when [Zring] = 0.

B.1.3 Concentration shifts due to Cytokinesis:

Swarmer Cell:

$$[\mathrm{PleC}]_{\mathrm{Sw}} = [\mathrm{PleC}] \cdot \frac{[\mathrm{PleC}]_{\mathrm{Pole}}}{0.46 \cdot [\mathrm{PleC}]_{\mathrm{tot}}} + ([\mathrm{PleC}]_{\mathrm{tot}} - [\mathrm{PleC}]_{\mathrm{Pole}}) \cdot \frac{[\mathrm{PleC}]}{[\mathrm{PleC}]_{\mathrm{tot}}}$$

$$[\mathrm{PleC{:}\ DivK{\sim}P_2}]_{\mathrm{Sw}} = [\mathrm{PleC{:}\ DivK{\sim}P_2}] \cdot \frac{[\mathrm{PleC}]_{\mathrm{Pole}}}{0.46 \cdot [\mathrm{PleC}]_{\mathrm{tot}}} + ([\mathrm{PleC}]_{\mathrm{tot}} - [\mathrm{PleC}]_{\mathrm{Pole}}) \cdot \frac{[\mathrm{PleC{:}\ DivK{\sim}P_2}]}{[\mathrm{PleC}]_{\mathrm{tot}}}$$

$$[\mathrm{PleC}]_{\mathrm{Pole,Sw}} = \frac{[\mathrm{PleC}]_{\mathrm{Pole}}}{0.46}$$

$$[\mathrm{PleD{\sim}P}]_{\mathrm{Sw}} = \left(\frac{1}{10}\right) \cdot [\mathrm{PleD{\sim}P}]$$

$$[\mathrm{PleD{\sim}P{:}\ cdG_2}]_{\mathrm{Sw}} = \left(\frac{1}{10}\right) \cdot [\mathrm{PleD{\sim}P{:}\ cdG_2}]$$

$$[\mathrm{DivJ}]_{\mathrm{Sw}} = 0$$

$$[\mathrm{DivJ{:}\ DivK}]_{\mathrm{Sw}} = 0$$

$$[\mathrm{DivJ{:}\ DivK{\sim}P}]_{\mathrm{Sw}} = 0$$

$$[\mathrm{CpdR}]_{\mathrm{Sw}} = 0$$

$$[\mathrm{RcdA}]_{\mathrm{Sw}} = [\mathrm{RcdA}] \cdot \left(1 - \frac{[\mathrm{CpdR}]}{[\mathrm{CpdR}] + \frac{K_{\mathrm{ClpXpCpdR}}}{V}}\right)$$

$$[\mathrm{PopA}]_{\mathrm{Sw}} = [\mathrm{PopA}] \cdot \left(1 - \frac{[\mathrm{CpdR}]}{[\mathrm{CpdR}] + \frac{K_{\mathrm{ClpXpCpdR}}}{V}} \cdot \frac{[\mathrm{RcdA{:}\ PopA}]_{\mathrm{T}}}{[\mathrm{PopA}]_{\mathrm{T}}}\right)$$

$$[\mathrm{PopA{:}\ cdG_2}]_{\mathrm{Sw}} = [\mathrm{PopA{:}\ cdG_2}] \cdot \left(1 - \frac{[\mathrm{CpdR}]}{[\mathrm{CpdR}] + \frac{K_{\mathrm{ClpXpCpdR}}}{V}} \cdot \frac{[\mathrm{RcdA{:}\ PopA}]_{\mathrm{T}}}{[\mathrm{PopA}]_{\mathrm{T}}}\right)$$

$$[\mathrm{CckA{:}\ cdG}]_{\mathrm{Sw}} = \left(\frac{[\mathrm{CckA{:}\ cdG}]}{[\mathrm{CckA}]_{\mathrm{T}}}\right)\left([\mathrm{CckA}]_{\mathrm{T}} - [\mathrm{CckA{:}\ DivL}]_{\mathrm{T}} + \frac{1}{0.46}\left([\mathrm{CckA{:}\ DivL}]_{\mathrm{T}} - \frac{[\mathrm{CckA{:}\ DivL}]_{\mathrm{T}} \cdot [\mathrm{DivL{:}\ DivK{\sim}P}]}{[\mathrm{DivL}]_{\mathrm{T}}}\right)\right)$$

$$[\mathrm{CckA}]_{\mathrm{T,Sw}} = \frac{[\mathrm{CckA{:}\ DivL}]_{\mathrm{T}}}{0.46}\left(1 - \frac{[\mathrm{DivL{:}\ DivK{\sim}P}]}{[\mathrm{DivL}]_{\mathrm{T}}}\right) + [\mathrm{CckA}]_{\mathrm{T}} - [\mathrm{CckA{:}\ DivL}]_{\mathrm{T}}$$

$$[\mathrm{DivL}]_{\mathrm{Sw}} = \frac{[\mathrm{DivL}]}{0.46}$$

$$[\mathrm{DivL{:}\ DivK{\sim}P}]_{\mathrm{Sw}} = 0$$

$$[\mathrm{DivL{:}\ DivK}]_{\mathrm{Sw}} = \frac{[\mathrm{DivL{:}\ DivK}]}{0.46}$$

$$[\mathrm{DivJ}]_{\mathrm{Sw}} = \frac{[\mathrm{DivJ}]}{0.46}$$

$$[\mathrm{V}]_{\mathrm{Sw}} = 0.46 \cdot [\mathrm{V}]$$

Stalked Cell:

$$[\mathrm{PleC}]_{\mathrm{St}} = ([\mathrm{PleC}]_{\mathrm{tot}} - [\mathrm{PleC}]_{\mathrm{Pole}}) \cdot \frac{[\mathrm{PleC}]}{[\mathrm{PleC}]_{\mathrm{tot}}}$$

$$[\mathrm{PleC{:}\ DivK{\sim}P_2}]_{\mathrm{St}} = ([\mathrm{PleC}]_{\mathrm{tot}} - [\mathrm{PleC}]_{\mathrm{Pole}}) \cdot \frac{[\mathrm{PleC{:}\ DivK{\sim}P_2}]}{[\mathrm{PleC}]_{\mathrm{tot}}}$$

$$[\mathrm{PleC}]_{\mathrm{Pole,St}} = 0$$

$$[\mathrm{PleD{\sim}P}]_{\mathrm{St}} = \left(\frac{9}{10}\right) \cdot \frac{[\mathrm{PleD{\sim}P}]}{0.54} + \left(\frac{1}{10}\right) \cdot [\mathrm{PleD{\sim}P}]$$

$$[\mathrm{PleD{\sim}P{:}\ cdG_2}]_{\mathrm{ST}} = \left(\frac{9}{10}\right) \cdot \frac{[\mathrm{PleD{\sim}P{:}\ cdG_2}]}{0.54} + \left(\frac{1}{10}\right) \cdot [\mathrm{PleD{\sim}P{:}\ cdG_2}]$$

$$[\mathrm{DivJ}]_{\mathrm{St}} = \frac{[\mathrm{DivJ}]}{0.54}$$

$$[\mathrm{DivJ{:}\ DivK}]_{\mathrm{St}} = \frac{[\mathrm{DivJ{:}\ DivK}]}{0.54}$$

$$[\mathrm{DivJ{:}\ DivK{\sim}P}]_{\mathrm{St}} = \frac{[\mathrm{DivJ{:}\ DivK{\sim}P}]}{0.54}$$

$$[\mathrm{CpdR}]_{\mathrm{St}} = \frac{[\mathrm{CpdR}]}{0.54}$$

$$[\mathrm{RcdA}]_{\mathrm{St}} = [\mathrm{RcdA}] \cdot \left(1 - \frac{[\mathrm{CpdR}]}{[\mathrm{CpdR}] + \frac{K_{\mathrm{ClpXpCpdR}}}{V}}\right) + \frac{1}{0.54} \cdot \frac{[\mathrm{RcdA}] \cdot [\mathrm{CpdR}]}{[\mathrm{CpdR}] + \frac{K_{\mathrm{ClpXpCpdR}}}{V}}$$

$$[\mathrm{PopA}]_{\mathrm{St}} = [\mathrm{PopA}] \cdot \left(1 - \frac{[\mathrm{CpdR}]}{[\mathrm{CpdR}] + \frac{K_{\mathrm{ClpXpCpdR}}}{V}} \cdot \frac{[\mathrm{RcdA{:}\ PopA}]_{\mathrm{T}}}{[\mathrm{PopA}]_{\mathrm{T}}} + \frac{1}{0.54} \cdot \frac{[\mathrm{CpdR}]}{[\mathrm{CpdR}] + \frac{K_{\mathrm{ClpXpCpdR}}}{V}} \cdot \frac{[\mathrm{RcdA{:}\ PopA}]_{\mathrm{T}}}{[\mathrm{PopA}]_{\mathrm{T}}}\right)$$

$$[\text{PopA: cdG}_2]_{\text{St}} = [\text{PopA: cdG}_2] \cdot \left(1 - \frac{[\text{CpdR}]}{[\text{CpdR}] + \frac{K_{\text{ClpXpCpdR}}}{V}} \cdot \frac{[\text{RcdA: PopA}]_{\text{T}}}{[\text{PopA}]_{\text{T}}} + \frac{1}{0.54} \cdot \frac{[\text{CpdR}]}{[\text{CpdR}] + \frac{K_{\text{ClpXpCpdR}}}{V}} \cdot \frac{[\text{RcdA: PopA}]_{\text{T}}}{[\text{PopA}]_{\text{T}}} \right)$$

$$[\text{CckA: cdG}]_{\text{St}} = \left(\frac{[\text{CckA: cdG}]}{[\text{CckA}]_{\text{T}}} \right) \left([\text{CckA}]_{\text{T}} - [\text{CckA: DivL}]_{\text{T}} + \frac{1}{0.56} \left(\frac{[\text{CckA: DivL}]_{\text{T}} \cdot [\text{DivL: DivK}\sim\text{P}]}{[\text{DivL}]_{\text{T}}} \right) \right)$$

$$[\text{CckA}]_{\text{T,St}} = \frac{1}{0.56} \left(\frac{[\text{CckA: DivL}]_{\text{T}} \cdot [\text{DivL: DivK}\sim\text{P}]}{[\text{DivL}]_{\text{T}}} \right) + [\text{CckA}]_{\text{T}} - [\text{CckA: DivL}]_{\text{T}}$$

$$[\text{DivL}]_{\text{St}} = 0$$

$$[\text{DivL: DivK}\sim\text{P}]_{\text{St}} = \frac{[\text{DivL: DivK}\sim\text{P}]}{0.54}$$

$$[\text{DivL: DivK}]_{\text{St}} = 0$$

$$[\text{DivJ}]_{\text{St}} = 0$$

$$[\text{V}]_{\text{St}} = 0.54 \cdot [\text{V}]$$

B.2 Figures

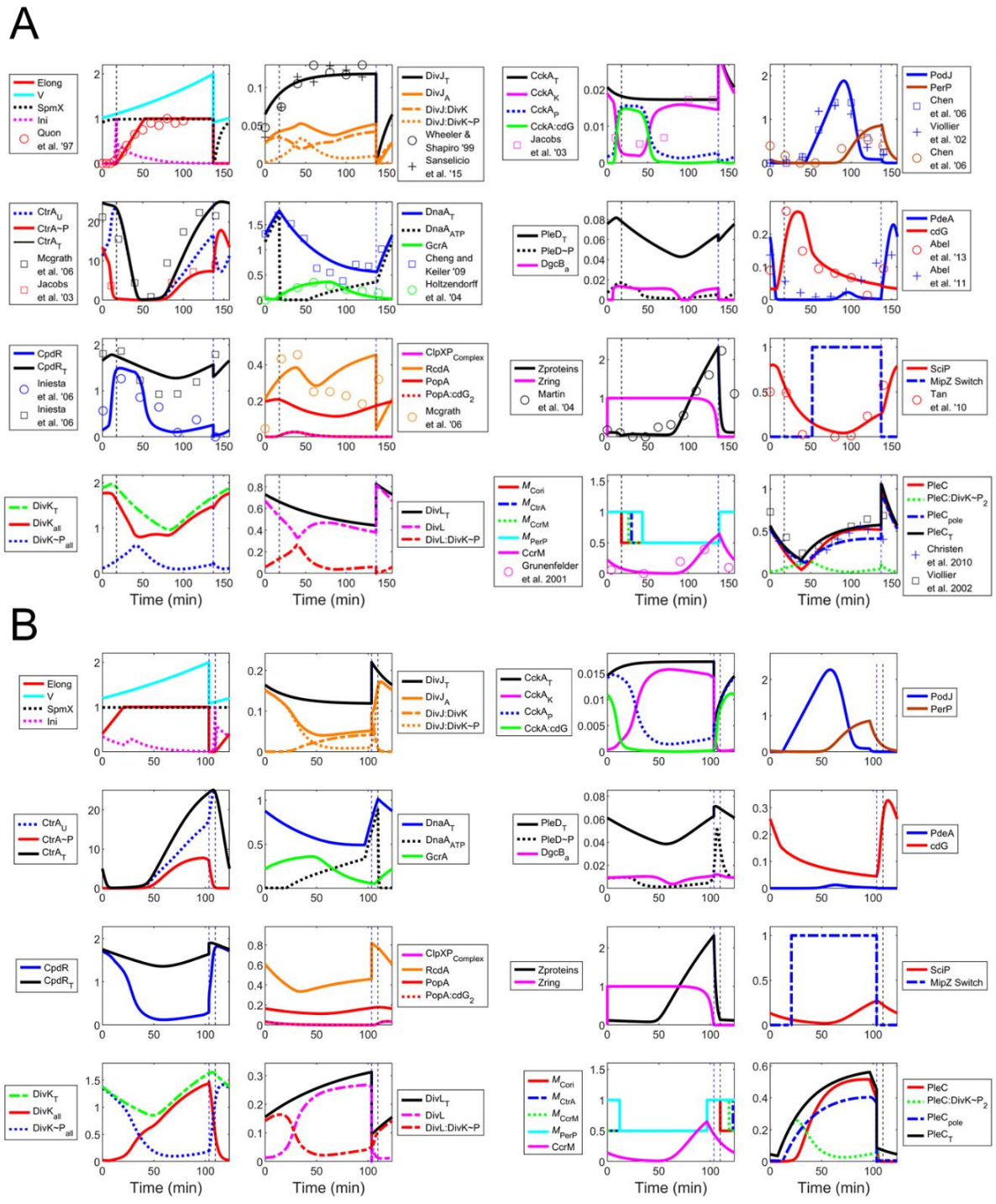

Figure B.1) Wild Type simulations with SLOW seed parameter set.
(A) Swarmer cell simulation. Variables in each subplot are indicated by the adjacent legend. X axis represents time, in minutes, and the y axis represents unitless concentration or activity. Exceptions are CtrA and cdG, which are both expressed in μM. Data points from literature are normalized to the simulation output. Vertical-dashed black and

blue lines correspond to the timing of chromosome replication and Z-ring constriction, respectively.
(B) Stalked cell simulation. Details are the same as in A.

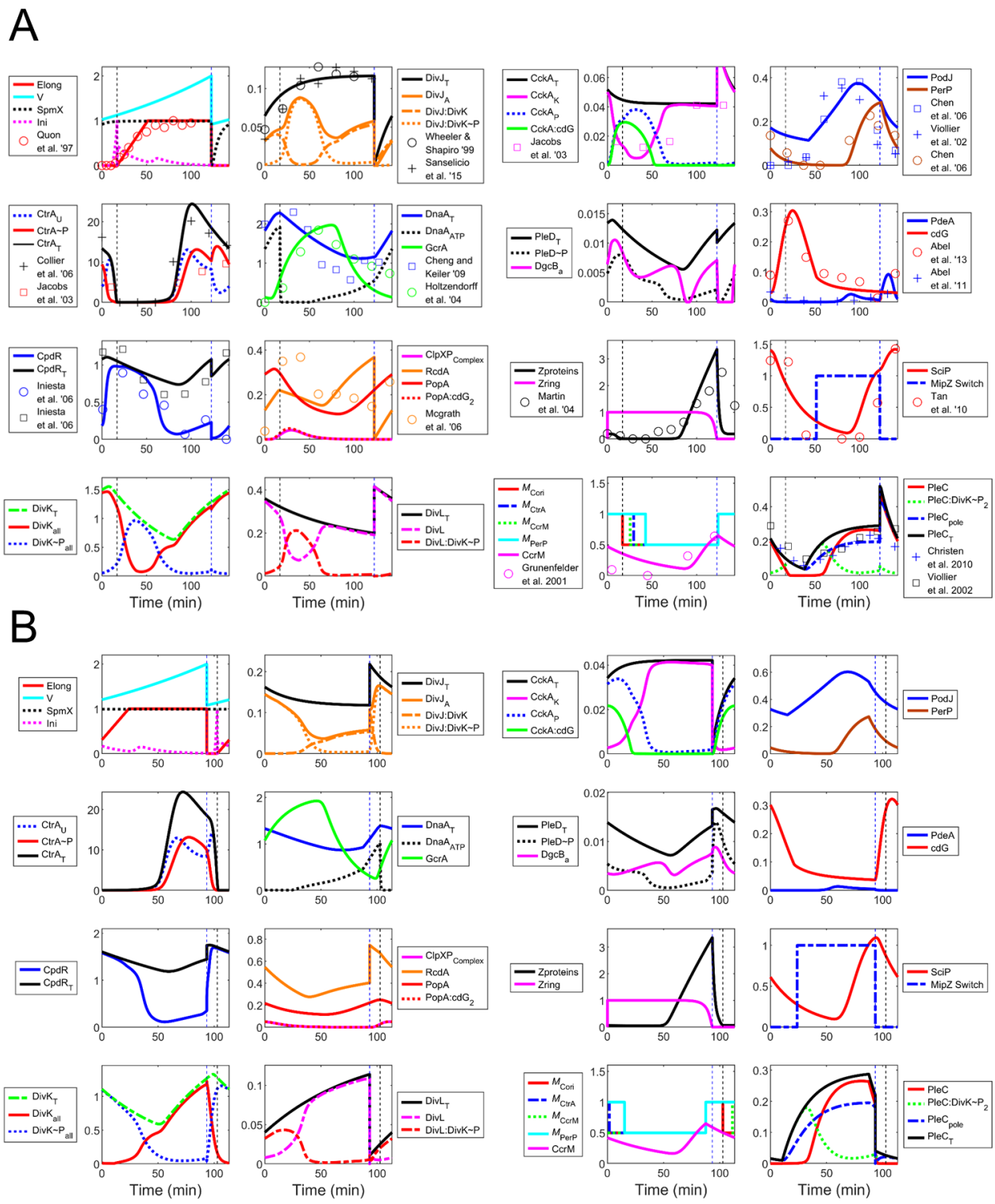

Figure B.2) Wild Type simulations with QUICK seed parameter set.
(A) Swarmer cell simulation. Details are the same as in Figure B.4A
(B) Stalked cell simulation. Details are the same as in Figure B.4A.

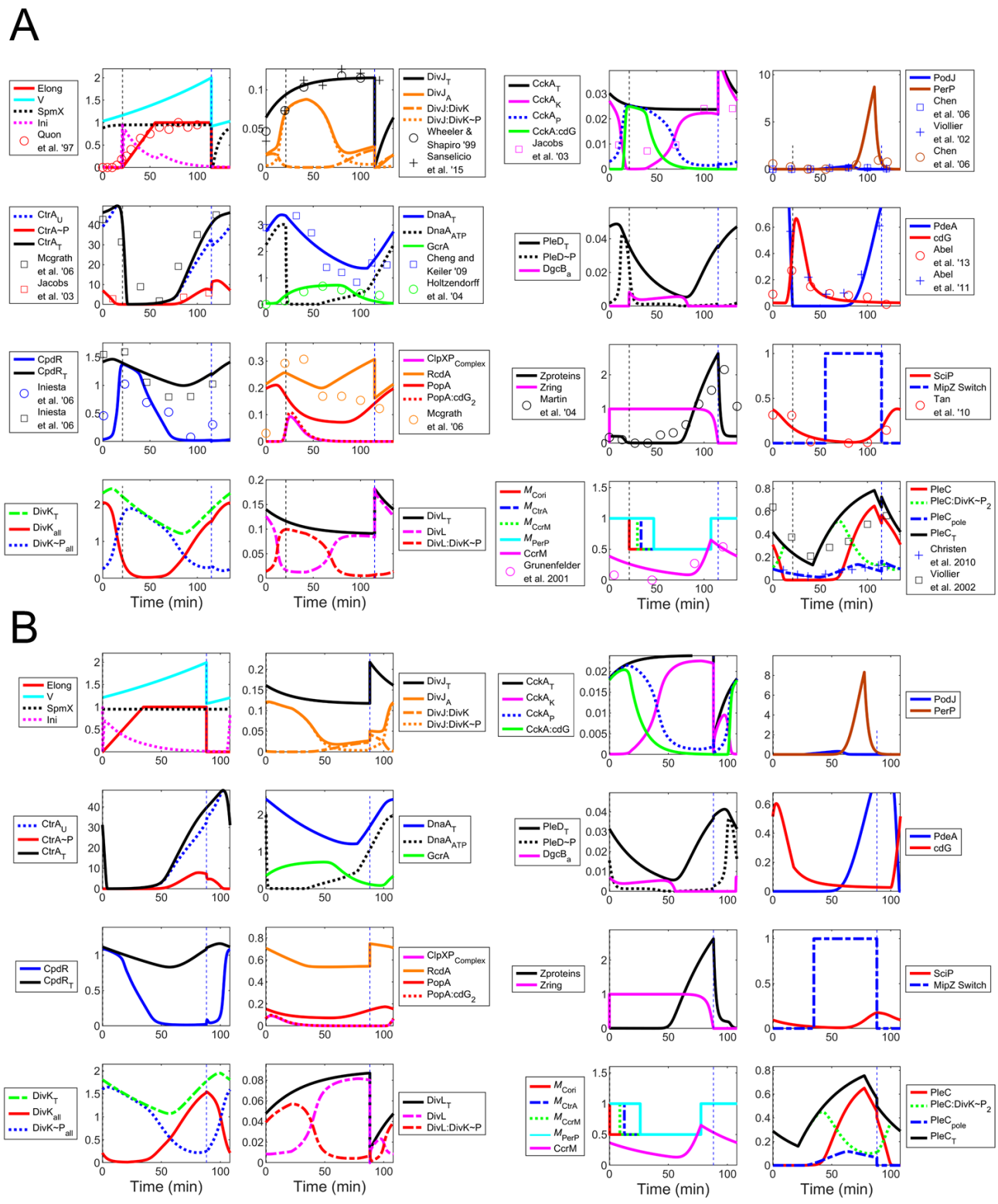

Figure B.3) Wild Type simulations with CORI- seed parameter set.
(A) Swarmer cell simulation. Details are the same as in Figure B.4A
(B) Stalked cell simulation. Details are the same as in Figure B.4A

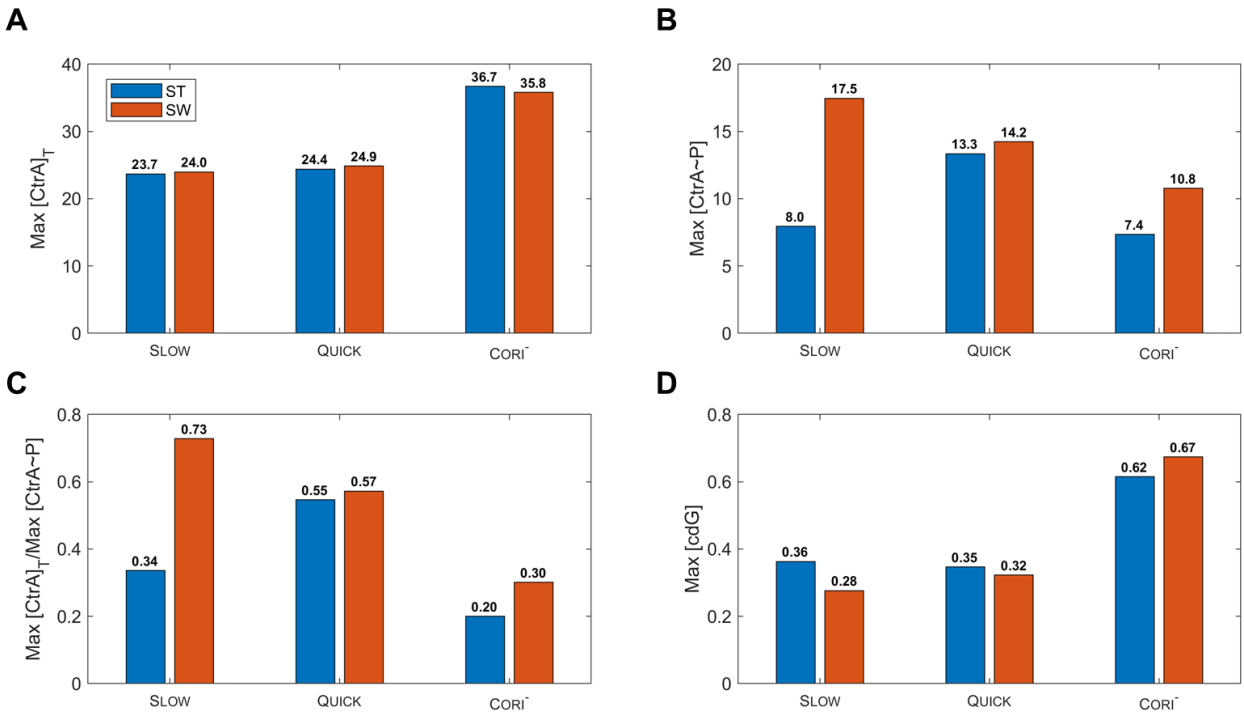

Figure B.4) $[CtrA]_T$ and [cdG] peaks are greater in CORI$^-$ parameter sets than in QUICK and SLOW.
(A) Peak $[CtrA]_T$ levels were recorded in the simulations of 150 random parameter sets from SLOW, QUICK and CORI$^-$ parameter collections. The average peak $[CtrA]_T$ is demonstrated in swarmer simulations (blue) and stalked simulations (orange).
(B) Average peak [CtrA~P] levels. See (A) for details.
(C) Average ratio of peak $[CtrA]_T$ levels to peak [CtrA~P] levels. See (A) for details.
(D) Average peak [cdG] levels. See (A) for details.

B.3 Tables

Table B.1) Parameters

	SLOW		QUICK		CORI-	
Param	Avg	Std	Avg	Std	Avg	Std
c	0.0350	0.0000	0.0350	0.0000	0.0350	0.0000
$DgcB$	0.0181	0.0005	0.0254	0.0019	0.0218	0.0015
$J_{a,CcrM\text{-}CtrA}$	15.6003	0.0000	15.6003	0.0000	7.8002	0.0000
$J_{a,CpdR\text{-}CtrA}$	11.0302	1.1218	34.0323	5.1554	5.5472	0.4899
$J_{a,CpdR\text{-}DnaA}$	1.0923	0.2628	0.0027	0.0002	0.9377	0.1504
$J_{a,CtrA\text{-}CtrA}$	0.3648	0.0595	0.6053	0.1327	0.3607	0.0138
$J_{a,CtrA\text{-}GcrA}$	0.1204	0.0268	0.0048	0.0009	0.1208	0.0397
$J_{a,DivK\text{-}CtrA}$	1.8130	0.2292	0.9628	0.0839	2.0288	0.1502
$J_{a,GcrA\text{-}DnaA}$	0.0007	0.0001	1.3894	0.9671	0.0112	0.0019
$J_{a,Ini\text{-}DnaA}$	0.0573	0.0076	0.2004	0.0317	0.1230	0.0195
$J_{a,PdeA\text{-}CtrA}$	0.4130	0.0357	0.5855	0.1174	9.3132	0.6828
$J_{a,PerP\text{-}CtrA}$	32.4729	4.3397	28.9291	7.8909	101.8380	14.0441
$J_{a,PleD\text{-}CtrA}$	4.2956	0.4761	4.3967	0.3686	2.0407	0.1281
$J_{a,PodJ\text{-}GcrA}$	0.0000	0.0000	0.0000	0.0000	0.0000	0.0000
$J_{a,RcdA\text{-}CtrA}$	0.0387	0.0044	0.0430	0.0088	0.0049	0.0004
$J_{a,SciP\text{-}CtrA}$	24.0900	1.9944	21.4873	1.5892	19.7682	2.0008
$J_{a,ZP\text{-}CtrA}$	0.8956	0.0844	0.8438	0.1346	0.4060	0.0359
$J_{d,cdG}$	0.0041	0.0003	0.0246	0.0061	0.0108	0.0014
$J_{d,CtrA}$	1.0000	0.0000	1.0000	0.0000	2.2085	0.1192
$J_{d,PdeA}$	0.0001	0.0000	0.0000	0.0000	0.0000	0.0000
$J_{d,PodJ}$	0.4484	0.0470	0.3177	0.0487	0.4918	0.1010
$J_{d,RcdA}$	0.0299	0.0044	0.2361	0.0768	0.0188	0.0008
$J_{i,CcrM\text{-}DnaA}$	0.5285	0.0346	1.4689	0.1847	0.5426	0.0343
$Ji_{,CpdR\text{-}GcrA}$	1.2787	0.1103	9.5389	3.1684	11.4860	0.8826
$J_{i,CtrA\text{-}CtrA}$	0.5481	0.0553	0.2400	0.0331	0.4034	0.0665
$J_{i,CtrA\text{-}SciP}$	0.3206	0.0316	0.2897	0.0454	0.2356	0.0563
$J_{i,DnaA\text{-}GcrA}$	0.8393	0.0808	0.4296	0.0781	0.2235	0.0299
$J_{i,GcrA\text{-}CtrA}$	1.2288	0.1368	0.6199	0.0835	1.2141	0.3191
$J_{i,PodJ\text{-}DnaA}$	0.7437	0.0954	0.0736	0.0099	0.3032	0.0725
$J_{i,PopA\text{-}GcrA}$	0.3349	0.0244	0.6010	0.1702	0.2758	0.0395
$J_{PlecPodJ}$	0.0095	0.0016	0.0051	0.0012	0.0879	0.0092
J_{zring}	0.3878	0.0467	1.4390	0.2301	0.4708	0.0360
$k^{+}_{CckAcdG}$	15.0516	1.5576	12.2513	2.1580	17.2733	2.1461
$k^{+}_{DgcBcdG}$	1.3523	0.1457	3.3801	0.3897	1.0029	0.1858
$k^{+}_{DivJDivK}$	2.2961	0.3485	2.3597	0.4199	1.3358	0.0820
$k^{+}_{DivJDivKP}$	1.4732	0.2168	1.9866	0.2070	0.7118	0.0877

$k^{+}_{DivLDivKP}$	11.3362	0.8402	4.7839	0.6752	15.0997	0.7145
$k^{+}_{PleCDivKP}$	0.0670	0.0111	0.0303	0.0062	0.0554	0.0040
$k^{+}_{PleDcdG}$	6.9691	0.5326	2.2692	0.5427	2.4104	0.3703
$k^{+}_{PopAcdG}$	1.5398	0.1337	1.4701	0.2382	2.6458	0.3283
$k^{-}_{CckAcdG}$	0.2345	0.0199	1.0357	0.1264	0.0257	0.0045
$K_{CckADivL}$	423.6030	47.1035	8284.3751	5310.8212	1384.2761	100.4964
$K_{ClpXpCpdR}$	0.0411	0.0083	0.0008	0.0001	0.0463	0.0105
$k_{d,CckA}$	0.0704	0.0056	0.0747	0.0229	0.0586	0.0045
$k_{d,CcrM}$	0.0462	0.0064	0.0108	0.0007	0.0140	0.0009
$k_{d,cdG}$	0.1719	0.0051	0.2043	0.0156	0.1905	0.0058
$k_{d,CpdR}$	0.0000	0.0000	0.0000	0.0000	0.0000	0.0000
$k_{d,CtrA1}$	0.0005	0.0001	0.0163	0.0020	0.0022	0.0002
$k_{d,CtrA2}$	41.8295	3.2197	193.7536	37.8655	169.7810	43.4643
$k_{d,DivJ}$	0.0346	0.0000	0.0346	0.0000	0.0346	0.0000
$k_{d,DivK}$	0.0083	0.0004	0.0085	0.0007	0.0057	0.0007
$k_{d,DivL}$	0.0077	0.0007	0.0075	0.0012	0.0241	0.0021
$k_{d,DnaA}$	0.0147	0.0013	0.0088	0.0016	0.0125	0.0015
$k_{d,GcrA}$	0.0475	0.0055	3.2177	0.7038	2.0975	0.1489
$k_{d,DnaAatp}$	1.6644	0.2978	0.0437	0.0029	0.0620	0.0039
$k_{d,Ini}$	0.0500	0.0000	0.0500	0.0000	0.0500	0.0000
$k_{d,PdeA1}$	0.0100	0.0000	0.0100	0.0000	0.0100	0.0000
$k_{d,PdeA2}$	0.3754	0.0381	0.4430	0.0361	0.1817	0.0131
$k_{d,PerP}$	0.1403	0.0094	0.0528	0.0115	0.3498	0.0807
$k_{d,PleC}$	0.0258	0.0011	0.0397	0.0032	0.0219	0.0007
$k_{d,PleD}$	0.0034	0.0004	0.0061	0.0013	0.0272	0.0034
$k_{d,PodJ1}$	0.0000	0.0000	0.0000	0.0000	0.0000	0.0000
$k_{d,PodJ2}$	0.5188	0.0375	0.0826	0.0158	0.5436	0.0824
$k_{d,PopA}$	0.0489	0.0015	0.0631	0.0101	0.0930	0.0078
$k_{d,RcdA1}$	0.0002	0.0000	0.0005	0.0001	0.0002	0.0001
$k_{d,RcdA2}$	0.0262	0.0038	0.0252	0.0039	0.0026	0.0003
$k_{d,SciP}$	0.0398	0.0049	0.0336	0.0062	0.0360	0.0046
$k_{d,ZP}$	0.0052	0.0005	0.0008	0.0001	0.0148	0.0024
K_{d1}	1.0650	0.0000	1.0000	0.0000	1.0000	0.0000
K_{d2}	0.0390	0.0000	1.0650	0.0000	1.0650	0.0000
K_{d3}	0.0001	0.0000	0.0390	0.0000	0.0390	0.0000
$k_{dephos,CpdR}$	102.6586	8.9236	0.0001	0.0000	0.0001	0.0000
$k_{dephos,CtrA}$	95.5259	7.9029	104.9305	17.3263	56.4686	4.5110
$k_{dephos,DivK}$	18.3931	1.6550	56.5665	9.5838	390.5269	29.7539
$k_{dephos,PleD}$	278.1202	23.3020	38.8009	5.1240	10.5977	0.6308
$k^{-}_{DivJDivK}$	4.7363	0.4369	126.7532	36.4716	592.3765	76.2864
$k^{-}_{DivJDivKP}$	0.0552	0.0073	2.6240	0.5486	7.6159	0.6869
$k^{-}_{DivLDivKP}$	0.9862	0.0614	0.1527	0.0205	0.1729	0.0261

$kelong$	0.0290	0.0000	1.0521	0.1823	2.6519	0.1953
$k_{phos,CpdR}$	77.6147	10.8694	0.0290	0.0000	0.0290	0.0000
$k_{phos,CtrA}$	9.0549	0.5410	26.8138	4.9936	242.5302	14.8424
$k_{phos,DivK1}$	1.5937	0.0901	2.8534	0.2554	7.7088	0.4835
$k_{phos,DivK2}$	0.0806	0.0176	1.5096	0.1647	1.5495	0.0790
$k_{phos,PleD}$	135.2211	5.3575	0.0286	0.0051	0.1569	0.0142
$k_{PleCbinding}$	0.1796	0.0171	51.8889	7.4986	339.8794	36.2888
$k^{-}_{PleCDivKP}$	61.6875	7.2210	0.1766	0.0392	0.0194	0.0027
$k_{PleCunbinding}$	0.0002	0.0000	161.4273	21.9412	114.6993	8.5413
$K_{RcdaPopa}$	806.2789	83.5852	0.0000	0.0000	0.0000	0.0000
$k_{s,CckA}$	0.0016	0.0002	733.7873	104.9682	54.1790	4.4222
$k_{s,CcrM}$	0.4475	0.0417	0.0041	0.0007	0.0013	0.0002
$k_{s,cdG1}$	1.0608	0.0765	0.1181	0.0085	0.4385	0.0144
$k_{s,cdG2}$	4.0132	0.2840	3.0936	0.5497	6.4971	0.5407
$k_{s,CpdR}$	0.0449	0.0056	2.3200	0.1545	3.9590	0.2027
$k_{s,CtrA-P1}$	0.0786	0.0090	0.0640	0.0111	0.0303	0.0023
$k_{s,CtrA-P2}$	0.5561	0.0306	0.0094	0.0019	0.1923	0.0261
$k_{s,DivJ}$	0.0047	0.0000	2.4014	0.3225	1.2263	0.0452
$k_{s,DivK1}$	0.0037	0.0007	0.0047	0.0000	0.0047	0.0000
$k_{s,DivK2}$	0.0350	0.0030	0.0016	0.0003	0.0016	0.0001
$k_{s,DivL}$	0.0050	0.0006	0.0276	0.0017	0.0455	0.0005
$k_{s,DnaA}$	0.0710	0.0072	0.0018	0.0003	0.0028	0.0005
$k_{s,GcrA}$	0.0188	0.0026	0.0841	0.0103	0.1152	0.0089
$k_{s,PdeA}$	0.0448	0.0039	0.1000	0.0117	0.0499	0.0037
$k_{s,PerP}$	0.1789	0.0151	0.0187	0.0017	0.0903	0.0041
$k_{s,PleC}$	0.0197	0.0008	0.0348	0.0073	8.0311	0.7985
$k_{s,PleD}$	0.0016	0.0001	0.0136	0.0017	0.0246	0.0015
$k_{s,PodJ}$	0.1104	0.0162	0.0003	0.0000	0.0021	0.0002
$k_{s,PopA}$	0.0139	0.0007	0.1347	0.0319	0.0581	0.0101
$k_{s,RcdA}$	0.0098	0.0017	0.0226	0.0088	0.0276	0.0042
$k_{s,SciP}$	0.1806	0.0204	0.0071	0.0011	0.0046	0.0009
$k_{s,SpmX}$	0.1400	0.0000	0.2415	0.0431	0.1771	0.0199
$k_{s,ZP}$	0.0533	0.0033	0.1400	0.0000	0.1400	0.0000
k^{-}_{XcdG}	0.0035	0.0004	0.0867	0.0051	0.0999	0.0043
$k_{Zconstrict}$	0.1871	0.0000	0.0035	0.0004	0.0032	0.0003
$m_{CtrA-P1}$	0.5537	0.0581	0.1871	0.0000	0.1871	0.0000
m_{DnaA}	0.8857	0.0287	0.0114	0.0025	0.1758	0.0170
m_{Ini}	0.3391	0.0280	0.4942	0.1047	0.5192	0.0672
PDE	0.3262	0.0111	0.0151	0.0029	0.1201	0.0135
$\varepsilon_{CpdR-DnaA}$	0.9819	0.0020	0.1337	0.0124	0.3216	0.0219
$\varepsilon_{CtrA-CtrA}$	0.0200	0.0000	1.0000	0.0000	0.9404	0.0070
$\varepsilon_{CtrA-GcrA}$	0.9958	0.0005	0.1796	0.0000	0.0200	0.0000
$\varepsilon_{GcrA-DnaA}$	0.5141	0.0449	0.9989	0.0002	0.9843	0.0020

θ_{DivJA}	0.0100	0.0000	0.8321	0.0647	0.7608	0.0864
θ_Z	3.0000	0.0000	0.0100	0.0000	0.0491	0.0006
$k_{d,ZP2}$	1.0000	0.0000	3.0000	0.0000	3.0000	0.0000

Table B.2) Mutant Descriptions

Mutant	Description	Cell Cycle Arrested?	Reference	Parameter Changes
*ctrA*Δ3Ω	Modification to the *ctrA* allele resulting in a non-proteolizable CtrA molecule. CtrA levels are constant in western blots.	FALSE	Domian et al. 1997 [210]	$k_{s,CtrAP1} = 0$ $k_{s,CtrAP2} = 0$ $k_{d,CtrA2} = 0$ $k_{s,CtrAΔ3Ω}$= 25x(k_{dCtrA1}+μ)
*ctrA*D51E	Modification to the *ctrA* allele resulting in an unphosphorylated, yet active CtrA molecule	FALSE	Domian et al. 1997 [210]	$k_{s,CtrAP1} = 0$ $k_{s,CtrAP2} = 0$ $k_{dephos,CtrA} = 0$ $K_{d3} = 0.039$ $k_{s,CtrAD51E}$ = 30x(k_{dCtrA1}+μ)
SM921	Knock out of *ctrA* P1	FALSE	Schredl et al. 2012 [262]	$k_{s,CtrAP1} = 0$
*ctrA*D51EΔ3Ω	Constitutively expressed, non degradable, constantly active CtrA	TRUE	Domian et al. 1997 [210]	$k_{s,CtrAP1} = 0$ $k_{s,CtrAP2} = 0$ $k_{d,CtrA2} = 0$ $k_{dephos,CtrA} = 0$ $K_{d3} = 0.039$ $k_{s,CtrAD51E}$ = 30x($k_{d,CtrA1}$+μ)
Δ*gcrA*	*gcrA* knock out	FALSE	Murray et al. 2013 [120]	$k_{s,GcrA} = 0$
Δ*ccrM*	*ccrM* knock out	FALSE	Gonzalez et al. 2013 [127]	$k_{s,CcrM} = 0$
LS1	Constitutively over expressed CcrM	FALSE	Zweiger et al. 1994 [263]	$\sigma_{\Delta SpmX} = 0.9$ $k_{s,LS1} = k_{s,CcrM}$
P*pleC*::Tn	Transposon inserted into *pleC* promoter to completely disrupt PleC synthesis	FALSE	Wheeler and Shapiro 1999 [24]; Biondi et al., 2006 [246]; Tsokos et al. 2011 [204]	$k_{s,PleC} = 0$ $\sigma_{\Delta SpmX} = 1$

divL^{ts}	Temperatures sensitive protein, inactivates at higher temp	TRUE	Tsokos et al. 2011 [204]	$k_{s,DivL} = k_{s,DivL}x10^{-4}$
divL(A601L)	Mutation that disrupts binding of DivK to DivL	TRUE	Tsokos et al. 2011 [204]	$k^{+}_{DivLDivKP} = k^{+}_{DivLDivKP}$ x10^{-4} $k^{-}_{DivLDivKP}$ = 100 x $k^{-}_{DivLDivKP}$
divL(Y550F)	Enhanced binding of DivK to DivL	FALSE	Tsokos et al. 2011 [204]	$k^{-}_{DivLDivKP}$ = 0.1 x $k^{-}_{DivLDivKP}$
P*pleC*::Tn & *divL*(Y550F)	Double mutant of DivL(Y550F) and PleC:: Tn5	FALSE	Tsokos et al. 2011 [204]	$k_{s,PleC} = 0$ $\sigma_{\Delta SpmX} = 0.98$ $k^{-}_{DivLDivKP} = 0.1x\ k^{-}_{DivLDivKP}$
Δ*divJ*	DivJ Knockout	FALSE	Wheeler and Shapiro 1999 [24]; Radhakrishnan 2008 [152]	$k_{s,DivJ} = 0$
PpleC::Tn & Δ*divJ*	Double mutant of Δ*divJ* and P*pleC*:: Tn	FALSE	Wheeler and Shapiro 1999 [24]	$k_{s,DivJ} = 0$ $k_{s,PleC} = 0$ $\sigma_{\Delta SpmX} = 0.98$
Δ*spmX*	*spmX* knock out	FALSE	Radhakrishnan et al. 2008 [152]	$\sigma_{\Delta SpmX} = 1$
P*pleC*::Tn & Δ*spmX*	Double mutant of Δ*spmX* and *pleC*::Tn5	FALSE	Radhakrishnan et al. 2008 [152]	$k_{s,PleC} = 0$ $\sigma_{\Delta SpmX} = 1$
P*divK*::Tn	Transposon (Tn) insertion in the promoter region of *divK*, resulting in 15% DivK expression compared to WT	FALSE	Lori et al. 2015 [160]	$k_{s,DivK1} = 0.4x k_{sDivK1}$ $k_{s,DivK2} = 0.4x k_{sDivK2}$
divK^{cs}	Cold sensitive DivK mutant	TRUE	Biondi et al. 2006 [246]	$k_{s,DivK1} = 0$ $k_{s,DivK2} = 0$ $k_{d,DivK} = 50x k_{dDivK}$
divK^{xyl}	Xylose induced overproduction of DivK.	TRUE	Biondi et al. 2006 [246]	$k_{s,DivK1}$=25x$k_{s,DivK1}$
cdG_0	Strain that is devoid of cdG	FALSE	Abel et al. 2013 [161]; Lori et al. 2015 [160]	$k_{s,cdG1} = 0$ $k_{s,cdG2}$=0
P*divK*::Tn & cdG_0	P*divK*::Tn and cdG_0 - double mutant	TRUE	Lori et al. 2015 [160]	$k_{s,cdG1} = 0$ $k_{s,cdG2}$=0 $k_{s,DivK1}$ =

				$0.1x k_{s,DivK1}$ $k_{s,DivK2} = 0.1x k_{s,DivK2}$
Δ*popA*	*popA* knock out	FALSE	Lori et al. 2015 [160]	$k_{s,PopA} = 0$
Δ*pleD*	*pleD* knock out	FALSE	Lori et al. 2015 [160]	$k_{s,PleD} = 0$
Δ*popA* & P*divK*::Tn	Double mutant of P*divK*::Tn and Δ*popA*	FALSE	Lori et al. 2015 [160]	$k_{s,DivK1} = 0.15x k_{s,DivK1}$ $k_{s,DivK2} = 0.15x k_{s,DivK2}$ $k_{s,PopA} = 0$
Δ*pleD* & P*divK*::Tn	Double mutant of P*divK*::Tn and Δ*pleD*	FALSE	Lori et al. 2015 [160]	$k_{s,DivK1} = 0.25x k_{s,DivK1}$ $k_{s,DivK2} = 0.25x k_{s,DivK2}$ $k_{s,PleD} = 0$
Δ*popA* & Δ*pleD*	Double mutant of Δ*pleD* and Δ*popA*	FALSE	Lori et al. 2015 [160]	$k_{s,PopA} = 0$ $k_{s,PleD} = 0$
Δ*dgcB*	*dgcB* knock out	FALSE	Abel et al. 2013 [161]	$DgcB = DgcB x10^{-6}$
Δ*pdeA*	*pdeA* knock out	FALSE	Abel et al. 2011 [167]	$k_{s,PdeA} = 0$
Δ*popA* & Δ*pleD* & P*divK::*Tn	Triple mutant of P*divK*::Tn, Δ*popA* and Δ*pleD*	TRUE	Lori et al. 2015 [160]	$k_{s,DivK1} = 0.25x k_{s,DivK1}$ $k_{s,DivK2} = 0.25x k_{s,DivK2}$ $k_{s,PleD} = 0$ $k_{s,PopA} = 0$
cckA(Y514D)	Mutant of CckA that is not influenced by cdG	FALSE	Lori et al. 2015 [160]	$k^{+}_{CckAcdG} = k^{+}_{CckAcdG} x10^{-4}$
cckA(Y514D) & P*divK*::Tn	Double mutant of *cckA*(Y514D) & P*divK*::Tn	TRUE	Lori et al. 2015 [160]	$k_{s,DivK1} = 0.1x k_{s,DivK1}$ $k_{s,DivK2} = 0.1x k_{s,DivK2}$ $k^{+}_{CckAcdG} = k^{+}_{CckAcdG} x10^{-4}$
Δ*podJ*	*podJ* knock out	FALSE	Viollier et al. 2002 [200]; Hinz et al. 2003 [156]	$k_{s,PodJ} = 0$

JC353 (Δ*hdaA* pX-HdaA)	*hdaA* knock out with xylose inducible plasmid containing *hdaA*	FALSE	Collier and Shapiro 2009 [224]	$k_{d,DnaAatp} = 0$
Δ*rcdA*	*rcdA* knock out	FALSE	Taylor et al. 2009 [221]	$k_{s,RcdA} = 0$ $k_{d,RcdA1} = 100x k_{d,RcdA1}$

Table B.3) Arrest in SLOW simulations
1 Cr and 2 Cr correspond to population of cells with cell cycle arrest that have 1 or 2 chromosomes, respectively. >2Cr are cells with cell cycle arrest with more than 2 chromosomes.

	SLOW SW				SLOW SW - $CtrA_U$:*Cori*			
Strain	Viable	1 Cr	2 Cr	>2 Cr	Viable	1 Cr	2 Cr	>2 Cr
WT	100.0%	0.0%	0.0%	0.0%	100.0%	0.0%	0.0%	0.0%
*ctrA*Δ3Ω	100.0%	0.0%	0.0%	0.0%	0.0%	97.3%	2.7%	0.0%
*ctrA*D51E	94.7%	4.0%	1.3%	0.0%	96.7%	2.7%	0.7%	0.0%
*ctrA*D51EΔ3Ω	0.0%	95.3%	4.7%	0.0%	0.0%	97.3%	2.7%	0.0%
SM921	100.0%	0.0%	0.0%	0.0%	100.0%	0.0%	0.0%	0.0%
Δ*gcrA*	99.3%	0.0%	0.0%	0.7%	100.0%	0.0%	0.0%	0.0%
Δ*ccrM*	92.7%	7.3%	0.0%	0.0%	0.0%	97.3%	2.7%	0.0%
LS1	98.0%	0.0%	0.0%	2.0%	0.0%	0.0%	6.0%	94.0%
P*pleC*::Tn	100.0%	0.0%	0.0%	0.0%	0.0%	86.0%	13.3%	0.7%
divL^{ts}	8.0%	72.0%	18.7%	1.3%	4.7%	88.7%	6.7%	0.0%
divL(A601L)	0.0%	86.7%	12.0%	1.3%	0.0%	87.3%	12.7%	0.0%
divL(Y550F)	99.3%	0.0%	0.7%	0.0%	98.7%	0.0%	1.3%	0.0%
P*pleC*::Tn & *divL(Y550F)*	98.7%	0.0%	0.0%	1.3%	0.0%	97.3%	2.7%	0.0%
Δ*divJ*	0.0%	95.3%	4.7%	0.0%	0.0%	97.3%	2.7%	0.0%
P*pleC*::Tn & Δ*divJ*	0.0%	95.3%	4.7%	0.0%	0.0%	97.3%	2.7%	0.0%
Δ*spmX*	98.7%	0.0%	0.7%	0.7%	100.0%	0.0%	0.0%	0.0%
P*pleC*::Tn & Δ*spmX*	99.3%	0.0%	0.0%	0.7%	0.7%	96.0%	3.3%	0.0%
P*divK*::Tn	100.0%	0.0%	0.0%	0.0%	98.7%	0.0%	0.0%	1.3%
divK^{cs}	0.0%	95.3%	4.7%	0.0%	0.0%	97.3%	2.7%	0.0%
divK^{xyl}	0.0%	0.0%	0.0%	100.0%	0.0%	0.0%	0.0%	100.0%
cdG0	98.7%	0.0%	0.0%	1.3%	0.0%	97.3%	2.7%	0.0%
P*divK*::Tn & cdG0	0.0%	95.3%	4.7%	0.0%	0.0%	97.3%	2.7%	0.0%
Δ*popA*	99.3%	0.0%	0.0%	0.7%	0.0%	97.3%	2.7%	0.0%
Δ*pleD*	99.3%	0.0%	0.0%	0.7%	0.0%	97.3%	2.7%	0.0%
Δ*popA* & P*divK*::Tn	100.0%	0.0%	0.0%	0.0%	0.0%	97.3%	2.7%	0.0%
Δ*popA* & Δ*pleD*	100.0%	0.0%	0.0%	0.0%	0.0%	97.3%	2.7%	0.0%
Δ*dgcB*	99.3%	0.0%	0.0%	0.7%	0.7%	96.7%	2.7%	0.0%
Δ*pdeA*	99.3%	0.7%	0.0%	0.0%	58.0%	40.7%	1.3%	0.0%
Δ*popA* & Δ*pleD* & P*divK*::Tn	100.0%	0.0%	0.0%	0.0%	0.0%	97.3%	2.7%	0.0%
cckA(Y514D)	99.3%	0.0%	0.0%	0.7%	100.0%	0.0%	0.0%	0.0%
cckA(Y514D) & P*divK*::Tn	92.0%	8.0%	0.0%	0.0%	98.0%	2.0%	0.0%	0.0%
Δ*podJ*	100.0%	0.0%	0.0%	0.0%	100.0%	0.0%	0.0%	0.0%
Δ*hdaA*	100.0%	0.0%	0.0%	0.0%	100.0%	0.0%	0.0%	0.0%
Δ*pleD* & P*divK*::Tn	100.0%	0.0%	0.0%	0.0%	0.0%	97.3%	2.7%	0.0%
Δ*rcdA*	99.3%	0.0%	0.7%	0.0%	0.0%	97.3%	2.7%	0.0%

	SLOW ST				SLOW ST - CtrA$_U$:*Cori*			
Strain	Viable	1 Cr	2 Cr	>2 Cr	Viable	1 Cr	2 Cr	>2 Cr
WT	98.7%	0.0%	0.0%	1.3%	91.3%	7.3%	1.3%	0.0%
*ctrA*Δ3Ω	95.3%	0.0%	0.0%	4.7%	0.0%	93.3%	6.7%	0.0%
*ctrA*D51E	95.3%	3.3%	0.7%	0.7%	97.3%	1.3%	1.3%	0.0%
*ctrA*D51EΔ3Ω	0.0%	93.3%	6.0%	0.7%	0.0%	93.3%	6.7%	0.0%
SM921	99.3%	0.0%	0.0%	0.7%	96.7%	1.3%	2.0%	0.0%
Δ*gcrA*	86.0%	13.3%	0.0%	0.7%	28.7%	66.0%	5.3%	0.0%
Δ*ccrM*	98.0%	0.0%	1.3%	0.7%	72.7%	25.3%	2.0%	0.0%
LS1	92.7%	0.0%	0.7%	6.7%	0.0%	2.7%	2.7%	94.7%
P*pleC*::Tn	98.7%	0.0%	0.0%	1.3%	0.0%	92.7%	7.3%	0.0%
divL^{ts}	0.0%	72.7%	18.0%	9.3%	0.0%	76.7%	22.7%	0.7%
divL(A601L)	0.0%	93.3%	6.0%	0.7%	0.0%	90.0%	10.0%	0.0%
divL(Y550F)	98.7%	0.0%	0.0%	1.3%	0.0%	93.3%	6.7%	0.0%
P*pleC*::Tn & *divL(Y550F)*	98.0%	0.0%	0.0%	2.0%	0.0%	10.0%	82.7%	7.3%
Δ*divJ*	0.0%	92.7%	6.7%	0.7%	0.0%	93.3%	6.7%	0.0%
P*pleC*::Tn & Δ*divJ*	0.0%	0.0%	4.0%	96.0%	0.0%	92.7%	7.3%	0.0%
Δ*spmX*	96.7%	2.7%	0.0%	0.7%	4.0%	85.3%	10.7%	0.0%
P*pleC*::Tn & Δ*spmX*	94.0%	0.0%	0.0%	6.0%	0.0%	93.3%	6.7%	0.0%
P*divK*::Tn	99.3%	0.0%	0.0%	0.7%	96.7%	2.0%	1.3%	0.0%
divK^{cs}	0.0%	93.3%	6.0%	0.7%	0.0%	93.3%	6.7%	0.0%
divK^{xyl}	0.0%	0.0%	0.0%	100.0%	0.0%	0.7%	1.3%	98.0%
cdG0	98.7%	0.0%	0.0%	1.3%	0.0%	93.3%	6.7%	0.0%
P*divK*::Tn & cdG0	0.0%	90.7%	8.7%	0.7%	0.0%	93.3%	6.7%	0.0%
Δ*popA*	98.7%	0.0%	0.7%	0.7%	0.0%	93.3%	6.7%	0.0%
Δ*pleD*	96.7%	0.0%	0.7%	2.7%	0.0%	93.3%	6.7%	0.0%
Δ*popA* & P*divK*::Tn	95.3%	3.3%	0.7%	0.7%	0.0%	93.3%	6.7%	0.0%
Δ*popA* & Δ*pleD*	98.0%	0.0%	0.0%	2.0%	0.0%	93.3%	6.7%	0.0%
Δ*dgcB*	98.0%	0.0%	0.0%	2.0%	0.0%	93.3%	6.7%	0.0%
Δpdea	98.0%	1.3%	0.0%	0.7%	52.0%	44.7%	3.3%	0.0%
Δ*popA* & Δ*pleD* & P*divK*::Tn	97.3%	1.3%	0.7%	0.7%	0.0%	93.3%	6.7%	0.0%
cckA(Y514D)	98.7%	0.0%	0.0%	1.3%	96.7%	2.0%	1.3%	0.0%
cckA(Y514D) & P*divK*::Tn	92.0%	5.3%	2.0%	0.7%	88.0%	9.3%	2.7%	0.0%
Δ*podJ*	90.7%	8.7%	0.0%	0.7%	72.7%	22.7%	3.3%	1.3%
Δ*hdaA*	99.3%	0.0%	0.0%	0.7%	88.0%	2.0%	1.3%	8.7%
Δ*pleD* & P*divK*::Tn	94.7%	4.7%	0.0%	0.7%	0.0%	93.3%	6.7%	0.0%
Δ*rcdA*	98.7%	0.0%	0.0%	1.3%	0.0%	93.3%	6.7%	0.0%

Table B.4) Arrest in QUICK simulations

1 Cr and 2 Cr correspond to population of cells with cell cycle arrest that have 1 or 2 chromosomes, respectively. >2Cr are cells with cell cycle arrest with more than 2 chromosomes.

	QUICK SW				QUICK SW - CtrA$_U$:*Cori*			
Strain	Viable	1 Cr	2 Cr	>2 Cr	Viable	1 Cr	2 Cr	>2 Cr
WT	97.3%	0.0%	2.7%	0.0%	98.7%	0.0%	1.3%	0.0%
*ctrA*Δ3Ω	96.0%	2.0%	2.0%	0.0%	0.0%	98.7%	1.3%	0.0%
*ctrA*D51E	98.0%	0.0%	2.0%	0.0%	98.7%	0.0%	1.3%	0.0%
*ctrA*D51EΔ3Ω	0.0%	98.7%	1.3%	0.0%	0.0%	98.7%	1.3%	0.0%
SM921	98.7%	0.0%	1.3%	0.0%	98.7%	0.0%	1.3%	0.0%
Δ*gcrA*	98.0%	0.0%	1.3%	0.7%	99.3%	0.0%	0.7%	0.0%
Δ*ccrM*	98.7%	0.0%	1.3%	0.0%	94.0%	5.3%	0.7%	0.0%
LS1	95.3%	0.0%	2.0%	2.7%	87.3%	11.3%	1.3%	0.0%
P*pleC*::Tn	98.7%	0.0%	1.3%	0.0%	99.3%	0.0%	0.7%	0.0%
divL^{ts}	20.7%	77.3%	2.0%	0.0%	28.7%	68.7%	2.7%	0.0%
divL(A601L)	0.0%	98.0%	2.0%	0.0%	0.0%	98.7%	1.3%	0.0%
divL(Y550F)	98.7%	0.0%	1.3%	0.0%	98.7%	0.0%	1.3%	0.0%
P*pleC*::Tn & *divL(Y550F)*	98.7%	0.0%	1.3%	0.0%	92.7%	6.7%	0.7%	0.0%
Δ*divJ*	0.0%	98.7%	1.3%	0.0%	0.0%	98.7%	1.3%	0.0%
P*pleC*::Tn & Δ*divJ*	0.0%	98.7%	1.3%	0.0%	0.0%	98.7%	1.3%	0.0%
Δ*spmX*	98.7%	0.0%	1.3%	0.0%	99.3%	0.0%	0.7%	0.0%
P*pleC*::Tn & Δ*spmX*	98.0%	0.0%	2.0%	0.0%	99.3%	0.0%	0.7%	0.0%
P*divK*::Tn	98.7%	0.0%	1.3%	0.0%	98.7%	0.0%	1.3%	0.0%
divK^{cs}	0.0%	98.7%	1.3%	0.0%	0.0%	98.7%	1.3%	0.0%
divK^{xyl}	2.0%	0.0%	1.3%	96.7%	0.0%	2.0%	37.3%	60.7%
cdG0	98.0%	0.0%	2.0%	0.0%	0.0%	98.7%	1.3%	0.0%
P*divK*::Tn & cdG0	0.0%	98.7%	1.3%	0.0%	0.0%	98.7%	1.3%	0.0%
Δ*popA*	98.7%	0.0%	1.3%	0.0%	0.0%	98.7%	1.3%	0.0%
Δ*pleD*	98.0%	0.0%	2.0%	0.0%	86.7%	12.7%	0.7%	0.0%
Δ*popA* & P*divK*::Tn	98.7%	0.0%	1.3%	0.0%	0.0%	98.7%	1.3%	0.0%
Δ*popA* & Δ*pleD*	98.7%	0.0%	1.3%	0.0%	0.0%	98.7%	1.3%	0.0%
Δ*dgcB*	98.7%	0.0%	1.3%	0.0%	65.3%	34.0%	0.7%	0.0%
Δ*pdeA*	98.0%	0.0%	2.0%	0.0%	91.3%	5.3%	3.3%	0.0%
Δ*popA* & Δ*pleD* & P*divK*::Tn	84.0%	14.0%	2.0%	0.0%	0.0%	98.7%	1.3%	0.0%
cckA(Y514D)	98.7%	0.0%	1.3%	0.0%	99.3%	0.0%	0.7%	0.0%
cckA(Y514D) & P*divK*::Tn	98.7%	0.0%	1.3%	0.0%	98.7%	0.0%	1.3%	0.0%
Δ*podJ*	98.7%	0.0%	1.3%	0.0%	98.0%	0.7%	1.3%	0.0%
Δ*hdaA*	98.7%	0.0%	1.3%	0.0%	99.3%	0.0%	0.7%	0.0%
Δ*pleD* & P*divK*::Tn	98.7%	0.0%	1.3%	0.0%	80.7%	18.7%	0.7%	0.0%
Δ*rcdA*	98.0%	0.0%	2.0%	0.0%	0.0%	98.7%	1.3%	0.0%

	QUICK ST				QUICK ST - CtrA$_U$:*Cori*			
Strain	Viable	1 Cr	2 Cr	>2 Cr	Viable	1 Cr	2 Cr	>2 Cr
WT	100.0%	0.0%	0.0%	0.0%	98.0%	1.3%	0.7%	0.0%
*ctrA*Δ3Ω	99.3%	0.0%	0.7%	0.0%	0.0%	99.3%	0.7%	0.0%
*ctrA*D51E	100.0%	0.0%	0.0%	0.0%	98.0%	0.7%	1.3%	0.0%
*ctrA*D51EΔ3Ω	0.0%	99.3%	0.7%	0.0%	0.0%	99.3%	0.7%	0.0%
SM921	100.0%	0.0%	0.0%	0.0%	98.7%	0.7%	0.7%	0.0%
Δ*gcrA*	100.0%	0.0%	0.0%	0.0%	95.3%	0.7%	1.3%	2.7%
Δ*ccrM*	100.0%	0.0%	0.0%	0.0%	98.7%	0.7%	0.7%	0.0%
LS1	98.7%	0.0%	0.0%	1.3%	30.0%	55.3%	14.7%	0.0%
P*pleC*::Tn	99.3%	0.0%	0.0%	0.7%	89.3%	10.0%	0.7%	0.0%
divL^{ts}	0.0%	99.3%	0.7%	0.0%	0.0%	98.7%	1.3%	0.0%
divL(A601L)	0.0%	99.3%	0.7%	0.0%	0.0%	99.3%	0.7%	0.0%
divL(Y550F)	99.3%	0.0%	0.7%	0.0%	89.3%	10.0%	0.7%	0.0%
P*pleC*::Tn & *divL(Y550F)*	96.7%	0.0%	0.7%	2.7%	42.7%	18.0%	36.0%	3.3%
Δ*divJ*	0.0%	99.3%	0.7%	0.0%	0.0%	99.3%	0.7%	0.0%
P*pleC*::Tn & Δ*divJ*	0.7%	40.7%	57.3%	1.3%	0.0%	98.0%	2.0%	0.0%
Δ*spmX*	99.3%	0.7%	0.0%	0.0%	98.0%	1.3%	0.7%	0.0%
P*pleC*::Tn & Δ*spmX*	98.0%	0.7%	0.7%	0.7%	89.3%	10.0%	0.7%	0.0%
P*divK*::Tn	98.7%	0.7%	0.7%	0.0%	98.0%	1.3%	0.7%	0.0%
divK^{cs}	0.0%	99.3%	0.7%	0.0%	0.0%	99.3%	0.7%	0.0%
divK^{xyl}	0.0%	0.0%	0.7%	99.3%	0.0%	0.7%	38.0%	61.3%
cdG0	94.0%	0.0%	1.3%	4.7%	0.0%	99.3%	0.7%	0.0%
P*divK*::Tn & cdG0	0.0%	99.3%	0.7%	0.0%	0.0%	99.3%	0.7%	0.0%
Δ*popA*	96.7%	0.7%	2.0%	0.7%	0.0%	99.3%	0.7%	0.0%
Δ*pleD*	98.7%	0.0%	0.7%	0.7%	48.7%	50.0%	1.3%	0.0%
Δ*popA* & P*divK*::Tn	94.0%	6.0%	0.0%	0.0%	0.0%	99.3%	0.7%	0.0%
Δ*popA* & Δ*pleD*	97.3%	0.0%	1.3%	1.3%	0.0%	99.3%	0.7%	0.0%
Δ*dgcB*	98.7%	0.7%	0.7%	0.0%	98.7%	0.7%	0.7%	0.0%
Δ*pdeA*	100.0%	0.0%	0.0%	0.0%	94.7%	2.7%	2.7%	0.0%
Δ*popA* & Δ*pleD* & P*divK*::Tn	81.3%	18.7%	0.0%	0.0%	0.0%	99.3%	0.7%	0.0%
cckA(Y514D)	100.0%	0.0%	0.0%	0.0%	98.7%	0.7%	0.7%	0.0%
cckA(Y514D) & P*divK*::Tn	96.0%	3.3%	0.7%	0.0%	96.0%	2.7%	1.3%	0.0%
Δ*podJ*	100.0%	0.0%	0.0%	0.0%	95.3%	2.7%	2.0%	0.0%
Δ*hdaA*	98.7%	0.0%	0.0%	1.3%	98.0%	0.7%	0.7%	0.7%
Δ*pleD* & P*divK*::Tn	84.0%	14.7%	1.3%	0.0%	46.0%	53.3%	0.7%	0.0%
Δ*rcdA*	98.7%	0.0%	0.7%	0.7%	0.0%	99.3%	0.7%	0.0%

Table B.5) Arrest in CORI⁻ simulations

	CORI⁻ SW				CORI⁻ SW + CtrA$_U$:*Cori*			
Strain	Viable	1 Cr	2 Cr	>2 Cr	Viable	1 Cr	2 Cr	>2 Cr
WT	98.0%	0.0%	2.0%	0.0%	97.3%	0.0%	1.3%	1.3%
*ctrA*Δ3Ω	98.0%	0.0%	2.0%	0.0%	95.3%	0.0%	1.3%	3.3%
*ctrA*D51E	98.0%	0.0%	2.0%	0.0%	98.7%	0.0%	1.3%	0.0%
*ctrA*D51EΔ3Ω	0.0%	97.3%	2.7%	0.0%	0.0%	0.7%	1.3%	98.0%
SM921	98.0%	0.0%	2.0%	0.0%	98.7%	0.0%	1.3%	0.0%
Δ*gcrA*	97.3%	0.0%	2.0%	0.7%	97.3%	0.0%	1.3%	1.3%
Δ*ccrM*	97.3%	0.0%	2.7%	0.0%	98.0%	0.0%	1.3%	0.7%
LS1	98.0%	0.0%	2.0%	0.0%	95.3%	0.0%	1.3%	3.3%
P*pleC*::Tn	98.0%	0.0%	2.0%	0.0%	97.3%	0.0%	1.3%	1.3%
divL^{ts}	0.0%	96.0%	4.0%	0.0%	0.0%	0.7%	1.3%	98.0%
divL(A601L)	0.0%	97.3%	2.7%	0.0%	0.0%	0.7%	1.3%	98.0%
divL(Y550F)	98.0%	0.0%	2.0%	0.0%	98.0%	0.0%	1.3%	0.7%
P*pleC*::Tn & *divL(Y550F)*	94.7%	0.0%	2.0%	3.3%	96.0%	0.0%	1.3%	2.7%
Δ*divJ*	0.0%	97.3%	2.7%	0.0%	0.0%	0.7%	1.3%	98.0%
P*pleC*::Tn & Δ*divJ*	0.0%	97.3%	2.7%	0.0%	0.0%	0.7%	1.3%	98.0%
Δ*spmX*	98.0%	0.0%	2.0%	0.0%	98.0%	0.0%	1.3%	0.7%
P*pleC*::Tn & Δ*spmX*	97.3%	0.0%	2.7%	0.0%	97.3%	0.0%	1.3%	1.3%
P*divK*::Tn	98.0%	0.0%	2.0%	0.0%	98.0%	0.0%	1.3%	0.7%
divK^{cs}	0.0%	97.3%	2.7%	0.0%	0.0%	0.7%	1.3%	98.0%
divK^{xyl}	0.0%	0.0%	2.0%	98.0%	0.0%	0.0%	1.3%	98.7%
cdG0	0.0%	97.3%	2.7%	0.0%	98.0%	0.0%	1.3%	0.7%
P*divK*::Tn & cdG0	0.0%	97.3%	2.7%	0.0%	98.7%	0.0%	1.3%	0.0%
Δ*popA*	98.0%	0.0%	2.0%	0.0%	94.0%	0.0%	1.3%	4.7%
Δ*pleD*	98.0%	0.0%	2.0%	0.0%	94.7%	0.0%	1.3%	4.0%
Δ*popA* & P*divK*::Tn	96.7%	0.0%	3.3%	0.0%	98.7%	0.0%	1.3%	0.0%
Δ*popA* & Δ*pleD*	0.0%	97.3%	2.7%	0.0%	98.7%	0.0%	1.3%	0.0%
Δ*dgcB*	98.0%	0.0%	2.0%	0.0%	98.0%	0.0%	1.3%	0.7%
Δ*pdeA*	98.0%	0.0%	2.0%	0.0%	98.0%	0.0%	1.3%	0.7%
Δ*popA* & Δ*pleD* & P*divK*::Tn	0.0%	97.3%	2.7%	0.0%	96.7%	0.0%	1.3%	2.0%
cckA(Y514D)	98.0%	0.0%	2.0%	0.0%	98.0%	0.0%	1.3%	0.7%
cckA(Y514D) & P*divK*::Tn	98.0%	0.0%	2.0%	0.0%	98.0%	0.0%	1.3%	0.7%
Δ*podJ*	97.3%	0.0%	2.7%	0.0%	97.3%	0.0%	1.3%	1.3%
Δ*hdaA*	97.3%	0.0%	2.0%	0.7%	98.7%	0.0%	1.3%	0.0%
Δ*pleD* & P*divK*::Tn	96.7%	0.0%	2.0%	1.3%	93.3%	0.0%	1.3%	5.3%
Δ*rcdA*	97.3%	0.7%	2.0%	0.0%	96.7%	0.0%	1.3%	2.0%

	CORI⁻ ST				CORI⁻ ST + CtrA$_U$:*Cori*			
Strain	Viable	1 Cr	2 Cr	>2 Cr	Viable	1 Cr	2 Cr	>2 Cr
WT	99.3%	0.0%	0.7%	0.0%	99.3%	0.0%	0.7%	0.0%
*ctrA*Δ3Ω	95.3%	3.3%	1.3%	0.0%	94.0%	0.0%	6.0%	0.0%
*ctrA*D51E	99.3%	0.0%	0.7%	0.0%	97.3%	0.0%	0.7%	2.0%
*ctrA*D51EΔ3Ω	0.0%	99.3%	0.7%	0.0%	0.0%	0.7%	93.3%	6.0%
SM921	99.3%	0.0%	0.7%	0.0%	99.3%	0.0%	0.7%	0.0%
Δ*gcrA*	99.3%	0.0%	0.7%	0.0%	99.3%	0.0%	0.7%	0.0%
Δ*ccrM*	99.3%	0.0%	0.7%	0.0%	98.7%	0.0%	0.7%	0.7%
LS1	98.7%	0.0%	0.7%	0.7%	98.7%	0.0%	0.7%	0.7%
P*pleC*::Tn	98.7%	0.0%	0.7%	0.7%	97.3%	0.0%	0.7%	2.0%
divL^{ts}	0.7%	97.3%	2.0%	0.0%	0.0%	0.7%	92.7%	6.7%
divL(A601L)	0.0%	98.7%	1.3%	0.0%	0.0%	0.7%	93.3%	6.0%
divL(Y550F)	42.7%	42.7%	14.7%	0.0%	95.3%	0.0%	0.7%	4.0%
P*pleC*::Tn & *divL(Y550F)*	82.0%	0.0%	1.3%	16.7%	98.7%	0.0%	0.7%	0.7%
Δ*divJ*	0.0%	99.3%	0.7%	0.0%	0.0%	0.7%	84.0%	15.3%
P*pleC*::Tn & Δ*divJ*	0.0%	74.7%	25.3%	0.0%	0.0%	0.0%	0.7%	99.3%
Δ*spmX*	98.0%	1.3%	0.7%	0.0%	97.3%	0.0%	2.7%	0.0%
P*pleC*::Tn & Δ*spmX*	99.3%	0.0%	0.7%	0.0%	98.0%	0.0%	0.7%	1.3%
P*divK*::Tn	97.3%	1.3%	1.3%	0.0%	94.0%	0.0%	4.7%	1.3%
divK^{cs}	0.0%	99.3%	0.7%	0.0%	0.0%	0.7%	93.3%	6.0%
divK^{xyl}	0.0%	0.0%	0.7%	99.3%	0.0%	0.0%	0.7%	99.3%
cdG0	0.0%	99.3%	0.7%	0.0%	97.3%	0.0%	0.7%	2.0%
P*divK*::Tn & cdG0	0.0%	99.3%	0.7%	0.0%	95.3%	0.0%	4.7%	0.0%
Δ*popA*	58.7%	40.7%	0.7%	0.0%	99.3%	0.0%	0.7%	0.0%
Δ*pleD*	99.3%	0.0%	0.7%	0.0%	72.7%	0.0%	0.7%	26.7%
Δ*popA* & P*divK*::Tn	97.3%	1.3%	1.3%	0.0%	96.7%	0.0%	3.3%	0.0%
Δ*popA* & Δ*pleD*	0.0%	99.3%	0.7%	0.0%	99.3%	0.0%	0.7%	0.0%
Δ*dgcB*	98.0%	0.0%	2.0%	0.0%	99.3%	0.0%	0.7%	0.0%
Δ*pdeA*	88.7%	0.7%	1.3%	9.3%	98.7%	0.0%	0.7%	0.7%
Δ*popA* & Δ*pleD* & P*divK*::Tn	0.0%	98.7%	1.3%	0.0%	96.0%	0.0%	3.3%	0.7%
cckA(Y514D)	98.7%	0.0%	1.3%	0.0%	98.0%	0.0%	0.7%	1.3%
cckA(Y514D) & P*divK*::Tn	97.3%	1.3%	1.3%	0.0%	96.0%	0.0%	4.0%	0.0%
Δ*podJ*	99.3%	0.0%	0.7%	0.0%	99.3%	0.0%	0.7%	0.0%
Δ*hdaA*	99.3%	0.0%	0.7%	0.0%	98.0%	0.0%	0.7%	1.3%
Δ*pleD* & P*divK*::Tn	94.7%	4.0%	1.3%	0.0%	92.7%	0.0%	3.3%	4.0%
Δ*rcdA*	52.0%	46.7%	1.3%	0.0%	97.3%	0.0%	0.7%	2.0%

Appendix C. Supplementary Material for Chapter 5

C.1 Equations and Simulation Events Governing Cell Cycle Model

In this section, we provide a complete list of equations governing the cell cycle model. For details on equation derivations, see Chapter 3 and 5. For a list of corresponding parameter values, Table C.1. Alternative parameter values utilized in mutant simulations are found in Table B.2. Parameters designated by red font are specifically included to accommodate mutant simulations, and are always set to zero unless specified otherwise for a given mutant simulation. Events and switches and concentration shifts upon cytokinesis are identical to those in Appendix B.1.

C.1.1 Governing Equations

$$\frac{\mathrm{d}[\mathrm{CtrA_U}]}{\mathrm{dt}} = k_{\mathrm{s,CtrA-P1}} \frac{\epsilon_{\mathrm{CtrA-GcrA}} \cdot J_{\mathrm{a,CtrA-GcrA}} + [\mathrm{GcrA}]}{J_{\mathrm{a,CtrA-GcrA}} + [\mathrm{GcrA}]} \cdot \left(1 - \frac{[\mathrm{CtrA{\sim}P}]}{J_{\mathrm{i,CtrA-CtrA}} + [\mathrm{CtrA}] + [\mathrm{CtrA{\sim}P}]}\right)$$
$$\cdot \left(1 - m_{\mathrm{CtrA-P1}} \cdot (2M_{\mathrm{ctrA}} - 1)\right) + k_{\mathrm{s,CtrA-P2}} \frac{\epsilon_{\mathrm{CtrA-CtrA}} \cdot {J_{\mathrm{a,CtrA-CtrA{\sim}P}}}^2 + [\mathrm{CtrA{\sim}P}]^2}{{J_{\mathrm{a,CtrA-CtrA}}}^2 + ([\mathrm{CtrA}] + [\mathrm{CtrA{\sim}P}])^2}$$
$$\cdot \frac{{J_{\mathrm{i,CtrA-SciP}}}^2}{{J_{\mathrm{i,CtrA-SciP}}}^2 + [\mathrm{SciP}]^2} - \left(\mu + k_{\mathrm{d,CtrA1}} + k_{\mathrm{d,CtrA2}} \cdot \frac{[\mathrm{ClpXP}]_{\mathrm{Complex}}}{J_{\mathrm{d,CtrA}} + [\mathrm{CtrA_U}] + [\mathrm{CtrA{\sim}P}]}\right) \cdot [\mathrm{CtrA_U}]$$
$$+ \; k_{\mathrm{dephos,CtrA}} \cdot [\mathrm{CckA}]_{\mathrm{P}} \cdot [\mathrm{CtrA{\sim}P}] - k_{\mathrm{phos,CtrA}} \cdot [\mathrm{CtrA_U}] \cdot [\mathrm{CckA}]_{\mathrm{K}} + k_{\mathrm{s,CtrA\Delta 3\Omega}}$$

$$\frac{\mathrm{d}[\mathrm{CtrA{\sim}P}]}{\mathrm{dt}} = -\left(\mu + k_{\mathrm{d,CtrA1}} + k_{\mathrm{d,CtrA2}} \cdot \frac{[\mathrm{ClpXP}]_{\mathrm{Complex}}}{J_{\mathrm{d,CtrA2}} + [\mathrm{CtrA_U}] + [\mathrm{CtrA{\sim}P}]}\right) \cdot [\mathrm{CtrA{\sim}P}] - \; k_{\mathrm{dephos,CtrA}} \cdot [\mathrm{CckA}]_{\mathrm{P}}$$
$$\cdot [\mathrm{CtrA{\sim}P}] + k_{\mathrm{phos,CtrA}} \cdot [\mathrm{CtrA_U}] \cdot [\mathrm{CckA}]_{\mathrm{K}} + k_{\mathrm{s,CtrAD51E}}$$

$$\frac{\mathrm{d}[\mathrm{DnaA}]_{\mathrm{T}}}{\mathrm{dt}} = k_{\mathrm{s,DnaA1}} \frac{J_{\mathrm{i,DnaA-GcrA}}}{J_{\mathrm{i,DnaA-GcrA}} + [\mathrm{GcrA}]} \cdot \left(1 - 2\, m_{\mathrm{DnaA}} \cdot (1 - M_{\mathrm{DnaA}})\right) - \left(\mu + k_{\mathrm{d,DnaA}}\right) \cdot [\mathrm{DnaA}]$$

$$\frac{\mathrm{d}[\mathrm{DnaA{\sim}ATP}]}{\mathrm{dt}} = k_{\mathrm{s,DnaA}} \frac{J_{\mathrm{i,DnaA-GcrA}}}{J_{\mathrm{i,DnaA-GcrA}} + [\mathrm{GcrA}]} \cdot \left(1 - 2\, m_{\mathrm{DnaA}} \cdot (1 - M_{\mathrm{DnaA}})\right)$$
$$- \left(\mu + k_{\mathrm{d,DnaA}} + k_{\mathrm{d,DnaAatp}} \cdot \mathrm{RepSwitch}\right) \cdot [\mathrm{DnaA{\sim}ATP}]$$

$$\frac{\mathrm{d}[\mathrm{GcrA}]}{\mathrm{dt}} = k_{\mathrm{s,GcrA}} \frac{\epsilon_{\mathrm{GcrA-DnaA}} \cdot J_{\mathrm{a,GcrA-DnaA}} + ([\mathrm{DnaA}]_{\mathrm{T}} - [\mathrm{DnaA{\sim}ATP}])}{J_{\mathrm{a,GcrA-DnaA}} + ([\mathrm{DnaA}]_{\mathrm{T}} - [\mathrm{DnaA{\sim}ATP}])} \cdot \frac{{J_{\mathrm{i,GcrA-CtrA}}}^2}{{J_{\mathrm{i,GcrA-CtrA}}}^2 + [\mathrm{CtrA{\sim}P}]^2}$$
$$- \left(\mu + k_{\mathrm{d,GcrA}}\right) \cdot [\mathrm{GcrA}]$$

$$\frac{\mathrm{d}[\mathrm{SciP}]}{\mathrm{dt}} = k_{\mathrm{s,SciP}} \frac{[\mathrm{CtrA{\sim}P}]^2}{{J_{\mathrm{a,SciP-CtrA}}}^2 + [\mathrm{CtrA{\sim}P}]^2} \cdot \frac{{J_{\mathrm{i,SciP-SciP}}}^2}{{J_{\mathrm{i,SciP-SciP}}}^2 + [\mathrm{SciP}]^2} - \left(\mu + k_{\mathrm{d,SciP}}\right) \cdot [\mathrm{SciP}]$$

$$\frac{\mathrm{d}[\mathrm{DivK}]}{\mathrm{dt}} = k_{\mathrm{s,DivK1}} + k_{\mathrm{s,DivK2}} \cdot \frac{[\mathrm{CtrA{\sim}P}]^2}{J_{\mathrm{a,DivK-CtrA{\sim}P}}{}^2 + [\mathrm{CtrA{\sim}P}]^2} - \left(\mu + k_{\mathrm{d,DivK}}\right) \cdot [\mathrm{DivK}] - (k_{\mathrm{phos,DivK1}} \cdot [\mathrm{DivJ}]_{\mathrm{A}} + k_{\mathrm{phos,DivK2}} \cdot [\mathrm{PleC}]_{\mathrm{K}} + k_{\mathrm{phos,DivK3}} \cdot MysK) \cdot [\mathrm{DivK}] + k_{\mathrm{dephos,DivK}} \cdot [\mathrm{PleC}] \cdot [\mathrm{DivK{\sim}P}] - k^{+}_{\mathrm{DivJDivK}} \cdot [\mathrm{DivJ}] \cdot [\mathrm{DivK}] + \left(k^{-}_{\mathrm{DivJDivK}} + k_{\mathrm{d,DivJ}}\right) \cdot [\mathrm{DivJ{:}\ DivK}] + k_{\mathrm{hyd,DivK}} \cdot [\mathrm{DivK{\sim}P}]$$

$$\frac{\mathrm{d}[\mathrm{DivK{\sim}P}]}{\mathrm{dt}} = -\left(\mu + \mathrm{k_{d,DivK}} + k_{\mathrm{hyd,DivK}}\right) \cdot [\mathrm{DivK{\sim}P}] + (k_{\mathrm{phos,DivK1}} \cdot [\mathrm{DivJ}]_{\mathrm{A}} + k_{\mathrm{phos,DivK2}} \cdot [\mathrm{PleC}]_{\mathrm{K}} + k_{\mathrm{phos,DivK3}} \cdot MysK) \cdot [\mathrm{DivK}] - k_{\mathrm{dephos,DivKP+}} \cdot [\mathrm{PleC}] \cdot [\mathrm{DivK{\sim}P}] + 2 \cdot \left(\left(k^{-}_{\mathrm{PleCDivKP}} + k_{\mathrm{d,PleC}} + k_{\mathrm{d,DivK}}\right) \cdot [\mathrm{PleC{:}\ DivK{\sim}P_2}] - k^{+}_{\mathrm{PleCDivKP}} \cdot [\mathrm{PleC}] \cdot [\mathrm{DivK{\sim}P}]^2\right) - k^{+}_{\mathrm{DivJDivKP}} \cdot [\mathrm{DivJ}] \cdot [\mathrm{DivK{\sim}P}] + \left(k^{-}_{\mathrm{DivJDivKP}} + \mathrm{k_{d,DivJ}}\right) \cdot [\mathrm{DivJ{:}\ DivK{\sim}P}] - k^{+}_{\mathrm{DivLDivKP}} \cdot [\mathrm{DivL}] \cdot [\mathrm{DivK{\sim}P}] + \left(k^{-}_{\mathrm{DivLDivKP}} + k_{\mathrm{d,DivL}}\right) \cdot [\mathrm{DivL{:}\ DivK{\sim}P}]$$

$$\frac{\mathrm{d}[\mathrm{DivJ}]}{\mathrm{dt}} = k_{\mathrm{s,DivJ}} - \left(\mu + k_{\mathrm{d,DivJ}}\right) \cdot [\mathrm{DivJ}] - k^{+}_{\mathrm{DivJDivK}} \cdot [\mathrm{DivJ}] \cdot [\mathrm{DivK}] + \left(k^{-}_{\mathrm{DivJDivK}} + k_{\mathrm{d,DivK}}\right) \cdot [\mathrm{DivJ{:}\ DivK}] - k^{+}_{\mathrm{DivJDivKP}} \cdot [\mathrm{DivJ}] \cdot [\mathrm{DivK{\sim}P}] + \left(k^{-}_{\mathrm{DivJDivKP}} + k_{\mathrm{d,DivK}}\right) \cdot [\mathrm{DivJ{:}\ DivK{\sim}P}]$$

$$\frac{\mathrm{d}[\mathrm{DivJ{:}\ DivK}]}{\mathrm{dt}} = k^{+}_{\mathrm{DivJDivK}} \cdot [\mathrm{DivJ}] \cdot [\mathrm{DivK}] - \left(\mu + k^{-}_{\mathrm{DivJDivK}} + \mathrm{k_{d,DivJ}} + \mathrm{k_{d,DivK}}\right) \cdot [\mathrm{DivJ{:}\ DivK}]$$

$$\frac{\mathrm{d}[\mathrm{DivJ{:}\ DivK{\sim}P}]}{\mathrm{dt}} = k^{+}_{\mathrm{DivJDivKP}} \cdot [\mathrm{DivJ}] \cdot [\mathrm{DivK{\sim}P}] - \left(\mu + k^{-}_{\mathrm{DivJDivKP}} + k_{\mathrm{d,DivJ}} + k_{\mathrm{d,DivK}}\right) \cdot [\mathrm{DivJ{:}\ DivK{\sim}P}]$$

$$[\mathrm{DivJ}]_{\mathrm{T}} = [\mathrm{DivJ}] + [\mathrm{DivJ{:}DivK}] + [\mathrm{DivJ{:}DivK{\sim}P}]$$

$$[\mathrm{DivJ}]_{\mathrm{A}} = ([\mathrm{DivJ{:}\ DivK{\sim}P}] + [\mathrm{DivJ{:}\ DivK}]) \cdot \left((1 - \epsilon_{\mathrm{DivJ\text{-}DivK}}) \cdot \left(\frac{\min([\mathrm{SpmX}], [\mathrm{DivJ}]_{\mathrm{T}})}{[\mathrm{DivJ}]_{\mathrm{T}}}\right) + \epsilon_{\mathrm{DivJ\text{-}DivK}}\right) + \epsilon_{\mathrm{DivJ\text{-}SpmX}} \cdot [\mathrm{DivJ}] \cdot \frac{\min([\mathrm{SpmX}], [\mathrm{DivJ}]_{\mathrm{T}})}{[\mathrm{DivJ}]_{\mathrm{T}}}$$

$$\frac{\mathrm{d}[\mathrm{DivL}]}{\mathrm{dt}} = k_{\mathrm{s,DivL}} - \left(\mu + k_{\mathrm{d,DivL}}\right) \cdot [\mathrm{DivL}] - k^{+}_{\mathrm{DivLDivKP}} \cdot [\mathrm{DivL}] \cdot [\mathrm{DivK{\sim}P}] + \left(k^{-}_{\mathrm{DivLDivKP}} + k_{\mathrm{d,DivK}}\right) \cdot [\mathrm{DivL{:}\ DivK{\sim}P}]$$

$$\frac{\mathrm{d}[\mathrm{DivL{:}\ DivK{\sim}P}]}{\mathrm{dt}} = k^{+}_{\mathrm{DivLDivKP}} \cdot [\mathrm{DivL}] \cdot [\mathrm{DivK{\sim}P}] - \left(\mu + k^{-}_{\mathrm{DivLDivKP}} + \mathrm{k_{d,DivK}} + k_{\mathrm{d,DivL}}\right) \cdot [\mathrm{DivL{:}\ DivK{\sim}P}]$$

$$[\mathrm{DivL}]_{\mathrm{T}} = [\mathrm{DivL}] + [\mathrm{DivL{:}\ DivK{\sim}P}]$$

$$\frac{\mathrm{d}[\mathrm{CckA}]_{\mathrm{T}}}{\mathrm{dt}} = k_{\mathrm{s,CckA}} - \left(\mu + k_{\mathrm{d,CckA}}\right) \cdot [\mathrm{CckA}]_{\mathrm{T}}$$

$$\frac{\mathrm{d}[\mathrm{CckA{:}\,CdG}]}{\mathrm{dt}} = k^{+}_{\mathrm{CckAcdG}} \cdot [\mathrm{cdG}] \cdot ([\mathrm{CckA}]_{\mathrm{T}} - [\mathrm{CckA{:}\,CdG}]) - k^{-}_{\mathrm{CckAcdG}} \cdot [\mathrm{CckA{:}\,cdG}] - (\mu + k_{\mathrm{d,CckA}}) \cdot [\mathrm{CckA{:}\,cdG}]$$

$$[\mathrm{CckA{:}\,DivL}]_{\mathrm{T}} = \frac{[\mathrm{CckA}]_{\mathrm{T}} + [\mathrm{DivL}]_{\mathrm{T}} + \frac{1}{K_{\mathrm{CckADivL}}} - \sqrt{\left([\mathrm{CckA}]_{\mathrm{T}} + [\mathrm{DivL}]_{\mathrm{T}} + \frac{1}{K_{CckA:DivL}}\right)^{2} - 4 \cdot [\mathrm{CckA}]_{\mathrm{T}} \cdot [\mathrm{DivL}]_{\mathrm{T}}}}{2}$$

$$[\mathrm{CckA}]_{\mathrm{P}} = \frac{[\mathrm{CckA{:}\,DivL}]_{\mathrm{T}} \cdot [\mathrm{DivL{:}\,DivK{\sim}P}]}{[\mathrm{DivL}]_{\mathrm{T}}} + [\mathrm{CckA{:}\,cdG}] - \frac{[\mathrm{CckA{:}\,cdG}] \cdot \frac{[\mathrm{CckA{:}\,DivL}]_{\mathrm{T}} \cdot [\mathrm{DivL{:}\,DivK{\sim}P}]}{[\mathrm{DivL}]_{\mathrm{T}}}}{[\mathrm{CckA}]_{\mathrm{T}}}$$

$$[\mathrm{CckA}]_{\mathrm{K}} = [\mathrm{CckA}]_{\mathrm{T}} - [\mathrm{CckA}]_{\mathrm{P}}$$

$$\frac{\mathrm{d}[\mathrm{PleC}]}{\mathrm{dt}} = k_{\mathrm{s,PleC}} \cdot (2 - 2 \cdot M_{\mathrm{PleC}}) - (\mu + k_{\mathrm{d,PleC}}) \cdot [\mathrm{PleC}] + k^{-}_{\mathrm{PleCDivKP}} \cdot [\mathrm{PleC{:}\,DivK{\sim}P_2}] - k^{+}_{\mathrm{PleCDivKP}} \cdot [\mathrm{PleC}] \cdot [\mathrm{DivK{\sim}P}]^{2} + 2 \cdot k_{\mathrm{d,DivK}} \cdot [\mathrm{PleC{:}\,DivK{\sim}P_2}]$$

$$\frac{\mathrm{d}[\mathrm{PleC{:}\,DivK{\sim}P_2}]}{\mathrm{dt}} = k^{+}_{\mathrm{PleCDivKP}} \cdot [\mathrm{PleC}] \cdot [\mathrm{DivK{\sim}P}]^{2} - (k_{\mathrm{d,PleC}} + k^{-}_{\mathrm{PleCDivKP}} + 2 \cdot k_{\mathrm{d,DivK}} + \mu) \cdot [\mathrm{PleC{:}\,DivK{\sim}P_2}]$$

$$[\mathrm{PleC}]_{\mathrm{tot}} = [\mathrm{PleC}] + [\mathrm{PleC{:}\,DivK{\sim}P_2}]$$

$$\frac{\mathrm{d}[\mathrm{PleC}]_{\mathrm{Pole}}}{\mathrm{dt}} = k_{\mathrm{PleCbinding}} \cdot ([\mathrm{PleC}]_{\mathrm{tot}} - [\mathrm{PleC}]_{\mathrm{Pole}}) \cdot \frac{[\mathrm{PodJ}]}{[\mathrm{PodJ}] \cdot [\mathrm{V}] + J_{\mathrm{PleCPodJ}}} - (k_{\mathrm{PleCunbinding}} + k_{\mathrm{d,PleC}} + \mu) \cdot [\mathrm{PleC}]_{\mathrm{Pole}}$$

$$\frac{\mathrm{d}[\mathrm{PodJ}]}{\mathrm{dt}} = k_{\mathrm{s,PodJ}} \cdot \frac{J_{\mathrm{i,PodJ-DnaA}}}{J_{\mathrm{i,PodJ-DnaA}} + [\mathrm{DnaA}]_{\mathrm{T}}} \cdot \frac{[\mathrm{GcrA}]}{J_{\mathrm{a,PodJ-GcrA}} + [\mathrm{GcrA}]} \cdot (2 - 2 \cdot M_{\mathrm{PodJ}}) - (\mu + k_{\mathrm{d,PodJ1}}) \cdot [\mathrm{PodJ}] - k_{\mathrm{d,PodJ2}} \cdot [\mathrm{PodJ}] \cdot [\mathrm{PerP}]$$

$$\frac{\mathrm{d}[\mathrm{PerP}]}{\mathrm{dt}} = k_{\mathrm{s,PerP}} \cdot \frac{[\mathrm{CtrA{\sim}P}]^{2}}{J_{\mathrm{a,PerP-CtrA}}{}^{2} + [\mathrm{CtrA{\sim}P}]^{2}} \cdot (2 - 2 \cdot M_{\mathrm{PodJ}}) - (\mu + k_{\mathrm{d,PerP}}) \cdot [\mathrm{PerP}]$$

$$[\mathrm{DNA}]_{\mathrm{F}} = \frac{K_{\mathrm{d1}}}{K_{\mathrm{d1}} + 2 \cdot [\mathrm{CtrA{\sim}P}] + \frac{[\mathrm{CtrA{\sim}P}]^{2}}{K_{\mathrm{d3}}} + (1 - \sigma_{\mathrm{CtrAU:}Cori}) \cdot \left(2 \cdot [\mathrm{CtrA_U}] + \frac{[\mathrm{CtrA_U}]^{2}}{K_{\mathrm{d2}}} + 2 \cdot \frac{[\mathrm{CtrA_U}] \cdot [\mathrm{CtrA{\sim}P}]}{K_{\mathrm{d2}}}\right)}$$

$$[\mathrm{DNA{:}\,CtrA{\sim}P2}] = \frac{[\mathrm{CtrA{\sim}P}]^{2} \cdot [\mathrm{DNA}]_{\mathrm{F}}}{K_{\mathrm{d1}} \cdot K_{\mathrm{d3}}}$$

$$\frac{\mathrm{d}[\mathrm{Ini}]}{\mathrm{dt}} = (1 - 2\, m_{\mathrm{Ini}} \cdot (1 - M_{\mathrm{Ini}})) \cdot (1 - [\mathrm{DNA{:}\,CtrA{\sim}P_2}])^{5} \cdot \left(\frac{[\mathrm{DnaA{\sim}ATP}]}{[\mathrm{DnaA{\sim}ATP}] + J_{\mathrm{a,Ini-DnaA}}}\right)^{2} - k_{\mathrm{d,Ini}} \cdot [\mathrm{Ini}]$$

$$\frac{\mathrm{d}[\mathrm{Elong}]}{\mathrm{dt}} = k_{\mathrm{elong}} \cdot RepSwitch$$

$$\frac{\mathrm{d}[\mathrm{CcrM}]}{\mathrm{dt}} = k_{\mathrm{s,CcrM}} \cdot \frac{[\mathrm{CtrA{\sim}P}]^2}{J_{\mathrm{a,CcrM-CtrA}}{}^2 + [\mathrm{CtrA{\sim}P}]^2} \cdot \frac{J_{\mathrm{I,CcrM-DnaA}}}{J_{\mathrm{I,CcrM-DnaA}} + [\mathrm{DnaA}]} \cdot (2 - 2 \cdot M_{\mathrm{CcrM}}) - \left(\mu + k_{\mathrm{d,CcrM}}\right) \cdot [\mathrm{CcrM}] + k_{\mathrm{s,LS1}}$$

$$\frac{\mathrm{d}[\mathrm{TacA}]}{\mathrm{dt}} = k_{\mathrm{s,TacA}} \cdot \frac{[\mathrm{CtrA{\sim}P}]}{[\mathrm{CtrA{\sim}P}]+J_{\mathrm{a,CtrA\text{-}TacA}}} - (\mu + k_{\mathrm{d,TacA1}}) \cdot [\mathrm{TacA}] - k_{\mathrm{d,TacA2}} \cdot [\mathrm{RcdA{:}CpdR}] \cdot \frac{[\mathrm{TacA}]}{[\mathrm{TacA}]+J_{\mathrm{d,TacA}}} - k_{\mathrm{phos,TacA}} \cdot [\mathrm{ShkA{:}cdG}] \cdot [\mathrm{TacA}] + k_{\mathrm{dephos,TacA}} \cdot [\mathrm{TacA{\sim}P}]$$

$$\frac{\mathrm{d}[\mathrm{TacA{\sim}P}]}{\mathrm{dt}} = -(\mu + k_{\mathrm{d,TacA1}}) \cdot [\mathrm{TacA{\sim}P}] - k_{\mathrm{d,TacA2}} \cdot [\mathrm{RcdA{:}CpdR}] \cdot \frac{[\mathrm{TacA{\sim}P}]}{[\mathrm{TacA{\sim}P}]+J_{\mathrm{d,TacA}}} + k_{\mathrm{phos,TacA}} \cdot [\mathrm{ShkA{:}cdG}] \cdot [\mathrm{TacA}] - k_{\mathrm{dephos,TacA}} \cdot [\mathrm{TacA{\sim}P}]$$

$$\frac{\mathrm{d}[\mathrm{SpmX}]}{\mathrm{dt}} = k_{\mathrm{s,SpmX}} \frac{[\mathrm{TacA{\sim}P}]}{[\mathrm{TacA{\sim}P}] + \mathrm{J}_{\mathrm{a,TacA-SpmX}}} - \left(k_{\mathrm{d,SpmX}} + \mu\right) \cdot [\mathrm{SpmX}]$$

$$\frac{\mathrm{d}[\mathrm{Zproteins}]}{\mathrm{dt}} = k_{\mathrm{s,Zp}} \frac{[\mathrm{CtrA{\sim}P}]^2}{J_{\mathrm{a,Zp-CtrA}}{}^2 + [\mathrm{CtrA{\sim}P}]^2} - \left(\mu + k_{\mathrm{d,Zp}} + k_{\mathrm{d,ZP2}} \cdot [\mathrm{ClpAP}]\right) \cdot [\mathrm{Zproteins}]$$

$$\frac{\mathrm{d}[\mathrm{Zring}]}{\mathrm{dt}} = -k_{\mathrm{Zconstrict}} \cdot MipZswitch \cdot \frac{[\mathrm{Zproteins}]^5}{\left(J_{\mathrm{Zring}} + \theta_{\mathrm{Z}} \cdot [\mathrm{Zring}]\right)^5 + [\mathrm{Zproteins}]^5}$$

$$\frac{\mathrm{d}[\mathrm{V}]}{\mathrm{dt}} = \mu \cdot [\mathrm{V}]$$

$$\mu = T^{-1} \cdot \ln \frac{V_{\mathrm{div}}}{V_{\mathrm{birth}}}$$

$$\frac{\mathrm{d}[\mathrm{CpdR}]}{\mathrm{dt}} = k_{\mathrm{s,CpdR}} \frac{\epsilon_{\mathrm{CpdR-DnaA}} \cdot J_{\mathrm{a,CpdR-DnaA}} + [\mathrm{DnaA}]_{\mathrm{T}}}{J_{\mathrm{a,CpdR-DnaA}} + [\mathrm{DnaA}]_{\mathrm{T}}} \cdot \frac{[\mathrm{CtrA{\sim}P}]}{J_{\mathrm{a,CpdR-CtrA}} + [\mathrm{CtrA{\sim}P}]} \cdot \frac{J_{\mathrm{i,CckAGcrA}}}{J_{\mathrm{i,CckAGcrA}} + [\mathrm{GcrA}]} + k_{\mathrm{dephos,CpdR}} \cdot [\mathrm{CpdR{\sim}P}] \cdot [\mathrm{CckA}]_{\mathrm{P}} - k_{\mathrm{phos,CpdR}} \cdot [\mathrm{CpdR}] \cdot [\mathrm{CckA}]_{\mathrm{K}} - (\mu + k_{\mathrm{d,CpdR}}) \cdot [\mathrm{CpdR}]$$

$$\frac{\mathrm{d}[\mathrm{CpdR{\sim}P}]}{\mathrm{dt}} = -k_{\mathrm{dephos,CpdR}} \cdot [\mathrm{CpdR{\sim}P}] \cdot [\mathrm{CckA}]_{\mathrm{P}} + k_{\mathrm{phos,CpdR}} \cdot [\mathrm{CpdR}] \cdot [\mathrm{CckA}]_{\mathrm{K}} - (\mu + k_{\mathrm{d,CpdR}}) \cdot [\mathrm{CpdR{\sim}P}]$$

$$[\mathrm{CpdR}]_{\mathrm{T}} = [\mathrm{CpdR}] + [\mathrm{CpdR{\sim}P}]$$

$$\frac{\mathrm{d}[\mathrm{RcdA}]}{\mathrm{dt}} = k_{\mathrm{s,RcdA}} \cdot \frac{[\mathrm{CtrA{\sim}P}]^2}{J_{\mathrm{a,RcdACtrA}}{}^2 + [\mathrm{CtrA{\sim}P}]^2} - \left(\mu + k_{\mathrm{d,RcdA}}\right) \cdot [\mathrm{RcdA}]$$

$$\frac{\mathrm{d}[\mathrm{PopA}]}{\mathrm{dt}} = k_{\mathrm{s,PopA}} \cdot \frac{J_{\mathrm{i,PopA-GcrA}}}{J_{\mathrm{i,PopA-GcrA}} + [\mathrm{GcrA}]} - (\mu + k_{\mathrm{d,PopA}}) \cdot [\mathrm{PopA}] - k^{+}_{\mathrm{PopACdG}} \cdot [\mathrm{PopA}] \cdot [\mathrm{cdG}]^2 + k^{-}_{\mathrm{XCdG}} \cdot [\mathrm{PopA{:}\,cdG_2}]$$

$$\frac{\mathrm{d}[\mathrm{PopA{:}\,cdG_2}]}{\mathrm{dt}} = k^{+}_{\mathrm{PopACdG}} \cdot [\mathrm{PopA}] \cdot [\mathrm{cdG}]^2 - (\mu + k^{-}_{\mathrm{XCdG}} + k_{\mathrm{d,PopA}}) \cdot [\mathrm{PopA{:}\,cdG_2}]$$

$$[\mathrm{PopA}]_{\mathrm{T}} = [\mathrm{PopA}] + [\mathrm{PopA{:}\,cdG_2}]$$

$$[\text{RcdA: CpdRT}] = \frac{[\text{CpdR}]_\text{T} + [\text{RcdA}] + \frac{1}{K_{\text{d,RcdACpdR}}} - \sqrt{\left([\text{CpdR}]_\text{T} + [\text{RcdA}] + \frac{1}{K_{\text{d,RcdACpdR}}}\right)^2 - 4 \cdot [\text{CpdR}]_\text{T} \cdot [\text{RcdA}]}}{2}$$

$$[\text{RcdA:CpdR}] = [\text{RcdA:CpdRT}] \cdot \frac{[\text{CpdR}]}{[\text{CpdR}]_\text{T}}$$

$$[\text{ClpXP}]_{\text{Complex}} = \frac{[\text{RcdA: CpdR}]}{[\text{RcdA: CpdR}] + \frac{K_{\text{ClpXpCpdR}}}{V}} \cdot [\text{PopA: cdG}_2]$$

$$\frac{\text{d}[\text{PdeA}]}{\text{dt}} = k_{\text{s,PdeA}} \cdot \frac{[\text{CtrA}\sim\text{P}]}{J_{\text{a,PdeA-CtrA}} + [\text{CtrA}\sim\text{P}]} - k_{\text{d,PdeA2}} \cdot [\text{CpdR}] \cdot \frac{[\text{PdeA}]}{J_{\text{d,PdeA}} + [\text{PdeA}]} - (\mu + k_{\text{d,PdeA1}}) \cdot [\text{PdeA}]$$

$$[\text{DgcB}]_\text{a} = \max(DgcB - [\text{PdeA}], 0) \cdot \frac{DgcB - [\text{DgcB: cdG}_2]}{DgcB}$$

$$\begin{aligned}\frac{\text{d}[\text{cdG}]}{\text{dt}} = {} & \left(k_{\text{s,cdG1}} \cdot [\text{PleD}\sim\text{P}] + k_{\text{s,cdG2}} \cdot [\text{DgcB}]_\text{a}\right) \cdot \frac{[\text{GTP}]^2}{J_{\text{s,cdG}}^2 + [\text{GTP}]^2} - k_{\text{d,cdG}} \cdot ([\text{PdeA}] + PDE) \cdot [\text{cdG}] - \mu \cdot [\text{cdG}] \\ & + 2 \cdot \left(-k_{\text{PopACdG}}^+ \cdot [\text{PopA}] \cdot [\text{cdG}]^2 + \left(k_{\text{XCdG}}^- + k_{\text{d,PopA}}\right) \cdot [\text{PopA: cdG}_2]\right) + 2 \\ & \cdot \left(-k_{\text{PleDcdG}}^+ \cdot ([\text{PleD}] + [\text{PleD}\sim\text{P}]) \cdot [\text{cdG}]^2 + \left(k_{\text{d,PleD}} + k_{\text{XCdG}}^-\right)\right. \\ & \left. \cdot ([\text{PleD: cdG}_2] + [\text{PleD}\sim\text{P: cdG}_2])\right) - k_{\text{CckAcdG}}^+ \cdot [\text{cdG}] \cdot ([\text{CckA}]_\text{T} - [\text{CckA: CdG}]) + k_{\text{CckAcdG}}^- \\ & \cdot [\text{CckA: cdG}] + 2 \cdot \left(-k_{\text{DgcBcdG}}^+ \cdot (DgcB - [\text{DgcB: cdG}_2]) \cdot [\text{cdG}]^2 + k_{\text{XCdG}}^- \cdot [\text{DgcB: cdG}_2]\right)\end{aligned}$$

$$\begin{aligned}\frac{\text{d}[\text{ShkA}]_\text{T}}{\text{dt}} = {} & k_{\text{s,ShkA}} \frac{[\text{CtrA}\sim\text{P}]}{[\text{CtrA}\sim\text{P}] + \text{J}_{\text{a,ShkA-CtrA}}} - \left(k_{\text{d,ShkA1}} + \mu\right) \cdot [\text{ShkA}]_\text{T} - k_{\text{d,ShkA2}} \cdot [\text{ClpXP}]_{\text{Complex}} \\ & \cdot \frac{[\text{ShkA}]_\text{T}}{[\text{ShkA}]_\text{T} + J_{\text{d,ShkA}}}\end{aligned}$$

$$[\text{ShkA}]_\text{T} = [\text{ShkA}] + [\text{ShkA:cdG}]$$

$$[\text{ShkA:cdG}] = [\text{ShkA}]_\text{T} \cdot \frac{[\text{cdG}]}{[\text{cdG}] + K_{\text{D,ShkAcdG}}}$$

$$\frac{\text{d}[\text{DgcB: cdG}_2]}{\text{dt}} = k_{\text{DgcBcdG}}^+ \cdot (DgcB - [\text{DgcB: cdG}_2]) \cdot [\text{cdG}]^2 - (\mu + k_{\text{XCdG}}^-) \cdot [\text{DgcB: cdG}_2]$$

$$\begin{aligned}\frac{\text{d}[\text{PleD}]}{\text{dt}} = {} & k_{\text{s,PleD}} \cdot \frac{[\text{CtrA}\sim\text{P}]^2}{J_{\text{a,PleD-CtrA}}{}^2 + [\text{CtrA}\sim\text{P}]^2} - \left(\mu + k_{\text{d,PleD}}\right) \cdot [\text{PleD}] - k_{\text{phos,PleD}} \cdot ([\text{DivJ}]_\text{A} + MysK) \cdot [\text{PleD}] \\ & + \left(\left(\frac{1}{10}\right) + \left(\frac{9}{10}\right) \cdot \frac{[\text{PleC}]_{\text{tot}} - [\text{PleC}]_{\text{pole}}}{[\text{PleC}]_{\text{tot}}}\right) \cdot k_{\text{dephos,PleD}} \cdot [\text{PleC}] \cdot [\text{PleD}\sim\text{P}] - k_{\text{PleDcdG}}^+ \cdot [\text{PleD}] \\ & \cdot [\text{cdG}]^2 + k_{\text{XCdG}}^- \cdot [\text{PleD: cdG}_2]\end{aligned}$$

$$\frac{\mathrm{d}[\mathrm{PleD}\sim\mathrm{P}]}{\mathrm{dt}} = -\left(\mu + k_{\mathrm{d,PleD}}\right)\cdot[\mathrm{PleD}\sim\mathrm{P}] + k_{\mathrm{phos,PleD}}\cdot\left([\mathrm{DivJ}]_{\mathrm{A}} + MysK\right)\cdot[\mathrm{PleD}]$$
$$-\left(\left(\frac{1}{10}\right)+\left(\frac{9}{10}\right)\cdot\frac{[\mathrm{PleC}]_{\mathrm{tot}}-[\mathrm{PleC}]_{\mathrm{pole}}}{[\mathrm{PleC}]_{\mathrm{tot}}}\right)\cdot k_{\mathrm{dephos,PleD}}\cdot[\mathrm{PleC}]\cdot[\mathrm{PleD}\sim\mathrm{P}] - k^{+}_{\mathrm{PleDcdG}}\cdot[\mathrm{PleD}\sim\mathrm{P}]$$
$$\cdot[\mathrm{cdG}]^2 + k^{-}_{\mathrm{XCdG}}\cdot[\mathrm{PleD}\sim\mathrm{P}\colon \mathrm{cdG}_2]$$

$$\frac{\mathrm{d}[\mathrm{PleD}\colon \mathrm{cdG}_2]}{\mathrm{dt}} = -\left(\mu + k_{\mathrm{d,PleD}}\right)\cdot[\mathrm{PleD}\colon \mathrm{cdG}_2] - k_{\mathrm{phos,PleD}}\cdot\left([\mathrm{DivJ}]_{\mathrm{A}} + MysK\right)\cdot[\mathrm{PleD}\colon \mathrm{cdG}_2]$$
$$+\left(\left(\frac{1}{10}\right)+\left(\frac{9}{10}\right)\cdot\frac{[\mathrm{PleC}]_{\mathrm{tot}}-[\mathrm{PleC}]_{\mathrm{pole}}}{[\mathrm{PleC}]_{\mathrm{tot}}}\right)\cdot k_{\mathrm{dephos,PleD}}\cdot[\mathrm{PleC}]\cdot[\mathrm{PleD}\sim\mathrm{P}\colon \mathrm{cdG}_2] + k^{+}_{\mathrm{PleDcdG}}$$
$$\cdot[\mathrm{PleD}]\cdot[\mathrm{cdG}]^2 - k^{-}_{\mathrm{XCdG}}\cdot[\mathrm{PleD}\colon \mathrm{cdG}_2]$$

$$\frac{\mathrm{d}[\mathrm{PleD}\sim\mathrm{P}\colon \mathrm{cdG}_2]}{\mathrm{dt}} = -\left(\mu + k_{\mathrm{d,PleD}}\right)\cdot[\mathrm{PleD}\sim\mathrm{P}\colon \mathrm{cdG}_2] + k_{\mathrm{phos,PleD}}\cdot\left([\mathrm{DivJ}]_{\mathrm{A}} + MysK\right)\cdot[\mathrm{PleD}\colon \mathrm{cdG}_2]$$
$$-\left(\left(\frac{1}{10}\right)+\left(\frac{9}{10}\right)\cdot\frac{[\mathrm{PleC}]_{\mathrm{tot}}-[\mathrm{PleC}]_{\mathrm{pole}}}{[\mathrm{PleC}]_{\mathrm{tot}}}\right)\cdot k_{\mathrm{dephos,PleD}}\cdot[\mathrm{PleC}]\cdot[\mathrm{PleD}\sim\mathrm{P}\colon \mathrm{cdG}_2] + k^{+}_{\mathrm{PleDcdG}}$$
$$\cdot[\mathrm{PleD}\sim\mathrm{P}]\cdot[\mathrm{cdG}]^2 - k^{-}_{\mathrm{XCdG}}\cdot[\mathrm{PleD}\sim\mathrm{P}\colon \mathrm{cdG}_2]$$

C.1.2 Reduced DivK Model

We note that, in this model $[\mathrm{X}]_{\mathrm{Tot}}$ refers to a predefined, targeted total level of protein X. This is clearly distinguished from $[\mathrm{X}]_{\mathrm{T}}$ which refers to total protein levels of X that are a sum of all forms of X. In other words, $[\mathrm{X}]_{\mathrm{Tot}}$ is a predetermined parameter and $[\mathrm{X}]_{\mathrm{T}}$ is a variable.

$$k_{\mathrm{s,DivK}} = \frac{[\mathrm{DivK}]_{\mathrm{Tot}}}{\mu + k_{\mathrm{d,DivK}}}$$

$$k_{\mathrm{s,DivJ}} = \frac{[\mathrm{DivJ}]_{\mathrm{Tot}}}{\mu + k_{\mathrm{d,DivK}}}$$

$$k_{\mathrm{s,PleC}} = \frac{[\mathrm{PleC}]_{\mathrm{Tot}}}{\mu + k_{\mathrm{d,PleC}}}$$

$$k_{\mathrm{s,DivL}} = \frac{[\mathrm{DivL}]_{\mathrm{Tot}}}{\mu + k_{\mathrm{d,DivL}}}$$

$$\frac{\mathrm{d}[\mathrm{DivK}]}{\mathrm{dt}} = k_{\mathrm{s,DivK}} - \left(\mu + k_{\mathrm{d,DivK}}\right)\cdot[\mathrm{DivK}] - \left(k_{\mathrm{phos,DivK1}}\cdot[\mathrm{DivJ}]_{\mathrm{A}} + k_{\mathrm{phos,DivK2}}\cdot[\mathrm{PleC}]_{\mathrm{K}} + k_{\mathrm{phos,DivK3}}\cdot MysK\right)$$
$$\cdot[\mathrm{DivK}] + k_{\mathrm{dephos,DivK}}\cdot[\mathrm{PleC}]\cdot[\mathrm{DivK}\sim\mathrm{P}] - k^{+}_{\mathrm{DivJDivK}}\cdot[\mathrm{DivJ}]\cdot[\mathrm{DivK}] + \left(k^{-}_{\mathrm{DivJDivK}} + k_{\mathrm{d,DivJ}}\right)$$
$$\cdot[\mathrm{DivJ}\colon \mathrm{DivK}] + k_{\mathrm{hyd,DivK}}\cdot[\mathrm{DivK}\sim\mathrm{P}]$$

$$\frac{\mathrm{d}[\mathrm{DivK}\sim\mathrm{P}]}{\mathrm{dt}} = -\left(\mu + \mathrm{k}_{\mathrm{d,DivK}} + k_{\mathrm{hyd,DivK}}\right)\cdot[\mathrm{DivK}\sim\mathrm{P}] + \left(k_{\mathrm{phos,DivK1}}\cdot[\mathrm{DivJ}]_{\mathrm{A}} + k_{\mathrm{phos,DivK2}}\cdot[\mathrm{PleC}]_{\mathrm{K}}\right.$$
$$\left. + k_{\mathrm{phos,DivK3}}\cdot MysK\right)\cdot[\mathrm{DivK}] - k_{\mathrm{dephos,DivKP+}}\cdot[\mathrm{PleC}]\cdot[\mathrm{DivK}\sim\mathrm{P}] + 2$$
$$\cdot\left(\left(k^{-}_{\mathrm{PleCDivKP}} + k_{\mathrm{d,PleC}} + k_{\mathrm{d,DivK}}\right)\cdot[\mathrm{PleC{:}\ DivK}\sim\mathrm{P}_2] - k^{+}_{\mathrm{PleCDivKP}}\cdot[\mathrm{PleC}]\cdot[\mathrm{DivK}\sim\mathrm{P}]^2\right)$$
$$- k^{+}_{\mathrm{DivJDivKP}}\cdot[\mathrm{DivJ}]\cdot[\mathrm{DivK}\sim\mathrm{P}] + \left(k^{-}_{\mathrm{DivJDivKP}} + \mathrm{k}_{\mathrm{d,DivJ}}\right)\cdot[\mathrm{DivJ{:}\ DivK}\sim\mathrm{P}] - k^{+}_{\mathrm{DivLDivKP}}\cdot[\mathrm{DivL}]$$
$$\cdot[\mathrm{DivK}\sim\mathrm{P}] + \left(k^{-}_{\mathrm{DivLDivKP}} + k_{\mathrm{d,DivL}}\right)\cdot[\mathrm{DivL{:}\ DivK}\sim\mathrm{P}]$$

$$\frac{\mathrm{d}[\mathrm{DivJ}]}{\mathrm{dt}} = k_{\mathrm{s,DivJ}} - \left(\mu + k_{\mathrm{d,DivJ}}\right)\cdot[\mathrm{DivJ}] - k^{+}_{\mathrm{DivJDivK}}\cdot[\mathrm{DivJ}]\cdot[\mathrm{DivK}] + \left(k^{-}_{\mathrm{DivJDivK}} + k_{\mathrm{d,DivK}}\right)\cdot[\mathrm{DivJ{:}\ DivK}]$$
$$- k^{+}_{\mathrm{DivJDivKP}}\cdot[\mathrm{DivJ}]\cdot[\mathrm{DivK}\sim\mathrm{P}] + \left(k^{-}_{\mathrm{DivJDivKP}} + k_{\mathrm{d,DivK}}\right)\cdot[\mathrm{DivJ{:}\ DivK}\sim\mathrm{P}]$$

$$\frac{\mathrm{d}[\mathrm{DivJ{:}\ DivK}]}{\mathrm{dt}} = k^{+}_{\mathrm{DivJDivK}}\cdot[\mathrm{DivJ}]\cdot[\mathrm{DivK}] - \left(\mu + k^{-}_{\mathrm{DivJDivK}} + \mathrm{k}_{\mathrm{d,DivJ}} + \mathrm{k}_{\mathrm{d,DivK}}\right)\cdot[\mathrm{DivJ{:}\ DivK}]$$

$$\frac{\mathrm{d}[\mathrm{DivJ{:}\ DivK}\sim\mathrm{P}]}{\mathrm{dt}} = k^{+}_{\mathrm{DivJDivKP}}\cdot[\mathrm{DivJ}]\cdot[\mathrm{DivK}\sim\mathrm{P}] - \left(\mu + k^{-}_{\mathrm{DivJDivKP}} + k_{\mathrm{d,DivJ}} + k_{\mathrm{d,DivK}}\right)\cdot[\mathrm{DivJ{:}\ DivK}\sim\mathrm{P}]$$

$$[\mathrm{DivJ}]_{\mathrm{A}} = ([\mathrm{DivJ{:}\ DivK}\sim\mathrm{P}] + [\mathrm{DivJ{:}\ DivK}])\cdot\left((1-\epsilon_{\mathrm{DivJ}})\cdot\left(\frac{\min([\mathrm{SpmX}],[\mathrm{DivJ}]_{\mathrm{T}})}{[\mathrm{DivJ}]_{\mathrm{T}}}\right) + \epsilon_{\mathrm{DivJ}}\right) + \epsilon_{\mathrm{DivJ\text{-}SpmX}}\cdot[\mathrm{DivJ}]$$
$$\cdot\frac{\min([\mathrm{SpmX}],[\mathrm{DivJ}]_{\mathrm{T}})}{[\mathrm{DivJ}]_{\mathrm{T}}}$$

$$\frac{\mathrm{d}[\mathrm{DivL}]}{\mathrm{dt}} = k_{\mathrm{s,DivL}} - \left(\mu + k_{\mathrm{d,DivL}}\right)\cdot[\mathrm{DivL}] - k^{+}_{\mathrm{DivLDivKP}}\cdot[\mathrm{DivL}]\cdot[\mathrm{DivK}\sim\mathrm{P}] + \left(k^{-}_{\mathrm{DivLDivKP}} + k_{\mathrm{d,DivK}}\right)$$
$$\cdot[\mathrm{DivL{:}\ DivK}\sim\mathrm{P}]$$

$$\frac{\mathrm{d}[\mathrm{DivL{:}\ DivK}\sim\mathrm{P}]}{\mathrm{dt}} = k^{+}_{\mathrm{DivLDivKP}}\cdot[\mathrm{DivL}]\cdot[\mathrm{DivK}\sim\mathrm{P}] - \left(\mu + k^{-}_{\mathrm{DivLDivKP}} + \mathrm{k}_{\mathrm{d,DivK}} + k_{\mathrm{d,DivL}}\right)\cdot[\mathrm{DivL{:}\ DivK}\sim\mathrm{P}]$$

Figures

C.1.2 Figures

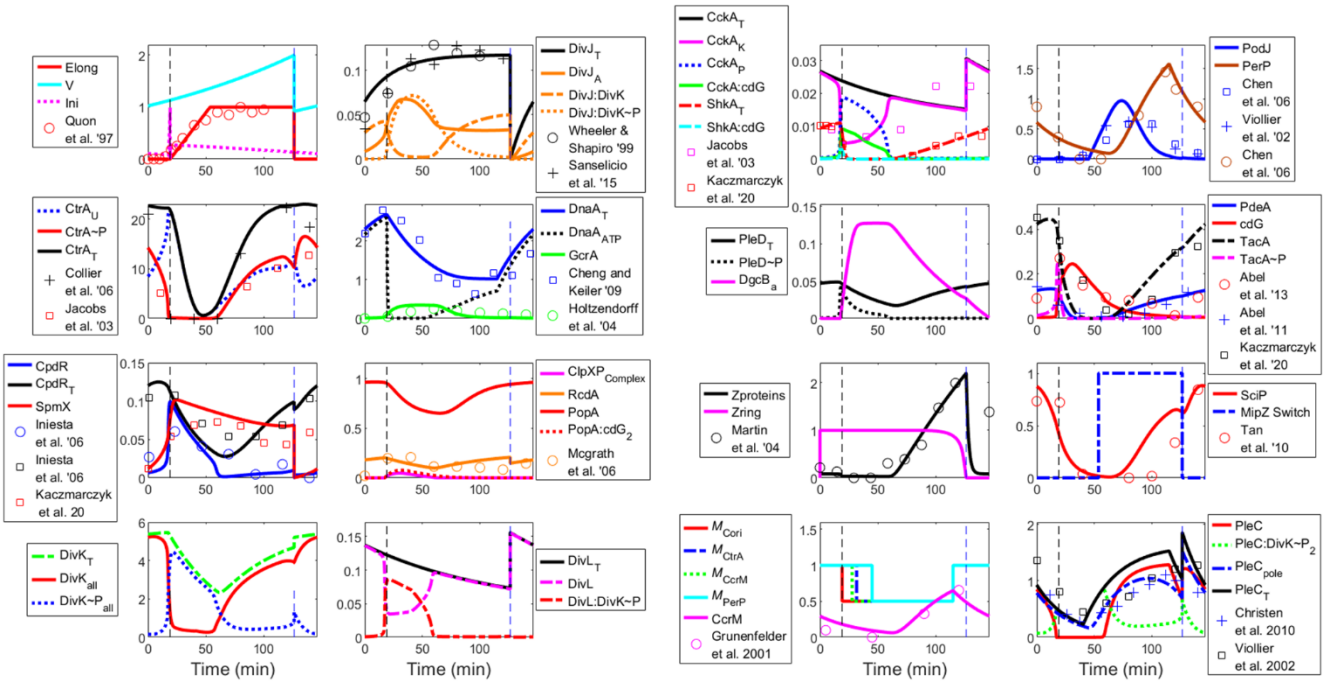

Figure C.1) Simulations of wild-type swarmer cell

(A) Swarmer cell simulation. Variables in each subplot are indicated by the adjacent legend. X axis represents time, in minutes, and the y axis represents unitless concentration or activity. Exceptions are CtrA and cdG, which are both expressed in µM. Data points from literature are normalized to the simulation output. Vertical-dashed black and blue lines correspond to the timing of chromosome replication and Z-ring constriction, respectively.

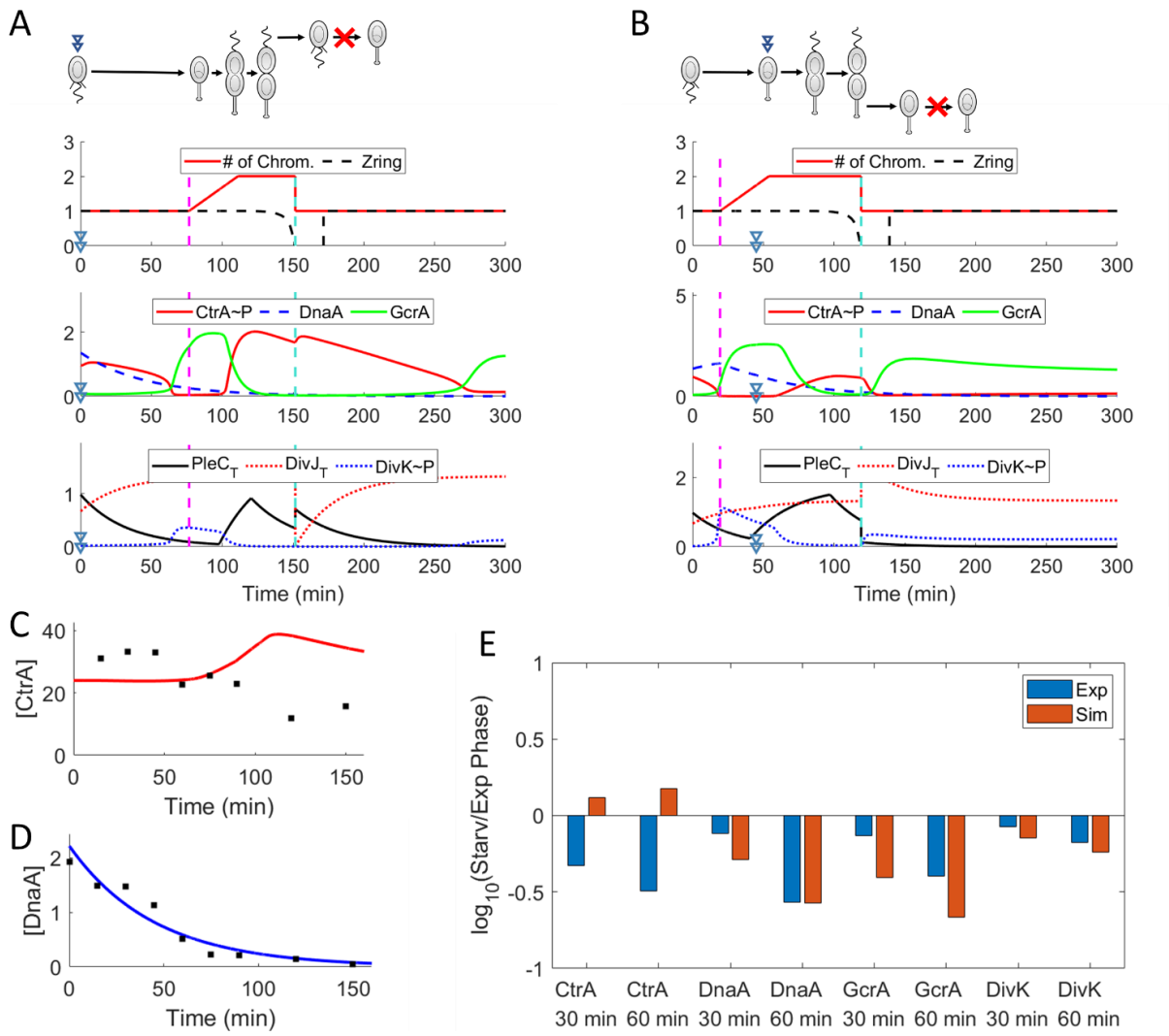

Figure C.2) Signal 2 simulation results.

(A) Swarmer cell simulation of Signal 2 response. Red "X" indicates secondary G1 arrest. Other details are identical to Figure 5.4A.

(B) Stalked cell simulation of Signal 2 response. Red "X" indicates G1 arrest in stalked daughter cell. Other details are identical to Figure 5.4A.

(C) CtrA expression levels in swarmer cell simulations relative to normalized data extracted from Gorbatyuk *et al*. [208].

(D) DnaA expression levels in swarmer cell simulations relative to normalized data extracted from Gorbatyuk *et al*. [208].

(E) Protein expression levels 30 and 60 minutes after nutrient depletion relative to nutrient rich conditions. Details specified in Figure 5.4E.

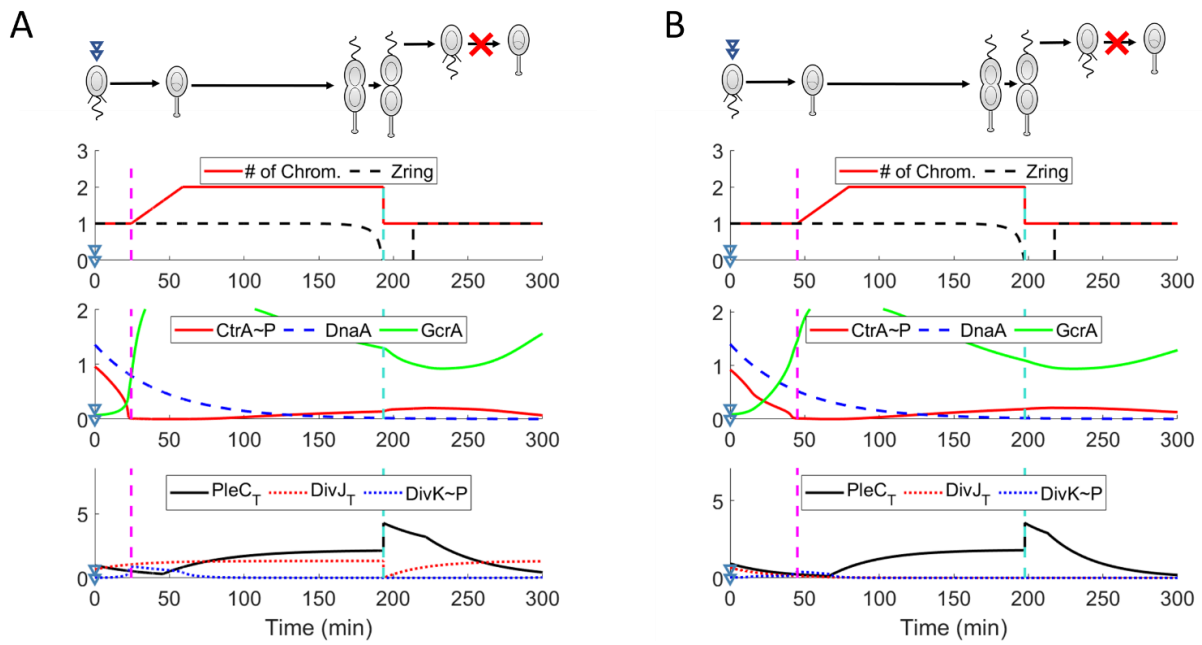

Figure C.3) Removing cdG and SpmX inhibition in Signal 4 and 5 results in secondary swarmer cell cycle arrest.

(A) Swarmer cell simulation of Signal 4' response. Red "X" indicates secondary G1 arrest. Other details are identical to Figure 5.4A. Result indicates that cdG/SpmX depletion are necessary to explain immediate G1 arrest in swarmer populations.

(B) Stalked cell simulation of Signal 5' response. Red "X" indicates G1 arrest in stalked daughter cell. Other details are identical to Figure 5.4A.

C.3 Tables

Table C.1) Parameters

Param	Avg	Std	Min	Max
DgcB	0.0898	0.0201	0.0709	0.1275
$J_{a,CcrM\text{-}CtrA}$	3.5000	0.0000	3.5000	3.5000
$J_{a,CpdR\text{-}CtrA}$	23.2826	2.6173	17.3469	25.0000
$J_{a,CpdR\text{-}DnaA}$	1.4742	0.1892	1.3628	2.0000
$J_{a,CtrA\text{-}CtrA}$	0.2301	0.0768	0.1000	0.3142
$J_{a,CtrA\text{-}GcrA}$	1.1208	0.5274	0.5452	1.7826
$J_{a,CtrA\text{-}TacA}$	7.4076	2.6632	4.4242	10.5860
$J_{a,DivK\text{-}CtrA}$	1.7277	0.4235	1.0838	2.1421
$J_{a,GcrA\text{-}DnaA}$	0.9699	0.4901	0.6723	2.0242
$J_{a,Ini\text{-}DnaA}$	0.2837	0.0140	0.2606	0.3028
$J_{a,PdeA\text{-}CtrA}$	0.8424	0.1508	0.5829	1.0329
$J_{a,PerP\text{-}CtrA}$	2.7774	2.2124	0.5425	5.0000
$J_{a,PleD\text{-}CtrA}$	2.1645	0.6052	1.6925	3.3112
$J_{a,PodJ\text{-}GcrA}$	0.6980	0.2606	0.4945	1.1721
$J_{a,RcdA\text{-}CtrA}$	0.4860	0.0545	0.4500	0.5816
$J_{a,SciP\text{-}CtrA}$	22.0899	2.3457	18.0224	25.0000
$J_{a,ShkA\text{-}CtrA}$	5.1731	0.6064	4.2277	6.0754
$J_{a,TacASpmX}$	0.6007	0.1850	0.3500	0.7779
$J_{a,ZP\text{-}CtrA}$	1.8310	0.4435	1.2370	2.2758
$J_{d,CtrA}$	0.1733	0.0808	0.1000	0.2936
$J_{d,PdeA}$	0.0180	0.0056	0.0126	0.0287
$J_{d,ShkA}$	0.0523	0.0061	0.0432	0.0605
$J_{d,TacA}$	0.0769	0.0225	0.0434	0.1177
$J_{i,CcrM\text{-}DnaA}$	1.3644	0.0995	1.1558	1.4358
$Ji_{,CpdR\text{-}GcrA}$	0.8225	0.1575	0.6408	1.0660
$J_{i,CtrA\text{-}CtrA}$	0.6001	0.2582	0.4500	1.4067
$J_{i,CtrA\text{-}SciP}$	0.5384	0.0775	0.4500	0.6169
$J_{i,DnaA\text{-}GcrA}$	0.6375	0.1156	0.4614	0.7596
$J_{i,GcrA\text{-}CtrA}$	3.3263	0.4705	2.9189	4.4409
$J_{i,PodJ\text{-}DnaA}$	0.6720	0.0787	0.6000	0.8224
$J_{i,PopA\text{-}GcrA}$	0.3798	0.1440	0.3000	0.6682
$J_{i,SciPSciP}$	1.8374	0.2012	1.4440	2.4333
$J_{PlecPodJ}$	0.2781	0.0207	0.2500	0.3152
J_{zring}	0.2606	0.0469	0.2111	0.3480
$k^{+}_{CckAcdG}$	12.9638	1.1600	11.2490	15.0230
$k^{+}_{DgcBcdG}$	0.0106	0.0054	0.0023	0.0237
$k^{+}_{DivJDivK}$	0.0592	0.0101	0.0426	0.0723

$k^{+}_{\mathrm{DivJDivKP}}$	0.0337	0.0133	0.0237	0.0616
$k^{+}_{\mathrm{DivLDivKP}}$	3.8238	0.4161	3.4342	4.6456
$k^{+}_{\mathrm{PleCDivKP}}$	0.0918	0.0229	0.0577	0.1232
k^{+}_{PleDcdG}	25.5109	3.4157	21.8516	30.1101
k^{+}_{PopAcdG}	5.5947	0.5831	4.8572	6.6406
k^{-}_{CckAcdG}	1.3281	0.2401	0.9156	1.5890
K_{CckADivL}	159.3230	24.3606	133.8992	200.3028
$K_{\mathrm{ClpXpCpdR}}$	0.0746	0.0146	0.0489	0.0884
$k_{\mathrm{d,CckA}}$	0.0128	0.0054	0.0043	0.0186
$k_{\mathrm{d,CcrM}}$	0.0200	0.0000	0.0200	0.0200
$k_{\mathrm{d,cdG}}$	1.02E+08	3.94E+06	9.91E+07	1.11E+08
$k_{\mathrm{d,CpdR}}$	0.0252	0.0021	0.0228	0.0290
$k_{\mathrm{d,CtrA1}}$	0.0041	0.0001	0.0040	0.0044
$k_{\mathrm{d,CtrA2}}$	35.6961	5.9842	25.7191	40.6032
$k_{\mathrm{d,DivJ}}$	0.0346	0.0000	0.0346	0.0346
$k_{\mathrm{d,DivK}}$	0.0140	0.0005	0.0135	0.0150
$k_{\mathrm{d,DivL}}$	0.0033	0.0006	0.0027	0.0043
$k_{\mathrm{d,DnaA}}$	0.0245	0.0026	0.0201	0.0276
$k_{\mathrm{d,DnaAatp}}$	1.6402	0.2499	1.2804	1.9909
$k_{\mathrm{d,GcrA}}$	0.1314	0.0062	0.1258	0.1433
$k_{\mathrm{d,Ini}}$	0.0504	0.0145	0.0285	0.0744
$k_{\mathrm{d,PdeA1}}$	0.0014	0.0006	0.0007	0.0020
$k_{\mathrm{d,PdeA2}}$	0.1454	0.0148	0.1252	0.1759
$k_{\mathrm{d,PerP}}$	0.1190	0.0945	0.0250	0.2321
$k_{\mathrm{d,PleC}}$	0.0282	0.0013	0.0267	0.0301
$k_{\mathrm{d,PleD}}$	0.0114	0.0031	0.0087	0.0170
$k_{\mathrm{d,PodJ1}}$	0.0187	0.0124	0.0043	0.0342
$k_{\mathrm{d,PodJ2}}$	0.0529	0.0521	0.0019	0.1172
$k_{\mathrm{d,PopA}}$	0.0591	0.0027	0.0546	0.0634
$k_{\mathrm{d,RcdA}}$	0.0142	0.0012	0.0123	0.0169
$k_{\mathrm{d,SciP}}$	0.0425	0.0378	0.0052	0.0865
$k_{\mathrm{d,ShkA1}}$	0.0001	0.0000	0.0000	0.0001
$k_{\mathrm{d,ShkA2}}$	1.7853	0.6624	1.0054	2.6442
$K_{\mathrm{D,ShkAcdG}}$	0.1182	0.0106	0.0989	0.1387
$k_{\mathrm{d,SpmX}}$	0.0000	0.0000	0.0000	0.0000
$k_{\mathrm{d,TacA1}}$	0.0030	0.0003	0.0026	0.0034
$k_{\mathrm{d,TacA2}}$	0.1722	0.1567	0.0183	0.3700
$k_{\mathrm{d,ZP}}$	0.0003	0.0001	0.0002	0.0005
$k_{\mathrm{depho,TacA}}$	1.3200	0.0237	1.2776	1.3796
$k_{\mathrm{dephos,CpdR}}$	175.9336	21.9482	148.3483	206.4629
$k_{\mathrm{dephos,CtrA}}$	351.1232	36.8360	317.0528	421.2882

$k_{dephos,DivK}$	121.1206	15.7037	108.8717	148.5310
$k_{dephos,PleD}$	536.1236	129.9153	390.7605	709.6334
$k^{-}_{DivJDivK}$	0.1709	0.0123	0.1488	0.1996
$k^{-}_{DivJDivKP}$	0.0157	0.0081	0.0032	0.0233
$k^{-}_{DivLDivKP}$	5.8189	0.3658	5.2611	6.9881
$k_{hyd,DivK}$	0.0715	0.0366	0.0466	0.1377
$k_{pho,TacA}$	732.0478	88.8777	571.1184	857.9806
$k_{phos,CpdR}$	60.0105	9.8839	47.1950	73.5091
$k_{phos,CtrA}$	8.0043	0.4529	7.5266	8.6997
$k_{phos,DivK1}$	13.0080	1.8830	9.9119	15.9928
$k_{phos,DivK2}$	0.0232	0.0416	0.0000	0.1000
$k_{phos,PleD}$	43.2607	4.1456	35.0696	56.5690
$k_{phosDivK3}$	0.6910	0.1382	0.4402	0.9444
$k_{PleCbinding}$	0.1385	0.0964	0.0421	0.2730
$k^{-}_{PleCDivKP}$	124.6004	15.5002	114.3784	155.8586
$k_{PleCunbinding}$	0.0000	0.0000	0.0000	0.0000
$K_{RcdAPopA}$	281.8729	34.9478	224.6234	385.0384
$k_{s,CckA}$	0.0001	0.0000	0.0001	0.0002
$k_{s,CcrM}$	0.0495	0.0010	0.0481	0.0505
$k_{s,cdG1}$	6.57E+07	8.22E+06	5.53E+07	7.93E+07
$k_{s,cdG2}$	16.0156	5.5947	6.6159	23.9706
$k_{s,CpdR}$	0.0104	0.0036	0.0067	0.0147
$k_{s,CtrA-P1}$	0.2783	0.0510	0.1791	0.3502
$k_{s,CtrA-P2}$	1.9875	0.7243	1.2083	2.9029
$k_{s,DivJ}$	0.0047	0.0000	0.0047	0.0047
$k_{s,DivK1}$	0.0004	0.0001	0.0002	0.0005
$k_{s,DivK2}$	0.1253	0.0070	0.1140	0.1313
$k_{s,DivL}$	0.0004	0.0000	0.0003	0.0005
$k_{s,DnaA}$	0.0844	0.0060	0.0764	0.0927
$k_{s,GcrA}$	0.0607	0.0237	0.0393	0.1009
$k_{s,PdeA}$	0.0025	0.0002	0.0023	0.0029
$k_{s,PerP}$	0.0428	0.0371	0.0029	0.0800
$k_{s,PleC}$	0.0527	0.0027	0.0494	0.0566
$k_{s,PleD}$	0.0013	0.0001	0.0011	0.0014
$k_{s,PodJ}$	0.4020	0.1189	0.3015	0.6176
$k_{s,PopA}$	0.0646	0.0041	0.0593	0.0727
$k_{s,RcdA}$	0.0073	0.0018	0.0046	0.0091
$k_{s,SciP}$	0.2579	0.0622	0.2065	0.3642
$k_{s,ShkA}$	0.0002	0.0000	0.0002	0.0002
$k_{s,SpmX}$	0.0398	0.0095	0.0257	0.0492
$k_{s,TacA}$	0.0138	0.0020	0.0110	0.0165
$k_{s,ZP}$	0.0473	0.0027	0.0432	0.0504

k^{-}_{XcdG}	0.0000	0.0000	0.0000	0.0000
$k_{\mathrm{Zconstrict}}$	0.1871	0.0000	0.1871	0.1871
$m_{\mathrm{CtrA\text{-}P1}}$	0.7042	0.1013	0.5000	0.8490
m_{DnaA}	0.6880	0.0085	0.6804	0.7094
m_{Ini}	0.6465	0.0306	0.5952	0.6764
MysK	0.0195	0.0071	0.0113	0.0321
PDE	0.0948	0.0126	0.0768	0.1092
$\varepsilon_{\mathrm{CpdR\text{-}DnaA}}$	0.6063	0.0149	0.5826	0.6237
$\varepsilon_{\mathrm{CtrA\text{-}CtrA}}$	0.3633	0.0224	0.3220	0.4226
$\varepsilon_{\mathrm{CtrA\text{-}GcrA}}$	0.6257	0.1056	0.3487	0.7278
$\varepsilon_{\mathrm{DivJ\text{-}DivK}}$	0.1180	0.0062	0.1070	0.1273
$\varepsilon_{\mathrm{DivJ\text{-}SpmX}}$	0.3249	0.0607	0.1789	0.4090
$\varepsilon_{\mathrm{GcrA\text{-}DnaA}}$	0.5815	0.1197	0.3574	0.7500

Table C.2) Alternative Signals

Paradigm	Description	Parameters changes	Fractional Arrested			
			1st G1	2nd G1	1st G2	2nd G2
Signal4'	• Inhibiting DnaA synthesis. • Decreasing DivK. • Increasing DivL. • Increasing CckA. • Slowing down PleC proteolysis. • Decreasing CtrA.	$k_{s,DnaA} = 0$ $\mu = 0.0018$ $k_{s,DivK1} = k_{s,DivK1}/5$ $k_{s,DivK2} = k_{s,DivK2}/5$ $k_{s,CckA} = k_{s,CckA} \times 1.8$ $k_{s,DivL} = k_{s,DivL} \times 3.8$ $k_{d,PleC} = k_{d,PleC} \times 0.8$ $k_{s,CtrA\text{-}P1} = k_{s,CtrA\text{-}P1}/30$ $k_{s,CtrA\text{-}P2} = k_{s,CtrA\text{-}P2}/30$	**SW** 27.0%	71.7%	1.3%	0
			ST 0	96.9%	0.6%	0
Signal5'	• Inhibiting DnaA synthesis. • Decreasing DivK. • Increasing DivL. • Increasing CckA. • Decreasing CtrA. • Inhibiting DivJ.	$k_{s,DnaA} = 0$ $\mu = 0.0018$ $k_{s,DivK1} = k_{s,DivK1}/5$ $k_{s,DivK2} = k_{s,DivK2}/5$ $k_{s,CckA} = k_{s,CckA} \times 1.8$ $k_{s,DivL} = k_{s,DivL} \times 3.8$ $k_{s,CtrA\text{-}P1} = k_{s,CtrA\text{-}P1}/30$ $k_{s,CtrA\text{-}P2} = k_{s,CtrA\text{-}P2}/30$ $k_{s,DivJ} = 0$	**SW** 27.0%	71.7%	1.3%	0
			ST 0	96.9%	0.6%	0

References

[1] C. Xu, B. R. Weston, J. J. Tyson, and Y. Cao, “Cell cycle control and environmental response by second messengers in Caulobacter crescentus,” *BMC Bioinformatics*, vol. 21, no. 14, pp. 1–19, 2020.

[2] T. Grinenko *et al.*, “Hematopoietic stem cells can differentiate into restricted myeloid progenitors before cell division in mice,” *Nat. Commun.*, vol. 9, no. 1, p. 1898, 2018, doi: 10.1038/s41467-018-04188-7.

[3] B. R. Weston, L. Li, and J. J. Tyson, “Mathematical Analysis of Cytokine-Induced Differentiation of Granulocyte-Monocyte Progenitor Cells,” *Front. Immunol.*, vol. 9, p. 2048, Sep. 2018, doi: 10.3389/fimmu.2018.02048.

[4] L. Britos, E. Abeliuk, T. Taverner, M. Lipton, H. McAdams, and L. Shapiro, “Regulatory response to carbon starvation in Caulobacter crescentus,” *PLoS One*, vol. 6, no. 4, p. e18179, 2011.

[5] D. R. Barreda, P. C. Hanington, and M. Belosevic, “Regulation of myeloid development and function by colony stimulating factors,” *Dev. Comp. Immunol.*, vol. 28, no. 5, pp. 509–554, 2004, doi: 10.1016/j.dci.2003.09.010.

[6] L. Thiele, B. Rothen-Rutishauser, S. Jilek, H. Wunderli-Allenspach, H. P. Merkle, and E. Walter, “Evaluation of particle uptake in human blood monocyte-derived cells in vitro. Does phagocytosis activity of dendritic cells measure up with macrophages?,” *J. Control. Release*, vol. 76, no. 1, pp. 59–71, 2001, doi: https://doi.org/10.1016/S0168-3659(01)00412-6.

[7] R. I. Abu-Ghazaleh *et al.*, “Eosinophil granule proteins in peripheral blood granulocytes,” *J. Leukoc. Biol.*, vol. 52, no. 6, pp. 611–618, Dec. 1992, doi: https://doi.org/10.1002/jlb.52.6.611.

[8] C. N. Jenne, S. Liao, and B. Singh, “Neutrophils: multitasking first responders of immunity and tissue homeostasis.” Springer, 2018.

[9] P. Laslo *et al.*, “Multilineage Transcriptional Priming and Determination of Alternate Hematopoietic Cell Fates,” *Cell*, vol. 126, no. 4, pp. 755–766, 2006, doi: 10.1016/j.cell.2006.06.052.

[10] D. Metcalf and N. A. Nicola, “The clonal proliferation of normal mouse hematopoietic cells: enhancement and suppression by colony-stimulating factor combinations.,” *Blood*, vol. 79, no. 11, pp. 2861–2866, 1992.

[11] D. Metcalf, “Clonal analysis of proliferation and differentiation of paired daughter cells: Action of granulocyte-macrophage colony-stimulating factor on granulocyte-macrophage precursors,” *Cell Biol.*, vol. 77, no. 9, pp. 5327–5330, 1980, doi: 10.1073/pnas.77.9.5327.

[12] M. A. Rieger, P. S. Hoppe, B. M. Smejkal, A. C. Eitelhuber, and T. Schroeder, “Hematopoietic Cytokines Can Instruct Lineage Choice,” *Science (80-.).*, vol. 325, no. 5937, pp. 217 LP – 218, Jul. 2009, doi: 10.1126/science.1171461.

[13] J. A. Hamilton, “Colony-stimulating factors in inflammation and autoimmunity,” *Nat Rev Immunol*, vol. 8, no. 7, pp. 533–544, Jul. 2008.

[14] H. M. Mehta, M. Malandra, and S. J. Corey, “G-CSF and GM-CSF in Neutropenia,” *J. Immunol.*, vol. 195, no. 4, pp. 1341–1349, 2015, doi: 10.4049/jimmunol.1500861.

[15] S. Cetean *et al.*, “The importance of the granulocyte-colony stimulating factor in oncology.,” *Clujul Med.*, vol. 88, no. 4, pp. 468–472, 2015, doi: 10.15386/cjmed-531.

[16] J. M. Skerker and L. Shapiro, “Identification and cell cycle control of a novel pilus system in Caulobacter crescentus,” *EMBO J.*, vol. 19, no. 13, pp. 3223–3234, 2000.

[17] J. S. Poindexter, “The caulobacters: ubiquitous unusual bacteria,” *Microbiol. Rev.*, vol. 45, no. 1, pp. 123–179, Mar. 1981.

[18] P. H. Tsang, G. Li, Y. V Brun, L. Ben Freund, and J. X. Tang, “Adhesion of single bacterial cells in the micronewton range,” *Proc. Natl. Acad. Sci.*, vol. 103, no. 15, pp. 5764 LP – 5768, Apr. 2006, doi: 10.1073/pnas.0601705103.

[19] M. T. Laub, L. Shapiro, and H. H. McAdams, “Systems Biology of Caulobacter,” *Annu. Rev. Genet.*, vol. 41, no. 1, pp. 429–441, Dec. 2007, doi: 10.1146/annurev.genet.41.110306.130346.

[20] J. M. AU - Schrader and L. AU - Shapiro, “Synchronization of Caulobacter Crescentus for Investigation of the Bacterial Cell Cycle,” *JoVE*, no. 98, p. e52633, 2015, doi: doi:10.3791/52633.

[21] J. Holtzendorff *et al.*, “Oscillating global regulators control the genetic circuit driving a bacterial cell cycle,” *Science (80-.).*, vol. 304, no. 5673, pp. 983–987, 2004.

[22] C. Jacobs, N. Ausmees, S. J. Cordwell, L. Shapiro, and M. T. Laub, “Functions of the CckA histidine kinase in Caulobacter cell cycle control,” *Mol. Microbiol.*, vol. 47, no. 5, pp. 1279–1290, 2003.

[23] L. Cheng and K. C. Keiler, “Correct timing of dnaA transcription and initiation of DNA replication requires trans translation,” *J. Bacteriol.*, vol. 191, no. 13, pp. 4268–4275, 2009.

[24] R. T. Wheeler and L. Shapiro, “Differential Localization of Two Histidine Kinases Controlling Bacterial Cell Differentiation,” *Mol. Cell*, vol. 4, no. 5, pp. 683–694, 1999, doi: https://doi.org/10.1016/S1097-2765(00)80379-2.

[25] C. G. Tsokos and M. T. Laub, “Polarity and cell fate asymmetry in Caulobacter crescentus,” *Curr. Opin. Microbiol.*, vol. 15, no. 6, pp. 744–750, 2012, doi: https://doi.org/10.1016/j.mib.2012.10.011.

[26] N. Ausmees and C. Jacobs-Wagner, “Spatial and Temporal Control of Differentiation and Cell Cycle Progression in Caulobacter crescentus,” *Annu. Rev. Microbiol.*, vol. 57, no. 1, pp. 225–247, Oct. 2003, doi: 10.1146/annurev.micro.57.030502.091006.

[27] S. Motta and F. Pappalardo, “Mathematical modeling of biological systems,” *Brief. Bioinform.*, vol. 14, no. 4, pp. 411–422, Jul. 2013, doi: 10.1093/bib/bbs061.

[28] J. J. Tyson, K. Chen, and B. Novak, “Network dynamics and cell physiology,” *Nat. Rev. Mol. Cell Biol.*, vol. 2, no. 12, pp. 908–916, 2001, doi: 10.1038/35103078.

[29] S. E. Fraser and R. M. Harland, “The molecular metamorphosis of experimental embryology,” *Cell*, vol. 100, no. 1, pp. 41–55, 2000.

[30] J. Holmberg and T. Perlmann, “Maintaining differentiated cellular identity,” *Nat. Rev. Genet.*, vol. 13, no. 6, pp. 429–439, 2012, doi: 10.1038/nrg3209.

[31] S. H. Orkin and L. I. Zon, “Hematopoiesis: An Evolving Paradigm for Stem Cell Biology,” *Cell*, vol. 132, no. 4, pp. 631–644, 2008, doi: 10.1016/j.cell.2008.01.025.

[32] K. Fiedler and C. Brunner, “The role of transcription factors in the guidance of granulopoiesis.,”

Am. J. Blood Res., vol. 2, no. 1, pp. 57–65, 2012, doi: 10.1111/j.1365-313X.2011.04605.x.

[33] F. Rosenbauer and D. G. Tenen, "Transcription factors in myeloid development: balancing differentiation with transformation.," *Nat. Rev. Immunol.*, vol. 7, no. 2, pp. 105–17, 2007, doi: 10.1038/nri2024.

[34] H. Hirai *et al.*, "C/EBPβ is required for 'emergency' granulopoiesis," *Nat Immunol*, vol. 7, no. 7, pp. 732–739, 2006, doi: 10.1038/ni1354.

[35] a C. Ward, D. M. Loeb, a a Soede-Bobok, I. P. Touw, and a D. Friedman, "Regulation of granulopoiesis by transcription factors and cytokine signals," *Leuk. Off. J. Leuk. Soc. Am. Leuk. Res. Fund, U.K*, vol. 14, no. June 2016, pp. 973–990, 2000, doi: 10.1038/sj.leu.2401808.

[36] G. D. Jack, L. Zhang, and A. D. Friedman, "M-CSF elevates c-Fos and phospho-C/EBPα(S21) via ERK whereas G-CSF stimulates SHP2 phosphorylation in marrow progenitors to contribute to myeloid lineage specification," *Blood*, vol. 114, no. 10, pp. 2172–2180, 2009, doi: 10.1182/blood-2008-11-191536.

[37] A. D. Friedman, "Transcriptional regulation of granulocyte and monocyte development," *Oncogene*, vol. 21, no. 21, p. 3377, 2002, doi: 10.1038/sj.onc.1205324.

[38] O. Ma, S. Hong, H. Guo, G. Ghiaur, and A. D. Friedman, "Granulopoiesis requires increased C/EBPα compared to monopoiesis, correlated with elevated Cebpa in immature G-CSF receptor versus M-CSF receptor expressing cells," *PLoS One*, vol. 9, no. 4, pp. 1–14, 2014, doi: 10.1371/journal.pone.0095784.

[39] D. I. Gabrilovich and S. Nagaraj, "Myeloid-derived supressor cells as regulators of the immune system," *Nat Rev Immunol*, vol. 9, no. 3, pp. 162–174, 2009, doi: 10.1038/nri2506.Myeloid-derived-suppressor.

[40] C. S. Netherby and S. I. Abrams, "Mechanisms overseeing myeloid-derived suppressor cell production in neoplastic disease," *Cancer Immunol. Immunother.*, pp. 1–8, 2017, doi: 10.1007/s00262-017-1963-5.

[41] D. Gabrilovich and Y. Nefedova, "ROR1C Regulates Differentiation of Myeloid-Derived Suppressor Cells," *Cancer Cell*, vol. 28, no. 2, pp. 147–149, May 2015, doi: 10.1016/j.ccell.2015.07.007.

[42] J. G. Cripps and J. D. Gorham, "MDSC in autoimmunity," *Int. Immunopharmacol.*, vol. 11, no. 7, pp. 789–793, Jul. 2011, doi: https://doi.org/10.1016/j.intimp.2011.01.026.

[43] A. G. Cuenca *et al.*, "A Paradoxical Role for Myeloid-Derived Suppressor Cells in Sepsis and Trauma," *Mol. Med.*, vol. 17, no. 3–4, pp. 281–292, Nov. 2011, doi: 10.2119/molmed.2010.00178.

[44] J. E. Talmadge and D. I. Gabrilovich, "History of myeloid-derived suppressor cells," *Nat Rev Cancer*, vol. 13, no. 10, pp. 739–752, 2013, doi: 10.1038/nrc3581.

[45] K. H. Parker, D. W. Beury, and S. Ostrand-Rosenberg, "Myeloid-Derived Suppressor Cells: Critical Cells Driving Immune Suppression in the Tumor Microenvironment," *Adv. Cancer Res.*, vol. 128, pp. 95–139, May 2015, doi: 10.1016/bs.acr.2015.04.002.

[46] S. J. Priceman *et al.*, "Targeting distinct tumor-infiltrating myeloid cells by inhibiting CSF-1 receptor: combating tumor evasion of antiangiogenic therapy," *Blood*, vol. 115, no. 7, pp. 1461 LP – 1471, Feb. 2010, doi: 10.1182/blood-2009-08-237412.

[47] J. Ozao-Choy *et al.*, "The Novel Role of Tyrosine Kinase Inhibitor in the Reversal of Immune

Suppression and Modulation of Tumor Microenvironment for Immune-Based Cancer Therapies," *Cancer Res.*, vol. 69, no. 6, pp. 2514–2522, Mar. 2009, doi: 10.1158/0008-5472.CAN-08-4709.

[48] M. Vanneman and G. Dranoff, "Combining immunotherapy and targeted therapies in cancer treatment," *Nat Rev Cancer*, vol. 12, no. 4, pp. 237–251, Apr. 2012, doi: 10.1038/nrc3237.

[49] D. I. Gabrilovich, M. P. Velders, E. M. Sotomayor, and W. M. Kast, "Mechanism of Immune Dysfunction in Cancer Mediated by Immature Gr-1+ Myeloid Cells," *J. Immunol.*, vol. 166, no. 9, pp. 5398 LP – 5406, May 2001, doi: 10.4049/jimmunol.166.9.5398.

[50] V. Bronte *et al.*, "Recommendations for myeloid-derived suppressor cell nomenclature and characterization standards," *Nat. Commun.*, vol. 7, p. 12150, Jul. 2016, doi: 10.1038/ncomms12150.

[51] V. Kumar, S. Patel, E. Tcyganov, and D. I. Gabrilovich, "The Nature of Myeloid-Derived Suppressor Cells in the Tumor Microenvironment," *Trends Immunol.*, vol. 37, no. 3, pp. 208–220, 2016, doi: https://doi.org/10.1016/j.it.2016.01.004.

[52] I. M. Stromnes, P. D. Greenberg, and S. R. Hingorani, "Molecular pathways: Myeloid complicity in cancer," *Clin. Cancer Res.*, vol. 20, no. 20, pp. 5157–5170, 2014, doi: 10.1158/1078-0432.CCR-13-0866.

[53] J.-I. Youn and D. I. Gabrilovich, "The biology of myeloid-derived suppressor cells: The blessing and the curse of morphological and functional heterogeneity," *Eur. J. Immunol.*, vol. 40, no. 11, pp. 2969–2975, Nov. 2010, doi: 10.1002/eji.201040895.

[54] R. Dahl *et al.*, "Regulation of macrophage and neutrophil cell fates by the PU.1:C/EBPα ratio and granulocyte colony-stimulating factor," *Nat Immunol*, vol. 4, no. 10, pp. 1029–1036, 2003, doi: 10.1038/ni973.

[55] A. D. Friedman, "C/EBPα in normal and malignant myelopoiesis," *Int. J. Hematol.*, vol. 101, no. 4, pp. 330–341, 2015, doi: 10.1007/s12185-015-1764-6.

[56] L. C. Jones *et al.*, "Expression of C/EBPβ from the *C/ebpα* gene locus is sufficient for normal hematopoiesis in vivo," *Blood*, vol. 99, no. 6, pp. 2032–2037, 2002.

[57] H. Zhang, H. Nguyen-Jackson, A. D. Panopoulos, H. S. Li, P. J. Murray, and S. S. Watowich, "STAT3 controls myeloid progenitor growth during emergency granulopoiesis," *Blood*, vol. 116, no. 14, pp. 2462–2471, 2010, doi: 10.1182/blood-2009-12-259630.

[58] M. G. Manz and S. Boettcher, "Emergency granulopoiesis," *Nat Rev Immunol*, vol. 14, no. 5, pp. 302–314, May 2014.

[59] M. Niehof, S. Kubicka, L. Zender, M. P. Manns, and C. Trautwein, "Autoregulation enables different pathways to control CCAAT/enhancer binding protein β (C/EBPβ) transcription," *J. Mol. Biol.*, vol. 309, no. 4, pp. 855–868, 2001.

[60] N. Timchenko *et al.*, "Autoregulation of the human C/EBPα gene by stimulation of upstream stimulatory factor binding.," *Mol. Cell. Biol.*, vol. 15, no. 3, pp. 1192–1202, Mar. 1995.

[61] T. Kummalue and A. D. Friedman, "Cross-talk between regulators of myeloid development : C/EBPα binds and activates the promoter of the PU.1 gene," vol. 74, no. September, pp. 464–470, 2003, doi: 10.1189/jlb.1202622.http.

[62] C. Yeamans, D. Wang, I. Paz-Priel, B. E. Torbett, D. G. Tenen, and A. D. Friedman, "C/EBPα binds and activates the PU.1 distal enhancer to induce monocyte lineage commitment," *Blood*, vol.

110, no. 9, pp. 3136–3142, 2007, doi: 10.1182/blood-2007-03-080291.

[63] M. R. Lidonnici *et al.*, "Expression of the transcriptional repressor Gfi-1 is regulated by C/EBPα and is involved in its proliferation and colony formation-inhibitory effects in p210BCR/ABL-expressing cells," *Cancer Res.*, vol. 70, no. 20, pp. 7949–7959, 2010, doi: 10.1158/0008-5472.CAN-10-1667.

[64] R. Dahl, S. R. Iyer, K. S. Owens, D. D. Cuylear, and M. C. Simon, "The transcriptional repressor GFI-1 antagonizes PU.1 activity through protein-protein interaction," *J. Biol. Chem.*, vol. 282, no. 9, pp. 6473–6483, 2007, doi: 10.1074/jbc.M607613200.

[65] H. Chen *et al.*, "PU. 1 (Spi-1) autoregulates its expression in myeloid cells.," *Oncogene*, vol. 11, no. 8, pp. 1549–1560, 1995.

[66] J. Schönheit *et al.*, "PU.1 level-directed chromatin structure remodeling at the Irf8 gene drives dendritic cell commitment," *Cell Rep.*, vol. 3, no. 5, pp. 1617–1628, 2013, doi: 10.1016/j.celrep.2013.04.007.

[67] F. Wang and Q. Tong, "Transcription factor PU.1 is expressed in white adipose and inhibits adipocyte differentiation," *Am. J. Physiol. - Cell Physiol.*, vol. 295, no. 1, p. C213 LP-C220, Jul. 2008.

[68] D. Kurotaki *et al.*, "IRF8 inhibits C/EBPα activity to restrain mononuclear phagocyte progenitors from differentiating into neutrophils," *Nat. Commun.*, vol. 5, 2014.

[69] C. Bornstein *et al.*, "A negative feedback loop of transcription factors specifies alternative dendritic cell chromatin states," *Mol. Cell*, vol. 56, no. 6, pp. 749–762, Dec. 2014, doi: 10.1016/j.molcel.2014.10.014.

[70] V. A. Reddy *et al.*, "Granulocyte inducer C/EBPα inactivates the myeloid master regulator PU.1: possible role in lineage commitment decisions," *Blood*, vol. 100, no. 2, pp. 483 LP – 490, Jun. 2002.

[71] H. Krysinska *et al.*, "A two-step, PU.1-dependent mechanism for developmentally regulated chromatin remodeling and transcription of the *c-fms* gene.," *Mol. Cell. Biol.*, vol. 27, no. 3, pp. 878–887, 2007, doi: 10.1128/MCB.01915-06.

[72] J. M. Curry *et al.*, "M-CSF Signals through the MAPK/ERK Pathway via Sp1 to Induce VEGF Production and Induces Angiogenesis In Vivo," *PLoS One*, vol. 3, no. 10, p. e3405, Oct. 2008.

[73] D.-E. Zhang *et al.*, "CCAAT enhancer-binding protein (C/EBP) and AML1 (CBFα2) synergistically activate the macrophage colony-stimulating factor receptor promoter," *Mol. Cell. Biol.*, vol. 16, no. 3, pp. 1231–1240, 1996.

[74] A. Zarebski *et al.*, "Mutations in Growth Factor Independent-1 Associated with Human Neutropenia Block Murine Granulopoiesis through Colony Stimulating Factor-1," *Immunity*, vol. 28, no. 3, pp. 370–380, Mar. 2008, doi: http://dx.doi.org/10.1016/j.immuni.2007.12.020.

[75] L. Zhang and A. D. Friedman, "SHP2 tyrosine phosphatase stimulates *CEBPA* gene expression to mediate cytokine-dependent granulopoiesis," *Blood*, vol. 118, no. 8, pp. 2266–2274, Aug. 2011.

[76] H. Huang *et al.*, "A Src family kinase–Shp2 axis controls RUNX1 activity in megakaryocyte and T-lymphocyte differentiation," *Genes Dev.*, vol. 26, no. 14, pp. 1587–1601, Jul. 2012, doi: 10.1101/gad.192054.112.

[77] M. Lie-A-Ling *et al.*, "RUNX1 positively regulates a cell adhesion and migration program in

murine hemogenic endothelium prior to blood emergence," *Blood*, vol. 124, no. 11, pp. e11–e20, Sep. 2014.

[78] C. S. Velu, A. M. Baktula, and H. L. Grimes, "Gfi1 regulates miR-21 and miR-196b to control myelopoiesis," *Blood*, vol. 113, no. 19, pp. 4720–4728, 2009, doi: 10.1182/blood-2008-11-190215.

[79] M. De La Luz Sierra *et al.*, "The transcription factor Gfi1 regulates G-CSF signaling and neutrophil development through the Ras activator RasGRP1," *Blood*, vol. 115, no. 19, pp. 3970–3979, 2010, doi: 10.1182/blood-2009-10-246967.

[80] G. Behre *et al.*, "Ras signaling enhances the activity of C/EBPα to induce granulocytic differentiation by phosphorylation of serine 248," *J. Biol. Chem.*, vol. 277, no. 29, pp. 26293–26299, 2002, doi: 10.1074/jbc.M202301200.

[81] E. E. Hjort, W. Huang, L. Hu, and E. A. Eklund, "Bcr-abl regulates Stat5 through Shp2 , the interferon consensus sequence binding protein (Icsbp / Irf8), growth arrest specific 2 (Gas2) and calpain," *Oncotarget*, vol. 7, no. 47, pp. 77635–77650, 2016, doi: 10.18632/oncotarget.12749.

[82] J. D. Waight *et al.*, "Myeloid-derived suppressor cell development is regulated by a STAT/IRF-8 axis," *J. Clin. Invest.*, vol. 123, no. 10, pp. 4464–4478, Oct. 2013, doi: 10.1172/JCI68189.

[83] A. Kimura *et al.*, "The transcription factors STAT5A/B regulate GM-CSF–mediated granulopoiesis," *Blood*, vol. 114, no. 21, pp. 4721–4728, Nov. 2009, doi: 10.1182/blood-2009-04-216390.

[84] X. Qi *et al.*, "Antagonistic Regulation by the Transcription Factors C/EBPα and MITF Specifies Basophil and Mast Cell Fates," *Immunity*, vol. 39, no. 1, pp. 97–110, Mar. 2013, doi: 10.1016/j.immuni.2013.06.012.

[85] T. B. van Dijk, B. Baltus, J. A. M. Raaijmakers, J.-W. Lammers, L. Koenderman, and R. P. de Groot, "A composite C/EBP binding site is essential for the activity of the promoter of the IL-3/IL-5/granulocyte-macrophage colony-stimulating factor receptor βc gene.," *J Immunol*, vol. 163, no. 5, pp. 2674–80, 1999.

[86] T. Laomettachit, K. C. Chen, W. T. Baumann, and J. J. Tyson, "A Model of Yeast Cell-Cycle Regulation Based on a Standard Component Modeling Strategy for Protein Regulatory Networks," *PLoS One*, vol. 11, no. 5, p. e0153738, May 2016.

[87] H. M. Mehta, T. Glaubach, and S. J. Corey, "Systems Approach to Phagocyte Production and Activation: Neutrophils and Monocytes," in *A Systems Biology Approach to Blood*, S. J. Corey, M. Kimmel, and J. N. Leonard, Eds. New York, NY: Springer New York, 2014, pp. 99–113.

[88] S. A. Cannistra, P. Groshek, R. Garlick, J. Miller, and J. D. Griffin, "Regulation of surface expression of the granulocyte/macrophage colony-stimulating factor receptor in normal human myeloid cells.," *Proc. Natl. Acad. Sci. U. S. A.*, vol. 87, no. 1, pp. 93–97, 1990.

[89] L. Edelstein-Keshet, *Mathematical Models in Biology*. Society for Industrial and Applied Mathematics, 2005.

[90] J. D. Murray, *Mathematical Biology: I. An Introduction*, 3rd ed. Springer New York, 2007.

[91] L. A. Segel, *Modeling dynamic phenomena in molecular and cellular biology*. Cambridge University Press, 1984.

[92] M. D. Bjerregaard, J. Jurlander, P. Klausen, N. Borregaard, and J. B. Cowland, "The in vivo

profile of transcription factors during neutrophil differentiation in human bone marrow," *Blood*, vol. 101, no. 11, pp. 4322–4332, 2003, doi: 10.1182/blood-2002-03-0835.

[93] M. L. Turgeon, *Clinical hematology: theory and procedures*. Lippincott Williams & Wilkins, 2005.

[94] H. R. Hill, A. Kumánovics, and K. D. Young, "Chapter 82 - Disorders of Leukocyte Function," in *Emery and Rimoin's Principles and Practice of Medical Genetics (Sixth Edition)*, D. Rimoin, R. Pyeritz, and B. B. T.-E. and R. P. and P. of M. G. Korf, Eds. Oxford: Academic Press, 2013, pp. 1–29.

[95] J. Lee, Y. Kim, J. Lim, M. Kim, and K. Han, "G-CSF and GM-CSF concentrations and receptor expression in peripheral blood leukemic cells from patients with chronic myelogenous leukemia," *Ann. Clin. Lab. Sci.*, vol. 38, no. 4, pp. 331–337, 2008.

[96] K. Y. Lee *et al.*, "Varying expression levels of colony stimulating factor receptors in disease states and different leukocytes," *Exp Mol Med*, vol. 32, no. 4, pp. 210–215, 2000, doi: 10.1038/emm.2000.34.

[97] D. H. Cai, D. Wang, J. Keefer, C. Yeamans, K. Hensley, and A. D. Friedman, "C/EBPα:AP-1 Leucine Zipper Heterodimers Bind Novel DNA Elements, Activate the PU.1 Promoter, and Direct Monocyte Lineage Commitment More Potently Than C/EBPα Homodimers or AP-1," *Oncogene*, vol. 27, no. 19, pp. 2772–2779, Apr. 2008, doi: 10.1038/sj.onc.1210940.

[98] L. M. Scott, C. I. Civin, P. Rorth, and a D. Friedman, "A novel temporal expression pattern of three C/EBP family members in differentiating myelomonocytic cells.," *Blood*, vol. 80, no. 7, pp. 1725–35, 1992.

[99] I. Marigo *et al.*, "Tumor-Induced Tolerance and Immune Suppression Depend on the C/EBPβ Transcription Factor," *Immunity*, vol. 32, no. 6, pp. 790–802, 2010, doi: http://dx.doi.org/10.1016/j.immuni.2010.05.010.

[100] L. Dolcetti *et al.*, "Hierarchy of immunosuppressive strength among myeloid-derived suppressor cell subsets is determined by GM-CSF," *Eur. J. Immunol.*, vol. 40, no. 1, pp. 22–35, 2010, doi: 10.1002/eji.200939903.

[101] L. J. Bayne *et al.*, "Tumor-derived granulocyte-macrophage colony-stimulating factor regulates myeloid inflammation and T cell immunity in pancreatic cancer," *Cancer Cell*, vol. 21, no. 6, pp. 822–835, 2012.

[102] S. I. Abrams and J. D. Waight, "Identification of a G-CSF-Granulocytic MDSC axis that promotes tumor progression," *Oncoimmunology*, vol. 1, no. 4, pp. 550–551, Jul. 2012, doi: 10.4161/onci.19334.

[103] Y. Zhao, T. Wu, S. Shao, B. Shi, and Y. Zhao, "Phenotype, development, and biological function of myeloid-derived suppressor cells," *Oncoimmunology*, vol. 5, no. 2, p. e1004983, Feb. 2016, doi: 10.1080/2162402X.2015.1004983.

[104] Z. Zhou *et al.*, "Development and Function of Myeloid-Derived Suppressor Cells Generated From Mouse Embryonic and Hematopoietic Stem Cells," *Stem Cells*, vol. 28, no. 3, pp. 620–632, Mar. 2010, doi: 10.1002/stem.301.

[105] L. Wang, H. Xiao, X. Zhang, W. Liao, S. Fu, and H. Huang, "Restoration of CCAAT enhancer binding protein α P42 induces myeloid differentiation and overcomes all-*trans* retinoic acid resistance in human acute promyelocytic leukemia NB4-R1 cells," *Int. J. Oncol.*, vol. 47, no. 5, pp. 1685–1695, 2015, doi: 10.3892/ijo.2015.3163.

[106] M. Jaguin, N. Houlbert, O. Fardel, and V. Lecureur, “Polarization profiles of human M-CSF-generated macrophages and comparison of M1-markers in classically activated macrophages from GM-CSF and M-CSF origin,” *Cell. Immunol.*, vol. 281, no. 1, pp. 51–61, 2013, doi: https://doi.org/10.1016/j.cellimm.2013.01.010.

[107] K. S. Akagawa, “Functional Heterogeneity of Colony-Stimulating Factor-Induced Human Nonocyte-Derived Macrophages,” *Int. J. Hematol.*, vol. 76, no. 1, pp. 27–34, 2002, doi: 10.1007/BF02982715.

[108] Y. Sonoda, Y. C. Yang, G. G. Wong, S. C. Clark, and M. Ogawa, “Analysis in serum-free culture of the targets of recombinant human hemopoietic growth factors: interleukin 3 and granulocyte/macrophage-colony-stimulating factor are specific for early developmental stages.,” *Proc. Natl. Acad. Sci. U. S. A.*, vol. 85, no. 12, pp. 4360–4364, 1988.

[109] M. Derive, Y. Bouazza, C. Alauzet, and S. Gibot, “Myeloid-derived suppressor cells control microbial sepsis,” *Intensive Care Med.*, vol. 38, no. 6, pp. 1040–1049, 2012, doi: 10.1007/s00134-012-2574-4.

[110] R. P. de Groot, P. J. Coffer, and L. Koenderman, “Regulation of Proliferation, Differentiation and Survival by the IL-3/IL-5/GM-CSF Receptor Family,” *Cell. Signal.*, vol. 10, no. 9, pp. 619–628, Oct. 1998, doi: https://doi.org/10.1016/S0898-6568(98)00023-0.

[111] M. Santillán, “On the Use of the Hill Functions in Mathematical Models of Gene Regulatory Networks,” *Math. Model. Nat. Phenom.*, vol. 3, no. 2, pp. 85–97, 2008.

[112] B. Zhou *et al.*, “The global regulatory architecture of transcription during the Caulobacter cell cycle,” *PLoS Genet.*, vol. 11, no. 1, 2015.

[113] K. Lasker *et al.*, “CauloBrowser: A systems biology resource for Caulobacter crescentus,” *Nucleic Acids Res.*, vol. 44, no. D1, pp. D640–D645, Oct. 2016, doi: 10.1093/nar/gkv1050.

[114] J. G. Belasco, *mRNA degradation in prokaryotic cells: an overview*. San Diego, CA, USA: Academic Press, 1993.

[115] D. Gonzalez, J. B. Kozdon, H. H. McAdams, L. Shapiro, and J. Collier, “The functions of DNA methylation by CcrM in Caulobacter crescentus: a global approach,” *Nucleic Acids Res.*, vol. 42, no. 6, pp. 3720–3735, Jan. 2014, doi: 10.1093/nar/gkt1352.

[116] J. Collier, H. H. McAdams, and L. Shapiro, “A DNA methylation ratchet governs progression through a bacterial cell cycle,” *Proc. Natl. Acad. Sci.*, vol. 104, no. 43, pp. 17111–17116, 2007.

[117] J. B. Kozdon *et al.*, “Global methylation state at base-pair resolution of the Caulobacter genome throughout the cell cycle,” *Proc. Natl. Acad. Sci.*, vol. 110, no. 48, p. E4658 LP-E4667, Nov. 2013, doi: 10.1073/pnas.1319315110.

[118] S. Cha, “Kinetic behavior at high enzyme concentrations magnitude of errors of michaelis-menten and other approximations,” *J. Biol. Chem.*, vol. 245, no. 18, pp. 4814–4818, 1970.

[119] S. Li, P. Brazhnik, B. Sobral, and J. J. Tyson, “Temporal controls of the asymmetric cell division cycle in Caulobacter crescentus,” *PLoS Comput. Biol.*, vol. 5, no. 8, pp. e1000463–e1000463, Aug. 2009, doi: 10.1371/journal.pcbi.1000463.

[120] S. M. Murray, G. Panis, C. Fumeaux, P. H. Viollier, and M. Howard, “Computational and genetic reduction of a cell cycle to its simplest, primordial components,” *PLoS Biol.*, vol. 11, no. 12, p. e1001749, 2013, doi: 10.1371/journal.pbio.1001749.

[121] B. Terrana and A. Newton, “Pattern of unequal cell division and development in Caulobacter crescentus,” *Dev. Biol.*, vol. 44, no. 2, pp. 380–385, 1975, doi: https://doi.org/10.1016/0012-1606(75)90409-1.

[122] J. Collier, “Regulation of chromosomal replication in Caulobacter crescentus,” *Plasmid*, vol. 67, no. 2, pp. 76–87, 2012, doi: https://doi.org/10.1016/j.plasmid.2011.12.007.

[123] R. Siam and G. T. Marczynski, “Cell cycle regulator phosphorylation stimulates two distinct modes of binding at a chromosome replication origin,” *EMBO J.*, vol. 19, no. 5, pp. 1138–1147, Mar. 2000, doi: 10.1093/emboj/19.5.1138.

[124] R. Siam and G. T. Marczynski, “Glutamate at the phosphorylation site of response regulator CtrA provides essential activities without increasing DNA binding,” *Nucleic Acids Res.*, vol. 31, no. 6, pp. 1775–1779, Mar. 2003, doi: 10.1093/nar/gkg271.

[125] A. Reisenauer, K. Quon, and L. Shapiro, “The CtrA Response Regulator Mediates Temporal Control of Gene Expression during the Caulobacter Cell Cycle,” *J. Bacteriol.*, vol. 181, no. 8, pp. 2430 LP – 2439, Apr. 1999, doi: 10.1128/JB.181.8.2430-2439.1999.

[126] W. Spencer, R. Siam, M.-C. Ouimet, D. P. Bastedo, and G. T. Marczynski, “CtrA, a global response regulator, uses a distinct second category of weak DNA binding sites for cell cycle transcription control in Caulobacter crescentus,” *J. Bacteriol.*, vol. 191, no. 17, pp. 5458–5470, 2009.

[127] D. Gonzalez and J. Collier, “DNA methylation by CcrM activates the transcription of two genes required for the division of C aulobacter crescentus,” *Mol. Microbiol.*, vol. 88, no. 1, pp. 203–218, 2013.

[128] S. Adhikari and P. D. Curtis, “DNA methyltransferases and epigenetic regulation in bacteria,” *FEMS Microbiol. Rev.*, vol. 40, no. 5, pp. 575–591, Jul. 2016, doi: 10.1093/femsre/fuw023.

[129] R. Wright, C. Stephens, G. Zweiger, L. Shapiro, and M. R. Alley, “Caulobacter Lon protease has a critical role in cell-cycle control of DNA methylation.,” *Genes Dev.*, vol. 10, no. 12, pp. 1532–1542, 1996.

[130] J. Holtzendorff, J. Reinhardt, and P. H. Viollier, “Cell cycle control by oscillating regulatory proteins in Caulobacter crescentus,” *BioEssays*, vol. 28, no. 4, pp. 355–361, Apr. 2006, doi: 10.1002/bies.20384.

[131] A. Reisenauer and L. Shapiro, “DNA methylation affects the cell cycle transcription of the CtrA global regulator in Caulobacter,” *EMBO J.*, vol. 21, no. 18, pp. 4969–4977, 2002.

[132] S. Crosson, H. McAdams, and L. Shapiro, “A Genetic Oscillator and the Regulation of Cell Cycle Progression in Caulobacter crescentus,” *Cell Cycle*, vol. 3, no. 10, pp. 1252–1254, Oct. 2004, doi: 10.4161/cc.3.10.1181.

[133] S. C. Smith *et al.*, “Cell cycle-dependent adaptor complex for ClpXP-mediated proteolysis directly integrates phosphorylation and second messenger signals,” *Proc. Natl. Acad. Sci.*, vol. 111, no. 39, pp. 14229–14234, 2014.

[134] K. K. Joshi, M. Bergé, S. K. Radhakrishnan, P. H. Viollier, and P. Chien, “An Adaptor Hierarchy Regulates Proteolysis during a Bacterial Cell Cycle,” *Cell*, vol. 163, no. 2, pp. 419–431, 2015, doi: https://doi.org/10.1016/j.cell.2015.09.030.

[135] U. Jenal and T. Fuchs, “An essential protease involved in bacterial cell-cycle control,” *EMBO J.*, vol. 17, no. 19, pp. 5658–5669, Oct. 1998, doi: 10.1093/emboj/17.19.5658.

[136] K. Subramanian, M. R. Paul, and J. J. Tyson, “Potential role of a bistable histidine kinase switch in the asymmetric division cycle of Caulobacter crescentus,” *PLoS Comput. Biol.*, vol. 9, no. 9, pp. e1003221–e1003221, Sep. 2013, doi: 10.1371/journal.pcbi.1003221.

[137] Y. E. Chen, C. G. Tsokos, E. G. Biondi, B. S. Perchuk, and M. T. Laub, “Dynamics of Two Phosphorelays Controlling Cell Cycle Progression in Caulobacter crescentus ,” *J. Bacteriol.* , vol. 191, no. 24, pp. 7417–7429, Dec. 2009, doi: 10.1128/JB.00992-09.

[138] T. H. Mann and L. Shapiro, “Integration of cell cycle signals by multi-PAS domain kinases,” *bioRxiv*, p. 323444, Jan. 2018, doi: 10.1101/323444.

[139] A. A. Iniesta, N. J. Hillson, and L. Shapiro, “Polar remodeling and histidine kinase activation, which is essential for Caulobacter cell cycle progression, are dependent on DNA replication initiation,” *J. Bacteriol.*, vol. 192, no. 15, pp. 3893–3902, 2010.

[140] W. S. Childers *et al.*, “Cell Fate Regulation Governed by a Repurposed Bacterial Histidine Kinase,” *PLOS Biol.*, vol. 12, no. 10, p. e1001979, Oct. 2014.

[141] B. N. Dubey *et al.*, “Cyclic di-GMP mediates a histidine kinase/phosphatase switch by noncovalent domain cross-linking,” *Sci. Adv.*, vol. 2, no. 9, pp. e1600823–e1600823, Sep. 2016, doi: 10.1126/sciadv.1600823.

[142] R. Wargachuk and G. T. Marczynski, “The Caulobacter crescentus homolog of DnaA (HdaA) also regulates the proteolysis of the replication initiator protein DnaA,” *J. Bacteriol.*, vol. 197, no. 22, pp. 3521–3532, 2015.

[143] C. Fernandez-Fernandez, K. Grosse, V. Sourjik, and J. Collier, “The β-sliding clamp directs the localization of HdaA to the replisome in Caulobacter crescentus,” *Microbiology*, vol. 159, no. Pt 11, p. 2237, 2013.

[144] C. Fernandez-Fernandez, D. Gonzalez, and J. Collier, “Regulation of the Activity of the Dual-Function DnaA Protein in Caulobacter crescentus,” *PLoS One*, vol. 6, no. 10, p. e26028, Oct. 2011.

[145] K. Jonas, J. Liu, P. Chien, and M. T. Laub, “Proteotoxic stress induces a cell-cycle arrest by stimulating Lon to degrade the replication initiator DnaA,” *Cell*, vol. 154, no. 3, pp. 623–636, 2013.

[146] J. Liu, L. I. Francis, K. Jonas, M. T. Laub, and P. Chien, “ClpAP is an auxiliary protease for DnaA degradation in Caulobacter crescentus,” *Mol. Microbiol.*, vol. 102, no. 6, pp. 1075–1085, Dec. 2016, doi: 10.1111/mmi.13537.

[147] J. Collier, S. R. Murray, and L. Shapiro, “DnaA couples DNA replication and the expression of two cell cycle master regulators,” *EMBO J.*, vol. 25, no. 2, pp. 346–356, Jan. 2006, doi: 10.1038/sj.emboj.7600927.

[148] U. Jenal, “The role of proteolysis in the Caulobacter crescentus cell cycle and development,” *Res. Microbiol.*, vol. 160, no. 9, pp. 687–695, 2009, doi: https://doi.org/10.1016/j.resmic.2009.09.006.

[149] R. Paul *et al.*, “Allosteric Regulation of Histidine Kinases by Their Cognate Response Regulator Determines Cell Fate,” *Cell*, vol. 133, no. 3, pp. 452–461, May 2008, doi: 10.1016/J.CELL.2008.02.045.

[150] S. Li, P. Brazhnik, B. Sobral, and J. J. Tyson, “A quantitative study of the division cycle of Caulobacter crescentus stalked cells,” *PLoS Comput. Biol.*, vol. 4, no. 1, 2008.

[151] R. Hengge, “Principles of c-di-GMP signalling in bacteria,” *Nat. Rev. Microbiol.*, vol. 7, no. 4, pp. 263–273, 2009, doi: 10.1038/nrmicro2109.

[152] S. K. Radhakrishnan, M. Thanbichler, and P. H. Viollier, “The dynamic interplay between a cell fate determinant and a lysozyme homolog drives the asymmetric division cycle of Caulobacter crescentus,” *Genes Dev.*, vol. 22, no. 2, pp. 212–225, 2008.

[153] J.-Y. Matroule, H. Lam, D. T. Burnette, and C. Jacobs-Wagner, “Cytokinesis Monitoring during Development: Rapid Pole-to-Pole Shuttling of a Signaling Protein by Localized Kinase and Phosphatase in Caulobacter,” *Cell*, vol. 118, no. 5, pp. 579–590, 2004, doi: https://doi.org/10.1016/j.cell.2004.08.019.

[154] R. Paul *et al.*, “Allosteric Regulation of Histidine Kinases by Their Cognate Response Regulator Determines Cell Fate,” *Cell*, vol. 133, no. 3, pp. 452–461, 2008, doi: https://doi.org/10.1016/j.cell.2008.02.045.

[155] P. Aldridge, R. Paul, P. Goymer, P. Rainey, and U. Jenal, “Role of the GGDEF regulator PleD in polar development of Caulobacter crescentus,” *Mol. Microbiol.*, vol. 47, no. 6, pp. 1695–1708, 2003.

[156] A. J. Hinz, D. E. Larson, C. S. Smith, and Y. V Brun, “The Caulobacter crescentus polar organelle development protein PodJ is differentially localized and is required for polar targeting of the PleC development regulator,” *Mol. Microbiol.*, vol. 47, no. 4, pp. 929–941, Feb. 2003, doi: 10.1046/j.1365-2958.2003.03349.x.

[157] M. L. Lawler, D. E. Larson, A. J. Hinz, D. Klein, and Y. V Brun, “Dissection of functional domains of the polar localization factor PodJ in Caulobacter crescentus,” *Mol. Microbiol.*, vol. 59, no. 1, pp. 301–316, 2006.

[158] J. C. Chen, A. K. Hottes, H. H. McAdams, P. T. McGrath, P. H. Viollier, and L. Shapiro, “Cytokinesis signals truncation of the PodJ polarity factor by a cell cycle-regulated protease,” *EMBO J.*, vol. 25, no. 2, pp. 377–386, Jan. 2006, doi: 10.1038/sj.emboj.7600935.

[159] M. Thanbichler, “Spatial regulation in Caulobacter crescentus,” *Curr. Opin. Microbiol.*, vol. 12, no. 6, pp. 715–721, 2009, doi: https://doi.org/10.1016/j.mib.2009.09.013.

[160] C. Lori *et al.*, “Cyclic di-GMP acts as a cell cycle oscillator to drive chromosome replication,” *Nature*, vol. 523, no. 7559, p. 236, May 2015.

[161] S. Abel *et al.*, “Bi-modal Distribution of the Second Messenger c-di-GMP Controls Cell Fate and Asymmetry during the Caulobacter Cell Cycle,” *PLOS Genet.*, vol. 9, no. 9, p. e1003744, Sep. 2013.

[162] K. S. Sprecher *et al.*, “Cohesive Properties of the Caulobacter crescentus Holdfast Adhesin Are Regulated by a Novel c-di-GMP Effector Protein,” *MBio*, vol. 8, no. 2, pp. e00294-17, May 2017, doi: 10.1128/mBio.00294-17.

[163] C. Chan *et al.*, “Structural basis of activity and allosteric control of diguanylate cyclase,” *Proc. Natl. Acad. Sci. U. S. A.*, vol. 101, no. 49, pp. 17084 LP – 17089, Dec. 2004, doi: 10.1073/pnas.0406134101.

[164] B. Christen *et al.*, “Allosteric control of cyclic di-GMP signaling,” *J. Biol. Chem.*, vol. 281, no. 42, pp. 32015–32024, 2006.

[165] S. Ardissone and P. H. Viollier, “Interplay between flagellation and cell cycle control in Caulobacter,” *Curr. Opin. Microbiol.*, vol. 28, pp. 83–92, 2015, doi:

https://doi.org/10.1016/j.mib.2015.08.012.

[166] K. Lasker, T. H. Mann, and L. Shapiro, “An intracellular compass spatially coordinates cell cycle modules in Caulobacter crescentus,” *Curr. Opin. Microbiol.*, vol. 33, pp. 131–139, 2016, doi: https://doi.org/10.1016/j.mib.2016.06.007.

[167] S. Abel *et al.*, “Regulatory cohesion of cell cycle and cell differentiation through interlinked phosphorylation and second messenger networks,” *Mol. Cell*, vol. 43, no. 4, pp. 550–560, Aug. 2011, doi: 10.1016/j.molcel.2011.07.018.

[168] B. Williams, N. Bhat, P. Chien, and L. Shapiro, “ClpXP and ClpAP proteolytic activity on divisome substrates is differentially regulated following the C aulobacter asymmetric cell division,” *Mol. Microbiol.*, vol. 93, no. 5, pp. 853–866, 2014.

[169] P. Szwedziak, Q. Wang, T. A. M. Bharat, M. Tsim, and J. Löwe, “Architecture of the ring formed by the tubulin homologue FtsZ in bacterial cell division,” *Elife*, vol. 3, p. e04601, 2014.

[170] G. Lan, B. R. Daniels, T. M. Dobrowsky, D. Wirtz, and S. X. Sun, “Condensation of FtsZ filaments can drive bacterial cell division,” *Proc. Natl. Acad. Sci.*, vol. 106, no. 1, pp. 121–126, 2009.

[171] F. Beaufay, J. Coppine, A. Mayard, G. Laloux, X. De Bolle, and R. Hallez, “A NAD-dependent glutamate dehydrogenase coordinates metabolism with cell division in Caulobacter crescentus,” *EMBO J.*, vol. 34, no. 13, pp. 1786–1800, 2015.

[172] N. W. Goehring and J. Beckwith, “Diverse paths to midcell: assembly of the bacterial cell division machinery,” *Curr. Biol.*, vol. 15, no. 13, pp. R514–R526, 2005.

[173] M. Thanbichler and L. Shapiro, “MipZ, a Spatial Regulator Coordinating Chromosome Segregation with Cell Division in Caulobacter,” *Cell*, vol. 126, no. 1, pp. 147–162, 2006, doi: https://doi.org/10.1016/j.cell.2006.05.038.

[174] H. P. Erickson, “Modeling the physics of FtsZ assembly and force generation,” *Proc. Natl. Acad. Sci.*, vol. 106, no. 23, pp. 9238–9243, 2009.

[175] E. R. Miraldi, P. J. Thomas, and L. Romberg, “Allosteric models for cooperative polymerization of linear polymers,” *Biophys. J.*, vol. 95, no. 5, pp. 2470–2486, 2008.

[176] G. Lan, C. W. Wolgemuth, and S. X. Sun, “Z-ring force and cell shape during division in rod-like bacteria,” *Proc. Natl. Acad. Sci.*, vol. 104, no. 41, pp. 16110–16115, 2007.

[177] J. F. Allard and E. N. Cytrynbaum, “Force generation by a dynamic Z-ring in Escherichia coli cell division,” *Proc. Natl. Acad. Sci.*, vol. 106, no. 1, pp. 145–150, 2009.

[178] M. Wortinger, M. J. Sackett, and Y. V Brun, “CtrA mediates a DNA replication checkpoint that prevents cell division in Caulobacter crescentus,” *EMBO J.*, vol. 19, no. 17, pp. 4503–4512, 2000.

[179] E. M. Judd, K. R. Ryan, W. E. Moerner, L. Shapiro, and H. H. McAdams, “Fluorescence bleaching reveals asymmetric compartment formation prior to cell division in Caulobacter,” *Proc. Natl. Acad. Sci.*, vol. 100, no. 14, pp. 8235–8240, 2003.

[180] E. L. Meier, S. Razavi, T. Inoue, and E. D. Goley, “A novel membrane anchor for FtsZ is linked to cell wall hydrolysis in Caulobacter crescentus,” *Mol. Microbiol.*, vol. 101, no. 2, pp. 265–280, 2016.

[181] J. Collier, “Cell division control in Caulobacter crescentus,” *Biochim. Biophys. Acta - Gene Regul. Mech.*, vol. 1862, no. 7, pp. 685–690, 2019, doi: https://doi.org/10.1016/j.bbagrm.2018.04.005.

[182] S. Pichoff, B. Shen, B. Sullivan, and J. Lutkenhaus, “FtsA mutants impaired for self-interaction bypass ZipA suggesting a model in which FtsA’s self-interaction competes with its ability to recruit downstream division proteins,” *Mol. Microbiol.*, vol. 83, no. 1, pp. 151–167, 2012.

[183] M. J. Sackett, A. J. Kelly, and Y. V Brun, “Ordered expression of ftsQA and ftsZ during the Caulobacter crescentus cell cycle,” *Mol. Microbiol.*, vol. 28, no. 3, pp. 421–434, Apr. 1998, doi: 10.1046/j.1365-2958.1998.00753.x.

[184] M. E. Martin, M. J. Trimble, and Y. V Brun, “Cell cycle-dependent abundance, stability and localization of FtsA and FtsQ in Caulobacter crescentus,” *Mol. Microbiol.*, vol. 54, no. 1, pp. 60–74, Oct. 2004, doi: 10.1111/j.1365-2958.2004.04251.x.

[185] N. Ohta, A. J. Ninfa, A. Allaire, L. Kulick, and A. Newton, “Identification, characterization, and chromosomal organization of cell division cycle genes in Caulobacter crescentus.,” *J. Bacteriol.*, vol. 179, no. 7, pp. 2169 LP – 2180, Apr. 1997, doi: 10.1128/jb.179.7.2169-2180.1997.

[186] L. I. Rothfield and S. S. Justice, “Bacterial cell division: the cycle of the ring,” *Cell*, vol. 88, no. 5, pp. 581–584, 1997.

[187] J. M. Schrader *et al.*, “Dynamic translation regulation in Caulobacter cell cycle control,” *Proc. Natl. Acad. Sci.*, vol. 113, no. 44, p. E6859 LP-E6867, Nov. 2016, doi: 10.1073/pnas.1614795113.

[188] C. N. Takacs *et al.*, “Growth medium-dependent glycine incorporation into the peptidoglycan of Caulobacter crescentus,” *PLoS One*, vol. 8, no. 2, 2013.

[189] T. Lott, N. Ohta, and A. Newton, “Order of gene replication in Caulobacter crescentus; use of in vivo labeled genomic DNA as a probe,” *Mol. Gen. Genet. MGG*, vol. 210, no. 3, pp. 543–550, 1987.

[190] D. P. Bastedo and G. T. Marczynski, “CtrA response regulator binding to the Caulobacter chromosome replication origin is required during nutrient and antibiotic stress as well as during cell cycle progression,” *Mol. Microbiol.*, vol. 72, no. 1, pp. 139–154, 2009.

[191] J. A. Taylor, M. Ouimet, R. Wargachuk, and G. T. Marczynski, “The Caulobacter crescentus chromosome replication origin evolved two classes of weak DnaA binding sites,” *Mol. Microbiol.*, vol. 82, no. 2, pp. 312–326, 2011.

[192] K. C. Quon, B. Yang, I. J. Domian, L. Shapiro, and G. T. Marczynski, “Negative control of bacterial DNA replication by a cell cycle regulatory protein that binds at the chromosome origin,” *Proc. Natl. Acad. Sci.*, vol. 95, no. 1, pp. 120–125, 1998.

[193] M. Campos *et al.*, “A Constant Size Extension Drives Bacterial Cell Size Homeostasis,” *Cell*, vol. 159, no. 6, pp. 1433–1446, 2014, doi: https://doi.org/10.1016/j.cell.2014.11.022.

[194] S. Sanselicio, M. Bergé, L. Théraulaz, S. K. Radhakrishnan, and P. H. Viollier, “Topological control of the Caulobacter cell cycle circuitry by a polarized single-domain PAS protein,” *Nat. Commun.*, vol. 6, no. 1, pp. 1–14, 2015.

[195] P. T. McGrath, A. A. Iniesta, K. R. Ryan, L. Shapiro, and H. H. McAdams, “A dynamically localized protease complex and a polar specificity factor control a cell cycle master regulator,” *Cell*, vol. 124, no. 3, pp. 535–547, 2006.

[196] B. Grünenfelder, G. Rummel, J. Vohradsky, D. Röder, H. Langen, and U. Jenal, “Proteomic analysis of the bacterial cell cycle,” *Proc. Natl. Acad. Sci.*, vol. 98, no. 8, pp. 4681–4686, 2001.

[197] A. A. Iniesta, P. T. McGrath, A. Reisenauer, H. H. McAdams, and L. Shapiro, “A phospho-

signaling pathway controls the localization and activity of a protease complex critical for bacterial cell cycle progression," *Proc. Natl. Acad. Sci.*, vol. 103, no. 29, pp. 10935–10940, 2006.

[198] P. H. Viollier, N. Sternheim, and L. Shapiro, "A dynamically localized histidine kinase controls the asymmetric distribution of polar pili proteins," *EMBO J.*, vol. 21, no. 17, pp. 4420–4428, Sep. 2002, doi: 10.1093/emboj/cdf454.

[199] B. Christen *et al.*, "High-throughput identification of protein localization dependency networks," *Proc. Natl. Acad. Sci.*, vol. 107, no. 10, pp. 4681–4686, 2010.

[200] P. H. Viollier, N. Sternheim, and L. Shapiro, "Identification of a localization factor for the polar positioning of bacterial structural and regulatory proteins," *Proc. Natl. Acad. Sci.*, vol. 99, no. 21, pp. 13831–13836, 2002.

[201] M. T. Laub, H. H. McAdams, T. Feldblyum, C. M. Fraser, and L. Shapiro, "Global Analysis of the Genetic Network Controlling a Bacterial Cell Cycle," *Science (80-.).*, vol. 290, no. 5499, pp. 2144 LP – 2148, Dec. 2000, doi: 10.1126/science.290.5499.2144.

[202] G. Zweiger, G. Marczynski, and L. Shapiro, "A Caulobacter DNA methyltransferase that functions only in the predivisional cell," *J. Mol. Biol.*, vol. 235, no. 2, pp. 472–485, 1994.

[203] D. Gonzalez and J. Collier, "Genomic adaptations to the loss of a conserved bacterial DNA methyltransferase," *MBio*, vol. 6, no. 4, pp. e00952-15, 2015.

[204] C. G. Tsokos, B. S. Perchuk, and M. T. Laub, "A Dynamic Complex of Signaling Proteins Uses Polar Localization to Regulate Cell-Fate Asymmetry in Caulobacter crescentus," *Dev. Cell*, vol. 20, no. 3, pp. 329–341, 2011, doi: https://doi.org/10.1016/j.devcel.2011.01.007.

[205] C. Jacobs, I. J. Domian, J. R. Maddock, and L. Shapiro, "Cell Cycle–Dependent Polar Localization of an Essential Bacterial Histidine Kinase that Controls DNA Replication and Cell Division," *Cell*, vol. 97, no. 1, pp. 111–120, 1999, doi: https://doi.org/10.1016/S0092-8674(00)80719-9.

[206] C. Stephens, A. Reisenauer, R. Wright, and L. Shapiro, "A cell cycle-regulated bacterial DNA methyltransferase is essential for viability," *Proc. Natl. Acad. Sci.*, vol. 93, no. 3, pp. 1210–1214, 1996.

[207] I. J. Domian, A. Reisenauer, and L. Shapiro, "Feedback control of a master bacterial cell-cycle regulator," *Proc. Natl. Acad. Sci.*, vol. 96, no. 12, pp. 6648 LP – 6653, Jun. 1999, doi: 10.1073/pnas.96.12.6648.

[208] B. Gorbatyuk and G. T. Marczynski, "Regulated degradation of chromosome replication proteins DnaA and CtrA in Caulobacter crescentus," *Mol. Microbiol.*, vol. 55, no. 4, pp. 1233–1245, Feb. 2005, doi: 10.1111/j.1365-2958.2004.04459.x.

[209] J. Mignolet *et al.*, "Functional dichotomy and distinct nanoscale assemblies of a cell cycle-controlled bipolar zinc-finger regulator," *Elife*, vol. 5, p. e18647, 2016.

[210] I. J. Domian, K. C. Quon, and L. Shapiro, "Cell Type-Specific Phosphorylation and Proteolysis of a Transcriptional Regulator Controls the G1-to-S Transition in a Bacterial Cell Cycle," *Cell*, vol. 90, no. 3, pp. 415–424, 1997, doi: https://doi.org/10.1016/S0092-8674(00)80502-4.

[211] L. K. Harris and J. A. Theriot, "Relative Rates of Surface and Volume Synthesis Set Bacterial Cell Size," *Cell*, vol. 165, no. 6, pp. 1479–1492, 2016, doi: https://doi.org/10.1016/j.cell.2016.05.045.

[212] K. R. Ryan, E. M. Judd, and L. Shapiro, "The CtrA Response Regulator Essential for Caulobacter

crescentus Cell-cycle Progression Requires a Bipartite Degradation Signal for Temporally Controlled Proteolysis," *J. Mol. Biol.*, vol. 324, no. 3, pp. 443–455, 2002, doi: https://doi.org/10.1016/S0022-2836(02)01042-2.

[213] J. M. Skerker and M. T. Laub, "Cell-cycle progression and the generation of asymmetry in Caulobacter crescentus," *Nat. Rev. Microbiol.*, vol. 2, no. 4, pp. 325–337, 2004, doi: 10.1038/nrmicro864.

[214] D. Y. Hung and L. Shapiro, "A signal transduction protein cues proteolytic events critical to Caulobacter cell cycle progression," *Proc. Natl. Acad. Sci.*, vol. 99, no. 20, pp. 13160 LP – 13165, Oct. 2002, doi: 10.1073/pnas.202495099.

[215] A. K. Brassinga and G. T. Marczynski, "Replication intermediate analysis confirms that chromosomal replication origin initiates from an unusual intergenic region in Caulobacter crescentus," *Nucleic Acids Res.*, vol. 29, no. 21, pp. 4441–4451, Nov. 2001, doi: 10.1093/nar/29.21.4441.

[216] R. B. Jensen, "Coordination between chromosome replication, segregation, and cell division in Caulobacter crescentus," *J. Bacteriol.*, vol. 188, no. 6, pp. 2244–2253, 2006.

[217] S. M. Shaheen, M.-C. Ouimet, and G. T. Marczynski, "Comparative analysis of Caulobacter chromosome replication origins," *Microbiology*, vol. 155, no. 4, pp. 1215–1225, 2009.

[218] C. Speck and W. Messer, "Mechanism of origin unwinding: sequential binding of DnaA to double- and single-stranded DNA," *EMBO J.*, vol. 20, no. 6, pp. 1469–1476, Mar. 2001, doi: 10.1093/emboj/20.6.1469.

[219] G. T. Marczynski, K. Lentine, and L. Shapiro, "A developmentally regulated chromosomal origin of replication uses essential transcription elements.," *Genes Dev.*, vol. 9, no. 12, pp. 1543–1557, 1995.

[220] R. Siam, A. K. C. Brassinga, and G. T. Marczynski, "A dual binding site for integration host factor and the response regulator CtrA inside the Caulobacter crescentus replication origin," *J. Bacteriol.*, vol. 185, no. 18, pp. 5563–5572, 2003.

[221] J. A. Taylor, J. D. Wilbur, S. C. Smith, and K. R. Ryan, "Mutations that Alter RcdA Surface Residues Decouple Protein Localization and CtrA Proteolysis in Caulobacter crescentus," *J. Mol. Biol.*, vol. 394, no. 1, pp. 46–60, 2009, doi: https://doi.org/10.1016/j.jmb.2009.08.076.

[222] E. G. Biondi *et al.*, "Regulation of the bacterial cell cycle by an integrated genetic circuit," *Nature*, vol. 444, no. 7121, pp. 899–904, 2006, doi: 10.1038/nature05321.

[223] A. Duerig *et al.*, "Second messenger-mediated spatiotemporal control of protein degradation regulates bacterial cell cycle progression," *Genes Dev.*, vol. 23, no. 1, pp. 93–104, 2009.

[224] J. Collier and L. Shapiro, "Feedback Control of DnaA-Mediated Replication Initiation by Replisome-Associated HdaA Protein in Caulobacter," *J. Bacteriol.*, vol. 191, no. 18, pp. 5706 LP – 5716, Sep. 2009, doi: 10.1128/JB.00525-09.

[225] G. Li, Y. V Brun, and J. X. Tang, "Holdfast spreading and thickening during Caulobacter crescentus attachment to surfaces," *BMC Microbiol.*, vol. 13, no. 1, p. 139, 2013, doi: 10.1186/1471-2180-13-139.

[226] T. Thanabalu, J. Hindley, S. Brenner, C. Oei, and C. Berry, "Expression of the mosquitocidal toxins of Bacillus sphaericus and Bacillus thuringiensis subsp. israelensis by recombinant Caulobacter crescentus, a vehicle for biological control of aquatic insect larvae.," *Appl. Environ.*

Microbiol., vol. 58, no. 3, pp. 905 LP – 910, Mar. 1992.

[227] D. K. Chatterjee and A. W. Bourquin, "Metabolism of aromatic compounds by Caulobacter crescentus.," *J. Bacteriol.*, vol. 169, no. 5, pp. 1993 LP – 1996, May 1987, doi: 10.1128/jb.169.5.1993-1996.1987.

[228] M. C. Yung, J. Ma, M. R. Salemi, B. S. Phinney, G. R. Bowman, and Y. Jiao, "Shotgun Proteomic Analysis Unveils Survival and Detoxification Strategies by Caulobacter crescentus during Exposure to Uranium, Chromium, and Cadmium," *J. Proteome Res.*, vol. 13, no. 4, pp. 1833–1847, Apr. 2014, doi: 10.1021/pr400880s.

[229] R. C. Wilhelm, "Following the terrestrial tracks of Caulobacter-redefining the ecology of a reputed aquatic oligotroph," *ISME J*, vol. 12, pp. 3025–3037, 2018.

[230] G. Li, C. S. Smith, Y. V Brun, and J. X. Tang, "The elastic properties of the caulobacter crescentus adhesive holdfast are dependent on oligomers of N-acetylglucosamine," *J. Bacteriol.*, vol. 187, no. 1, pp. 257–265, Jan. 2005, doi: 10.1128/JB.187.1.257-265.2005.

[231] J. Patel, Q. Zhang, R. M. L. McKay, R. Vincent, and Z. Xu, "Genetic Engineering of Caulobacter crescentus for Removal of Cadmium from Water," *Appl. Biochem. Biotechnol.*, vol. 160, no. 1, pp. 232–243, 2010, doi: 10.1007/s12010-009-8540-0.

[232] P. Brazhnik and J. J. Tyson, "Cell Cycle Control in Bacteria and Yeast: A Case of Convergent Evolution?," *Cell Cycle*, vol. 5, no. 5, pp. 522–529, Mar. 2006, doi: 10.4161/cc.5.5.2493.

[233] Y. E. Chen, C. Tropini, K. Jonas, C. G. Tsokos, K. C. Huang, and M. T. Laub, "Spatial gradient of protein phosphorylation underlies replicative asymmetry in a bacterium," *Proc. Natl. Acad. Sci.*, vol. 108, no. 3, pp. 1052 LP – 1057, Jan. 2011, doi: 10.1073/pnas.1015397108.

[234] K. Subramanian, M. R. Paul, and J. J. Tyson, "Dynamical Localization of DivL and PleC in the Asymmetric Division Cycle of Caulobacter crescentus: A Theoretical Investigation of Alternative Models," *PLOS Comput. Biol.*, vol. 11, no. 7, p. e1004348, Jul. 2015.

[235] F. Li, K. Subramanian, M. Chen, J. J. Tyson, and Y. Cao, "A stochastic spatiotemporal model of a response-regulator network in theCaulobacter crescentuscell cycle," *Phys. Biol.*, vol. 13, no. 3, p. 35007, 2016, doi: 10.1088/1478-3975/13/3/035007.

[236] J. A. Lesley and L. Shapiro, "SpoT regulates DnaA stability and initiation of DNA replication in carbon-starved Caulobacter crescentus," *J. Bacteriol.*, vol. 190, no. 20, pp. 6867–6880, 2008.

[237] S. Ronneau, K. Petit, X. De Bolle, and R. Hallez, "Phosphotransferase-dependent accumulation of (p) ppGpp in response to glutamine deprivation in Caulobacter crescentus," *Nat. Commun.*, vol. 7, no. 1, pp. 1–12, 2016.

[238] C. C. Boutte and S. Crosson, "The complex logic of stringent response regulation in Caulobacter crescentus: starvation signalling in an oligotrophic environment," *Mol. Microbiol.*, vol. 80, no. 3, pp. 695–714, 2011.

[239] T. Hogg, U. Mechold, H. Malke, M. Cashel, and R. Hilgenfeld, "Conformational antagonism between opposing active sites in a bifunctional RelA/SpoT homolog modulates (p) ppGpp metabolism during the stringent response," *Cell*, vol. 117, no. 1, pp. 57–68, 2004.

[240] B. S. Powell *et al.*, "Novel proteins of the phosphotransferase system encoded within the rpoN operon of Escherichia coli enzyme IIANtr affects growth on organic nitrogen and the conditional lethality of an erats mutant," *J. Biol. Chem.*, vol. 270, no. 9, pp. 4822–4839, 1995.

[241] M. Chavarría, T. Fuhrer, U. Sauer, K. Pflüger-Grau, and V. de Lorenzo, “Cra regulates the cross-talk between the two branches of the phosphoenolpyruvate: phosphotransferase system of Pseudomonas putida,” *Environ. Microbiol.*, vol. 15, no. 1, pp. 121–132, 2013.

[242] P. D. Curtis and Y. V Brun, “Getting in the loop: regulation of development in Caulobacter crescentus,” *Microbiol. Mol. Biol. Rev.*, vol. 74, no. 1, pp. 13–41, 2010.

[243] D. J. Leslie *et al.*, “Nutritional control of DNA replication initiation through the proteolysis and regulated translation of DnaA,” *PLoS Genet.*, vol. 11, no. 7, p. e1005342, 2015.

[244] C. C. Boutte, J. T. Henry, and S. Crosson, “ppGpp and polyphosphate modulate cell cycle progression in Caulobacter crescentus,” *J. Bacteriol.*, vol. 194, no. 1, pp. 28–35, 2012.

[245] D. Gonzalez and J. Collier, “Effects of (p) ppGpp on the progression of the cell cycle of Caulobacter crescentus,” *J. Bacteriol.*, vol. 196, no. 14, pp. 2514–2525, 2014.

[246] E. G. Biondi, J. M. Skerker, M. Arif, M. S. Prasol, B. S. Perchuk, and M. T. Laub, “A phosphorelay system controls stalk biogenesis during cell cycle progression in Caulobacter crescentus,” *Mol. Microbiol.*, vol. 59, no. 2, pp. 386–401, Jan. 2006, doi: 10.1111/j.1365-2958.2005.04970.x.

[247] C. G. Tsokos, B. S. Perchuk, and M. T. Laub, “A dynamic complex of signaling proteins uses polar localization to regulate cell-fate asymmetry in Caulobacter crescentus,” *Dev. Cell*, vol. 20, no. 3, pp. 329–341, 2011.

[248] A. Kaczmarczyk *et al.*, “Precise timing of transcription by c-di-GMP coordinates cell cycle and morphogenesis in Caulobacter,” *Nat. Commun.*, vol. 11, no. 1, pp. 1–16, 2020.

[249] M. H. Tan, J. B. Kozdon, X. Shen, L. Shapiro, and H. H. McAdams, “An essential transcription factor, SciP, enhances robustness of Caulobacter cell cycle regulation,” *Proc. Natl. Acad. Sci. U. S. A.*, vol. 107, no. 44, pp. 18985–18990, Nov. 2010, doi: 10.1073/pnas.1014395107.

[250] A. N. Bittner, A. Kriel, and J. D. Wang, “Lowering GTP level increases survival of amino acid starvation but slows growth rate for Bacillus subtilis cells lacking (p) ppGpp,” *J. Bacteriol.*, vol. 196, no. 11, pp. 2067–2076, 2014.

[251] W. Zhao, S. W. Duvall, K. A. Kowallis, D. T. Tomares, H. N. Petitjean, and W. S. Childers, “A circuit of protein-protein regulatory interactions enables polarity establishment in a bacterium,” *bioRxiv*, p. 503250, 2018.

[252] J. Coppine, A. Kaczmarczyk, K. Petit, T. Brochier, U. Jenal, and R. Hallez, “Regulation of bacterial cell cycle progression by redundant phosphatases,” *bioRxiv*, 2020.

[253] K. K. Joshi, M. Sutherland, and P. Chien, “Cargo engagement protects protease adaptors from degradation in a substrate-specific manner,” *J. Biol. Chem.*, vol. 292, no. 26, pp. 10973–10982, 2017.

[254] M. Brilli *et al.*, “The diversity and evolution of cell cycle regulation in alpha-proteobacteria: a comparative genomic analysis,” *BMC Syst. Biol.*, vol. 4, no. 1, p. 52, 2010, doi: 10.1186/1752-0509-4-52.

[255] C. Ramírez and L. Mendoza, “Phenotypic stability and plasticity in GMP-derived cells as determined by their underlying regulatory network,” *Bioinformatics*, vol. 34, no. 7, pp. 1174–1182, 2018.

[256] D. G. Tenen, “Disruption of differentiation in human cancer: AML shows the way,” *Nat. Rev.*

cancer, vol. 3, no. 2, pp. 89–101, 2003.

[257] T. Hu, R. Murdaugh, and D. Nakada, “Transcriptional and Microenvironmental Regulation of Lineage Ambiguity in Leukemia ,” *Frontiers in Oncology* , vol. 7. p. 268, 2017.

[258] K. Heinrich, P. Sobetzko, and K. Jonas, “A Kinase-Phosphatase Switch Transduces Environmental Information into a Bacterial Cell Cycle Circuit,” *PLOS Genet.*, vol. 12, no. 12, p. e1006522, Dec. 2016.

[259] E. D. Goley, A. A. Iniesta, and L. Shapiro, “Cell cycle regulation in Caulobacter: location, location, location,” *J. Cell Sci.*, vol. 120, no. 20, pp. 3501 LP – 3507, Oct. 2007, doi: 10.1242/jcs.005967.

[260] M. Chen, F. Li, K. Subramanian, J. Tyson, and Y. Cao, “Two-dimensional model of bipolar PopZ polymerization in caulobacter crescentus,” in *Proceedings of the 6th ACM Conference on Bioinformatics, Computational Biology and Health Informatics*, 2015, pp. 37–46.

[261] T. B. K. Le, M. V Imakaev, L. A. Mirny, and M. T. Laub, “High-resolution mapping of the spatial organization of a bacterial chromosome,” *Science (80-.).*, vol. 342, no. 6159, pp. 731–734, 2013.

[262] A. T. Schredl, Y. G. P. Mora, A. Herrera, M. P. Cuajungco, and S. R. Murray, “The Caulobacter crescentus ctrA P1 promoter is essential for the coordination of cell cycle events that prevent the overinitiation of DNA replication,” *Microbiology*, vol. 158, no. Pt 10, p. 2492, 2012.

[263] G. Zweiger and L. Shapiro, “Expression of Caulobacter dnaA as a function of the cell cycle.,” *J. Bacteriol.*, vol. 176, no. 2, pp. 401–408, 1994.